X-ray spectroscopy and variability of the luminous quasar PDS 456

Gabriele Matzeu

A thesis submitted to Keele University
for the Degree of Doctor of Philosophy

Department of Physics, University of Keele.

January 2017

Abstract

In this thesis I present contemporary X-ray observations of the "Rosetta Stone" of black hole winds, the luminous quasar PDS 456. I perform a detailed analysis of a recent, long *Suzaku* campaign in 2013 (of ~ 1 Ms duration) where the X-ray flux was unusually low. During this campaign PDS 456 displays significant short-term X-ray spectral variability, on time-scales of ~ 100 ks, due to variable absorbing gas crossing the line-of-sight. By investigating the physical properties of these X-ray absorbers I find that they constitute the same inhomogeneous ultra fast accretion disc-wind ($v_{\mathrm{w}} \sim 0.25c$), which is characterized by highly ionized gas, relatively close to the SMBH and colder, denser clumpy material located further out.

A series of five simultaneous observations of PDS 456 with *XMM-Newton* & *NuSTAR* then resolved the P-Cygni like profile at Fe K, confirming that the absorption originates from a fast ($v_{\max} = 0.35 \pm 0.02c$), wide angle (i.e., $\Omega \gtrsim 2\pi$) wind, capable of causing significant feedback between the black hole and its host galaxy. Collating all the *Suzaku* and *XMM-Newton* & *NuSTAR* observations from 2007–2014, I show that the wind velocity appears correlated with the X-ray luminosity, which may imply that the wind is radiatively driven.

The last part of the project is focused on the broadband analysis of PDS 456 from the 2007 archival *Suzaku* data (~ 370 ks in duration), where the quasar was observed in a high-flux state and the unabsorbed AGN primary continuum was revealed. Significant spectral variability is present during the intrinsic X-ray flares that are present in this observation, which are likely driven by fluctuations in a two-component (accretion disc plus corona) continuum. This takes the form of a variable soft X-ray excess (< 1 keV), likely to be the Comptonized tail of the accretion disc emission, as well as a high energy powerlaw. The X-ray emission in PDS 456 appears to originate from two distinct regions:- (i) a warm, optically thick layer of gas blanketing the disc, which is responsible for the soft X-ray excess and (ii) a hot/thin electron corona above the disc, which produces the hard X-ray emission. The latter is typically $10R_{\mathrm{g}}$ in extent and appears to be Compton cooled by soft X-ray emission.

Acknowledgements

I would like to express my ultimate gratitude to my supervisor, Dr. James Reeves who, due to his enormous knowledge and passion for X-ray astronomy, has provided me with indispensable guidance over the last four years. Without his immeasurable support this thesis would not have materialized. His devotion to, and his excitement for science made me "step up my game" and for this I will be for ever grateful.

I would also like to thank Dr. Emanuele Nardini for his invaluable support, his scientific knowledge and for helping me keep my 'sanity' intact. During this Ph.D I also had the pleasure of working with Dr. Valentina Braito whose technical and scientific advice I am very grateful for. These past four years have certainly not been a solitary journey and I was lucky enough to share mine with Michele Costa whose exceptional computing skills helped me a great deal and I cannot thank him enough. I would also like to thank Dr. Jason Gofford for his reassuring support throughout.

Without the immense emotional support, strength and patience provided by the wonderful Dawn Waddell I would not have made it this far in any way shape or form! I would also like to thank Clint Clements for being a great friend who I shared many a night cap with as we chatted science late into the night. During this Ph.D I also lost two beloved members of my family, my uncle Toni Gabriele and my brother-in-law Darren Waddell and they will be always in my thoughts.

Lastly (but not least) I would like to thank my parents Tina and Raimondo Matzeu who I have not seen enough of during these four years, however their moral support has always been present and strong.

Publications

Refereed

- Reeves, J. N.; Braito,V. ; Gofford, J.; Sim, S. A.; Behar, E.; Costa, M. T.; Kaspi, S.; **Matzeu, G. A.**; Miller, L.; O'Brien, P. T.; Turner, T. J.; Ward, M. J.; 2014, ApJ, 780, 45,*Variability of the High-velocity Outflow in the Quasar PDS456.*
- Gofford, J.; Reeves, J. N.; Braito, V.; Nardini, E.; Costa, M. T.; **Matzeu, G. A.**; O'Brien, P. T.; Ward, M. J.; Turner, T. J.; Miller, L.; 2014, ApJ, 784, 77, *Revealing the Location and Structure of the Accretion Disk Wind in PDS456.*
- Nardini, E.; Reeves, J. N.; Gofford, J.; Harrison, F. A.; Risaliti, G.; Braito, V.; Costa, M. T.; **Matzeu, G. A.**, G. A.; Walton, D. J.; Behar, E.; Boggs, S. E.; Christensen, F. E.; Craig, W. W.; Hailey, C. J.;Matt, G.; Miller, J. M.; O'Brien, P. T.; Stern, D.; Turner, T. J.; Ward, M. J.; Science, 2015, 347, 860, *Black hole feedback in the luminous quasar PDS456.*
- **Matzeu, G. A.**; Reeves, J. N.; Nardini, E.; Braito, V.; Costa, M. T.; Tombesi, F.; Gofford, J.; MNRAS, 2016, **458**, 1311-1329, *Short-term spectral variability of the quasar PDS456 observed in a low flux state.*
- **Matzeu, G. A.**; Reeves, J. N.; Nardini, E.; Braito, V.; Costa, M. T.; Tombesi, F.; Gofford, J.; Astronomische Nachrichten, 2016, Vol.337, Issue 4-5, p.495, *Broadband short term variability of the quasar PDS 456.*
- **Matzeu, G. A.**; Reeves, J. N.; Nardini, E.; Braito, V.; Turner, T. J.; Costa, M. T., MNRAS 2017, **465**, 2804-2819, *X-ray Flaring in PDS 456 Observed in a High Flux State*, Monthly Notices of the Royal Astronomical Society

Contents

List of Figures

List of Tables

1 Introduction

It is now established that most galaxies contain a *Super Massive Black Hole* (SMBH) at their centre, with typical mass ranging from $\sim 10^6 - 10^{10}\,M_\odot$ (Salpeter 1964; Lynden-Bell 1969; Kormendy & Richstone 1995; Magorrian et al. 1998; Kormendy & Ho 2013). In most galaxies it is largely the nuclear fusion reactions, that take place at the core of their hosted stars, that is responsible for the majority of their energy output (i.e. through the combined electromagnetic radiation emitted from all stars) typically $\sim 10^{11}\,L_\odot$ (where $L_\odot \sim 3.8 \times 10^{33}\,\mathrm{erg\,s^{-1}}$). However a small proportion of these galaxies (approximately $10 - 20\,\%$) release an enormous amount of radiation usually observed across the entire electromagnetic spectrum coming from within their inner regions (typically $< 100\,\mathrm{pc}$ in size). In these small regions bolometric luminosities of the order of $L_{\mathrm{bol}} \sim 10^{44} - 10^{48}\,\mathrm{erg\,s^{-1}}$ are produced (e.g., Woo & Urry 2002; Lusso et al. 2010) often outshining the rest of the host galaxy by a factor of 100 or more. Galaxies with these properties are identified as *active galaxies* whilst their central inner regions, or nuclei, are consequentially named as *Active Galactic Nuclei* (AGN hereafter).

Furthermore it has been observed that the large fraction of radiation emitted in active galaxies does not follow the typical pseudo-blackbody spectra observed in stars but rather the contribution of *non-thermal* radiation (see § 1.3.1) extended over a broader energy distribution. More specifically, the Spectral Energy Distribution (SED hereafter) of an active galaxy differs considerably from a normal galaxy where its emission ranges over the entire electromagnetic spectrum i.e., from radio to γ-rays as shown in Fig 1.1. Consequently in active galaxies, the vast majority of the emitted bolometric luminosity cannot be supplied by stars or interstellar gas but instead is released through different radiation mechanisms, some of which I will discuss later in § 1.3. For these reasons AGN are considered the most energetically persistent astrophysical objects in the Universe that can be observed (in particular quasars) at extremely high redshifts (e.g., $z \gtrsim 7$ Mortlock et al. 2011, corresponding to a time when the universe was only $\sim 6\%$ of its current age). These unique properties allow astronomers to probe the early Universe and subsequently investigate the evolution of both normal and active galaxies over cosmic time.

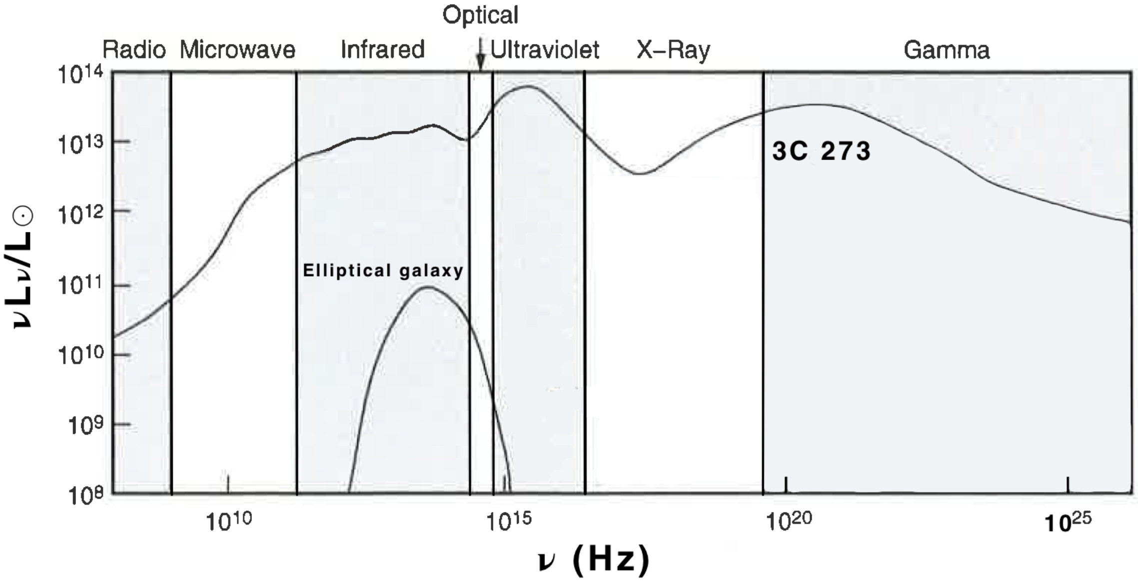

Figure 1.1: The SED of the luminous quasar 3C 273 in comparison to that of a more common elliptical galaxy. It is clear that the quasar emission is extended over the full range of the electromagnetic spectrum (from radio to γ-rays) originating from a range of completely different radiation mechanisms while the radiation from the elliptical galaxy is very narrow as it only corresponds to the superposition of stellar spectra. Figure adapted from Schneider (2015).

In this thesis I present the results of my research which concentrates on the X-ray spectroscopic study of the luminous quasar PDS 456. This is particularly focused on the X-ray energy band from the observations carried out with *Suzaku*, *XMM-Newton* and *NuSTAR* space observatories. In this chapter I will explain how the radiation produced by an AGN can undergo different types of reprocessing before reaching the observer, detected through a modified continuum spectrum (by absorption and/or emission) that can supply important information e.g., through variability, on the physical nature of the re-processor. The main motivation of my work has been to investigate the time-scales at which the X-ray spectral variability occurs in PDS 456, which allowed me to gain a deeper understanding of its physical origin.

The structure of this chapter consists of: (§ 1.1) an initial general overview of active galaxies, where I will introduce the various classes of AGN in the context of the proposed unified scheme. I then in (§ 1.2) give an outline of the accretion process and the structure of the widely accepted Shakura-Sunyaev accretion disc (Shakura & Sunyaev 1973) as part of the central engine of an AGN. Next in (§ 1.3), I will introduce the most relevant radiation processes that are important at the X-ray energies and in (§ 1.4) I will give a summary of the typical spectral components that characterize an AGN spectrum. Lastly, the outline of the remaining thesis chapters will be presented in (§ 1.6).

1.1 Taxonomy of AGN and the proposed unified scheme

There are different physical features that have been observed in AGN such as collimated jet emission together with radio lobes, compact luminous centres, long and short time scale spectral variability, strongly Doppler-broadened emission lines. Thus a broad class of AGN including a large variety of sub-classes have been identified. The principal differentiation that characterizes the AGN phenomenology is based on their degree of radio loudness. Thus the ratio between their radio emission at 5GHz and optical in B-band luminosity was investigated in a sample of 114 objects by Kellermann et al. (1989). Hence in the case when $\frac{L_\nu(5\mathrm{GHz})}{L_\nu} \geq 10$ then the object is defined as *radio-loud* and if not it is *radio-quiet* (e.g., Wilkes & Elvis 1987; Reeves & Turner 2000a).

An additional division can be made in relation to their optical luminosity. On one hand we have a very luminous subclass of AGN named quasi-stellar radio sources or *quasars* for short, with absolute (B-band) magnitudes brighter than $M_\mathrm{B} = -23$ (Schmidt & Green 1983) and on the other, the less luminous ($M_\mathrm{B} > -23$) AGN called *Seyfert* galaxies. A further categorization, leading to yet more diverse subtypes of AGN, depends on the presence or absence of broad optical Balmer lines (i.e. Hα and Hβ) and hence type I or type II AGN respectively. Using these three major divisions, it is possible to place AGN within the three dimensional classification scheme shown in Fig. 1.2 (Tadhunter 2008).

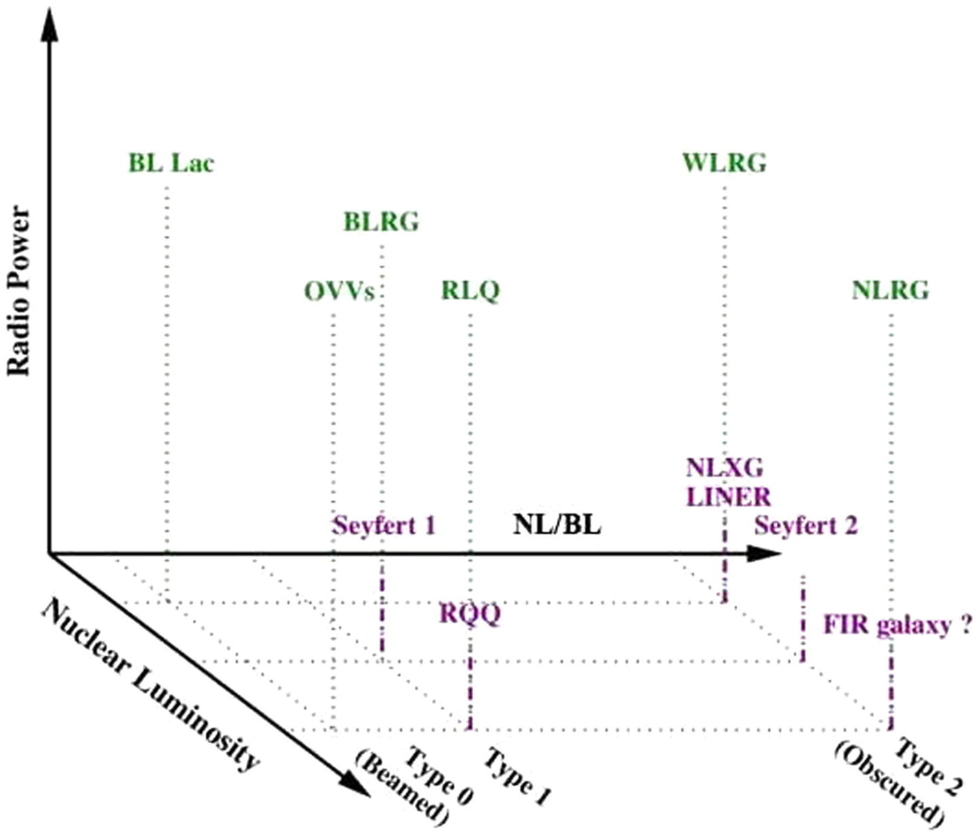

Figure 1.2: A three dimensional classification for AGN in terms of the three major divisions amongst the various classes of AGN: the presence or absence of broad Balmer lines, optical luminosity and radio loudness . The acronyms used are RLQ - Radio Loud Quasar; BL Lac - BL Lacertae Blazar; OVV - Optical Violent Variables; BLRG - Broad Line Radio Galaxy; WLRG - Weak Line Radio Galaxy; RQQ - Radio Quiet Quasar; NLRG - Narrow Line Radio Galaxy; FIR - Far Infrared galaxies; LINER - Low ionization Nuclear Emission-line Region. Figure taken directly from Tadhunter (2008)

1.1.1 Seyfert galaxies

Seyfert galaxies (Seyfert 1943) are considered the most common class of AGN observed in the local Universe (i.e. $z < 0.05$). Their bolometric luminosity ranges from $L_{\mathrm{bol}} \sim 10^{43} - 10^{45}\,\mathrm{erg\,s^{-1}}$. Due to their relative proximity, most Seyfert galaxies are in fact excellent "cosmic" laboratories as their physical processes have been (and currently are) successfully investigated by means of continuously evolving observational techniques (to be discussed in Chapter 3). Seyfert galaxies are separated into two broad types, which are mainly dependent on their relative line widths together with the presence or absence of narrow forbidden lines and Balmer lines (Khachikian & Weedman 1974). These are Seyfert 1 (broad permitted and narrow forbidden lines; Sy1 hereafter) and Seyfert 2 (narrow forbidden lines only; Sy2 hereafter).

Sy1 are characterized by the presence of broad optical permitted lines with Full-Width at Half-Maximum (FWHM) $> 1000\,\mathrm{km\,s^{-1}}$, such as the prominent hydrogen Balmer Hα, Hβ, Hγ as well as C IV and Mg II lines, and narrow forbidden lines with FWHM $< 1000\,\mathrm{km\,s^{-1}}$ like those from [O III] lines, and [N II] among others (e.g., Bianchi, Maiolino & Risaliti 2012). The broad Balmer lines are generated from dense matter with electron density $n_\mathrm{e} \sim 10^9\,\mathrm{cm^{-3}}$ and their line widths are typically observed with FWHM ranging between $10^3 - 10^4\,\mathrm{km\,s^{-1}}$. In contrast the narrow forbidden lines arise from low density gas (i.e. $n_\mathrm{e} \approx 10^3 - 10^6\,\mathrm{cm^{-3}}$), as they are subject to collisional de-excitation at higher densities, with Doppler widths of a few hundreds $\mathrm{km\,s^{-1}}$ (e.g, Osterbrock 1989; Peterson 1997). The broad line emission originates from a region that is typically located relatively close, typically $2 - 27$ light days, to the centre (Kollatschny & Zetzl 2013), also referred to as the Broad Line Region (BLR). On the other hand, the narrow emission lines originate in a region that is more extended from a few pc up to $\sim$ kpc scales (Hainline et al. 2013), which is referred as the Narrow-Line Region (NLR).

In Sy2 objects, sometimes named as ‘narrow-line AGN’, both the forbidden and the permitted emission lines show the same narrow widths and they reveal a much weaker continuum which is frequently dominated by their host galaxy, however they do show strong narrow emission lines, especially from forbidden transitions (Trump et al. 2011). The lack of observed emitted broad lines from Sy2s, indicates that their innermost nuclear gas is obscured along the line of sight by a dusty structure, typically at parsec scales, thought to consist of a toroidal geometry surrounding the central accretion disc (e.g., Antonucci 1993; Urry & Padovani 1995; Veilleux, Goodrich & Hill 1997; Nenkova et al. 2008; Bianchi, Maiolino & Risaliti 2012). However, it was discovered that some Seyfert galaxies are characterized by intermediate variants, such as Seyfert 1.5, 1.8 and

1.9, where the broad lines are still present but with a smaller strength ratio with respect to the narrow lines than Sy1 (Osterbrock 1981).

1.1.2 Narrow-line Seyfert 1 galaxies

An important subset of Sy1 galaxies are categorized as narrow line emission Seyfert 1 galaxies (NLSy1 hereafter), where one of their main distinctions is based on their optical spectra. The Hβ is narrow of the order of FWHM $\lesssim 2000\,\mathrm{km\,s^{-1}}$ which is comparable to a typical Seyfert 1.9 (Osterbrock & Pogge 1985; Goodrich 1989) and they also show strong Fe II lines, where the ratio Fe II/Hβ is twice as strong as other Seyferts. NLSy1 are generally radio quiet and X-ray bright, with strong soft (see § 1.4.4) X-ray excesses (e.g., Laor et al. 1994; Boller, Brandt & Fink 1996; Nardini, Fabian & Walton 2012) and exhibit rapid temporal X-ray variability (e.g., Vaughan et al. 1999, 2011; Lobban et al. 2011; Legg et al. 2012; Giustini et al. 2015). Furthermore, these objects are typically characterized by lower black hole masses than other Seyferts, ranging between $10^{5-7}\,M_{\odot}$; however, as their bolometric luminosities are still comparable to Seyferts it is suggested that they are accreting at an appreciable fraction of their Eddington rate, defined in § 1.2.1, (Collin & Kawaguchi 2004).

1.1.3 Quasars

Quasars were initially identified during a series of large surveys of the sky carried out using radio telescopes in the late 50s and early 60s. Their redshifted Balmer emission lines were soon recognised as one of their main features as well as their high luminosities. The quasar 3C 273 was first identified with a cosmological redshift (Schmidt 1963). Two decades later, with the aid of more sensitive observational instrumentation, it was soon recognized that QSOs are a common phenomenon and hence very numerous in the Universe (Schmidt & Green 1983).

Quasars are considered the most luminous subclass of AGN outshining their own host galaxy by a factor of $10^2 - 10^3$ or more, such that only the core is visible, with

$L_{\rm bol} \simeq 10^{45} - 10^{47}\,{\rm erg\,s^{-1}}$ and they can be seen very far across the Universe. It follows that these objects are characterized by a stellar-like point source emission, and for this reason the term *Quasi-Stellar Object* (QSO) was initially adopted in the mid/late 60s. Even though the terms quasar and QSO have been used as a distinction between radio-loud and radio-quiet AGN respectively, nowadays they equally identify a generic AGN where about 10% are radio-loud (Kellermann et al. 1989) producing strong radio emission, powered by collimated relativistic jet, perpendicular to the plane of the accretion disc (see § §1.2.1 and 1.2.2).

An interesting class of AGN are named as Broad Absorption Line Quasars BALQSOs (see Hamann & Sabra 2004 for a detailed review), characterized by outflows detected in the optical/UV band. The characteristic spectral signatures imprinted on BALQSOs are the blueshifted (from few $\sim 1000 - 10000\,{\rm km\,s^{-1}}$) broad (FWHM $\sim 10^4$ ${\rm km\,s^{-1}}$) absorption line (BAL) troughs due to resonant transitions of ionized metals e.g., C IV, N V, O VI, Si IV, emitted from a fast UV wind. Later on in this thesis I will show that some QSOs present very similar characteristics to the BALQSOs in X-rays, such as the broad blueshifted absorption lines that are detected in the iron K band.

1.1.4 Unification of AGN

The AGN classification can be considered as a stepping stone in identifying their different patterns in behaviour, whereas the AGN unification can be thought as an attempt to understand their fundamental physical properties based on that classification. The basic idea behind the unification scheme is that all types of AGN are intrinsically the same objects. Thus the standard model describes their structure in terms of a central engine, which consists of a central SMBH and an accretion disc. This system is further surrounded by a dusty, pc scale, toroidal structure which is geometrically axisymmetric (e.g., Krolik & Begelman 1988). It follows that the observational differences are due to orientation effects in respect of the line of sight of the observer relative to the "obscuring" toroidal absorber (e.g., Antonucci 1993; Urry & Padovani 1995; Bianchi, Maiolino & Risaliti 2012). A more recent variation of this model is where the "toroidal" structure is thought to be intrinsically clumpy (e.g., Elitzur 2012). In addition to the central engine, AGN comprise of two further regions, already mentioned in (§ 1.1.1), the broad line region (BLR) and the narrow line region (NLR). It is important to note that the size of the toroidal absorber is large enough to obscure the BLR but small enough not to obscure the NLR (Kaspi et al. 2005; Bianchi, Maiolino & Risaliti 2012)

An overall unification scheme is represented schematically in Fig. 1.3, where the type of object that is observed depends on the extent to which the nuclear region is visible. If, for instance, the viewing angle allows the central engine (together with the BLR) to be directly seen, then it follows that the object in question can be classified as type 1 source (or Sy1) where the optical continuum shows broad and narrow lines emitted from the BLR and NLR respectively. On the other hand, if the viewing angle is such that the nuclear region (including the BLR) is impeded by an obscuring opaque torus, then all that is observed are the reprocessed emissions (i.e. absorbed, scattered and reflected) coming from the torus and the NLR. This results in the optical spectrum (in obscured AGN) being dominated by narrow emission lines, hence classifying the object as type 2 source (or Sy2). As it stands, the unification scheme can provide a first order understanding of the AGN phenomenon, predicting differences in appearance based only on the orientation angles relative to the observer, but not accounting for differences in physical properties of the AGN.

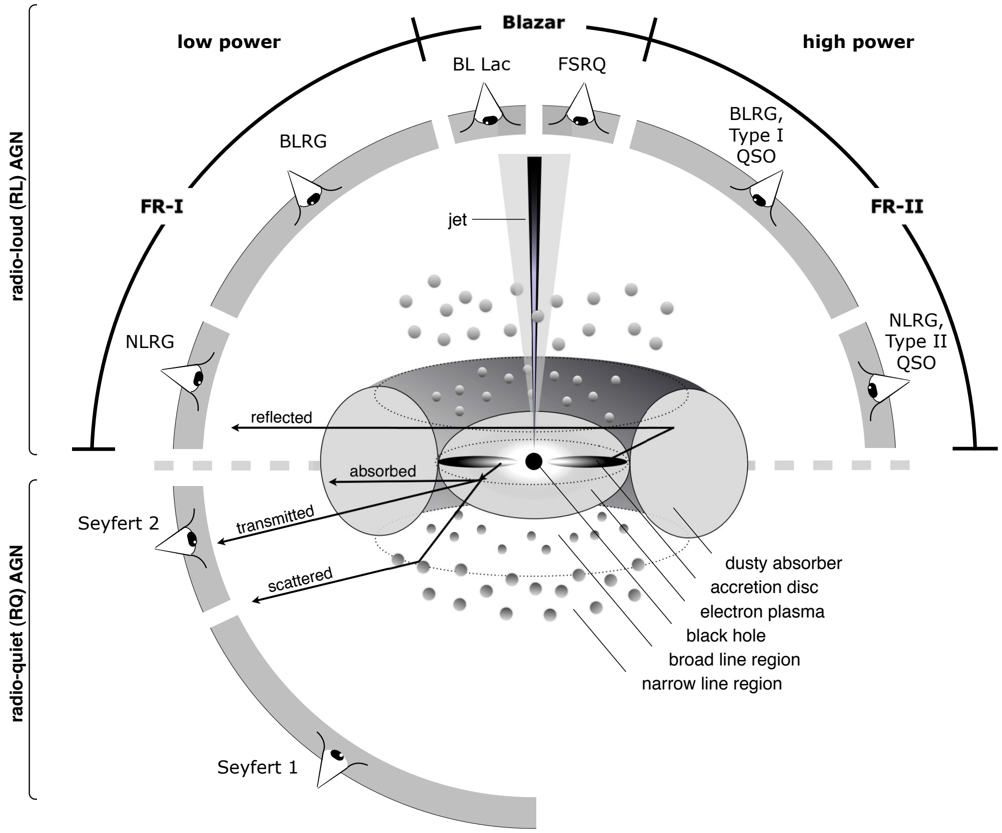

Figure 1.3: Schematic representation of our understanding of the AGN phenomenon in the unified scheme. The central engine is a SMBH that is actively accreting matter from an accretion disc. Note that the electron plasma region can be also defined as *"corona"*. Surrounding the nuclear region is a dusty medium of absorbing material of toroidal geometrical shape and the observer line of sight with respect to it determines if the AGN is a type 1 or type 2 Seyfert. The BLR is responsible for the broad permitted emission lines located at sub-parsec scales. The NLR is further out at kpc scales, responsible for the observed narrow forbidden and permitted lines. The same viewing principle applies for the radio-loud objects with the difference that collimated relativistic jet emission is present. FR-I and FR-II are Fanaroff Riley class I and II galaxy respectively, where FSRQ and BL Lac are Flat Spectrum Radio Quasar and BL Lacertae respectively. Figure taken from Beckmann & Schrader (2012).

1.2 The central engine

In this section, the different physical processes that characterize all different types of AGN will be explored, in particular what is recognised as the AGN main source of energy: the accretion of matter onto a SMBH (e.g., Salpeter 1964; Rees 1984).

1.2.1 The accretion process

One of the most important and efficient astrophysical processes in the Universe is *mass accretion*, (accretion hereafter) where a gravitational body grows in mass via accumulating (i.e. accreting) matter from an external reservoir. Matter accreting on to a central massive object (such as a SMBH) with mass M_{BH} forms a disc if its angular momentum J is too large for it to fall in directly into the central object. This dynamical argument suggests that the matter will be orbiting the central massive object in a Keplerian manner into a flattened structure called an *accretion disc* where its angular momentum at circulation radius R_{circ} is:

$$J_k = \sqrt{GM_{\mathrm{BH}}R_{\mathrm{circ}}}. \tag{1.1}$$

where $G = 6.67 \times 10^{-11}\,\mathrm{m}^3\,\mathrm{kg}^{-1}\,\mathrm{s}^{-2}$ (in SI units) is the universal gravitational constant. The total angular momentum of the system is conserved, however for the matter to fall onto the central compact object, the angular momentum of matter from within the inner region of the disc has to be transported outwards far from the centre. Under these conditions the outer regions of the disc gain angular momentum at the expense of the inner regions allowing matter to fall further inward towards the centre. Shakura & Sunyaev (1973) proposed that the accretion disc has a geometrically thin but optically thick structure where in an AGN, matter is accreted constantly into a SMBH.

The basic assumption in the accretion disc scenario is that matter falling in towards a black hole with mass M_{BH} liberates gravitational potential energy E_{GR}. For a test mass m which is moved from ∞ to a distance r from the central body, the change in gravitational potential energy is:

$$\Delta E_{\mathrm{GR}}(r) = -\frac{GmM_{\mathrm{BH}}}{r}. \tag{1.2}$$

Thus if we consider the rate at which matter M is accreted, (where $\dot{M} = \frac{dM}{dt}$) and the *virial theorem* (i.e., $2\Delta E_{\mathrm{kin}} + \Delta E_{\mathrm{GR}} = 0$) which implies that (for any particle in a stable orbit) only half of the decrease of the gravitational potential (E_{GR}) is transmitted into the increase in kinetic energy (E_{kin}) of the particle, whilst the other half is radiated away as a result of viscosity in the accretion disc (i.e., $\Delta E_{\mathrm{kin}} = -\frac{1}{2}\Delta E_{\mathrm{GR}}$) then the accretion luminosity of the system is:

$$L_{\mathrm{disc}} = -\frac{1}{2}\frac{\mathrm{d}E_{\mathrm{GR}}}{\mathrm{d}t} = \frac{GM_{\mathrm{BH}}\dot{M}}{2R_{\mathrm{in}}} \equiv \eta \dot{M} c^2, \tag{1.3}$$

where η is the degree of accretion efficiency, $\dot{M}$ is the accretion rate, R_{in} is the inner radial distance from the black hole and $c = 2.998 \times 10^8\,\mathrm{m\,s^{-1}}$ is the speed of light in free space.

As matter continues to fall inwards, it eventually reaches the edge of the *innermost stable circular orbit* (R_{isco} hereafter) which is strongly dependent on the black hole spin. For a non-rotating (Schwarzschild) black hole this is $R_{\mathrm{isco}} = 6\,R_{\mathrm{g}}$, where $R_{\mathrm{g}} = GM_{\mathrm{BH}}/c^2$ is the gravitational radii. For a maximally rotating (Kerr) black hole this reduces to $R_{\mathrm{isco}} = 1.235\,R_{\mathrm{g}}$. Thus in the Schwarzschild case where $R_{\mathrm{in}} = R_{\mathrm{isco}} = \frac{6GM_{\mathrm{BH}}}{c^2}$ gives an efficiency of $\eta = 1/12$; however by taking into account general relativistic effects such as photon capture and space-time curvature, the maximum "radiative" efficiency is $\eta = 0.057$ in a Schwarzschild metric (Salpeter 1964) and $\eta = 0.32$ for a maximally spinning black hole (Thorne 1974). Furthermore for an accretion rate of $\dot{M} = 10\,M_{\odot}\,\mathrm{year}^{-1}$, which is a reasonable value for the quasar PDS 456 (Torres et al. 1997), which I will discuss in the later chapters, I get a disc luminosity of $L_{\mathrm{disc}} \sim 5 \times 10^{46}\,\mathrm{erg\,s^{-1}}$ if it is accreting down to $R_{\mathrm{in}} = 6\,R_{\mathrm{g}}$ and $L_{\mathrm{disc}} \sim 2 \times 10^{47}\,\mathrm{erg\,s^{-1}}$ if $R_{\mathrm{in}} = 1.235\,R_{\mathrm{g}}$.

The luminosity produced by accretion is fundamentally limited to a critical value where the outward radiation pressure equals the inward pressure generated by the gravitational force exerted on the in-falling matter by the SMBH. This critical value is named as *Eddington luminosity* L_{Edd} and it is expressed as:

$$L_{\mathrm{Edd}} = \frac{4\pi G M_{\mathrm{BH}} m_{\mathrm{p}} c}{\sigma_{\mathrm{T}}} \simeq 1.3 \times 10^{38} \frac{M}{M_{\odot}} \,\mathrm{erg\,s^{-1}}, \tag{1.4}$$

where $m_{\mathrm{p}} = 1.673 \times 10^{-27}\,\mathrm{kg}$ is the proton rest mass and $\sigma_{\mathrm{T}} = \frac{8\pi}{3}\left(\frac{e^2}{4\pi\varepsilon_0 m_{\mathrm{e}} c^2}\right)^2 \simeq 6.65 \times 10^{-29}\,\mathrm{m^2} \equiv 6.65 \times 10^{-25}\,\mathrm{cm^2}$ (in cgs units) is the Thompson cross-section, where $e = 1.602 \times 10^{-19}\,\mathrm{C}$ is the electron charge, $\varepsilon_0 = 8.854 \times 10^{-12}\,\mathrm{F\,m^{-1}}$ is the permittivity of free space and $m_{\mathrm{e}} = 9.109 \times 10^{-31}\,\mathrm{kg}$ is the electron rest mass. To sustain the Eddington luminosity a critical mass accretion rate is needed:

$$\dot{M}_{\mathrm{Edd}} = \frac{L_{\mathrm{Edd}}}{\eta c^2}, \tag{1.5}$$

where $\dot{M}_{\mathrm{Edd}}$ is the *Eddington accretion rate*. In the case when $\dot{M}_{\mathrm{acc}} > \dot{M}_{\mathrm{Edd}}$ resulting in $L_{\mathrm{acc}} > L_{\mathrm{Edd}}$ then the excess accreting material will be blown away due to the radiation pressure exceeding the gravitational pull of the SMBH.

1.2.2 Accretion disc structure

If the disc proposed by Shakura & Sunyaev (1973) is optically thick, then each annulus with area $2\pi r\Delta r$, radiates as a blackbody with temperature $T(r)$, thus from the Stefan-Boltzmann law we have:

$$\Delta L = 2 \times 2\pi r \Delta r \sigma_{\mathrm{SB}} T(r)^4 = \frac{G M_{\mathrm{BH}} \dot{M} \Delta r}{2r^2}. \tag{1.6}$$

Here in the left hand side, $\sigma_{\mathrm{SB}} T(r)^4$ is the flux radiated at a radius r on the disc per unit area and $2 \times 2\pi r\Delta r$ is the area of the emitting annulus (top plus bottom because the disc has two sides). The whole term on the right hand side is half of the change in gravitational potential through an annulus Δr of the accretion disc as the particle flows inward. This yields for $T(r)$:

$$T(r) = \left(\frac{G M_{\mathrm{BH}} \dot{M}}{8\pi \sigma_{\mathrm{SB}} r^3}\right)^{\frac{1}{4}}. \tag{1.7}$$

A more complex derivation accounting for the viscous dissipation and in the limiting case where $r >> R_{\mathrm{g}}$ gives:

$$T(r) = \left(\frac{3GM_{\mathrm{BH}}\dot{M}}{8\pi\sigma_{\mathrm{SB}}R_{\mathrm{s}}^{3}}\right)^{\frac{1}{4}} \left(\frac{r}{R_{\mathrm{s}}}\right)^{-\frac{3}{4}} \tag{1.8}$$

where $R_{\mathrm{s}} = \frac{2GM_{\mathrm{BH}}}{c^2}$ is the Schwarzschild radius. After further algebra which includes substituting for R_{s} in the brackets and expressing $\dot{M}$ in terms of the Eddington mass accretion rate $\dot{M}_{\mathrm{Edd}}$ (equation 1.5), this can be expressed more conveniently as (see Peterson 1997, page 37):

$$T(r) = 3.5 \times 10^{7}\eta^{-\frac{1}{4}} \left(\frac{\dot{M}}{\dot{M}_{\mathrm{Edd}}}\right)^{\frac{1}{4}} \left(\frac{M_{\mathrm{BH}}}{M_{\odot}}\right)^{-\frac{1}{4}} \left(\frac{r}{R_{\mathrm{s}}}\right)^{-\frac{3}{4}} \mathrm{K}. \tag{1.9}$$

From this it is clear that $T(r) \propto r^{-\frac{3}{4}}$ so the temperature increases radially inwards, suggesting that the structure of the disc may be characterized by a series of circular annular segments, each emitting as a blackbody. The overall contribution of these annuli can also be described as a superposition of the different blackbody emission in the accretion disc (i.e., multi-colour disc blackbody emission). Furthermore at a given radius, the overall temperature of the disc increases with mass accretion rate but scales down with increasing black hole mass. Thus for a QSO with a typical black hole mass of $M_{\mathrm{BH}} \sim 10^{9} M_{\odot}$ accreting with $\eta \sim 0.1$ close to its Eddington rate, this would imply the temperature of the inner disc at $r = 10\,R_{\mathrm{s}}$ is $T \sim 10^{5}\,\mathrm{K}$ (corresponding to $\sim 10\,\mathrm{eV}$). Therefore, the thermal blackbody emission for the innermost accretion disc around a SMBH is expected to peak in the UV band (see Fig. 1.6).

1.3 Radiative processes

In the above section I described the accretion mechanism that powers the central engine of AGN and earlier in § 1.1, I also discussed how the luminosity in specific energy bands and the width of AGN main optical line emissions is adopted as the principal criteria on classifying active galaxies into the sub-groups. In this section I describe the relevant radiative and atomic processes caused by the interaction between photons and particles (atoms, ions and electrons) that are important in the X-ray domain.

1.3.1 Comptonization

Compton scattering is a physical process where an interaction between an high-energy photon and an free non-relativistic ($v_{\mathrm{e}} \ll c$) electron takes place. In this process, when the (X-ray or γ-ray) incident photons are colliding, a portion of the energy and momentum that is carried is transferred to the electrons, which subsequently recoil from the collision. As a result, the photons are scattered off in a new direction with reduced energy and change in momentum. Thus the larger the change in direction of the photon, the larger the energy transfer towards the electron will be. This relationship can be described, in wavelength space, as:

$$\lambda' - \lambda = \Delta\lambda = \frac{h}{m_{\mathrm{e}}c}(1 - \cos\theta), \tag{1.10}$$

where λ is the wavelength of the incident photon, λ' is the post-scattering wavelength of the photon, θ is the scattering angle and $h = 6.626 \times 10^{-34}\,\mathrm{J\,s^{-1}}$ is the Plank constant.

Depending on the kinematics of the incident photons and electrons the outcome of the collision would differ rather drastically. Thus when the electrons are relativistic ($v_{\mathrm{e}} \sim c$) and have more energy than the incident photons, the Compton process can lead to the opposite effect, which is referred as *inverse Compton scattering* (or Comptonization). In this physical process the low-energy photons can gain in energy and momentum when propagating through a field of relativistic electrons (e.g. in a corona above the accretion disc). The more photon–electron interactions occur the more energy is given to the photons and as the electrons lose their energy, the process will reach a state of energetic equilibrium at the 'Compton temperature' (e.g., Fabian et al. 2015). Thus the Compton up-scattering process can be regarded as a cooling mechanism of the electron field (see § 5.6.2) which follows the Comptonization of less energetic photons into the X-ray regime. As I discussed in the previous section the inner accretion disc temperature of a typical AGN would be too low to radiate in the X-ray band, thus Comptonization is considered the principal mechanism that is responsible for the observed X-ray emission in the spectrum. Comptonization models used in this thesis will be discussed in § 3.4.

1.3.2 Photoelectric absorption and line emission

As I mentioned at the beginning of this chapter, the intrinsic X-ray continuum produced in an AGN can be modified by the presence of absorbing material along the line-of-sight observed as spectral features imprinted in the spectrum. At X-ray energies, the most likely photon-matter interaction is through the photoelectric effect, where an atom absorbs a photon with enough energy to remove its single primary electron, usually from the lowest energy level K (n=1), as its binding energy is exceeded. As a result the atom becomes ionized and the atomic transition of the electron through this process is termed as bound-free transition. On the other hand if the energy of the absorbed photon does not exceed the binding energy, the electron will not be ejected but instead it may transit to a higher energy level via bound-bound transition inducing the atom into an excited state. During both transitions a photon is removed from the continuum observed as an absorption feature (or line) into the spectrum.

1.3.2.1 Bound-free absorption

The key factor that regulates the amount of photoelectric absorption for a given atom/ion i is the *optical depth*, which is defined as:

$$\tau_i = \sigma(E)_i N_i \tag{1.11}$$

where $\sigma(E)_i$ is the photoelectric absorption cross-section due to i atom/ion and N_i is the column density of the element i along the line-of-sight with cross-sectional area of $1\,\mathrm{cm}^2$. The former is essentially defined as the cross-sectional area of the atom/ion presented to the photon, which has a complex energy dependence. In the simplest framework, the absorption cross-section of neutral hydrogen is zero below the ionization threshold energy of $E = 13.6\,\text{eV}$ and increases sharply at $E_{\text{edge}} = 13.6\,\text{eV}$ (peaking at $\sigma = 6 \times 10^{-18}\,\text{cm}^{-2}$) and then declines as approximately $\sigma(E) \propto (E/E_{\text{edge}})^{-3}$ at higher energies. Note that the column is made up by heavier elements as well as hydrogen thus the total photo-electric absorption cross-section can be regarded a sum of abundance weighted cross-sections for each element. In X-rays the dominant photo-electric cross-section arises from the K-shell edges of carbon through to iron, as well, as the cross sections of hydrogen and helium above their respective ionization thresholds.

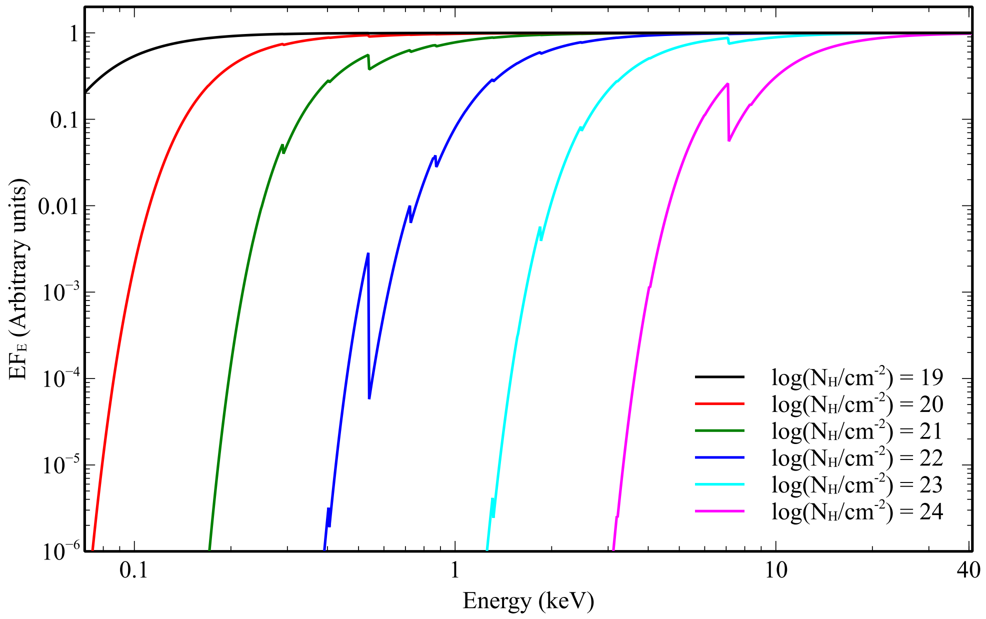

Figure 1.4: Plot showing how the photoelectric absorption in X-rays increases with column density as $\log(N_{\text{H}}/\text{cm}^{-2}) = 19, 20, 21, 22, 23, 24$. Figure adapted from Done (2010)

The transmitted (absorbed) and intrinsic continuum emissions are then related by:

$$F_{\text{obs}}(E) = F_{\text{intr}}(E) \times e^{-\sigma_{\text{eff}}(E) N_{\text{H}}};\ \text{where } \sigma_{\text{eff}}(E) = \sum^{i} \sigma_i(E) \frac{n_i}{n_{\text{H}}}. \tag{1.12}$$

F_{obs} is the observed observed spectrum and F_{intr} is the intrinsic continuum spectrum. Thus the bound-free absorption is a process in which an atom becomes ionized as it loses one or more electrons depending the energy of the incoming photon. This can have an important effect on the overall photoelectric cross-section as the unbalance in the nuclear charge of the ion (surplus of protons), leads to a greater (electron-nucleus) binding energy and the remaining electrons are more tightly bound. This results in a shift in the E_{edge} to higher energies for more highly charged ions as shown schematically in Fig. 1.4.

1.3.2.2 Bound-bound absorption and emission

When an atom absorbs a photon with an energy below the ionization threshold and given that there are sufficient vacancies in the outer electron orbital shells, it can cause a transition of an electron to one of those shells via a line (bound-bound) transition. This process can only occur if the absorbed photon has an energy very close to the quantised energy separation between the different shells. Furthermore when this transition occurs, its signature can be observed as an atomic absorption line imprinted in the spectrum with characteristic energy depending on both the element, its charge state and the specific electron transition. On the other hand when the excited atom returns back to the ground state, the absorption energy is re-emitted as a single (or more) photon with energy characteristic corresponding to the separation between the two orbital shells, which is observed in the spectrum as an emission line. Thus these spectral line features can be considered as the element's unique 'fingerprint' providing information relating to the components and abundances of these elements within the material that is being observed.

The strength of these absorption/emission features is measured through its *equivalent width* (EW) which is defined as the width of a rectangular segment of continuum (down to zero intensity) centred at the energy of the line, whose area contains the same photon flux as in the line profile. In X-rays, the EW is often measured in units of eV which can be effectively expressed as:

$$EW = \frac{\text{Line intensity}\,(\text{photons}\,\text{cm}^{-2}\,\text{s}^{-1})}{\text{Continuum flux}\,(\text{photons}\,\text{cm}^{-2}\,\text{s}^{-1}\,\text{eV}^{-1})} \tag{1.13}$$

1.3.2.3 Photoionized absorption

Normally a free electron can also recombine with ions, however if the X-ray radiation is intense enough the probability of encountering a high energy photon is more likely before recombination. This leads to the overall absorption cross-section being dominated by photoionized ions, rather than neutral atoms, making the highly ionized gas more transparent to the continuum radiation. Furthermore $\sigma(E)$ is also strongly dependent on the ionization state of the material as at increasing ionizations the number of bound electrons are dropping resulting in a decreasing contribution of the lighter elements (as they are completely stripped of all their electrons) to the overall absorption cross-section to the limit where there is no photoelectric absorption at all. Fig. 1.5 shows the flux transmitted through a $\log(N_{\mathrm{H}}/\mathrm{cm}^{-2}) = 22$ column of gas at various ionization stages, ranging from $\log(\xi/\mathrm{erg\,cm\,s^{-1}}) = 0 - 5$, highlighting the decreasing absorption cross-section (and therefore more transmitted flux) at higher ionizations.

The ionization state of a gas can provide vital information of various physical properties of the absorber (as I will discuss later in Chapter 4 and 5) and can be obtained through the definition of the ionization parameter ξ derived in Tarter, Tucker & Salpeter (1969):

$$\xi = L_{\mathrm{ion}}/n_{\mathrm{H}}R^{2}\,\mathrm{erg\,cm\,s^{-1}}, \tag{1.14}$$

where L_{ion} is the typically ionizing source luminosity integrated between $1-1000$ Rydberg, n_{H} is the hydrogen number density and R is the distance of the ionizing source from the absorbing clouds.

Depending on the number of electrons left in the ion, there is a nomenclature that I will also adopt throughout this thesis. More specifically in highly ionized atoms, when they are left with one or two bound electrons they are refereed as hydrogen like (H-like) or helium like (He-like) respectively as the electron configuration resembles that of the hydrogen or helium. Moreover in terms of the H-like ions (e.g., Fe XXVI) I will discuss in later chapters, I will refer to Lyα as the transition from shell transition $n = 1\mathrm{s} \rightarrow 2\mathrm{p}$ (in an absorption line) while Lyβ is from $n = 1\mathrm{s} \rightarrow 3\mathrm{p}$. Furthermore I will refer to Kα and

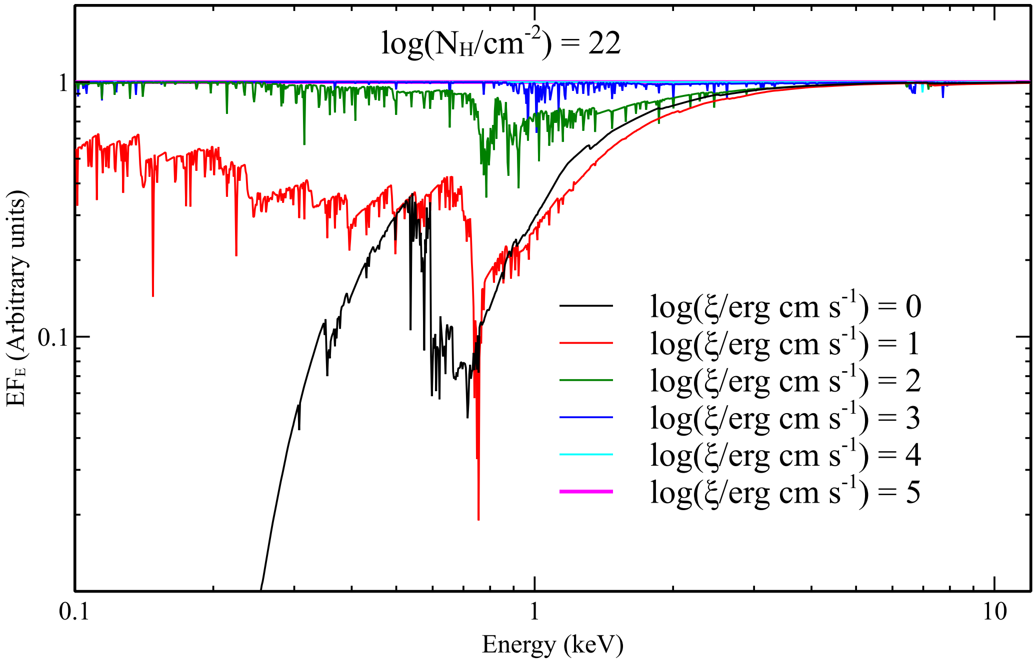

Figure 1.5: Plot showing how the increase of the ionization state of a constant $\log(N_{\rm H}/{\rm cm}^{-2}) = 22$ layer of gas alters the transmitted flux. Note that when the ionization state is at its highest, the photoelectric absorption is virtually absent as the gas becomes fully ionized to most elements.

Kβ a shell transition from $n = 2 \rightarrow 1$ and $n = 3 \rightarrow 1$ (in a fluorescent line emission) respectively.

1.3.2.4 Fluorescence

Fluorescence can occur when a neutral atom (with all its electrons bound) absorbs a high-energy photon that causes the most inner shell (i.e., K-shell) electron to be removed from it. Subsequently the ion may stabilize by filling the electron 'hole' with another electron from a less bound shell via the emission of a 'fluorescence' photon. Alternatively in the case where the electron hole in the K-shell is filled by an electron from the L-shell, the energy released in the process can auto-ionize an M-shell (or L-shell) electron. The ionization process is also known as the 'Auger' effect. The relative probability between fluorescence emission and ionization, given by the fluorescence yield, is strongly dependent upon the nuclear charge i.e., $\propto \sim Z^3$ (Krause 1979) where Z is the proton number. This suggests that a fluorescence line from an heavier element (e.g., as iron) has a much higher probability to be emitted from a lighter one.

1.4 The complex AGN spectrum

The different spectral model components that characterize the observed AGN X-ray spectra are now introduced. An overview of all these components is schematically represented in Figure 1.6. It is important to clarify that not all of these components are observable in every X-ray spectrum of AGN and the origin of some of them is still subject to debate.

1.4.1 Power-law Continuum

The accretion disc around a SMBH with typical temperatures $kT \sim 10-100\,\mathrm{eV}$ (Shakura & Sunyaev 1973), emits the majority of its thermal blackbody radiation at EUV (Extreme Ultra Violet) wavelengths and thus cannot be responsible (at least directly) for the observed X-ray emission. The currently accepted model invokes non-thermal processes as multiple up-scatterings (or inverse-Compton scattering) of photons, originating from the accretion disc, in a putative "corona" of hot (relativistic) electrons typically of a few hundred keV (Haardt & Maraschi 1991; Haardt & Maraschi 1993). The total contribution of these interactions is modelled, over a relatively narrow energy range, (i.e. $2-10\,\mathrm{keV}$) as a law continuum. This is parametrized by the photon flux i.e. $F(E) \propto E^{-\Gamma}\,\mathrm{photons\,cm^{-2}\,s^{-1}\,keV^{-1}}$, where the photon-index values have been typically observed in the $\Gamma \sim 1.7-2.5$ range (e.g., Nandra & Pounds 1994; Reeves & Turner 2000a; Porquet et al. 2004b). At higher energies the hard X-ray emission may show a characteristic "roll-over" depending on the temperature of the coronal electrons.

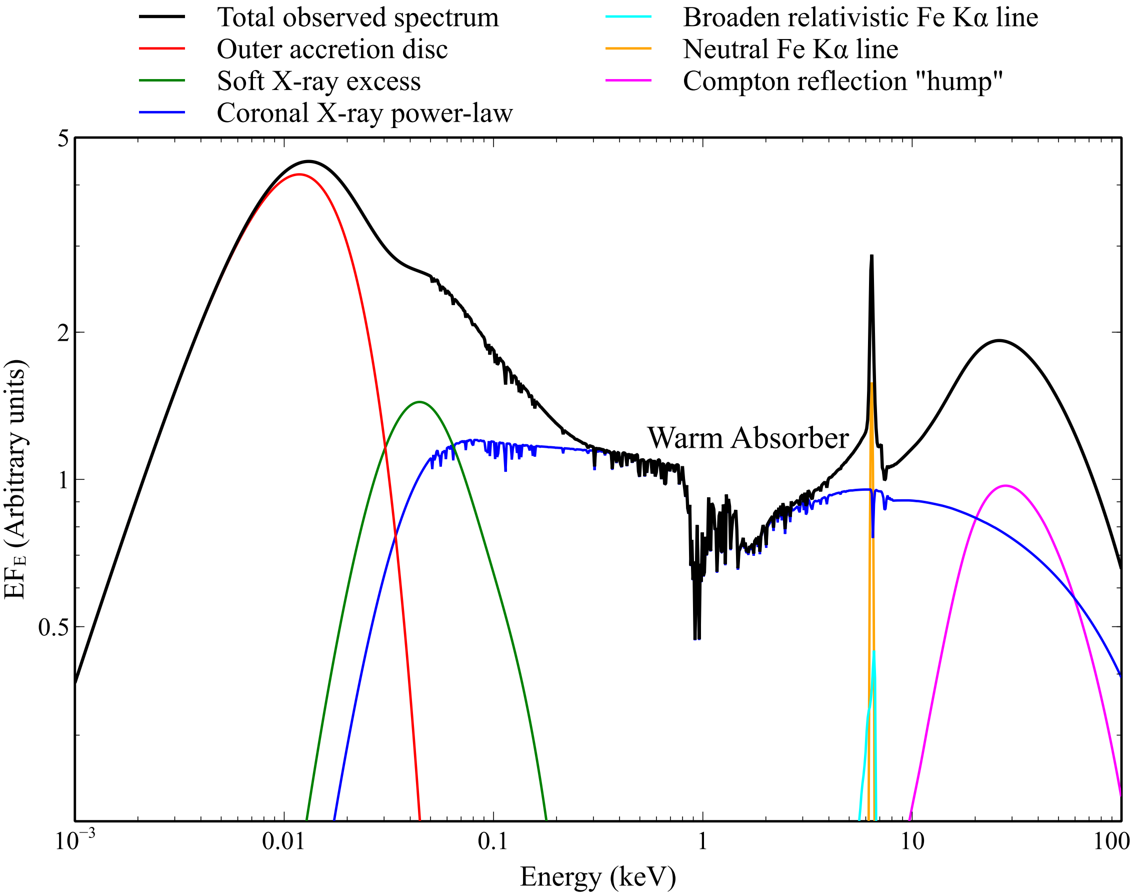

Figure 1.6: Plot showing a toy model including all the main components that characterize the observed AGN optical/UV to X-ray spectrum of a typical Seyfert galaxy. The total observed spectrum is shown in black. The other components shown are: (1, red) the outer disc component which emits as a (colour temperature corrected) blackbody; (2, green) the soft X-ray excess which may arise from the Comptonised disc photons in the 'warm' region of the inner disc; (3, blue) primary X-ray power-law continuum arising from the Comptonized inner disc photons in the hot X-ray corona; (4, cyan) relativistically broadened fluorescence Fe Kα emission line; (5, orange) narrow Fe Kα fluorescence line; (6, magenta) Compton reflection component showing the characteristic 'Compton' hump peaking at ~ 30 keV. The typical spectrum can also show strong atomic features from photo-ionized material at energies $E \lesssim 2-3$ keV, also known as the warm absorber, as well as at iron K. All these features are explained in more detail in the text.

1.4.2 X-ray Reflection

The observed hard X-ray excess (see Figure 1.6) is thought to originate from reprocessing of "primary" X-ray photons continuum in a Compton-thick structure of relatively cold ($T < 10^6$ K) gas present in the nuclear region (Guilbert & Rees 1988; Ferland & Rees 1988; Lightman & White 1988). The physics involved in this process can be modelled as an X-ray continuum isotropically illuminating a slab of cold gas (Zdziarski et al. 1994) or gas in a toroidal geometry (e.g., Yaqoob et al. 2007). Thus in context of the AGN unification schemes, the reflection may arise from scattering off the (slab-like) accretion disc, or off the putative pc-scale torus. The X-ray photons entering the slab, interact with the reflector in different manners. For instance, they can be Compton (down) scattered out of the slab by either free or bound electrons; they can be photoelectrically absorbed, subsequently resulting in fluorescent line emission such as from Fe Kα or Fe Kβ. Due to the energy dependence of photoelectric absorption, most of the incident soft X-ray photons are absorbed whereas hard X-ray photons, on the other hand, are rarely absorbed and hence are Compton down scattered back out of the slab. This interplay between the scattering and absorption cross section gives rise to a broad hump-like shape named "Compton-hump" peaking ~ 30 keV as shown in Figures 1.6 and 1.7.

Reflection per se refers to Compton scattered emission *and* fluorescent line emission produced via the coronal continuum photons illuminating the surface of the disc (or the torus). Thus the reflection spectrum is characterized by a Compton scattering "hump" together with line emission (see Figure 1.7 left panel). Figure 1.7 (right panel) also shows how the reflection spectrum can be *blurred* by transverse Doppler shifts from the relativistic motion of gas in the inner disc. Spinning black holes are also referred to as Kerr black holes (Kerr 1963), where the unit of the spin parameter a is characterized by the black hole's angular momentum J divided by its mass $M_{\rm BH}$ where $a = J/M_{\rm BH} = 0.998$ is for a maximal spin. Especially when the black hole spin is maximal, the spectrum is gravitationally redshifted to lower energies as the *inner most stable circular orbit* (ISCO) reduces to $\sim 1.24\,R_{\rm g}$ (Thorne 1974), as opposed to $6\,R_{\rm g}$ for a non-spinning Schwarzschild black hole with $a = 0$ (see § 1.2.1) and the photons have to "climb" a higher gravitational potential.

Both panels of Figure 1.7 provide a general overview of how the ionization parameter $\xi = 4\pi F/n_{\rm e}$ — where F (erg cm^{-2} s^{-1}) is the flux of the illuminating source and $n_{\rm e}$ (cm^{-3}) is the gas electron density — have an effect on the reflected spectra from an optically thick slab. In the low ionization case i.e. $\log(\xi/{\rm erg\,cm\,s^{-1}}) = 1-2$, the reflection spectra are a combination of a rich and complex set of emission lines superimposed on a strongly absorbed continuum as the photoelectric absorption opacity dominates the electron scattering opacity. As the ionization of the scattering gas increases, i.e. $\log(\xi/{\rm erg\,cm\,s^{-1}}) \gtrsim 3$, all the lighter elements (e.g., O, Ne, Mg, Al, Ar and Ca) and eventually Fe, will become completely ionized and the photoelectric absorption will become negligible while the continuum will resemble the original shape of the illuminating powerlaw (i.e. $\Gamma = 2$ in this case).

1.4.3 Fe Kα complex emission

In the iron K-shell band (5 – 10 keV), the X-ray spectra are characterized by two important emission features, the *narrow* Fe Kα line and *broad* Fe Kα line, that can provide fundamental information regarding the AGN central engine, from the inner regions of the accretion disc to the parsec scale molecular torus. The majority of AGN spectra show narrow line emission from the neutral iron at 6.4 keV originating from distant reflection from material such as the torus, BLR or the outer region of the accretion disc (Krolik & Kallman 1987; Nandra 2006) whilst its strength also depends on iron abundance.

It was also suggested by Fabian et al. (1989) that Fe Kα emissions originating from the inner region of the accretion disc — close to the central SMBH — are subject to broadening due to transverse Doppler shift and gravitational redshift producing the so called “red-wing” (see Figures 1.6 and 1.7) of emission below the central Fe Kα line energy (Fabian et al. 1989; Laor 1991; Tanaka et al. 1995). The X-ray reflection spectra (Figure 1.7) suggest that the narrow Fe Kα can result from non blurred reflection (left panel) from distant gas, while the broad Fe Kα is the result of blurred reflection from

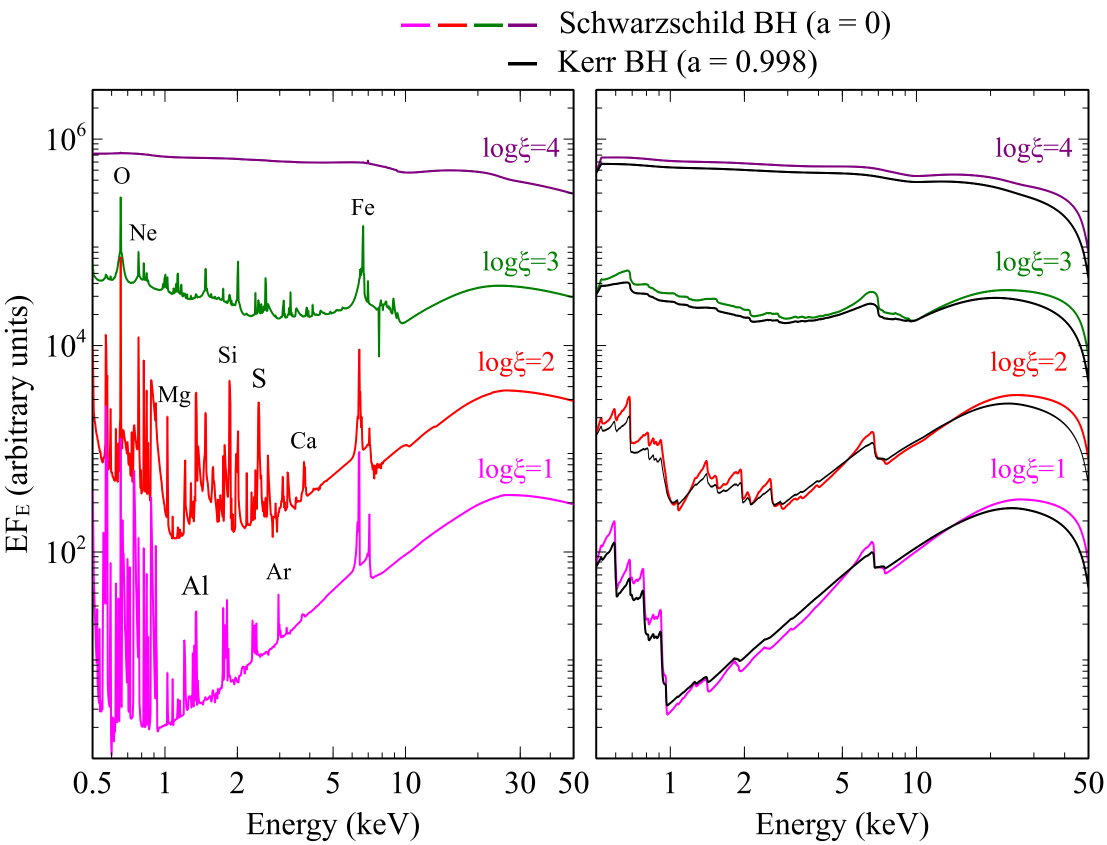

Figure 1.7: Left: Reflection spectra due to the illumination of a uniform slab with varying ionization parameter ξ together with line emission corresponding to various chemical elements. Right: Relativistic blurred reflection spectra; the coloured spectra correspond to a non-rotating Schwarzschild black hole ($a = 0$), while the black spectra correspond to a maximally spinning Kerr black hole ($a = 0.998$).

relativistic gas close to the black hole (right panel).

Furthermore by observing accretion close to the SMBH, the black hole angular momentum could be determined if highly redshifted emission is measured (e.g., Brenneman & Reynolds 2006; Patrick et al. 2011a, 2012). There have been numerous investigations of Seyfert AGN where an apparent broadening of the Fe K feature has been detected (e.g., Reeves et al. 2004; Miller, Turner & Reeves 2008; Reynolds et al. 2009; Patrick et al. 2011b), however the degree of broadening is still debated. Miller, Turner & Reeves (2008, 2009) have also argued that this spectral feature at iron K could be caused by layers of absorbing gas, instead of "blurred" reflected emission from an accretion disc occurring very close to the SMBH due to the continuum curvature imparted by the warm absorber from soft X-rays up to Fe Kα.

1.4.4 Soft Excess

A smooth soft X-ray emission component below $\sim$ 1 keV is commonly observed in unabsorbed AGN (Singh, Garmire & Nousek 1985; Turner & Pounds 1988; Porquet et al. 2004a; Nardini et al. 2011; Nardini, Fabian & Walton 2012), where the power-law component simply fails to account for this extra emission. Studies conducted by Gierliński & Done (2004); Porquet et al. (2004a); Piconcelli et al. (2005) have shown that the soft excess cannot originate directly from the Wien tail (i.e. hard tail) of the accretion disc observed in the UV, arising from the black body emission, as previously thought (e.g., Walter & Fink 1993; Czerny et al. 2003) as this thermal continuum requires disc temperatures far higher than expected. More recently Done et al. (2012) suggested that an increase of the disc effective temperature, caused by Comptonisation of the "seed" photons in a cold ($kT < 1$ keV) optically thick plasma, may be the reason for the observed excess. However a limitation to this scenario is that the physical model requires electron temperatures of the putative "soft" corona to be virtually constant ($\sim 0.1 - 0.2$ keV) over several decades in AGN mass (Gierliński & Done 2004).

Another viable explanation is that the soft excess is due to reflection from the photoionized surface layers located in the inner region (near the SMBH) of the disc itself, where the extreme relativistic blurring, as seen in Figure 1.7, reduces the (narrow) soft X-ray atomic features into a featureless continuum (Fabian et al. 2002; Crummy et al. 2006). Regardless of the validity of the above interpretations, the physical origin of this component it still an open issue and I will discuss it further in chapter 6.

1.4.5 X-ray absorption

Having introduced the principal physical processes involved in both emission and absorption, the latter has also an important role when observed in different parts of the X-ray spectrum. One initial degree of absorption is given by the cold dusty interstellar material (ISM) present in our Galaxy which requires to be accounted for, depending on the position of the target relative to the Galactic plane. Furthermore in the context of AGN, it has been established through numerous spectroscopic studies that X-ray absorption, as revealed through the presence of discrete absorption lines below $E \lesssim 2-3$keV from cosmically abundant elements such as C, N, O, Ne, Mg, Si, S and Fe, is a characteristic of at least $\sim 50\%$ of AGN in the local Universe (e.g., Blustin et al. 2005; McKernan, Yaqoob & Reynolds 2007). Thus the presence of these absorption lines can be associated with circum-nuclear material located in the vicinity of the AGN. In more recent studies, it has been revealed that X-ray absorption associated with He- and H-like iron at $E \gtrsim 6.7\,\mathrm{keV}$ is present in approximately 40% of AGN (Tombesi et al. 2010; Gofford et al. 2013). These absorption lines are usually blueshifted with respect to the AGN rest-frame, strongly suggesting that this material is moving along the line-of-sight towards the observer and hence outflowing. In the next section I will describe in more detail the physical properties of the AGN outflows where I will outline their importance in terms of AGN-host galaxy feedback and their spectral signatures in the X-ray spectrum.

1.5 AGN-host feedback and outflows

AGN may also play an important role in the evolution of their host galaxies. It is now established that the mass of the SMBH is correlated with different properties of the host galaxy bulge e.g., the stellar velocity dispersion (Fig. 1.8). More specifically, the velocity dispersion corresponds to the standard deviation of stellar rotational velocities relative to the mean. Note that from the virial theorem, the kinetic energy (and thus rotational velocity) is directly related to the potential energy of the system. Thus the stellar velocity provides an indirect estimate of the depth of gravitational potential well of the galaxy, which provides an indirect measurement for how massive the galaxy is. Thus the mass of the SMBH is now known to be correlated with several of the host galaxy bulge properties such as:

(i) with the stellar velocity dispersion ($M_{\mathrm{BH}} - \sigma_{*}$, Ferrarese & Merritt 2000; Gebhardt et al. 2000; Merritt & Ferrarese 2001; Ferrarese & Ford 2005; Gültekin et al. 2009; Larkin & McLaughlin 2016),

(ii) with the bulge binding energy (Aller & Richstone 2007),

(iii) with the bulge luminosity ($M_{\mathrm{BH}} - L_{\mathrm{bulge}}$, e.g., Magorrian et al. 1998; Gültekin et al. 2009)

(iv) with the mass of stellar material ($M_{\mathrm{BH}} - M_{\mathrm{bulge}}$, Marconi & Hunt 2003; Häring & Rix 2004; Reines & Volonteri 2015).

Furthermore, it was found that the inferred rate of SMBH growth between $z \sim 1-2$ star-forming galaxies is positively correlated to the star formation rate (SFR), with a constant ratio between the two of $\sim 10^{-3}$ (Mullaney et al. 2012). An almost identical ratio is found for $M_{\mathrm{BH}}/M_{\mathrm{bulge}}$ in quiescent galaxies (e.g., Marconi & Hunt 2003; Häring & Rix 2004), suggesting that there is close coupling between the evolution of the central black hole and the stellar content in the host galaxies. One of these linear correlations between the mass of the black hole and of the stellar material i.e., $M_{\mathrm{BH}} - M_{\mathrm{stellar}}$ (Bennert et al. 2011) is plotted in the left panel of Fig. 1.8, whereas the relationship between the black hole mass and the stellar velocity dispersion is shown on the right panel. Most importantly from these results, it was found that these correlations are present in both active and quiescent galaxies. This suggests that the great majority of galaxies harbour a SMBH at their centre and that at some point during their lifetime they might go through an active quasar phase (common at redshift $z = 2 - 3$), a self-regulating feedback mechanism that insures an ‘equilibrium growth’ between the SMBH and its host environment.

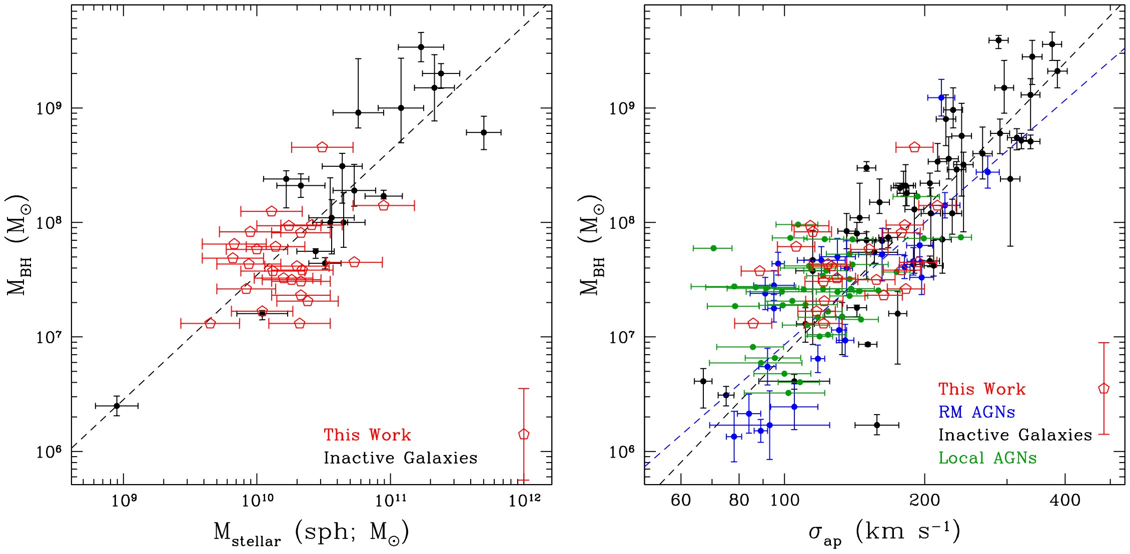

Figure 1.8: Plots showing two of the important linear correlations found between the properties of the host galaxy bulge and the mass of the central black hole. Left panel: the $M_{\rm BH} - M_{\rm stellar}$ relation. Right panel: recent results in relation to the $M_{\rm BH} - \sigma_*$ relation. 'RM AGNs' refers to AGN with a reverberation mapped black-hole mass available in the literature. The $M_{\rm BH} - \sigma_*$ relation currently represents one of the strongest evidences for there being self-regulating feedback at play in AGN. 'This work' refers to results by Bennert et al. (2011), from which both figures are taken.

Furthermore, several works have tried to understand this relation in terms of the negative mechanical feedback, which was found to be likely provided by powerful outflows (or winds) produced by an accreting super-massive black hole (e.g., King 2003, 2010; Di Matteo, Springel & Hernquist 2005; McQuillin & McLaughlin 2013). This correlation is expressed in terms of the mass of SMBH and the stellar velocity dispersion of the host galaxy's bulge and scales as $M_{\rm BH} \propto \sigma^x$ (where $x = 4 - 5$ for SMBH e.g., Ferrarese & Merritt 2000; Gebhardt et al. 2000; Gültekin et al. 2009). In the next section I will discuss the observational evidence and the importance of these outflows.

1.5.1 The importance of winds in context of feedback

A number of massive and high velocity outflows have been detected in luminous AGN (Chartas, Brandt & Gallagher 2003; Reeves, O'Brien & Ward 2003; Pounds et al. 2003; Reeves et al. 2009) through the presence of resonance iron K-shell absorption lines blue-shifted to energies of $E > 7$ keV (in the rest-frame) and are now considered an essential component in the overall understanding of AGN. The faster components of these winds are thought to occur as a result of the accretion process (King 2003; Ohsuga et al. 2009) and the warm absorbers at lower velocities probably are located much further out e.g., pc-scales and greater (e.g., Blustin et al. 2005; Laha et al. 2014). The importance of these winds is supported by their frequent detection, as they are observed in the X-ray spectra of approximately 40% of AGN (Tombesi et al. 2010; Gofford et al. 2013), suggesting that their geometry is characterized by a wide solid angle. This was recently confirmed in the quasar PDS 456 by Nardini et al. (2015) and will be the subject of much discussion in this thesis. These fast outflows are characterized by a considerably high column density ($N_{\rm H} \sim 10^{23}\,{\rm cm}^{-2}$) and a mean velocity $\langle v_{\rm w} \rangle \sim 0.1c$ (Tombesi et al. 2010). However, the velocity of the Fe K absorbers can cover a wide range, from as low as a few $\times 100 - 1000$ km s^{-1} (more typical of what is seen in the soft X-ray warm absorbers (see § 1.5.2.1); Kaastra et al. 2000; Blustin et al. 2005; McKernan, Yaqoob & Reynolds 2007) up to mildly relativistic values of $\sim 0.2 - 0.4c$ in the more extreme cases (e.g., Chartas et al. 2002; Reeves et al. 2009 see § 1.5.2.2). These high velocities can result in a large amount of mechanical power, possibly exceeding the $0.5 - 5\%$ of the bolometric luminosity $L_{\rm bol}$ required for a significant AGN feedback contribution to the evolution of the host galaxy (King 2003; King & Pounds 2003; Di Matteo, Springel & Hernquist 2005; Hopkins & Elvis 2010; Tombesi et al. 2015).

In principle the physical properties of these fast outflows/winds can provide more insight in the mechanism through which they are driven/accelerated, thus two proposed scenarios such as, *radiatively driven winds* (e.g., Proga, Stone & Kallman 2000; King 2003; Proga & Kallman 2004; Sim et al. 2008, 2010; Matthews et al. 2016) and/or *magneto-centrifugally driven winds* (e.g., Ohsuga et al. 2009; Kazanas et al. 2012; Fukumura et al. 2015), are currently investigated. Most studies of the outflows so far have been concentrated on radiatively driven winds and although the magneto-centrifugally driven winds are considered a plausible cause, this mechanism is still less understood.

The former scenario suggests that the AGN radiation pressure drives a wind from the accretion disc around the super massive black hole (SMBH). The detection of blueshifted Broad Absorption Lines (BALs), associated with the UV permitted lines (e.g., Luo et al. 2014), strongly demonstrates that substantial momentum can be transferred from a powerful radiation field to the gas. These type of outflows are described as *line driven winds* and their strength depends on the opacity of the lines (i.e. the amount of radiation that is taken out from the continuum by the lines). The other radiatively driven acceleration mechanism involves Thompson (or Compton) scattering (e.g., King & Pounds 2003; King 2010). In fast outflows some radiation is absorbed from the continuum by the iron K absorption; however, the dominant interaction between the outflowing gas and the radiation field is probably Thompson scattering given the high ionization state of the gas. A direct correlation between the momentum rate of the outflow and the momentum rate of the radiation field i.e. $\dot{P}_{out} \sim \dot{P}_{rad}(= L/c)$, would be expected if the Thomson depth $\tau \sim 1$. This indeed appears to be the case in observations of fast, highly ionized winds (Tombesi et al. 2013) but does require the AGN to radiate at sufficient fraction of L_{Edd}. These types of radiatively driven fast outflows are also described as *Thompson-driven winds.*

1.5.2 Spectral signature of outflows

1.5.2.1 Warm absorbers

The presence of photo-ionized material along the line of sight is observable as absorption features of discrete atomic lines and edges in the soft X-ray spectra at energies $\lesssim 2-3$ keV. The limited energy resolution of earlier X-ray instruments, allowed only to interpret these features as broad absorption edges due to O VII and O VIII (Halpern 1984). The importance of warm absorber features was soon recognised as they were observed in at least ~ 50 per cent of Seyfert galaxies (e.g., Reynolds 1997; George et al. 1998), thus establishing them as a common feature of AGN.

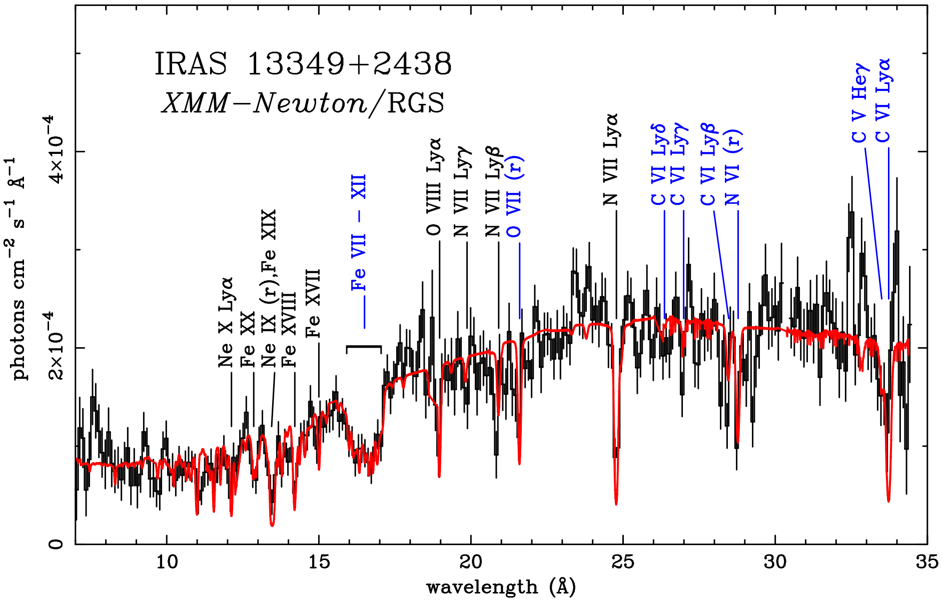

Figure 1.9: X-ray spectrum showing a detailed view of the 'warm absorber' detected in the *XMM-Newton* RGS observation of IRAS 13349+2438 by Sako et al. (2001). The absorber is clearly complex, with a multitude of absorption lines present from ions ranging from He-like carbon through to H-like neon as well as from low ionization iron (Fe VII–XII) in the form of the M-shell UTA. As is shown by the different colour labels, two different ionization state absorbers are required to adequately describe the data. Image taken directly from Sako et al. (2001).

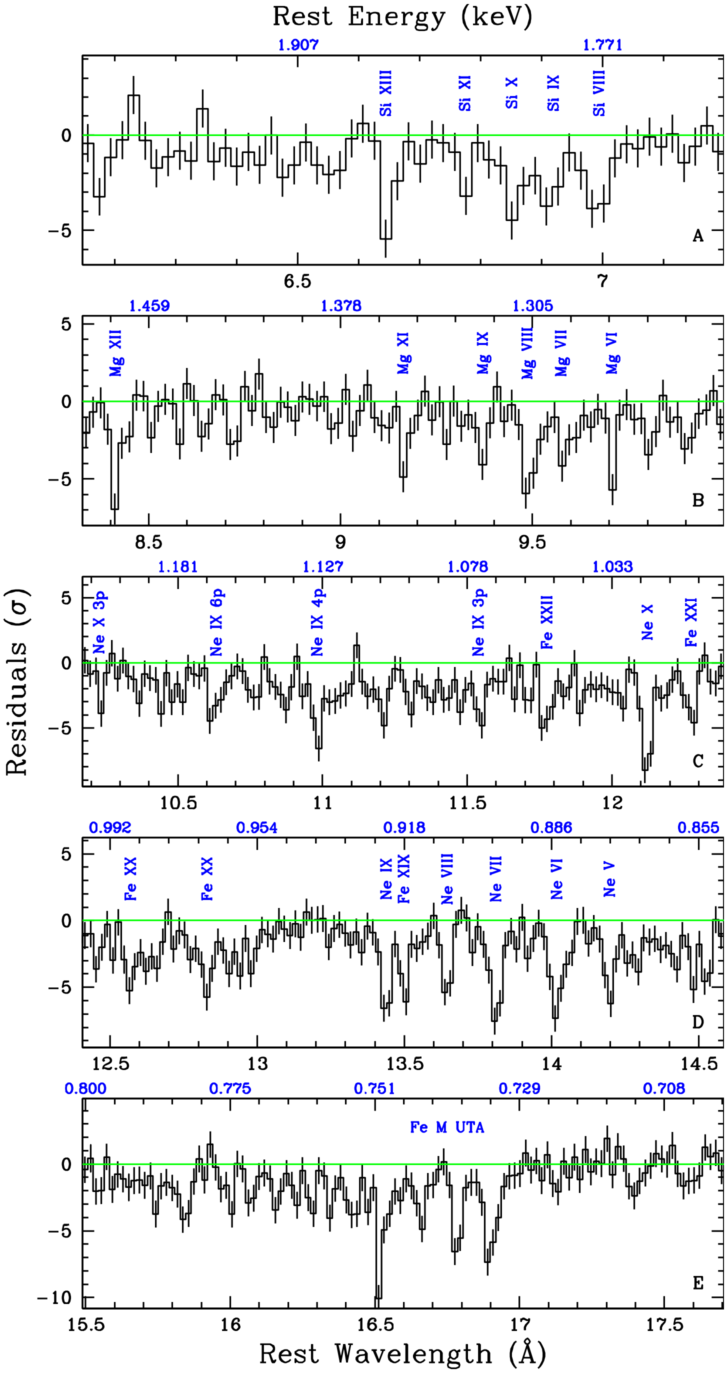

Figure 1.10: Spectrum showing a detailed view of the warm absorber detected in the *Chandra* Medium Energy Grating (MEG) observation of MR 2251–178 showing the large number of blueshifted absorption features present < 2 keV revealing its complexity. The absorption lines present are from: panel (A) Si K band including the inner shell absorption from Si VIII–XIII; panel (B) the Mg K band, including inner shell absorption from Mg VI–XI; panel (C) absorption from Ne IX–X and Fe L-shell; panel (D) inner shell absorption from Neon ions Ne V–IX and panel (E) the iron M-shell unresolved transition array (UTA) band. Figure taken directly from Reeves et al. (2013).

Advances in technology in the following years brought unprecedented throughput and spectral resolution, from grating instruments such as *Chandra* HETG (Canizares et al. 2005) and the *XMM-Newton* RGS (den Herder et al. 2001). These allowed to resolve the discrete soft X-ray absorption as well as emission lines. The presence of the warm absorber is illustrated in Fig. 1.9 in the *XMM-Newton* RGS spectrum of the QSO IRAS 13349+2438, which was one of the first grating observation of an AGN (Sako et al. 2001). Fig. 1.10 shows the *Chandra* MEG (Medium Energy Grating) spectrum of the nearby QSO MR 2251–178 (Reeves et al. 2013) which displays a wealth of blueshifted absorption lines. Perhaps the classic observation of a warm absorber came from the deep (900 ks) *Chandra* HETG observation of the X-ray bright Sy1 NGC 3783 (Kaspi et al. 2002).

As can be seen from the examples, the absorption lines originate from ions covering a wide range of ionization and charge states. High ionization absorption lines are present from the H/He-like ions of C through to Si/S. Low ionization absorption is observed trough the inner K-shell lines of O through to Si (Behar & Netzer 2002), where the L-shell is partially occupied e.g., O I–VI or Mg IV–X. Furthermore absorption is also seen from low charge states of iron (lower than Fe XVIII) in the form of the Fe M-shell Unresolved Transition Array (UTA) (e.g., Sako et al. 2001; Behar, Sako & Kahn 2001), which consists to a blend of lines observed over a typical wavelength range of $16 - 17$ Å. Thus the complexity of these absorbers is evident covering a wide range in ionization and column densities.

The resulting picture of the warm absorber is that it is associated with an outflow where multiple blueshifted narrow absorption lines correspond to different ionization states of the absorbing material (Kaastra et al. 2000; Kaspi et al. 2000; Blustin et al. 2005; McKernan, Yaqoob & Reynolds 2007). In recent studies it was found that, the fraction of sources with reported warm absorbers is > 60 per cent (Tombesi et al. 2013), confirming their relevance in the studies of AGN. The other important feature that characterizes the warm absorber lines is their blueshift, indicating the outflow velocities in the range $v \sim 100 - 1000\,\mathrm{km\,s^{-1}}$ (Kaastra et al. 2000; Kaspi et al. 2000; Blustin et al. 2005; McKernan, Yaqoob & Reynolds 2007; Reeves et al. 2013). There are still significant uncertainties on the exact location of the absorbing material, due to the degeneracy between the density and the distance (estimated to be typically from $\sim$ pc to $\sim$ kpc scales). Thus it has been suggested by Blustin et al. (e.g., 2005); McKernan, Yaqoob & Reynolds (e.g., 2007); Laha et al. (e.g., 2014) that the warm absorber may originate at locations comparable to the obscuring molecular torus or from the NLR. The low velocity of warm absorbing gas tends to indicate an origin much more distant than the sub-parsec accretion disc-wind (e.g., Mrk 509: Kaastra et al. 2012; MR 2251-178: Reeves et al. 2013; NGC 5548: Whewell et al. 2015). Furthermore there have been some cases where faster components in the soft X-ray bands emerged, possibly associated to a disc-wind (e.g., NGC 3516: Turner et al. 2008; Holczer & Behar 2012; NGC 4051: Steenbrugge et al. 2009; Lobban et al. 2011; Pounds & Vaughan 2011; MGC-6-39-15: Holczer, Behar & Arav 2010) with velocities of few thousands $\mathrm{km\,s^{-1}}$ or even faster in some cases up to $\sim 0.1c$ (e.g., PG 1211+143: Pounds et al. 2016; PDS 456: Reeves et al. 2016; IRAS 17020+4544: Longinotti et al. 2015).

1.5.2.2 High velocity iron K absorbers

Besides warm absorbers, highly blueshifted iron K-shell absorption lines (in the $6-9\,\mathrm{keV}$ band) have been detected in more recent years in the X-ray spectra of several AGN (e.g., Chartas et al. 2002; Chartas, Brandt & Gallagher 2003; Pounds et al. 2003; Reeves, O'Brien & Ward 2003; Markowitz, Reeves & Braito 2006; Braito et al. 2007; Chartas et al. 2009; Cappi et al. 2009; Reeves et al. 2009; Giustini et al. 2011; Lobban et al. 2011; Gofford et al. 2013). These lines are commonly associated with resonant absorption from Fe XXV/XXVI, originating from a region of photoionized gas (with ionization parameter $\log\xi \sim 3-6$ erg cm s^{-1}) surrounding the (photoionizing) central X-ray source, with (blueshifted) energies corresponding to velocities from $\lesssim 10000\,\mathrm{km\,s^{-1}}$ reaching (up to) mildly relativistic values of $\sim 0.1-0.4c$ (Reeves, O'Brien & Ward 2003; Reeves et al. 2009; Tombesi et al. 2011; Gofford et al. 2013).

The properties of these absorption lines provided strong evidence of a previously unknown massive (column density $N_{\mathrm{H}} \sim 10^{22}-10^{24}$ cm^{-2}) and highly ionized absorbing material outflowing very rapidly from the active nuclei, possibly in the form of disc-wind/ejecta (King & Pounds 2003; Proga & Kallman 2004; Sim et al. 2008, 2010; Ohsuga et al. 2009; King 2010) or the base of a weak jet (e.g., Ghisellini, Haardt & Matt 2004), also described as *Ultra Fast Outflows*. One of the earliest examples of a fast outflow was in the nearby ($z = 0.0809$) QSO PG1211+143 (Pounds et al. 2003). Indeed in this AGN a characteristic P-Cygni profile is evident (Pounds & Reeves 2009) which is shown in Fig. 1.11 at iron K. This is comprised of both broad emission and absorption lines centred at the rest-frame energies of $E \sim 6.5\,\mathrm{keV}$ and $E \sim 7.7\,\mathrm{keV}$, where the latter is blueshifted implying an outflow velocity of $\sim 0.1c$. On the other hand, as the emission results from a range of angles and not just along the line-of-sight, it will be redshifted with respect to the absorption. The presence of a P-Cygni profile has also been detected in PDS 456 and I will present the results later in Chapter 4.

Although initially controversial, ultra fast outflows are now thought to be a common phenomena in AGN and Tombesi et al. (2013) investigated the possible relations between these fast outflows, and the soft X-ray warm absorbers. It was found that the fraction of AGN observed with ultra fast outflows was > 34 per cent, of which > 67 per cent also show warm absorbers and for the first time significant correlations among them were evaluated. Tombesi et al. (2013) showed that there is a continuous range in properties from the ultra fast outflow to the much slower warm absorber observed at greater distance (pc scales). Tombesi et al. (2013) devised a scheme whereby the disc-wind can be launched (either radiatively or by MHD process) over a range of scales. Thus the properties of the wind derived from the X-ray spectrum will depend upon where in our line-of-sight we observe the wind and at which radius the gas is launched. A simple schematic where it is illustrated a typical stratified accretion disc-wind is shown in Fig. 1.12.

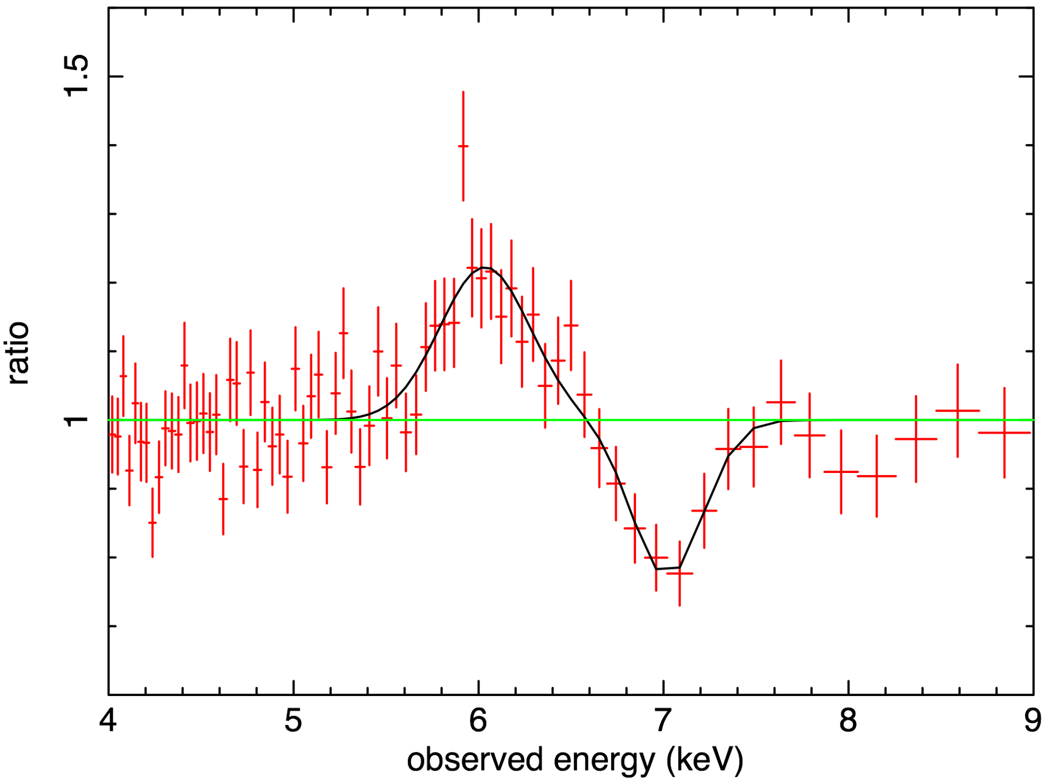

Figure 1.11: Spectrum showing the characteristic P-Cygni profile in the Fe K band (shown here in the observed frame), arising from the contribution of broad emission and blueshifted absorption lines. Thus after accounting for the AGN redshift ($z = 0.0809$), the centroid energies of the emission and absorption are $E \sim 6.5\,\mathrm{keV}$ and $E \sim 7.6\,\mathrm{keV}$, which suggests an outflow velocity of $\sim 0.1c$ if identified with Fe XXV Heα or Fe XXVI Lyα. Note the red-wing of the emission (compared to the blueshifted absorption) may be as a result of the re-emission from the receding part of the wind. In this case, the wind covers a wide range of solid angles, where the authors inferred a half opening angle of $\sim 50°$ for the wind. Figure taken directly from Pounds & Reeves (2009).

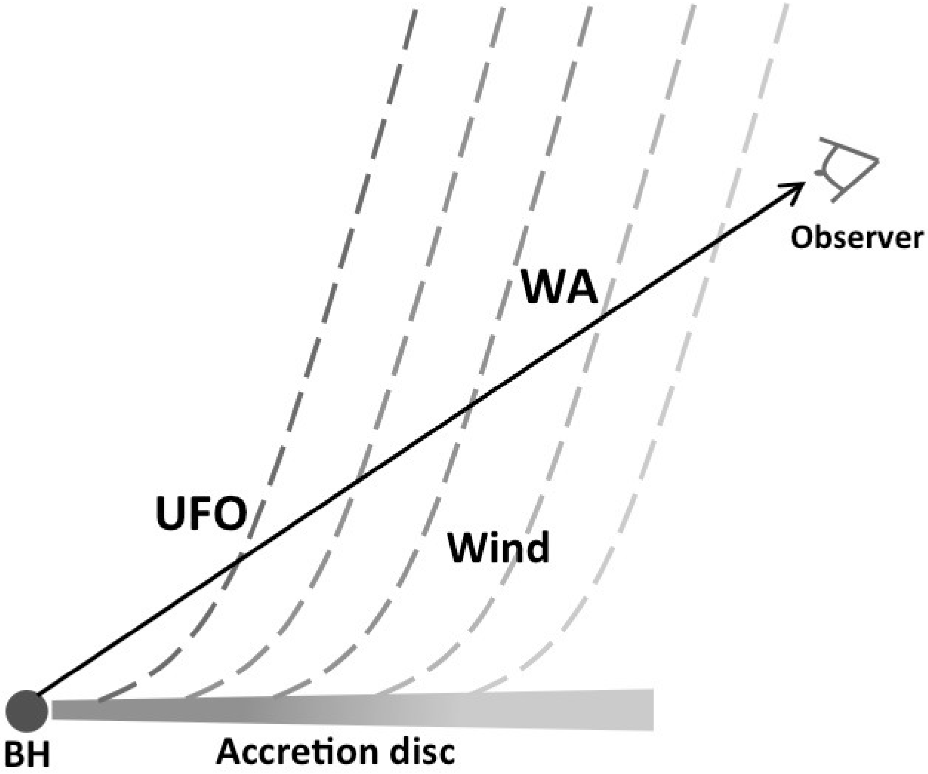

Figure 1.12: A schematic illustration of a stratified accretion disc-wind (not to scale) showing the different components of the wind. Note that as ultra fast outflows (UFOs) are more ionized, this implies that they are launched closer in the black hole where the radiation is more intense. On the other hand, the less ionised outflows are likely to be located further out. Figure taken directly from Tombesi et al. (2013).

1.6 Aims and motivations of this thesis

Following from this, the aim of the thesis is to understand the physical properties and the nature of the ultra fast outflows by studying one prototype example that is known, the quasar PDS 456. Thus the subsequent chapters in this thesis are organised as follows:

Chapter 2 I introduce PDS 456, including its discovery and the initial multiwavelength and X-ray properties.

Chapter 3 Here I give an overview of the X-ray observatories used in this work (*Suzaku*, *XMM-Newton*, *NuSTAR*), the data analysis and an introduction to the spectral models commonly used.

Chapter 4 Describes the multi-epoch *Suzaku* and *XMM-Newton*/*NuSTAR* observation of PDS 456, from 2007–2014, where the long term variability of the wind is discussed.

Chapter 5 I will present the short-term variability of the absorbers in PDS 456, from an unusually low flux state observation with *Suzaku* in 2013.

Chapter 6 Here I present the short-term variability in PDS 456 observed in an unobscured state and I discuss the intrinsic continuum variability.

Chapter 7 I will summarise the major conclusions that are drawn from this work, by putting my findings into a broader context to other AGNs and some avenues for future work.

2 The luminous radio-quiet quasar PDS 456

2.1 Discovery of PDS 456

The luminous radio-quiet quasar PDS 456 was discovered serendipitously during the course of the Pico dos Dias Survey (PDS) by Torres et al. (1997). Based on the position of the H$\beta\lambda$4860 narrow emission line (Torres et al. 1997) and on the basis of the [Fe II]λ1.6435 μm forbidden emission (Simpson et al. 1999), PDS 456 is located at redshift of $z = 0.184 \pm 0.001$. PDS 456 is also located very close to the Galactic plane with column density of $N_{\rm H} = 2 \times 10^{21}\,{\rm cm}^{-2}$. Torres et al. (1997) calculated a de-reddened absolute blue (B) magnitude of $M_{\rm B} \sim -26.7$ for PDS 456 and after being corrected for optical extinction $A_{\rm V} \sim 1.5$, it was found that it is more luminous than the well known radio-loud quasar 3C 273 ($z = 0.158$ and $M_{\rm B} \sim -26.3$). This comparison is shown on the left panel of Fig. 2.1, where these two objects are compared with the complete list of quasars from the Veron-Cetty & Veron (1996) catalogue where the bolometric luminosity of PDS 456 is $\sim 30\%$ larger than 3C 273, making it the most luminous quasar in the local Universe ($z < 0.3$) with a bolometric luminosity of $L_{\rm bol} \sim 10^{47}\,{\rm erg\,s^{-1}}$ (Reeves et al. 2000; Yun et al. 2004). Another important aspect revealed by Fig. 2.1 (left panel) is that such a high value is more typical of quasars at redshift $z = 2 - 3$, which is considered the peak of the quasar activity, when AGN feedback is thought to have played a major role in the evolution of galaxies (Di Matteo, Springel & Hernquist 2005).

Moreover, plotted on the right panel of Fig. 2.1 is the optical spectrum of PDS 456 obtained by Torres et al. (1997). This spectrum shows a prominent Hβ emission profile that consisted of a broad (FWHM $= 3974 \pm 794\,{\rm km\,s^{-1}}$) and a narrow (FWHM $= 1239 \pm 56\,{\rm km\,s^{-1}}$) component, where the latter was used for the calculation of the redshift of PDS 456 as it allowed for a more accurate measurement. The other features are the multitude of the Fe II lines that dominate the spectrum; furthermore the [O III]λ5007 forbidden emission line is weak and blended with the Fe II multiplets. This is therefore consistent with an anti-correlation between the Fe II and [O III] found by Boroson &

Green (1992), where a low [O III] to Fe II ratio can be a tracer of the Eddington ratio $L_{\rm bol}/L_{\rm Edd}$. This suggests that PDS 456 is accreting at a high fraction of the Eddington rate, which is quantified later in chapters 4 and 6. In § 1.1.2 I discuss that NLSy1 are characterized by a high accretion rate (high $L_{\rm Edd}/L_{\rm bol}$) and regardless of whether the FWHM of the Hβ in PDS 456 is beyond the expected threshold of $2000\,{\rm km\,s^{-1}}$ for being identified as a NLSy1, it certainly shows similar properties. Furthermore in the later chapters, I will show that PDS 456 exhibits rapid X-ray variability, while it also presents a relatively steep intrinsic continuum; these are both regarded as common properties of a high accretion rate as seen in NLSy1s.

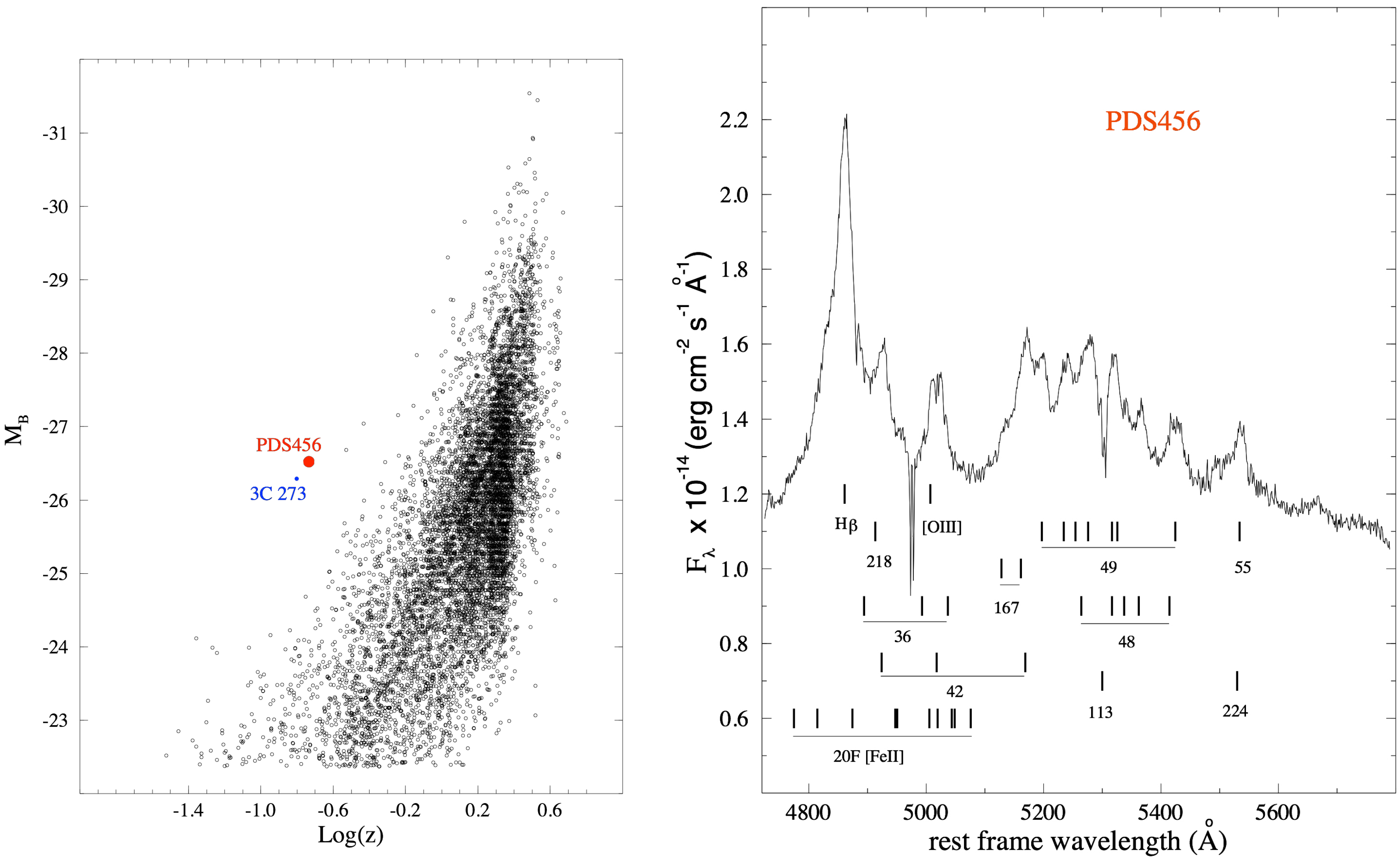

Figure 2.1: Left: absolute magnitude comparison between PDS 456 and the complete list of quasars in the Veron-Cetty & Veron (1996) compendium. This is also showing that PDS 456 is more luminous than the radio-loud quasar 3C 273 making it the most luminous object in the local Universe ($z < 0.3$). Right: The optical spectrum of PDS 456 where the most prominent features detected are the Hβ emission line and a multitude of Fe II emissions. A weak [O III] forbidden emission blended with the Fe II multiplets is also detected. Note that a low [O III]/Fe II can be an accurate indication of high accretion rates, which seems to be the case in PDS 456. Both Figures are adapted from Torres et al. (1997).

A later study of PDS 456 by Simpson et al. (1999), where broad band infrared to optical spectroscopy was performed, found a striking similarity of the shape and luminosity of the SED when compared with 3C 273, as is shown on Fig. 2.2. This led to the conclusion that PDS 456 can be regarded as the radio-quiet counterpart of 3C 273 (Simpson et al. 1999; Yun et al. 2004). After being de-reddened the PDS 456 spectrum rises steeply towards the UV forming a strong "big blue bump", arising as a result of the accretion disc emission. At longer wavelengths, there is the presence of an "infrared bump", possibly produced by re-radiation from any pc-scale molecular dust. Furthermore Simpson et al. (1999), found that the optical and the infrared spectra were characterized by Balmer and Paschen lines with very broad wings, with a corresponding Full Width at Zero Intensity of FWZI $\gtrsim 30000\,\mathrm{km\,s^{-1}}$ (see Simpson et al. 1999, Figs. 2 and 3).

From a radio observation carried out with the Very Large Telescope (VLT), Simpson et al. (1999) detected a total 6 cm flux of $F_{6\,\mathrm{cm}} = 8\,\mathrm{mJy}$, yielding a radio-loudness parameter (R_{L}, defined earlier in § 1.1) of $R_{\mathrm{L}} \sim -0.74$. By comparing it with 3C 273, which has a radio-loudness parameter of $R_{\mathrm{L}} \sim 3$, PDS 456 is $\sim 10^3$ times less luminous in the radio band, clearly confirming that PDS 456 is indeed a radio-quiet quasar. Nonetheless Yun et al. (2004) confirmed the detection of radio emission from PDS 456 in the GHz frequency range, implying a weak (unresolved) relativistic jet, but several order of magnitudes fainter than 3C 273.

Yun et al. (2004) also found that PDS 456 is characterized by strong far-infrared to mid-infrared (FIR to MIR) emission which implies an enrichment of warm and hot ($\sim 100 - 1000\,\mathrm{K}$) dust that may be exposed to a significantly higher mean radiation field caused by the high energy photons originating from the AGN. Furthermore PDS 456 has a high ($L_{\mathrm{IR}} > 10^{12}\,L_{\odot}$) FIR luminosity comparable to other very bright Ultra Luminous Infrared Galaxies (ULIRG) and QSOs such as Mrk 231 (Feruglio et al. 2010). Also PDS 456 has a rather high ratio of far infrared to molecular CO luminosity, which Yun et al. (2004) suggest may arise as a result of PDS 456 going through a "short-lived" transition phase from dusty ULIRG to QSO, with winds/radiation pressure accelerating a process of clearing out the surrounding dust and gas. Furthermore K-band imaging obtained with *Keck* revealed three compact and faint ($M_K \sim -21$) companions within $\sim 10\,\mathrm{kpc}$, which might suggest that PDS 456 has undergone a recent interaction or merging with one of these near by objects. However little is currently known about the host-galaxy morphology of PDS 456, given the brightness of the central QSO at most wavelengths.

No direct reverberation measurement as such is available for the black hole mass in PDS 456. Nonetheless, adopting a bolometric luminosity of $10^{47}\,\mathrm{erg\,s^{-1}}$ and the assumption that PDS 456 does not exceed the Eddington luminosity, the likely lower limit on its black hole mass is $> 8 \times 10^{8}\,M_{\odot}$. Furthermore, the black hole mass can be estimated from the assumption of a virialized BLR and thus using the standard BLR radius (R_{BLR}) versus black hole scaling relations. These are derived from the reverberation studies of other AGN such as the virial relation between M_{BH}, R_{BLR} and the Keplerian velocity of the BLR clouds (V_{BLR}), where $M_{\mathrm{BH}} \propto V_{\mathrm{BLR}}^{2} R_{\mathrm{BLR}}$. In practice these empirical relations are normalized to the 5100Å luminosity and the Hβ FWHM (e.g, McLure & Jarvis 2002; Bentz et al. 2013). For example the equivalent relation in McLure & Jarvis (2002) is given by:

$$M_{\mathrm{BH}} = 4.74(\lambda L_{5100\text{Å}}/10^{44}\,\mathrm{erg\,s^{-1}})^{0.61\pm0.10}[\mathrm{FWHM(H}\beta)]^{2} M_{\odot}. \tag{2.1}$$

Thus taking into account these relations, the black hole mass of PDS 456 was estimated to be $\log(M_{\mathrm{BH}}) = 9.3 \pm 0.4\,M_{\odot}$ by Reeves et al. (2009) and more recently $\log(M_{\mathrm{BH}}) = 9.24 \pm 0.17\,M_{\odot}$ by Nardini et al. (2015). In comparison, the reverberation estimate for the black hole mass of 3C 273 was found to be higher, with $\log(M_{\mathrm{BH}}) = 9.82^{+0.10}_{-0.07}\,M_{\odot}$ (Paltani & Türler 2005).

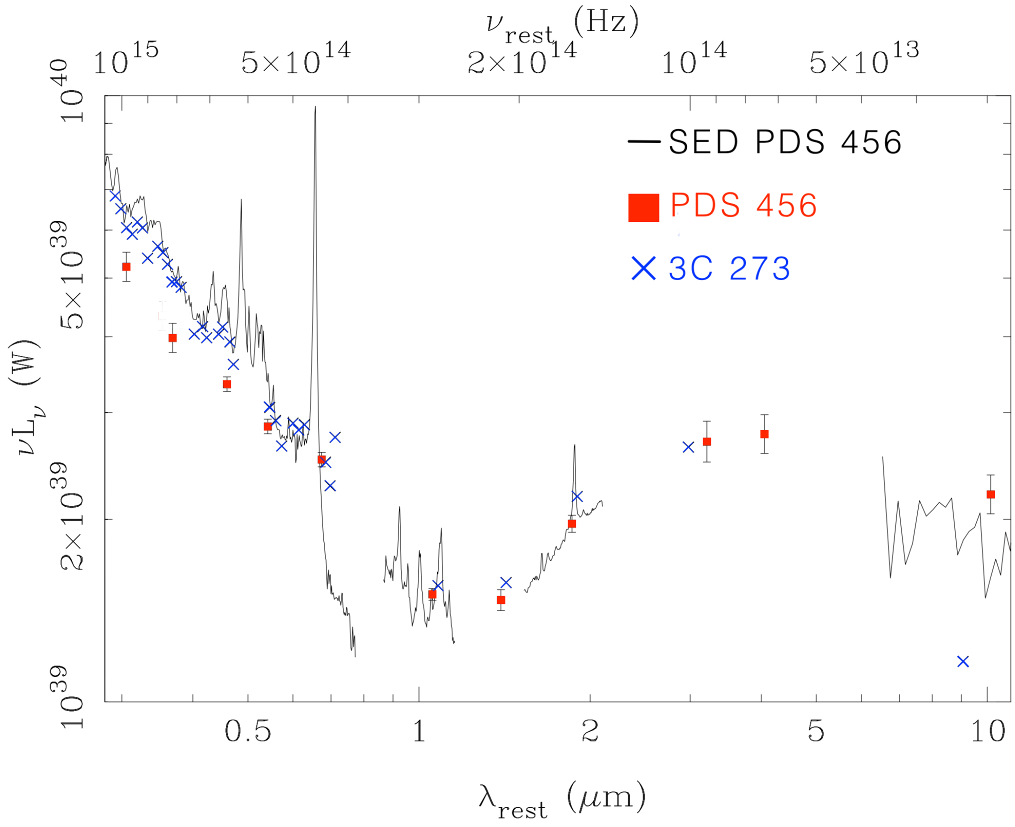

Figure 2.2: Dereddened optical-infrared spectra (black line) and photometric points (red squares) of PDS 456 plotted in the rest-frame, where the photometric points of 3C 273 (blue crosses) are also plotted for comparison showing that essentially the two quasars have largely a striking similarity in this energy band. The 3C 273 photometric points have been scaled upwards by ×1.77 to closely match those of PDS 456. Figure adapted from Simpson et al. (1999).

2.2 The Spectral Energy Distribution of PDS 456

The SED of an AGN can reveal underlying information such as the temperature and physical processes responsible in producing the observed energy output corresponding to specific bands, regardless of the (often) insufficient angular resolution provided by the current instrumentation. Furthermore it is also possible to gain information as to whether the source in question is *beamed* (e.g., Blazars and radio-loud quasars) or *not beamed* (e.g., Seyferts galaxies and radio-quiet quasars) as they would show a very different SED spectrum.

Fig. 2.3 shows a contemporary SED of PDS 456, which is also tabulated in Table 2.1. The X-ray data adopted represent the extreme highest and the lowest X-ray fluxes from the recent *Suzaku*, *XMM-Newton* & *NuSTAR* campaign, which will be presented in Chapter 4. In this figure I also included an extract of data points in the radio and X-ray bands of 3C 273, which are superimposed for a direct comparison. As I mentioned earlier the two quasars have a strong resemblance in the optical-infrared band, however the radio and X-ray properties differ considerably.

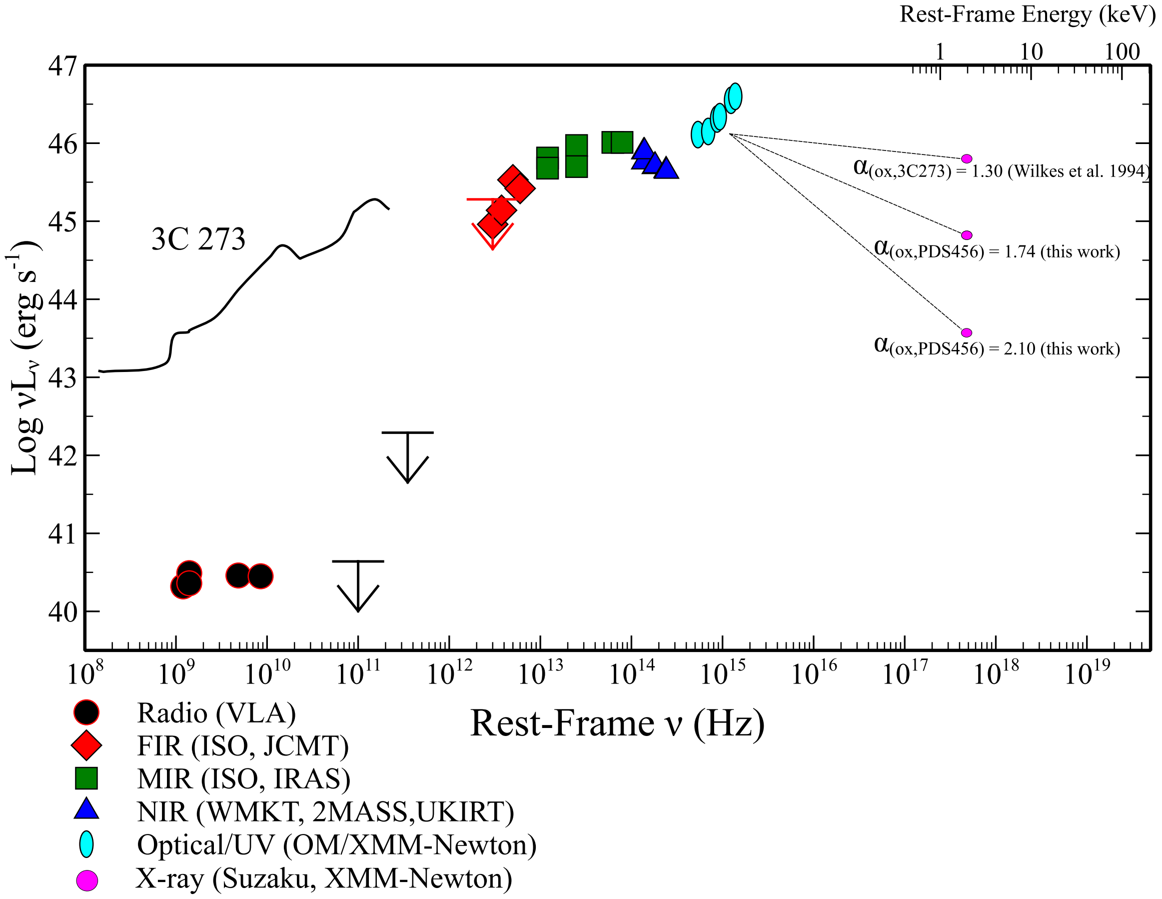

Figure 2.3: The radio to X-ray SED of PDS 456 constructed by using multiwavelength observations spanning 1998 to 2014 together with an extract of radio data points of 3C 273 for comparison. Radio (*VLA* black and downwards arrow), far-IR (*ISO, JCMT*), mid-IR (*ISO, IRAS*), near-IR (*WMKT, 2MASS, UKIRT*), optical/UV (Optical Monitor/*XMM-Newton*) and X-ray (*Einstein*, *Suzaku*, *XMM-Newton*). The $\alpha_{\rm ox}$ indices corresponding to the two PDS 456 extremes of X-ray bright and faint observed with *XMM-Newton* and *Suzaku* are shown together with the 3C 273 average $\alpha_{\rm ox}$ resulting from $\sim$ 30 years of X-ray observations. These indices show that PDS 456 is X-ray weak (compared to 3C 273) but very variable in the X-ray band. This SED also confirms that PDS 456 is radio-quiet when compared to the quasar 3C 273, where the radio emission of the latter is at least two order of magnitude higher, also form the contribution of the relativistic jet which is typical for a radio-loud quasar.

On the other hand, the radio loudness of 3C 273 compared to PDS 456 is very apparent from the SED as the contribution from the jet considerably increases the radio emission. The distribution of the X-ray to optical/UV ratio (or X-ray loudness) in quasars is parametrized by the optical to X-ray spectral index ($\alpha_{\rm ox}$) defined as $\alpha_{\rm ox} = -0.384 \log(L_{2\,\rm keV}/L_{2500\,\rm \AA})$, where $\alpha_{\rm ox} = 1$ corresponds to a flat SED in νF_{ν} space. Thus between the optical/UV and the two extremes observed in the X-rays in PDS 456, the $\alpha_{\rm ox}$ spectral index varies from $\alpha_{\rm ox,PDS\,456,bright} = 1.74$ and $\alpha_{\rm ox,PDS\,456,faint} = 2.10$. On the other hand in 3C 273, $\alpha_{\rm ox,3C\,273} = 1.30$ (Wilkes et al. 1994), which clearly points out that PDS 456 is X-ray weak compared to 3C 273. Thus may be as a result of the presence of a strong relativistic jet in 3C 373, which is typical in radio-loud quasars (e.g., Reeves & Turner 2000b). The corresponding $\alpha_{\rm ox}$ are plotted in Fig. 2.3.

I also compared the $\alpha_{\rm ox}$ measured in PDS 456 with other work, such as the analysis of a large sample of QSOs carried out by Yuan et al. (1998). I find that when PDS 456 is X-ray bright, its $\alpha_{\rm ox,PDS\,456,bright} = 1.74$ falls close to the mean values typically expected for a high luminosity QSO (see Fig. 9 from Yuan et al. 1998). This is also confirmed in recent work by Lusso & Risaliti (2016) where a mean $\langle \alpha_{\rm ox} = 1.63 \pm 0.01 \rangle$ for QSOs was measured. Furthermore, these works found that the mean $\alpha_{\rm ox}$ has a luminosity dependence, which ranges from $\langle \alpha_{\rm ox} = 1.53 \pm 0.03 \rangle$ to $\langle \alpha_{\rm ox} = 1.73 \pm 0.02 \rangle$, suggesting that more optically luminous QSOs are also X-ray weaker. On the other hand when PDS 456 is faintest, the measured $\alpha_{\rm ox,PDS\,456,faint} = 2.10$ falls at the tail end of the QSO distribution of Yuan et al. (1998, Fig. 9). Indeed from a study of a large *Chandra* AGN sample, Brandt & Alexander (2010) found that the BAL QSOs, with values $\alpha_{\rm ox} \gtrsim 2$, can be very X-ray quiet, probably as a result of their high X-ray obscuration. Thus PDS 456 might comfortably fall onto the BAL QSO territory, but only when it is X-ray faint. Indeed in Chapter 4 and 5, I will show that during such a low X-ray flux state, PDS 456 is dominated by considerable X-ray absorption (with $N_{\rm H} > 10^{23}\,\rm cm^{-2}$). This may be as a result of the dominance of the accretion disc-wind during these states, analogous to the behaviour of BAL QSOs.

Band	$\log(\nu)$ (Hz)	S_ν (mJy)	$\log(\nu L_\nu)$	Reference
Radio	9.08	24 ± 5	40.32	(Yun et al. 2004)
	9.15	30.4	40.49	(Reeves et al. 2000)
	9.15	22.7 ± 5	40.36	(Condon et al. 1998)
	9.69	8.23	40.46	(Reeves et al. 2000)
	9.93	4.6 ± 0.9	40.45	(Yun et al. 2004)
	11.0	< 0.6	< 40.64	(Yun et al. 2004)
	11.54	< 7.5	< 42.29	(Yun et al. 2004)
FIR	12.48	420 ± 140	44.96	(Reeves et al. 2000)
	12.48	< 882	< 45.28	(Yun et al. 2004)
	12.57	510 ± 110	45.14	(Reeves et al. 2000)
	12.70	930 ± 69	45.53	(Yun et al. 2004)
	12.78	610 ± 110	45.42	(Reeves et al. 2000)
MIF	13.08	750 ± 41	45.81	(Yun et al. 2004)
	13.08	550 ± 120	45.68	(Reeves et al. 2000)
	13.40	514 ± 24	45.97	(Yun et al. 2004)
	13.40	280 ± 30	45.70	(Reeves et al. 2000)
	13.79	225 ± 36	46.01	(Simpson et al. 1999)
	13.90	180 ± 23	46.01	(Simpson et al. 1999)
NIR	14.14	78 ± 6	45.89	(Simpson et al. 1999)
	14.14	73 ± 7	45.76	(Yun et al. 2004)
	14.14	78.0 ± 0.8	45.89	(Yun et al. 2004)
	14.25	38.6 ± 0.6	45.70	(Yun et al. 2004)
	14.26	39 ± 3	45.71	(Simpson et al. 1999)
	14.38	26 ± 2	45.65	(Simpson et al. 1999)
	14.39	24.8 ± 0.3	45.64	(Yun et al. 2004)
Optical	14.73	26.3	46.11	**this work**
	14.84	21.2	46.15	**this work**
	14.94	24.8	46.31	**this work**
UV	14.97	25.9	46.34	**this work**
	15.09	30.9	46.55	**this work**
	15.14	31.2	46.60	**this work**
X-ray	17.68	0.026	45.79	–
	17.68	8.8×10^{-4}	44.82	**this work**
	17.68	9.1×10^{-5}	43.57	**this work**

Table 2.1: Data and photometric points and the corresponding references adopted for the SED plotted in Fig. 2.3

2.2.1 UV properties of PDS 456

Subsequent observations in the UV, carried out with the *HST*/STIS, by O'Brien et al. (2005) revealed the presence of broad FWHM $\sim 7000 - 15000$ km s^{-1} and blueshifted emission lines in PDS 456. More specifically, these correspond to the broad C IV λ 1549 and Si IV/O IV λ 1400 emission lines which are strongly blueshifted, when compared to their rest-frame, by $\sim$ 5000 and $\sim$ 4000 km s^{-1} respectively (although the blended Lyα/N V λ 1240 emission profile is less blueshifted at $\sim$ 2000 km s^{-1}). These are quite extreme values for QSOs, for which Richards et al. (2002) found a median blueshift of C IVλ1549 of 824 km s^{-1} (with a dispersion of $\pm$511 km s^{-1}) relative to Mg II. In that sample (consisting of $\sim$ 800 QSOs) none of the QSOs were found with emission lines with blueshifted velocities above 3000 km s^{-1}.

These characteristic emission profiles are shown in Fig. 2.4 where the PDS 456 *HST*/STIS spectrum is compared with the mean *HST*/FOS UV spectrum obtained from 184 QSOs (cf. Fig. 4 from Telfer et al. 2002). The other striking feature in the UV spectrum in PDS 456 was the presence of a broad absorption feature blue-ward of the Lyα/N V λ 1240 profile shown in Fig. 2.5. Here the UV spectrum of PDS 456 is compared with a typical low redshift ($z = 0.00973$) Seyfert 1.5 AGN NGC 3783. Three narrow absorption features (see Fig. 2.5), due the ISM in our Galaxy are clearly detected in both spectra, however the absorption trough is virtually absent in NGC 3783. Furthermore, if associated with Lyα absorption, the broad absorption profile in PDS 456 corresponds to a blueshift of $14000 - 24000$ km s^{-1}, which is a clear indication that PDS 456 might have some similarities to BAL QSOs. Another difference compared to the mean QSO spectrum is the lack of "narrow" cores in Lyα, C IV profiles in PDS 456.

The presence of these broad/blueshifted emission and absorption features suggest that PDS 456 is characterized by the presence of outflowing material, with its signature imprinted in the UV spectrum. In the next subsection I will describe the analogous X-ray spectral imprints that also characterized fast outflows in PDS 456. Nonetheless, the detection of these profiles in both energy bands may suggest a connection (but not well understood) between UV and X-ray properties of the outflow.

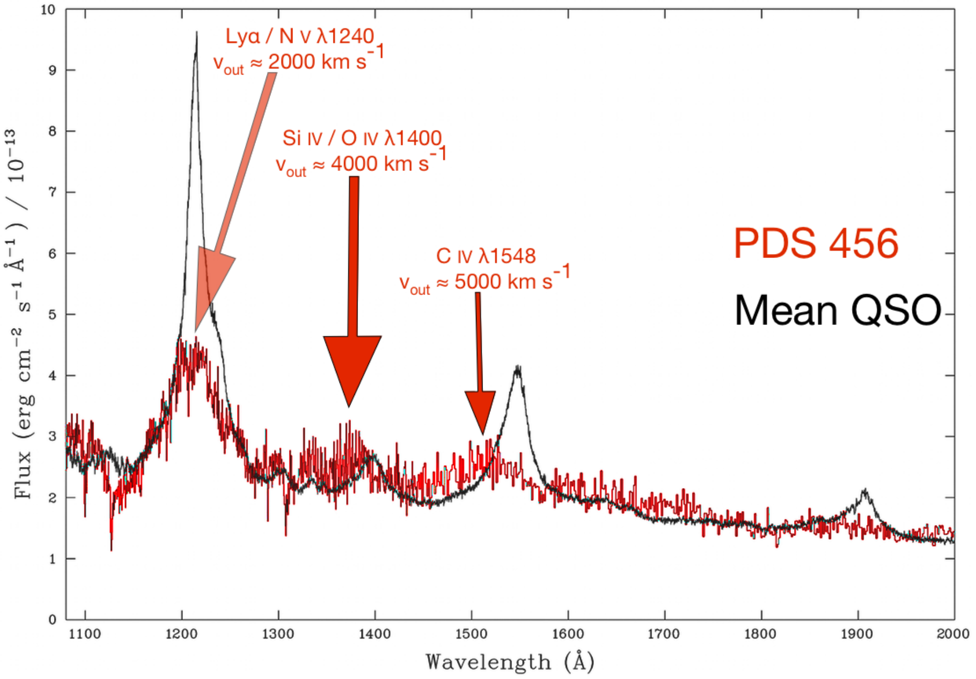

Figure 2.4: The dereddened *HST*/STIS UV spectrum of PDS 456 (red) compared to the mean QSO *HST*/FOS UV (black) archival spectra from Telfer et al. (2002). The Broad C IV λ 1549, Si IV/O IV λ 1400 and Lyα/N V λ 1240 with blueshifted velocity of $v_{\rm out} \sim 5000$, $v_{\rm out} \sim 4000$ and $v_{\rm out} \sim 2000$ km s^{-1} respectively are indicated by the red arrows. Figure adapted from O'Brien et al. (2005).

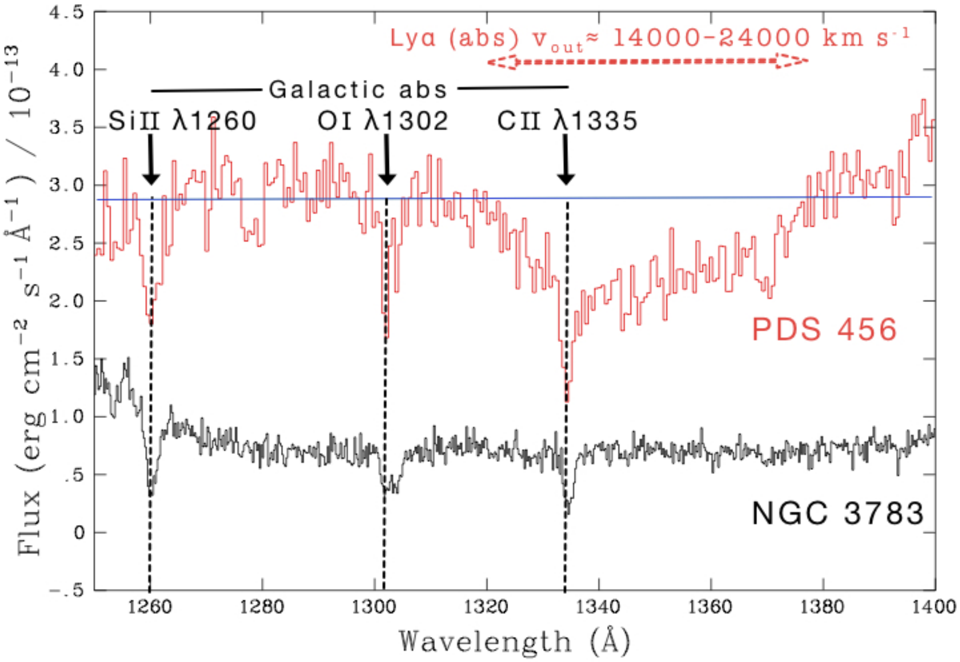

Figure 2.5: A comparison between the UV observed-frame wavelength of PDS 456 (red) and the Seyfert 1.5 AGN NGC 3783. The narrow absorption lines corresponding to the Galactic ISM, due to Si II λ1260, O I λ1302 and C II λ1335, are clearly detected in both spectra indicated by the vertical dashed lines. The broad absorption trough is only detected in the PDS 456 spectrum suggesting the presence of an outflow of $v_{\rm w} \sim 14000 - 24000$ km s^{-1} if attributed to Lyα absorption. Note that more controversially if the absorption trough is associated with C IV it implies an outflow velocity of $v_{\rm w} \sim 0.3c$. The horizontal blue line was drawn on PDS 456 spectrum purposely to guide the eye. Figure adapted from O'Brien et al. (2005).

2.3 The Discovery of the broad Fe K absorption profile

The extreme X-ray nature of PDS 456 was first noticed by Reeves et al. (2000), where very rapid X-ray variability, on time-scales of ~ 15 ks (~ 4 hrs), was observed from *RXTE* monitoring observations in the $3-10$ keV band carried out in early 1998. This indicates, by the light-crossing time argument for the likely black hole mass of $\sim 10^9\,M_\odot$, a very compact X-ray source of a few gravitational radii (R_g) in extent (where $R_\mathrm{g} = GM_\mathrm{BH}/c^2$). Furthermore, through this observation, it was possible to initially recognize the uniqueness of its X-ray spectrum with the presence of a deep absorption trough at ~ 9 keV in the quasar rest-frame as shown in Fig. 2.6 implying the presence of highly ionized gas, of a large column ($\log(N_\mathrm{H}/\mathrm{cm}^{-2}) \sim 24$ or $\tau \sim 1$ at Fe K/9 keV) surrounding the central X-ray source. Due to the limited energy resolution of the *RXTE* detector, at the time of writing Reeves et al. (2000) parametrized the absorption trough with a simple phenomenological edge at ~ 9 keV in order to match the energy of the observed feature.

The presence of a deep iron K absorption trough at $E \sim 8.5-9$ keV was confirmed by Vignali et al. (2000) through an 80 ks net exposure with *BeppoSAX* carried out in August 1998, as shown in the data/model residuals in Fig. 2.7. In addition to this PDS 456 showed a soft excess below ~ 1 keV that may be related to the high energy counterpart of the strong UV (blue) bump present in the SED (see Fig. 2.3).

In Fig. 2.8 the residuals of the data/model ratio, from a simple Galactic absorbed power-law, revealed a strong absorption trough in the iron K band from an initial short (40 ks) observation carried out with *XMM-Newton* in 2001 (Reeves, O'Brien & Ward 2003). Furthermore, by observing with the higher resolution CCD (*XMM-Newton* EPIC-pn) detector, compared to *RXTE* or *BeppoSAX*, it was clear that the absorption profile was too broad to be a single K-shell edge and hence it was identified as a resolved broad trough. Thus at this point in time, the systematic detection of a deep absorption feature above 7 keV (in the quasar rest-frame) was thought to be associated with the Fe XXVI Lyα (H-like iron) and comparing the expected versus the observed energy led to a strong

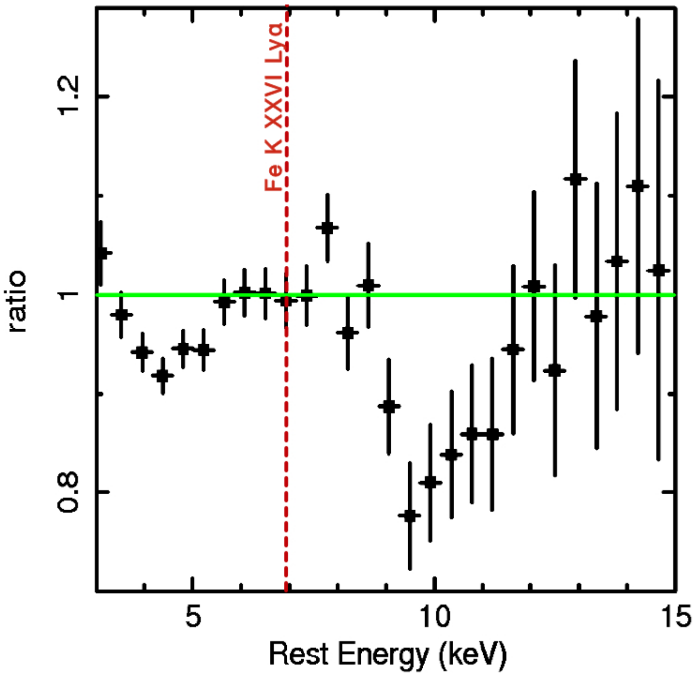

Figure 2.6: The data to model ratio showing the residuals in the $3-15$ keV band *RXTE* data from a simple power-law. The deep absorption profile is clearly seen in the residual, centred at rest-frame energy of ~ 9 keV. At the time the absorption was thought to correspond to the highly ionized Fe K edge of Fe XXV or Fe XXVI. The red vertical line represents the expected position of the Fe XXVI Lyα line at 6.97 keV. Figure adapted from Reeves et al. (2000)

evidence of a large column of highly ionized matter with an associated outflow velocity of $v_{\rm w} \gtrsim 0.1c$. From this point on, it was recognised that PDS 456 was an ideal target for studying black hole winds in the Eddington-limited regime. Note that a similar broad absorption trough was also revealed (near 1 keV) in the soft X-ray band with the RGS in the same *XMM-Newton* observation. Reeves, O'Brien & Ward (2003) suggested that the soft X-ray band absorption originated from a broad blend of iron L-shell absorption, with an initial outflow velocity of $v_{\rm w} \sim 50000\,{\rm km\,s^{-1}}$. Moreover, this fast soft band absorption was later confirmed by Reeves et al. (2016) in a re-analysis of all of the soft X-ray grating observations of PDS 456 from 2001–2014.

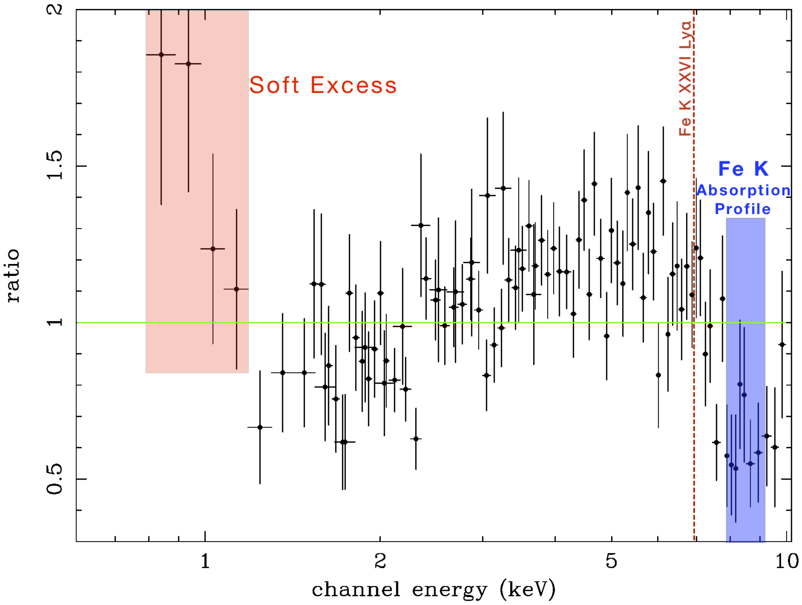

Figure 2.7: The data/model residuals from *BeppoSAX* observation of PDS 456 for a single power law showing both a soft excess below ∼ 1 keV (red shaded area) and a deep Fe K absorption trough at $8.5-9$ keV (blue shaded area). The red vertical line represents the expected position of the Fe XXVI Lyα line at 6.97 keV. Figure adapted from Vignali et al. (2000).

A longer (190 ks) 2007 *Suzaku* observation confirmed the evidence for this fast outflow, resolving two highly significant absorption lines centred at 9.09 ± 0.05 keV and 9.64 ± 0.08 keV (as shown in Fig. 2.9) in the quasar rest-frame. At these energies, no strong atomic absorption is expected above the iron K band, as the abundances of heavier elements (such as Ni, Co) are much lower than Fe. On the other hand, higher order ($1s \rightarrow n$p) iron absorption lines may be expected above 7 keV, but these would usually be substantially weaker than the Fe XXVI Lyα transition. It follows that the association of these lines to the nearest expected strong line, the Fe XXVI Lyα transition at 6.97 keV, implied an outflow velocity of $\sim 0.25-0.30c$ (Reeves et al. 2009). Similarly, in a more

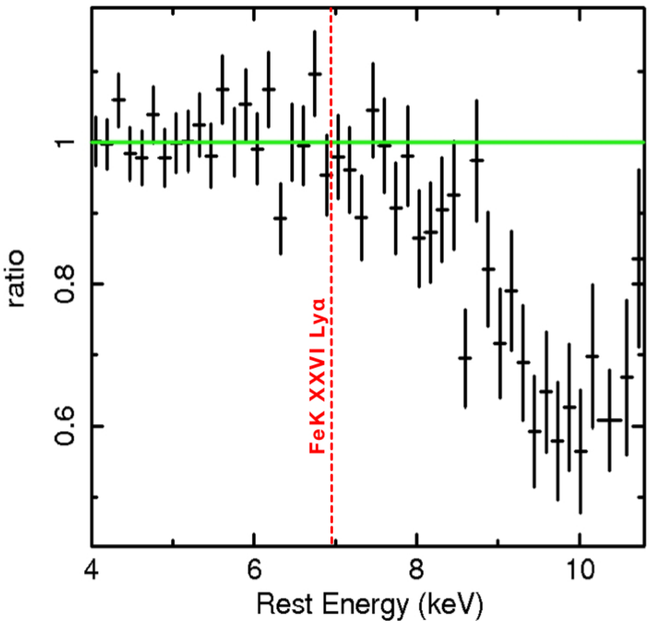

Figure 2.8: Data/model ratio to a power-law fit to the $4 - 12\,\mathrm{keV}$ EPIC-pn spectrum. A 50% drop in counts above the iron K-shell band is observed and through the higher resolution spectrum compared to previous instruments, it was possible to associate the broad absorption trough to the highly ionized blueshifted Fe XXVI Lyα line implying an outflow velocity of $v_\mathrm{w} \gtrsim 0.1c$. Note that the energy scale is plotted in units of keV in the observed frame. The red line represents the expected position of the Fe XXVI Lyα line at 6.97 keV. Figure adapted from Reeves, O'Brien & Ward (2003).

recent (2011) 120 ks *Suzaku* follow-up observation, a broad absorption trough at $\sim 9\,\mathrm{keV}$ (in the source rest frame) was again found, confirming that in both the 2007 and 2011 observations the changes in the absorption features could be due to the same flow of gas in photo-ionization equilibrium with the emergent X-ray emission (Reeves et al. 2014).

Indeed, PDS 456 has a proven track record of strong X-ray spectral variability over the last two decades, whilst being observed by practically all telescopes available across the all energy bands, where its historical spectra point to a complex nature of the source likely due to absorption and intrinsic continuum variations (e.g., Reeves et al. 2002; Behar et al. 2010). The scarcity of PDS 456-like objects in the local universe, makes it a very important source of research, in particular, on the extreme physical processes that govern this AGN.

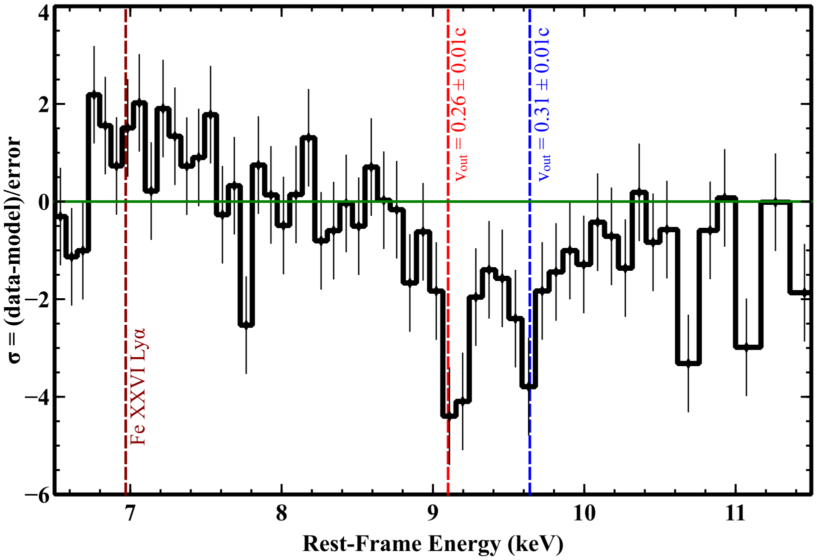

Figure 2.9: The $\sigma = $ (data - model)/error residual to a simple power-law fit to the 6.5 − 11.5 keV XIS03 *Suzaku* spectrum. The dark red vertical line represents the expected position of the Fe XXVI $1s \rightarrow 2p$ line at 6.97 keV while the red and blue vertical lines correspond to the centroid energies of the detected absorption lines. Note also the excess in emission present near 7 keV. Figure adapted from Reeves et al. (2009).

In the subsequent Chapters 4, 5 and 6, I will present the analysis and results from two large campaigns on PDS 456. These were conducted with *Suzaku* (in Feb/March 2013) and then simultaneously with *XMM-Newton* & *NuSTAR* over 5×100 ks observations commencing six months later. In particular these concentrate on the X-ray spectral analysis, with a particular focus on the fast wind in the iron K band, as well as the short-term spectral variability. The latter will reveal the variable nature of both the wind, as well as the broad-band (optical/UV–X-ray) emission from PDS 456. In the next chapter I introduce the observatories (*Suzaku*, *XMM-Newton* and *NuSTAR*) used in the analysis. This includes the reduction of the data and the fitting methods applied, as well as an overview of the main spectral models used on these contemporary datasets.

3 Instrumentation, data analysis, statistics and spectral models

3.1 Current X-ray observatories

In this section I will describe the principal detectors on board the space telescopes *Suzaku*, *XMM-Newton* and *NuSTAR* that produced the data that I will be using for the spectral analysis in this work.

3.1.1 *Suzaku*

The fifth Japanese *Suzaku* (Mitsuda et al. 2007) X-ray observation satellite mission was led by the Japanese Aerospace Exploration Agency (JAXA) in close collaboration with the US National Aeronautics and Space Administration (NASA), and was jointly developed at the Institute of Space and Astronautical Science (ISAS) at JAXA and NASA's Goddard Space Flight Center (GSFC). It was launched on the 10^{th} July 2005 and terminated officially on the 2^{nd} of September 2015 due to irreparable spacecraft conditions and hence exceeding its predicted lifespan of eight-years. *Suzaku* resided in a near-circular low-Earth orbit with an apogee of 568 km, an inclination angle of 31.9° to the equator and an orbital period of ~ 96 minutes.

A schematic of the *Suzaku* observatory is shown in Fig. 3.1 where it is characterized by a deployed extendible optical bench (EOB) with an operating length of ~ 6.5 m. On the EOB there are five X-ray Telescopes (XRT, Serlemitsos et al. 2007) which correspond to each of the five focal plane detectors on the base panel of the spacecraft. One of these is an X-ray micro-calorimeter (the X-ray spectrometer, XRS Kelley et al. 2007), which was unfortunately rendered incapable of science observations on 2005 August 8 by a series of in-orbit coolant malfunctions[1]. The remaining four X-ray telescopes were

---

[1] NASA press release: http://heasarc.gsfc.nasa.gov/docs/astroe/news/xrsend.html

designed to focus the X-ray photons onto CCDs (Charge-Coupled Device) forming part of X-ray Imaging Spectrometer array (XIS) (Koyama et al. 2007). *Suzaku* also carries a non-imaging Hard X-ray Detector (HXD, Takahashi et al. 2007) made from silicon positive intrinsic negative (PIN) diodes covering an energy range of $15-70\,\mathrm{keV}$ and a $35' \times 35'$ Field-Of-View (FOV hereafter), as well as a gadolinium silicate (GSO) crystal scintillators providing data over energy range $75-600\,\mathrm{keV}$. In this thesis, the analysis concentrates on the XIS over the $0.5-10\,\mathrm{keV}$ energy range, while the HXD/PIN is only used to determine upper-limits on the flux above $15\,\mathrm{keV}$.

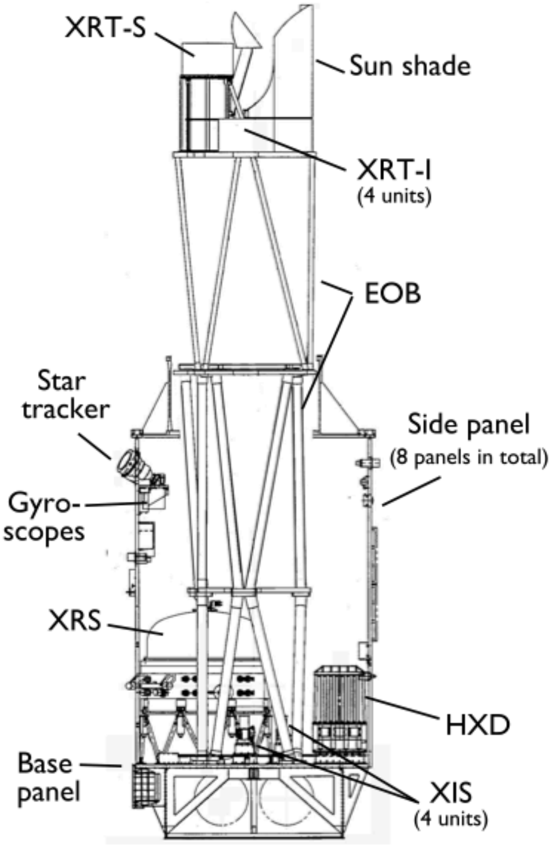

Figure 3.1: Diagram of the *Suzaku* X-ray satellite showing a cut-away schematic of the satellite highlighting the location of the various detectors and instruments. This image is taken from Mitsuda et al. (2007).

The X-ray Imaging Spectrometer (XIS)

The XIS instrument consisted of four discrete detectors, each of which has a silicon based CCD operating by individual photon counting mode. Here the X-ray CCDs convert an incident X-ray photon into a cloud of electrons, the magnitude of which is proportional to the energy of the absorbed X-ray photon. The four XIS cameras (named XIS $0, 1, 2, 3$) were each located in the focal plane of their corresponding XRT, which had a focal length of $\sim 4.5\,\mathrm{m}$ and provided an angular resolution with a Half Power Diameter (HPD) of $\sim 2'$. The XIS had a field of view of $17.8\,\mathrm{arcmin}^2$ and an energy resolution of $\sim 130\,\mathrm{eV}$ (FWHM) at $\sim 6\,\mathrm{keV}$. The XIS $0, 2, 3$ detectors are front illuminated (FI) and covered an energy range of $0.4 - 10.0\,\mathrm{keV}$ whereas the XIS 1 is a back-illuminated CCD with a higher soft-band resolution that covered an energy range of $0.2 - 10.0\,\mathrm{keV}$ but with lower resolution at 6 keV than the FI CCDs as well as a larger background at larger energies.

A single FI chip had an effective area of $147\,\mathrm{cm}^2$ at $\sim 8\,\mathrm{keV}$, leading to a theoretical total effective area of $\sim 440\,\mathrm{cm}^2$ at $\sim 8\,\mathrm{keV}$ for the sum of the FI chips. However, on 2006 November 9 the XIS 2 suffered a suspected micro-meteoroid impact and was deemed incapable of producing useful scientific data[2]. After the XIS 2 damage, the effective area for the two remaining FI chips was $\sim 294\,\mathrm{cm}^2$ at $\sim 8\,\mathrm{keV}$.

3.1.2 *XMM-Newton*

The *XMM-Newton* space observatory (X-ray Multi-mirror Mission–Newton, Jansen et al. 2001) is a European Space Agency (ESA) led mission launched in December 1999 with the aim of producing data for carrying out X-ray spectroscopy at high sensitivity and high spectral resolution. The satellite has a payload of three X-ray telescopes, each constituted of 58 concentric mirror shells and a focal length of 7.5 m. It has an elliptical orbit at an angle of $\sim 40^\circ$ to the equator, with a long orbital period of ~ 48 hours which allows continuous observing for $\sim 145\,\mathrm{ks}$. The X-ray detectors at the foci of the

---

[2] ftp://legacy.gsfc.nasa.gov/suzaku/doc/xis/suzakumemo-2007-08.pdf

three telescopes consist of: the European Photon Imaging Camera (EPIC), for imaging and spectroscopy, and the Reflection Grating Spectrometer (RGS) for high resolution spectroscopy. This is shown schematically in Fig. 3.2. The combined effective area of the mirrors is 4650 cm^2 at 1.5 keV, and ~ 3000 cm^2 at 6 keV.

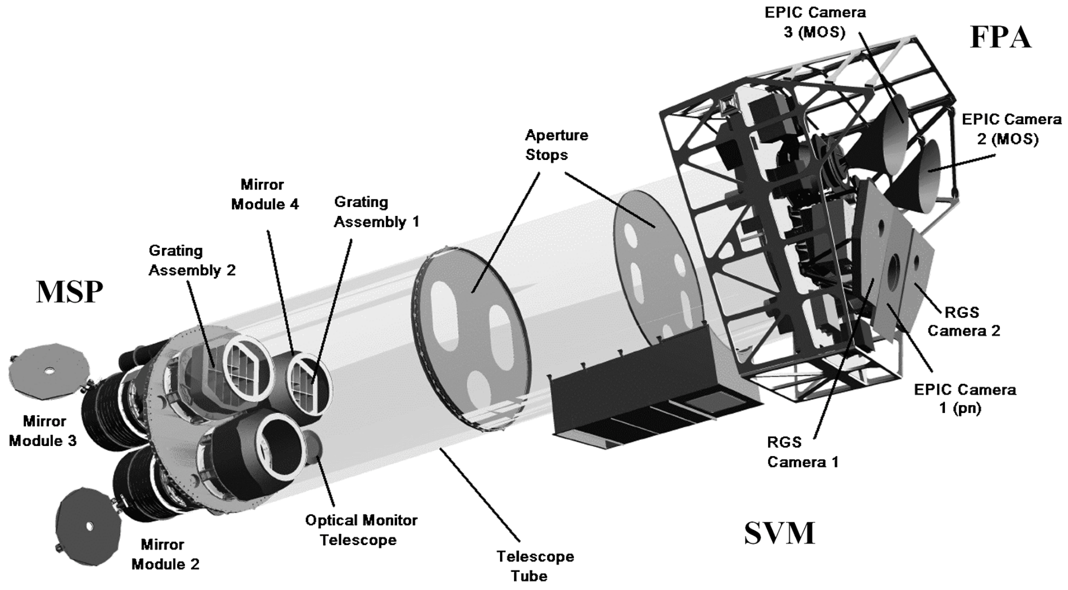

Figure 3.2: Diagram of the *XMM-Newton* X-ray satellite, where the subsystems are shown, with the external cover removed for clarity. Image taken directly from: Lumb, Schartel & Jansen (2012).

Fig. 3.2 also illustrates that there are three EPIC cameras, where two of these make up the EPIC-MOS (Turner et al. 2001), incorporating front-illuminated CCD detectors situated at the prime focus of two of the concentric mirror shells. Each MOS camera has a $\sim 30'$ FOV, and is sensitive to X-rays over the $0.15 - 15$ keV energy range offering a FWHM energy resolution of ~ 140 eV at 6 keV. The third EPIC camera is the EPIC-pn (Strüder et al. 2001), which is a back-side illuminated CCD camera located at the primary focus of the third X-ray telescope. It has comparable capabilities to the EPIC-MOS, having a $30'$ FOV, sensitivity also between the $0.15 - 15$ keV energy range, and offers a similar energy resolution. However what differs between the EPIC-MOS and the EPIC-pn is that only $\sim 44\%$ of the incident X-ray photons focused by the mirrors actually reach the EPIC-MOS CCDs. This is because there are two Reflection Grating Arrays (RGAs) situated behind the X-ray telescopes which scatter $\sim 40\%$ of the incident X-rays from each telescope towards the CCD arrays which are each located at the secondary focus of each mirror. In this thesis, I primarily make use of the EPIC-pn camera, which has a higher effective area at Fe K.

Thus, the combined effective area of the two EPIC-MOS cameras is below that of the single EPIC-pn camera, which provides a maximum effective area of $\sim 1300\,\mathrm{cm}^2$ at $E \sim 1.5$ keV and $\sim 700-800\,\mathrm{cm}^2$ at the energies of the Fe Kα line (i.e., $E \simeq 6-7\,\mathrm{keV}$ as shown in Fig 3.3). The RGAs and associated dedicated CCD units make up by the Reflection Grating Spectrometer (RGS; den Herder et al. 2001), which provides the high-resolution spectroscopic capability of *XMM-Newton* with a resolving power of $E/\Delta E = 150-800$ over the $0.3-2.5\,\mathrm{keV}$ band.

Furthermore, *XMM-Newton* also houses an Optical/UV Monitor imaging telescope (*XMM-Newton* OM, Mason et al. 2001) as part of the Mirror Support Platform (MSP) as shown in Fig. 3.2. It permits a coverage between 170 nm (UV) and 650 nm (optical, red) of the central 17 arc-minute square region of the X-ray FOV. This allows routine multiwavelength observations of *XMM-Newton* targets simultaneously in the X-ray and optical/UV band allowing, for example, to construct an optical to X-ray spectral energy distribution (see Chapters 4 and 6). The OM is equipped with a set of broadband filters for colour discrimination, where their wavelength band ranges are:

- V ($580-510$ nm),
- B ($490-390$ nm),
- U ($390-300$ nm),
- UVW1 ($345-320$ nm),
- UVM2 ($245-205$ nm),

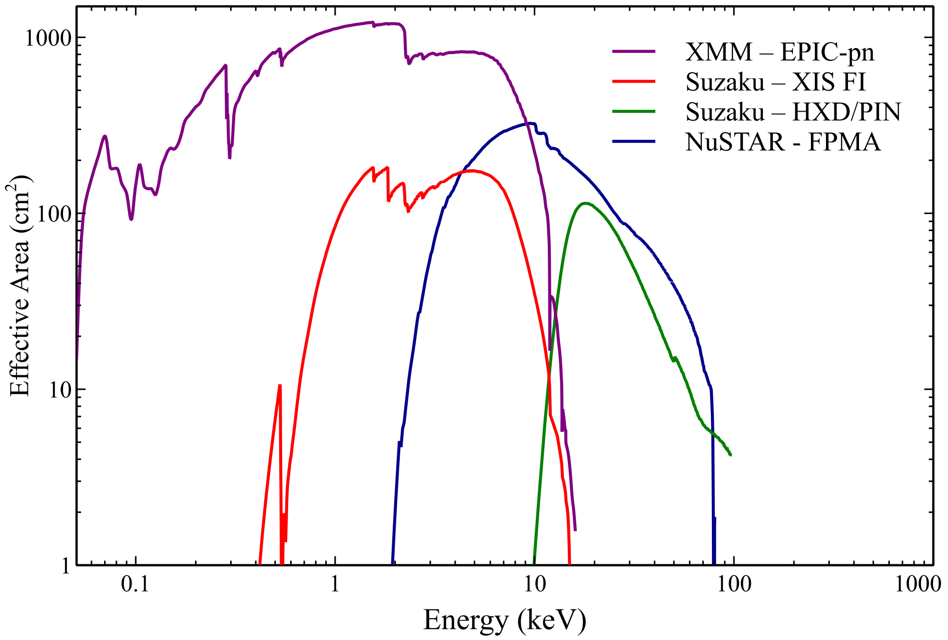

Figure 3.3: A plot showing the relative instrumental effective areas as a function of energy for the primary cameras on board of *Suzaku*, *XMM-Newton* and *NuSTAR*. The individual *Suzaku* XIS-FI (single camera) and HXD/PIN detectors are shown in red and green respectively. The *XMM-Newton* EPIC-pn detector is shown in purple, whereas the *NuSTAR* FPMA detector is shown in blue.

- UVW2 (225 – 180 nm).

The *XMM-Newton* OM filter selection has to be executed in a particular order during a given target observation as the filter wheel rotates in one direction only. Moreover to conserve the total number of wheel rotations over the expected lifetime of *XMM-Newton*, the number of filter wheel rotations per pointing is limited to one.

3.1.3 *NuSTAR*

The Nuclear Spectroscopic Telescope Array (*NuSTAR*, Harrison et al. 2013) was launched on the 13th of June 2012 into a low-inclination orbit, where passages through the

South Atlantic Anomaly (SAA) are minimized. The *NuSTAR* spacecraft consists of two co-aligned hard X-ray grazing incidence telescopes forming the core of the payload. Two optics modules are mounted, along with one of the star tracker heads, to composite thermally stable benches (see Fig. 3.4). The two benches are separated by a mast, which was deployed after launch, consisting of 57 rectangular structures made stiff after deployment.

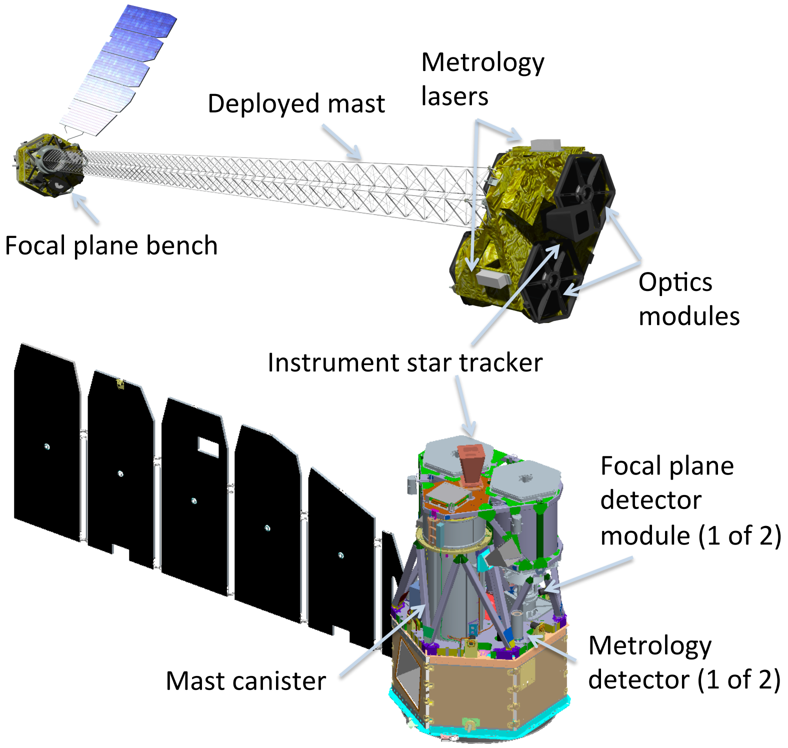

Figure 3.4: Diagram of *NuSTAR* observatory (top) and deployed (bottom) configurations. Figure taken directly from Harrison et al. (2013).

The *NuSTAR* science instruments consist of two Wolter-I conical approximation (Petre & Serlemitsos 1985) X-ray optics, each containing 133 nested multilayer-coated grazing incidence shells which focus onto two independent solid-state focal plane detectors separated from the optics by a $\sim 10\,\mathrm{m}$ focal length. The optics and detectors are designed to be as identical as possible, so that the focal plane images can be co-added to gain sensitivity. An incorporated aspect/metrology system allows for variations in the pointing (e.g., tip, tilt, and relative rotation during an observation), allowing images to be combined. Furthermore when these measurements are combined during data processing on the ground they aid to remove image blurring and correct response files are produced.

Each telescope has its own focal plane module, consisting of solid state four Cadmium-Zinc-Telluride (CdZnTe) pixel detectors (Harrison et al. 2010) shielded by Cesium-Iodide (CsI) crystals that surround the instrument. This 2×2 array of detectors, each with an array of 32×32, $0.6\,\mathrm{mm}$ pixels, provides a $12'$ FOV. The crystal shields detect the high energy photons (and cosmic rays) which cross the focal plane from directions other than along the *NuSTAR* optical axis. Such high energy events are the primary source of background for *NuSTAR* and must be properly identified and subtracted in order to identify high energy photons from cosmic sources.

The main characteristics of *NuSTAR* are as follows:

- the energy range is between $3 - 79\,\mathrm{keV}$
- both the detectors are imaging with an angular resolution of $18''$ (FWHM) which is made possible via its grazing incidence optics and its long focal length
- the FWHM spectral resolution at $10\,\mathrm{keV}$ is $\sim 400\,\mathrm{eV}$, power than for the CCD detectors on *XMM-Newton* and *Suzaku*
- the effective area is high at hard X-ray energies, peaking at $600\,\mathrm{cm}^2$ at $10\,\mathrm{keV}$ (both telescopes combined) which is more sensitive than *Suzaku* HXD (above $10\,\mathrm{keV}$) as shown in Fig. 3.3
- this and the low background of $1.1 \times 10^{-3}\,\mathrm{cts\,s^{-1}arcmin^{-2}}$ at $10 - 30\,\mathrm{keV}$ make it

at least two orders of magnitude more sensitive than the *Suzaku* HXD (above 10 keV)

- subsequently the 3σ detection limit of $1 \times 10^{-14}\,\mathrm{erg\,cm^{-2}\,s^{-1}}$ $(10 - 30\,\mathrm{keV})$ for 1 Ms exposure.

3.2 Data reduction

Having introduced the space observatories, I will now describe the main steps that are involved in the *data-reduction* process, which effectively converts the "raw" data collected by the detectors (typical photon counts per seconds) into a stage that is suitable for a scientific analysis.

3.2.1 Data processing

The current generation of X-ray observatories measure the properties of the detected individual photons. This is in contrast to many instruments designed to operate at lower energies (or longer wavelengths) which measure the integrated photon fluxes. A motivation for this difference is that the X-ray photons are characterized by relatively high energies, which allow to be detected individually, but also by a relatively low-flux, so they can be easily counted. Thus, modern X-ray instruments typically measure the time, position of the X-ray photon and some attribute which relates to its energy as it strikes the detector, defining an X-ray detection event. This is characterized by a 'pulse height amplitude' (PHA hereafter), which is effectively the charge (per pixel) integrated over a given read-out time, a detection time, a grade and typically two position coordinate which correspond to a specific location on the CCD.

When an observation has been completed, all the PHA events together with their specific attributes are listed in an *event file* which is made available to the observer soon after being processed.[3] The event files are stored in a multi-layered FITS (Flexible Image Transport System); file (Wells, Greisen & Harten 1981)[4]. However, the raw events attributes are unsuitable for scientific analysis and detection events must be screened according to various criteria which I will cover in the next section, before any meaningful results can be obtained.

3.2.2 Data screening

During the screening process the main considerations are:
In CCD detectors an event is recorded to a specific value depending upon the charges registered in the surrounding pixels, forming either a 3 × 3 or a 5 × 5 grid. The grades assigned are in accordance to the convention established with *ASCA*[5] where grades 0, 2, 3, 4, 6 are considered 'good' X-ray detection whilst grade 7 almost certainly indicates a particle impact as opposed to an X-ray photon detection. Thus the grade of an event provides an initial indication of whether it is suitable for scientific analysis.

In addition to the unavoidable background of cosmic rays, some pixels in the CCD detectors can produce an apparent signal event without the influence of an external photon. These events are known as bad 'flickering' pixels or 'hot-spots' and can be minimised by: (i) adopting CCDs where the pixel size is smaller than the detectors point spread function and (ii) keeping the detector to sufficiently cooled operating temperature.

The "raw" data need to undergo a screening process according to the time intervals during which the source is occulted by the Earth and the periods for which the telescope passes through the SAA caused by the Van Allen radiation belts. The SAA is a region of the Earth's atmosphere located above the South Atlantic characterized with an intense particle flux, thus combined with a low-Earth orbits of some space telescopes (e.g., *Suzaku*, *NuSTAR*), the data produced in this time frame are not usable. The same applies for the

---

[3] As the X-ray observatories are funded by governmental bodies, it is therefore required that the events files have to be made public (on-line) within a time-frame of usually one year from the end of the observation.

[4] More information available at http://fits.gsfc.nasa.gov

[5] http://www2.astro.psu.edu/xray/docs/TARA/TARA_users_guide/node12.html

following (436 seconds in case of *Suzaku*) the SAA passage as particle bombardment can generate short-lived radioactives that produce background while decaying.

Another important requirement in the screening process is the cut-off rigidity of the instrument, which provides a measurement of how charged particles interact with the telescope. Furthermore, the rigidity of a charged particle is a measure of how the Earth's magnetosphere influences the momentum of such particle. More specifically, a particle with higher momentum (and hence rigidity) will have a larger resistance to being deflected away by the magnetic field and hence more probability to be detected by the instruments on board of the spacecraft. On this basis an observational cut-off rigidity can be applied during data reduction in order to insure that such events recorded when the satellite might be susceptible to cosmic particles are excluded.

An intuitive consideration to be made when evaluating the collected data is the satellite pointing angle to a particular direction. This is important as the angular distance between the pointing angle and the Earth's limb provides information of whether the Earth's outer atmosphere absorbed softer X-rays. Furthermore, the angle between the pointing direction and the Earth's day–night boundary should also be considered as the scattering of cosmic rays in the Earth's atmosphere could also give rise to apparent X-ray detections. Lastly, the angle between the satellite's pointing direction and the Sun is also to be considered as Solar X-rays might scatter into the detector, leading to further apparent detections. Each of these factors should be considered individually during the data reduction process to ensure a clean source spectrum that can be suitable for scientific spectral analysis. A summary of these essential screening criteria for the case of *Suzaku* is tabulated in Table 3.1.

The data that I use in the subsequent chapters of this thesis are predominantly obtained with the *Suzaku* X-ray observatory, and their reduction is described further below. The *XMM-Newton* and *NuSTAR* spectra that are subsequently used in Chapter 4, are identical to the ones used in Nardini et al. (2015) and hence they were reduced according to the procedures described in supplementary material in Nardini et al. (2015).

Criteria	XIS
XIS Grade	0, 2, 3, 4, 6
Telemetry bit rate	Superhigh
Flickering pixels	Removed
`ANG_DIST`	$< 1.5'$
ELV	$> 5^\circ$
`DYE_ELV`	$> 20^\circ$
`SAA_HXD`	0 or excluded
`T_SAA_HXD`	$> 436\,\mathrm{s}$
`TN_SAA_HXD`	$> 180\,\mathrm{s}$
cut-off-rigidity	$> 6\,\mathrm{GeV}$

Table 3.1: Summary of the the essential data screening and selection criteria for *Suzaku* XIS detectors.

3.2.3 *Suzaku* data reduction

Cleaned *Suzaku* data files are available to be downloaded from the HEASARC *Data Archive*. However before this is possible, the "raw" data undergo a standard processing pipeline (see Table 3.1) that reduces, screens and processes them accordingly into "cleaned" event files suitable for analysis. In this section I will briefly outline the main analysis steps for the XIS detectors on board *Suzaku*. Once the cleaned event files are obtained, the first stage of the data reduction process consists of the extraction of the images of the source which is needed to define the source and background regions. From these regions I extract the source and background spectra and the light curves. All the above steps are achieved by using the XSELECT FTOOLS program[6]. The HXD data (utilised for the upper-limit adopted in Chapter 4) have been reduced by following the standard procedures available on the *Suzaku* ABC Guide[7]

---

[6] http://heasarc.gsfc.nasa.gov/ftools/

[7] https://heasarc.gsfc.nasa.gov/docs/suzaku/analysis/abc/

3.2.4 Reducing data from XIS detectors

The spectral data for the functioning XIS $(0, 1, 3)$ CCDs in each sequence were extracted using HEASOFT (v6.14) and the latest version of the calibration database (Aug 2013). Furthermore, the data were selected from the 3×3 and 5×5 edit-modes and then processed according to the recommended screening criteria (see Table 3.1). The XIS source products were selected from circular regions $1.5'$ in radius, with the background contribution estimated from four offset circular regions of equal radius. In another step of the data reduction process, two *response files* have to be generated; the *Redistribution Matrix File* (RMF) and the *Ancilliary Response File* (ARF) using the *HEAsoft* tools XISRMFGEN and XISSIMARFGEN respectively. The RMF can be described as a table containing the probability of a photon of given energy being registered in a particular spectral channel and thus contains the energy resolution and mapping of the channels (pulse-height) into energy. The ARF is the energy-dependent effective area of the telescope and detector system (in cm^2) generated for on-axis pointing used in this thesis. Both RMF and ARF constitute the integral components of the overall instrument response system and can be grouped together (using the GRPPHA tool), along with the source and background spectra and assumed spectral models in order to obtain the reduced fluxed spectrum ready to be analysed using the XSPEC package (Arnaud 1996).

3.3 Data analysis

X-ray spectral analysis requires theoretical models as well as statistical and computational techniques to deal with the instrumental response and (in some cases) a small number of photons. X-ray spectral analysis is carried out using the command-driven XSPEC program. The main spectral models in this thesis are introduced later in § 3.4.

3.3.1 Spectral fitting

Once the data have been reduced, the next approach is to gain insight in the intrinsic properties of the source which is obtained by analysing the spectra. This is achieved normally by adopting a ‘forward-fitting’ process, where a possible model source spectrum is initially defined and then compared to the actual data. Fig. 3.5 shows a schematic of the forward-fitting technique which is carried out as follows:

(1) a physically motivated theoretical model is constructed according to which components are expected to be present in the source,

(2) the hypothesised model spectrum is folded through the full instrument response (i.e., RMF×ARF) and fitted to the observed counts spectrum,

(3) the resulting fit is assessed according to an appropriate fit-statistic (see § 3.3.2 for more details), which measures the agreement between the data and a distinct set of model parameters,

(4) if the agreement is poor, the model parameters are iteratively adjusted until the best value of fit-statistic in found for that particular model,

(5) a *goodness-of-fit* test is carried out (see § 3.3.3), which determines whether or not the model parameters are an appropriate description of the data. This step is important as the real data are always subject to measurement uncertainties (noise) and they will never match exactly a given model, even if it gives a plausible description,

(6) if the best-fit parameters are found to be unacceptable by a statistical test, the model can either be rejected or modified in an effort to achieve a better description to the data.

This forward-fitting process is repeated in a cycle as long as it is required in order to achieve an acceptable fit. However it is very important to verify whether the validity of the adopted model is physically appropriate given to what it is known about the AGN environment, even in the case that the goodness-of-fit is acceptable.

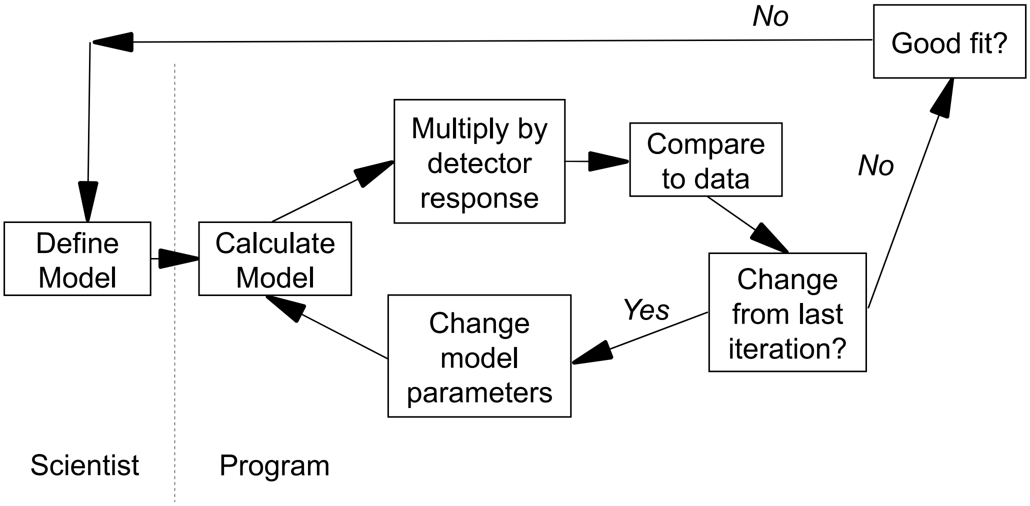

Figure 3.5: Flowchart outlining the steps involved with forward-fitting. Figure taken directly from Arnaud, Smith & Siemiginowska (2011).

3.3.1.1 Construction of the 'fluxed' spectra

X-ray spectra are conventionally given in count rate per detector channel i. Thus the relationship between the source spectrum $S(E)$, in units of photons $\mathrm{s}^{-1}\,\mathrm{cm}^{-2}\,\mathrm{keV}^{-1}$ and the observed counts spectrum (in channel space i) as mediated by the telescope and detector can be described by the following Fredholm integral:

$$C(i) = \int RMF(i, E)ARF(E)S(E)dE, \tag{3.1}$$

where $RMF(i, E)$ and $ARF(E)$ are the unitless response matrix and the energy-dependent effective area (defined in § 3.2.4) respectively. Here the observed spectrum $C(i)$ is assumed to be background-subtracted and the instrumental response $RMF(i, E)ARF(E)$ to be independent of the value of $S(E)$. As discussed in Vaughan et al. (2011), in reality the data are not continuous and thus the discrete energy range is divided into N bins each defined with an energy E_j, the above integral can be approximated as:

$$C_i = \sum_{j=1}^{N} R_{ij} A_j S_j, \tag{3.2}$$

where R_{ij} is the average probability that a photon of energy E_j will be detected in a channel i. A_j and S_j are the area and the source spectrum integrated over the range of each energy bin of their continuous counterparts, i.e. $ARF(E)$ and $S(E)$ in equation 3.1. At this point, to recover $S(E)$ I need to adopt the 'forward fitting' technique discussed in § 3.3.1. However during this work, I find that it is useful to view a 'fluxed' spectrum, prior fitting, which is largely free from the distorting effect of the instrument efficiency to *only* give a better visual representation of the underlying source spectrum. This can be achieved by normalizing the observed source count spectrum by an effective area curve that has been blurred using the redistribution function:

$$S_i = \frac{C_i}{\sum_{j=1}^{N} R_{ij} A_j}. \tag{3.3}$$

This method, as discussed in Nowak (2005), gives an estimate of the spectrum in true flux units, i.e. photons $\mathrm{s}^{-1}\,\mathrm{cm}^{-2}\,\mathrm{keV}^{-1}$. In practice this is achieved by defining a constant model spectrum, within XSPEC, such as a power-law (defined in § 1.4.1) with $\Gamma = 2$ and normalization 1 and then plotting the 'unfolded' spectrum (`plot euf` command) which is also converted to the more conventional flux density units of $\mathrm{erg\,s}^{-1}\,\mathrm{cm}^{-2}\,\mathrm{keV}^{-1}$. It is important to note that this method *does not* produce a deconvolved spectrum and it has the advantage to be independent of the spectral model and hence providing a more objective visualization of the 'fluxed' spectrum. In this way the energy resolution of the observed spectrum is preserved in the output 'flux' spectrum.

3.3.2 Probability distribution and fit statistics

The two most widely applied probability distributions in X-ray astronomy are Gaussian (or normal) and Poisson distributions which both describe the fraction of events happening in a large number of identical trials. As I mentioned earlier in § 3.2.1, X-ray photons can be counted individually, thus the X-ray detectors operate in photon-counting mode, thus we have the probability of observing D_i events in bin i of dataset D, assuming events occur independently at a predicted number of counts M_i.

Poisson distribution and the Cash statistic

In the case when the detected events are comprised by a small-number statistic (i.e., small D_i), in a given read-out time, the probability distribution is 'Poissonian'. In this regime, the probability of observing D_i events in bin i of dataset D, assuming events occur independently at a predicted number of counts M_i, is given by

$$\mathrm{Prob}(D_i) = \mathcal{P}(D_i|M_i) = \frac{M_i^{D_i}}{D_i!} e^{-M_i}. \tag{3.4}$$

The most frequently adopted maximum likelihood function in the Poisson data limit is the C-statistic (Cash 1979), which follows:

$$C = 2 \sum_{i=1}^{N} (M_i - D_i \ln M_i), \tag{3.5}$$

and is appropriate when fitting data which has few counts per bin, or when performing high resolution (grating) data which has many resolution elements. The factor of 2 arises to ensure that inferences made from the C-statistic agree with the widely used χ^2 statistic at high D_i. Moreover, the (linear) nature of the C-statistic allows it to be used independently of the number of counts per bin of an X-ray spectrum. The analysis that I present in this thesis is based on data generated with a relatively large number of counts per bin i.e., large D_i typically $\gtrsim 50\,\mathrm{cts\,bin^{-1}}$ (see below) that varies with a Gaussian distribution with an independent standard deviation and hence this is where I will focus in the next subsection.

Gaussian distribution and χ^2 statistic

In the Gaussian limit the probability of observing D_i events in bin i of dataset D, given a predicted number of counts M in bin i (M_i) is:

$$\mathrm{Prob}(D_i) = P(D_i|M_i, \sigma_i) = \frac{1}{\sigma_i\sqrt{2\pi}} \exp\left[-\frac{(D_i - M_i)^2}{2\sigma_i^2}\right], \tag{3.6}$$

where σ_i is the standard deviation (or error) of the counts in channel i (thus σ_i^2 is the variance). In other words as the number of counts increase, the Poisson distribution becomes more symmetrical and when $D_i \geq 20$, the distribution becomes virtually indistinguishable from a Gaussian with mean value equal to D_i and $\sigma_i = \sqrt{D_i}$. The true importance of the Gaussian distribution in experimental science arises from the *central-limit-theorem*. This theorem states that provided certain conditions are met (and they usually are), a little averaging will produce a Gaussian distribution of results regardless the shape of the initial distribution from which the sample is drawn; in other words the errors on averaged samples will always look 'Gaussian'. Thus this distribution is appropriate if the number of counts per bin is at least $\gtrsim 20 - 25$ and for this reason the most common fit statistic that is applied is the χ^2 statistic defined as:

$$\chi^2 = \sum_{n=i}^{N} \frac{(O_i - E_i)^2}{E_i}. \tag{3.7}$$

where O_i is the observed numbers in each bin i and E_i are the expected values from the model. However in the more familiar case where the individual measurements carry uncertainties, the above equation can be expressed as:

$$\chi^2 \equiv S^2 = \sum_{n=i}^{N} \frac{(D_i - M_i)^2}{\sigma_i^2}. \tag{3.8}$$

where σ_i^2 is the (unknown) variance of the Poisson distribution from which D_i is sampled. χ^2 fitting assumes that the errors are also "bell-shaped", normally distributed into a Gaussian profile thus, due to the central-limit-theorem, the count spectra *cannot* be binned with less than $\lesssim 25\,\mathrm{cts\,bin}^{-1}$.

3.3.3 The goodness-of-fit

One of the main reasons that the χ^2 fit statistic is widely adopted throughout X-ray astronomy is that it also doubles as a 'goodness-of-fit' test originally presented by Pearson (1900). After varying and/or "freezing" (or fixing) some of the values of the model parameters during the forward-fitting process, described in § 3.3.1 and once the value of the χ^2 has been minimised, the quality of the fit can be defined by considering the number of data points minus the number of free parameters, also named as number of degrees of freedom (ν). Thus a good fit is then achieved when the *reduced chi-square* $\chi^2_\nu = \chi^2/\nu \simeq 1$, consequently values much greater than this suggest that the model is not a good representation of the observed data (a bad fit). On the other hand, χ^2_ν indicates that the error bars on the data are too large or the model is just too complex for a good fit to be achieved.

Errors on free parameters are then calculated, as long as a good fit is achieved, usually quoted at a 90% confidence level; this is obtained by varying the parameter of interest until a deviation of $\Delta\chi^2 \sim 2.71$ for one parameter.

3.4 Continuum spectral models

In this section I describe some frequently used (accretion disc plus corona) models, in the analysis of PDS 456 in Chapters 4, 5 & 6, to provide a physical representation of the X-ray continuum. Then, in § § 3.5 and 3.6, I describe the multiplicative absorption as well as the emission models from photoionized plasmas, which are used in modelling the outflow in PDS 456.

A common initial phenomenological step which is frequently used in the literature, is to parameterise the X-ray continuum by a combination of a power law and blackbody usually modelled in XSPEC as (`powerlaw` + `bbody`). A simple power-law (defined earlier in § 1.4.1) approximates the hard X-ray continuum above 1 keV (over a narrow enough range) and the soft X-ray excess (described in § 1.4.4) is modelled as a simple disc blackbody. Now I will describe more physically realistic models that are adopted here to account for the production of the X-rays, which are thought to be produced via Comptonization in the corona.

3.4.1 Comptonization model: `compTT`

The `compTT` model describes the process of inverse Compton scattering (already described earlier in § 1.3.1) of soft "seed" disc photons in a hot plasma in the corona. The former, emitted as a disc blackbody spectrum, peaks in the UV band for most AGN and these seed disc photons need to be up-scattered to reproduce either the hard X-ray "power-law" or soft excess. This model, developed by Titarchuk (1994), also includes the relativistic effects due to very high energy electrons and can be applied to both optically thin (i.e., $\tau < 1$ low opacity) or optically thick (i.e., $\tau \gtrsim 1$ high opacity) plasma. The model also considers either spherical or disc geometries. Thus the key parameters in this model are as follows:

- the initial soft photon temperature T_0 that will be Compton (up)scattered,
- the plasma electron temperature ($kT_{\rm e}$) where the up-scattering events occur
- the optical depth τ of the plasma.

Fig. 3.6 shows how changing these key parameters affects the resulting spectrum with an input temperature of $T_0 = 20\,\mathrm{eV}$, which is typical of the blackbody temperature in the inner disc of an AGN (see equation 1.9 in Chapter 1). In the top panel I show how a change in τ drastically affects the resulting spectrum with constant plasma temperature of $kT = 50\,\mathrm{keV}$. So a thicker plasma would result in a higher number of photon-electron scattering events, resulting in a harder ($\Gamma < 2$) spectrum out to 10 keV. At much higher energies beyond 10 keV, a characteristic "roll-over" in the spectrum is seen which is frequently present in *NuSTAR* observations of bright AGNs (e.g., Fabian et al. 2015). In the mid panel I consider an optically thin 'hot' plasma ($\tau = 0.1$) where an increase in plasma temperature also increases the energy of the up-scattered disc photons. Finally in the bottom panel I consider a typically optically thick “warm” Comptonizing region ($\tau = 2$), which might originate on the surface of the disc and reproduces the soft X-ray excess. Here higher electron temperatures (or a thicker plasma) result in a stronger soft excess.

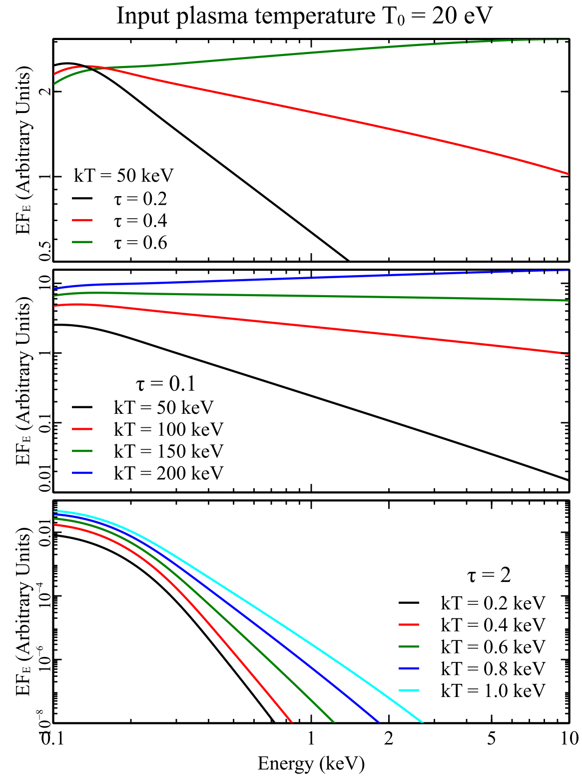

Figure 3.6: `CompTT` model simulations in both optically thin and thick plasmas produced in XSPEC. Top panel: shows how a changing optical depth drastically increases the energy of the up-scattered photons in a plasma with temperature of $kT = 50\,\mathrm{keV}$. Mid panel: shows how an increase in temperature in an optically thin ($\tau = 0.1$) and ‘hot’ plasma also increases the energy of the up-scattered hard photons resulting in a harder spectrum for higher temperatures and a harder ($\Gamma < 2$) power-law component. Bottom panel: The same as above but in an optically thick ‘warm’ Comptonizing region showing that the photons affected are in the lower energy band where the higher temperature regions produce a stronger observed soft excess below $2\,\mathrm{keV}$.

3.4.2 Multi-temperature Comptonized disc model: `optxagnf`

A more physically self-consistent disc–corona model was developed by Done et al. (2012), referred as "`optxagnf`" which assumes that the energy of the system is conserved self-consistently. Since then it has been frequently used in fitting the optical to X-ray SEDs of AGN (e.g., Jin et al. 2012; Nardini et al. 2014) and will be subsequently used in Chapter 4 and 6 where I will construct optical/UV to hard X-ray SEDs that will allow me to investigate the properties of the overall broadband continuum of PDS 456. The `optxagnf` model is characterized by three separate components, as illustrated in Fig. 3.7, which are self-consistently powered by dissipation in the accretion flow:

(i) the thermal emission from the outer accretion disc in the optical/UV;

(ii) the up-scattering of the UV disc photons into a soft X-ray excess from a warm disc atmosphere;

(iii) high temperature Comptonisation from the corona (i.e. the standard hard X-ray power-law continuum) which is hard-wired in the model at $kT_{\mathrm{e}} = 100\,\mathrm{keV}$.

In this model the radius $\mathrm{R}_{\mathrm{corona}}$ acts as a transition point between the outer optically thick accretion disc and the inner corona as shown in Fig. 3.7. Outside the disc radius the classic multi-colour blackbody emission is observed (component 1 above). Inside the radius $\mathrm{R}_{\mathrm{corona}}$, the disc emission is Comptonized by a two-temperature plasma. The first component results from the scattering of disc photons by the warm atmosphere into the soft X-ray band (component 2). In addition a hot but optically thin corona produces the standard X-ray power-law continuum at higher energies (component 3 above). The parameter $\mathtt{F}_{\mathrm{pl}}$ then characterizes the fraction of energy released in the power-law versus the soft excess. The parameters kT and τ correspond to the temperature and optical depth of the warm Comptonization region.

Unlike `compTT` the `optxagnf` model self-consistently reproduces the accretion disc spectrum for both a given black hole mass and accretion rate. In addition the energy is also conserved i.e., with a self-consistent luminosity is produced. Both the Eddington ratio and black hole mass are variable parameters. Increasing the $\mathrm{L/L_{Edd}}$ will increase the overall luminosity (for a given M_{BH}) and varing M_{BH} will also adjust the peak of the SED for a given $\mathrm{L/L_{Edd}}$ as $T \propto M_{\mathrm{BH}}^{-1/4}$ (see equation 1.9). The black hole spin can also be varied between $a = 0$ (Schwarzschild) and $a = 0.998$ (maximal prograde Kerr). A higher spin will produce a hotter and more intense disc component.

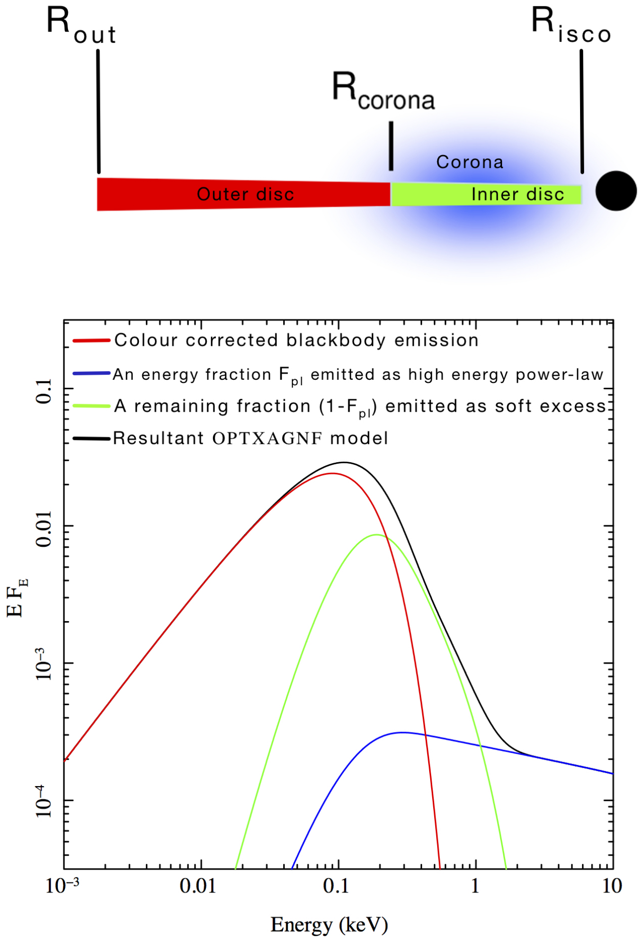

Figure 3.7: Top: a schematic representation of the geometry of the `optxagnf` model. This is split into 3 regions; (i) the optically thick outer disc emission (red), (ii) the inner Comptonized disc emission (green), (iii) the hot power-law like coronal emission (blue). Note that $\mathrm{R_{corona}}$ correspond to the transition radius between the outer disc and the inner corona. $\mathrm{R_{out}}$ represents the outer radius of the disc ($10^5\,R_{\mathrm{g}}$) whereas $\mathrm{R_{ISCO}}$ is the inner radius ($1.2 - 6\,R_{\mathrm{g}}$). Lower panel: The corresponding spectral emission for the above components where the black curve represents the total disc plus corona SED. Figure adapted from Done et al. 2012.

3.5 Absorption models

3.5.1 Neutral partial covering models

The presence of complex X-ray absorption variability is a common feature in AGN (Miller, Turner & Reeves 2008). A scenario that accounts for the changes of spectral shape possibly involves the presence of absorbing zones that only *partially cover* the X-ray source allowing a fraction $(1 - f_{\rm cov})$ of the continuum emission to emerge unattenuated. These partial covering absorbers might be described as compact clouds of gas or inhomogeneous structures within the X-ray absorber with typical size-scales comparable to that of the X-ray emission region (of the order of tens of $R_{\rm g}$). Therefore the absorbing matter has to be compact enough in order to partially obscure the compact coronal X-ray emission and the physical nature of the material might be neutral or mildly ionized. Thus throughout this thesis, to parametrize the presence of neutral partial covering absorbers, I adopted the phenomenological `zpcfabs` model in XSPEC as it provides a first-order parametrization of the broadband shape of the absorbed spectrum, which can then later be investigated with more physically realistic photoionization models such as those produced by the XSTAR code (see § 3.5.4). The model mathematical construction where I include the (partially absorbed) power-law continuum is as follows:

$$F(E) = \{f_{\rm cov} \exp\{-N_{\rm H}\sigma[E(1+z)]\} + (1 - f_{\rm cov})\} \times KE^{-\Gamma}, \tag{3.9}$$

where $N_{\rm H}$ is the column density of the absorber, $\sigma[E(1+z)]$ is the photoelectric absorption cross-section, introduced in § 1.3.2, where $E(1+z)$ is the rest-frame energy of the source (z is its redshift); $f_{\rm cov}$ is the dimensionless covering fraction ranging from $0 < f_{\rm cov} \leq 1$ which is fully covering at $f_{\rm cov} = 1$ and the vice-versa at $f_{\rm cov} = 0$. The factor K is the power-law continuum normalization in units of photons $\rm keV^{-1}\,cm^{-2}\,s^{-1}$ measured at 1 keV and Γ is the photon index.

Fig. 3.8 shows an example of a broad range of line-of-sight covering fractions and how it can significantly vary the spectrum according to the amount of the continuum that ‘leaks’ through while the column density is kept constant. On the other hand the

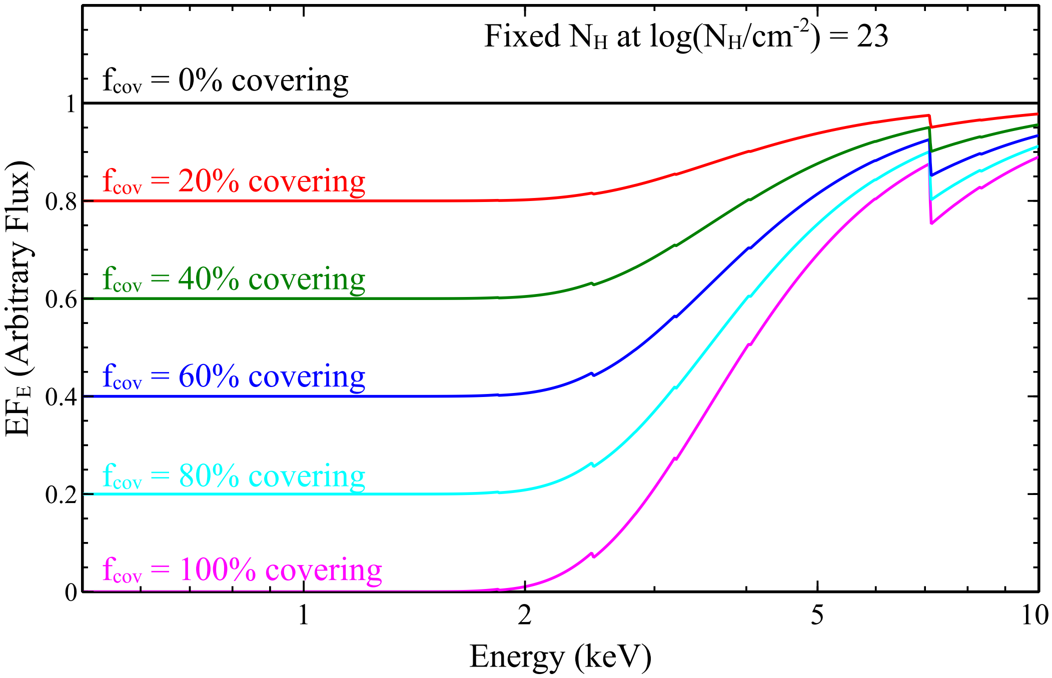

Figure 3.8: Plot of the different spectral shapes influenced by the proportion of covering fractions obstructing the observer's line-of-sight modelled as `zpcfabs`×`powerlaw` with constant $\log(N_{\rm H}/{\rm cm}^{-2}) = 23$ and $\Gamma = 2$. The black through magenta lines vary from 0% to 100%. The absorption feature at 7.1 keV is due to the iron-K absorption edge.

column density of the partial covering medium can also have a significant effect upon the spectrum. This is schematically represented in Fig 3.9 where high column density partial covering material (e.g., $\log(N_{\rm H}/{\rm cm}^{-2}) > 22$) effects hard X-rays energies > 2 keV, sometimes producing an apparent hard excess. Indeed Tatum et al. (2013) demonstrated that the hard excess can be fitted with more sophisticated partial covering models, such as from an inhomogeneous distribution of reprocessing clouds. The lower column density partial covering material ($\log(N_{\rm H}/{\rm cm}^{-2}) < 22$) predominately affects the spectral curvature below < 2 keV whilst the continuum is unattenuated at higher energies. One limitation of simple neutral partial covering models (like `zpcfabs`) is that its cross-section only contains the contributions from photoelectric absorption from neutral K (and L) shells edges. It does not account for the ionization state of the absorbing gas, nor include any bound-bound (line) absorption or re-emission.

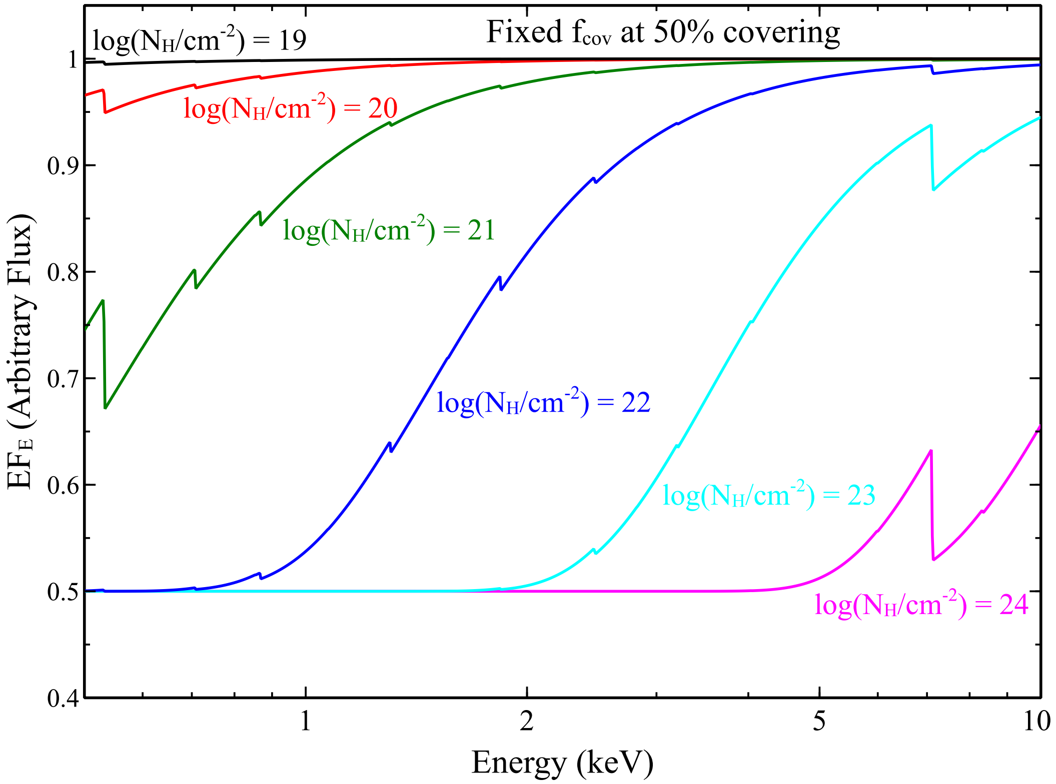

Figure 3.9: Plot of the different spectral shapes influenced by the size of column density modelled as `zpcfabs`×`powerlaw` with constant $f_{\rm cov} = 0.5$ and $\Gamma = 2$. Note how the hard X-ray spectra are affected with partial covering material with $\log(N_{\rm H}/{\rm cm}^{-2}) > 22$.

Partial covering models have been successfully adopted many times in order to explain complex spectral behaviour such as: pronounced continuum curvature below 10 keV (e.g., Reeves et al. 2005; Miller, Turner & Reeves 2008), spectral variability and X-ray occultation (e.g., Reeves et al. 2005; Turner et al. 2009; Behar et al. 2010; Lobban et al. 2011; Nardini & Risaliti 2011; Reeves et al. 2016) and pronounced hard excesses above 10 keV (e.g., Reeves et al. 2009; Risaliti et al. 2009a; Turner et al. 2010; Tatum et al. 2013). A more realistic variant on the partial covering model occurs when the material is partially ionized (see § 3.5.4).

3.5.2 XSTAR photoionization code

The parametrization of the absorption and emission in the Fe K band and over the entire spectrum (13.6 eV to 13.6 keV corresponding to $1 - 1000$ Rydberg) can be achieved by using XSTAR models[8]. The XSTAR photoionization model (Kallman et al. 2004) is a command-driven computer program that calculates the physical conditions producing absorption and emission spectra of photoionized gases. The main assumption is that each model consists of a spherical gas shell surrounding a central source of ionizing continuum radiation; the model also assumes a set of initial conditions such as the shape of the photoionizing continuum and its luminosity, electron density of photoionized gas and the chemical abundance of the gas. This shell of gas absorbs some of this radiation before re-radiating it in other parts of the spectrum. Each XSTAR grid contains a series of pre-calculated photoionized spectra for characteristic column density N_{H}, a redshift z and the ionization parameter defined in Tarter, Tucker & Salpeter 1969:

$$\xi = L_{\mathrm{ion}}/n_{\mathrm{e}}R^2 \equiv 4\pi F_{\mathrm{rad}}/n_{\mathrm{e}} \tag{3.10}$$

where L_{ion} is the ionizing luminosity computed over the range $1 - 1000$ Rydbergs, n_{e} is the electron density measured in cm^{-3}, R is the distance from the nucleus (cm) and F_{rad} is the ionizing flux measured in $\mathrm{erg\,cm^{-2}\,s^{-1}}$. In addition, each grid is associated with an intrinsic turbulent velocity v_{turb} (i.e., $v_{\mathrm{turb}} = \sqrt{2}\sigma$ measured in $\mathrm{km\,s^{-1}}$ where σ is the line width; see Kallman et al. 2004), allowing extra line broadening above that due to the natural or thermal widths of the lines, which are often negligible in the X-ray spectra. Also another additional cause of broadening can be due to the effect of Doppler broadening (emission), or the outflow velocity shear (absorption).

In terms of spectral fitting, after the XSTAR grid is generated, the absorption (through the shell of gas) is included in the forward (transmitted) direction through a *multiplicative* table of calculated spectra (i.e., $\mathrm{XSTAR_{abs}}\times$`powerlaw`). The re-emission from the gas is included both in the forward transmitted direction from the shell and

---

[8] https://heasarc.gsfc.nasa.gov/xstar/xstar.html

reflected (or scattered) emission components (averaged from all angles) through a separate *additive* table. Thus the combination of both additive and multiplicative grids gives the total emission and absorption from the plasma.

3.5.3 Modelling the Fe K absorption with XSTAR

If broad and deep absorption troughs are detected in the Fe K band, as in PDS 456, a (fully-covering) highly ionized XSTAR grid would parameterise successfully the column density ($N_{\rm H}$), the ionization (ξ) and the outflow velocity of the absorbing material. High velocity turbulence is also needed here in order to model the width of the absorption lines and to account for their high equivalent width provided they are not saturated.

It is found that for a low turbulence velocity, the absorption lines will saturate at relatively modest column densities, while for a higher $v_{\rm turb}$ and $N_{\rm H}$, the absorption lines may fall in the linear part (or the unsaturated section) of the 'curve-of-growth' where the equivalent width grows linearly with the column density. Furthermore I ran some XSTAR simulations of a highly ionized absorber at iron K, by adopting an absorption grid with $v_{\rm turb} = 5000\,{\rm km\,s^{-1}}$, with parameters similar to what I will use in later chapters to model the fast wind in PDS 456. This illustrates how the Fe K absorption varies as function of either column density or ionization. Thus Fig. 3.10 shows that for the same degree of ionization of $\log(\xi/{\rm erg\,cm\,s^{-1}}) = 5.5$ (which is typically seen in PDS 456 given its input SED) the absorption line is hardly present at low column density ($\log(N_{\rm H}/{\rm cm^{-2}}) = 22$) and completely saturated at $\log(N_{\rm H}/{\rm cm^{-2}}) = 24.5$ when the absorber is optically thick. In the thin range $22 < \log(N_{\rm H}/{\rm cm^{-2}}) < 24$, the absorber is in the linear part of the curve-of-growth.

On the other hand at a constant column density $N_{\rm H}$, an increase in ionization results in the iron ions becoming increasingly stripped of their bound electrons to the point where all electrons are removed and a smooth continuum is revealed. Thus this behaviour is schematically shown in Fig. 3.11, which shows six simulations of the XSTAR absorption spectrum over an ionization of $\log(\xi/{\rm erg\,cm\,s^{-1}}) = 5 - 8$ and for a constant column density $N_{\rm H} = 10^{23}\,{\rm cm^{-2}}$. As the ionization increases, the ratio between

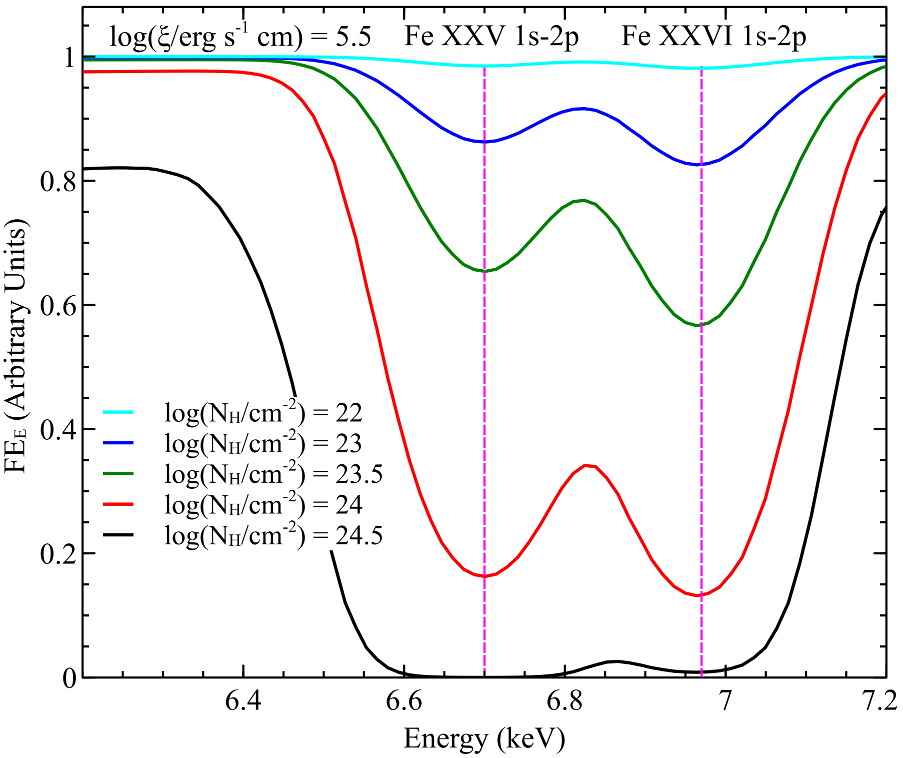

Figure 3.10: XSTAR photoionization model with $v_{\rm turb} = 5000\,{\rm km\,s^{-1}}$ showing how the Fe K absorption trough increases with constant ionization at $\log(\xi/{\rm erg\,cm\,s^{-1}}) = 5.5$ and increasing column density from $\log(N_{\rm H}/{\rm cm^{-2}}) = 22 - 24.5$ (black through cyan curves). This plot clearly shows the effect that the increase in the absorbing material column density has on the depth of absorption line which reaches saturation point when the absorber is optically thick (i.e., $\tau \gtrsim 1$ when $N_{\rm H} \gtrsim 1.5 \times 10^{24}\,{\rm cm^{-2}}$). The expected laboratory-frame energies of Fe XXV Heα and Fe XXVI Lyα are indicated by the vertical magenta lines.

the Fe XXVI/Fe XXV absorption gradually increases, from Fe XXVI/Fe XXV ~ 0.5 for the lowest ionization considered ($\log(\xi/{\rm erg\,cm\,s^{-1}}) = 5$) to Fe XXVI/Fe XXV ~ 3 for $\log(\xi/{\rm erg\,cm\,s^{-1}}) = 6$, while at much higher ionization Fe will be mainly fully ionized.

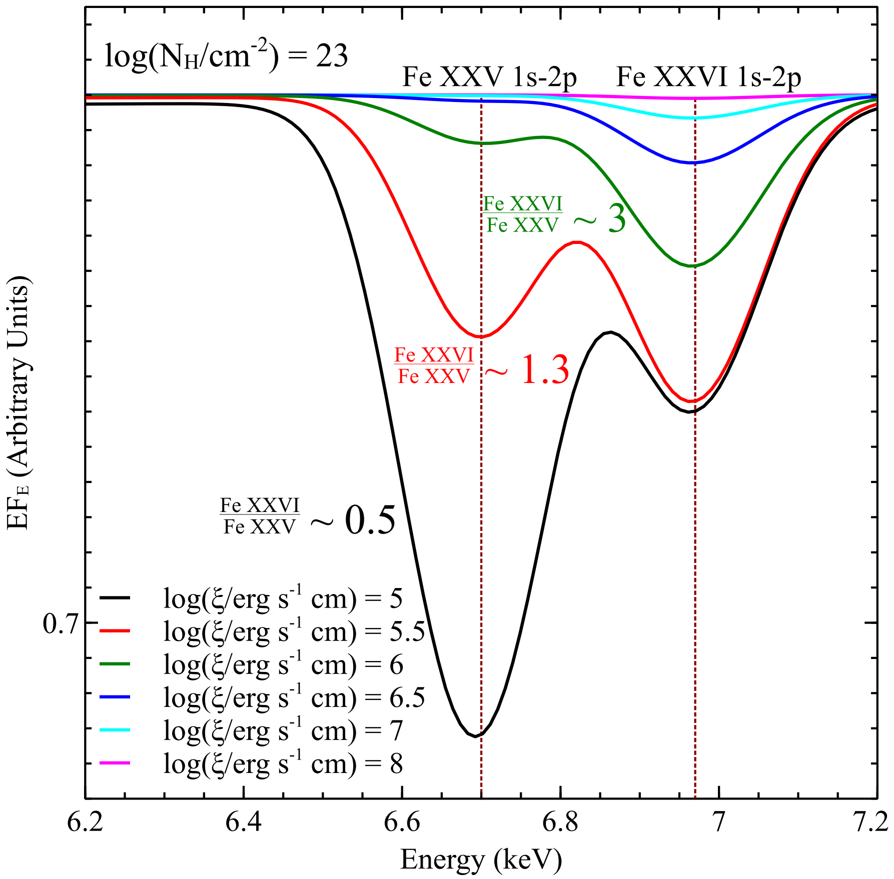

Figure 3.11: XSTAR photoionization model with $v_{\rm turb} = 5000\,{\rm km\,s^{-1}}$ showing the relative contribution of the Fe XXV and Fe XXVI resonance absorption as the ionization increases from $\log(\xi/{\rm erg\,cm\,s^{-1}}) = 5 - 8$ (black through magenta curves) with constant column density at $\log(N_{\rm H}/{\rm cm^{-2}}) = 23$. This plot clearly brings out the significant differences in the Fe XXV and Fe XXVI contribution in the Fe K absorption in particular between $\log(\xi/{\rm erg\,cm\,s^{-1}}) = 5$ and $\log(\xi/{\rm erg\,cm\,s^{-1}}) = 6$ where the Fe XXVI/Fe XXV ratio increases from ~ 0.5 to ~ 3 and thus is sensitive to the ionization. At higher ionization only a trace of Fe XXVI absorption remains and the gas is fully ionized. The expected laboratory-frame energies of Fe XXV and Fe XXVI are indicated by the vertical dark red lines.

3.5.4 Mildly ionized partial covering absorption

The photoionization modelling is not only restricted to the Fe K absorption profiles but also to the soft X-ray band, which can produce extensive/significant absorption, from K-shell lines and edges of O–Si as well as L-shell Fe. Earlier in § 3.5.1 I introduced the neutral partial covering model (`zpcfabs`) in which the absorbing materials are all characterized by neutral atoms. In reality the partial covering material can have some degree of ionization typically of the order of $\log(\xi/\mathrm{erg\,cm\,s^{-1}}) \sim 0-4$ (e.g., Sako et al. 2001; Reeves et al. 2013), thus in this work I adopted the XSTAR grids to model a partially ionized partial covering where the model is usually constructed as follow:

$$\texttt{powerlaw}_{\rm unabs} + (\textsc{xstar} \times \texttt{powerlaw}_{\rm abs}) \tag{3.11}$$

where $\texttt{powerlaw}_{\rm abs}$ and $\texttt{powerlaw}_{\rm unabs}$ are the absorbed and unabsorbed powerlaw components respectively with their photon-index tied and their normalization $K_{\rm abs}$ and $K_{\rm unabs}$ free to vary, giving the covering fraction as $f_{\rm cov} = K_{\rm abs}/(K_{\rm abs} + K_{\rm unabs})$ and XSTAR represents the multiplicative absorption $e^{-\tau(E)}$. The ionized absorbing material can have a smooth (homogeneous) or a clumpy (inhomogeneous) consistency. If homogeneous, *all* the observer's line-of-sight to the X-ray source passes the absorbing medium which then fully covers the X-ray continuum with the resulting flux possibly reaching zero if the opacity and column density of the material are high enough (e.g., $N_{\rm H} \gtrsim 10^{23} - 10^{24}\,\mathrm{cm^{-2}}$). As in the neutral partial coverer, the change in the relative covering fraction $f_{\rm cov}$ will affect the X-ray spectrum considerably as shown in Fig. 3.12 where the bound-bound absorption lines are dominating across the $0.6 - 10\,\mathrm{keV}$ X-ray spectrum. As the covering is increased, more the sight lines of the X-ray continuum intercept the absorbing gas so the absorption lines become progressively deeper and the spectrum therefore becomes progressively more absorbed to the point where the partial covering is at 100%, and all the sight lines pass through the partially ionized absorber.

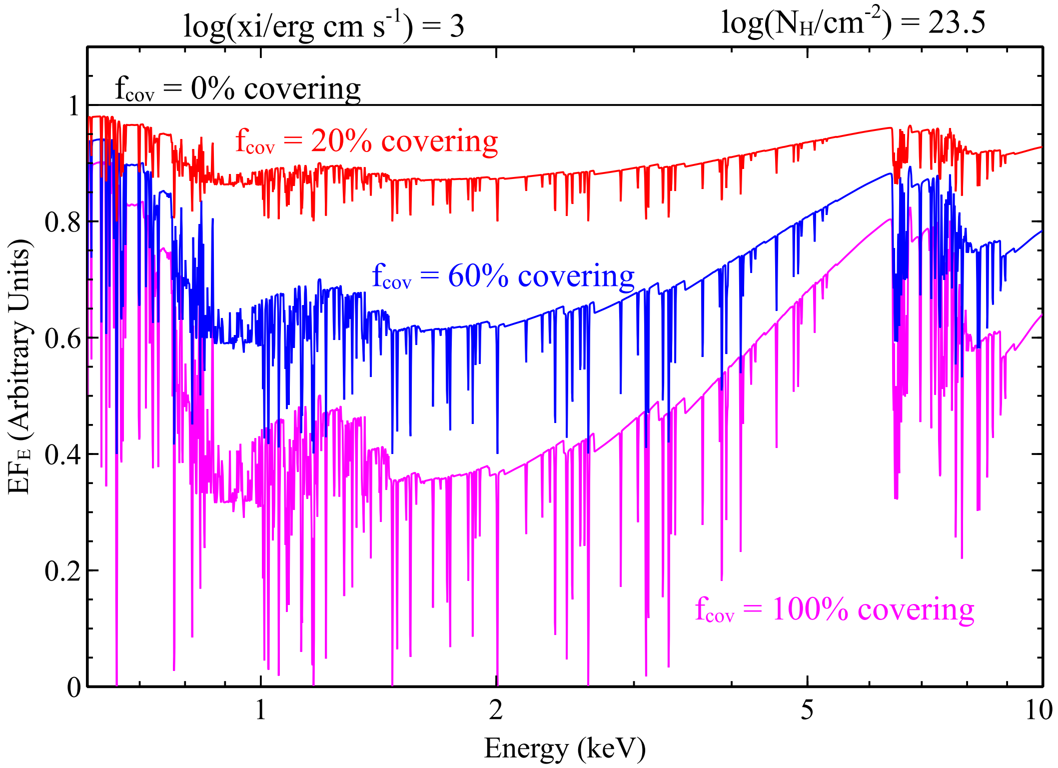

Figure 3.12: Illustration of a partially ionized partial covering model. Here this is modelled with a low turbulence XSTAR grid ($v_{\rm turb} = 200\,{\rm km\,s^{-1}}$) and illustrates how the changes in the absorber covering fractions affect the X-ray spectrum for a given ξ and $N_{\rm H}$. Thus low ionization simulations simply display a wealth of absorption lines from low Z (as well as Fe) elements with the spectrum becoming harder and more absorbed as the covering fraction increases.

3.6 Photoionized emission models

3.6.1 Modelling photoionized Fe K-shell emission

In this work I also expect to see emission from the highly ionized gas and it is modelled in the form of an additive XSTAR table (see § 3.5.2). In this scenario photons that are absorbed within a wide angled wind might be re-emitted over all angles. The combination of both absorption and emission could lead to the characteristic P-Cygni profile introduced in § 1.5.2.2. It is also assumed that the emitter sees the same unabsorbed SED as the absorber and that on average their turbulent velocity, ionization state and column density are the same. One exception for the emission component is that its normalization, or flux, (κ) is defined by XSTAR[9] as:

$$\kappa = f_{\rm cov} \frac{L_{38}}{D^2_{\rm kpc}} \tag{3.12}$$

where L_{38} is the ionizing luminosity, over the $1 - 1000$ Ryd band, normalized to $10^{38}\,{\rm erg\,s^{-1}}$ and $D_{\rm kpc}$ is the distance to the AGN in kpc. The $f_{\rm cov}$ term is simply the covering fraction of the gas, defined as $f_{\rm cov} = \Omega/4\pi$ where Ω is the total solid angle; thus for a fully covering spherical shell $f_{\rm cov} = 1$. Furthermore this allows me to set the normalization within XSPEC from the ionizing luminosity that I expect from a fully covering shell of gas for a given column density. So if the normalization of the emitter is less than expected, based upon the incident luminosity upon the shell, then this might imply that the gas has a lower covering fraction ($f_{\rm cov} < 1$) or a lower column density (see § 4.5.1).

As for the XSTAR absorption, I ran a few simulations also adopting $v_{\rm turb} = 5000\,{\rm km\,s^{-1}}$ and assuming a column density of $\log(N_{\rm H}/{\rm cm^{-2}}) = 23.8$ (as measured in PDS 456 later in Chapter 4) each for $\log(\xi/{\rm erg\,cm\,s^{-1}}) = 5 - 6$ in order to see how the contribution of each line varies with increasing ionization. Here the He or H-like emission includes the contribution from Lyα (or Heα), Lyβ (or Heβ) emission lines, as well as their respective Radiative Recombination Continua (RRC) emissions as shown in the top panel of Fig. 3.13. The bottom panel of Fig. 3.13 zooms into the $6 - 10$ keV band, where the relative contributions of Fe XXV and Fe XXVI, with increasing ionization are also plotted.

---

[9] https://heasarc.gsfc.nasa.gov/xstar/docs/html/xstarmanual.html

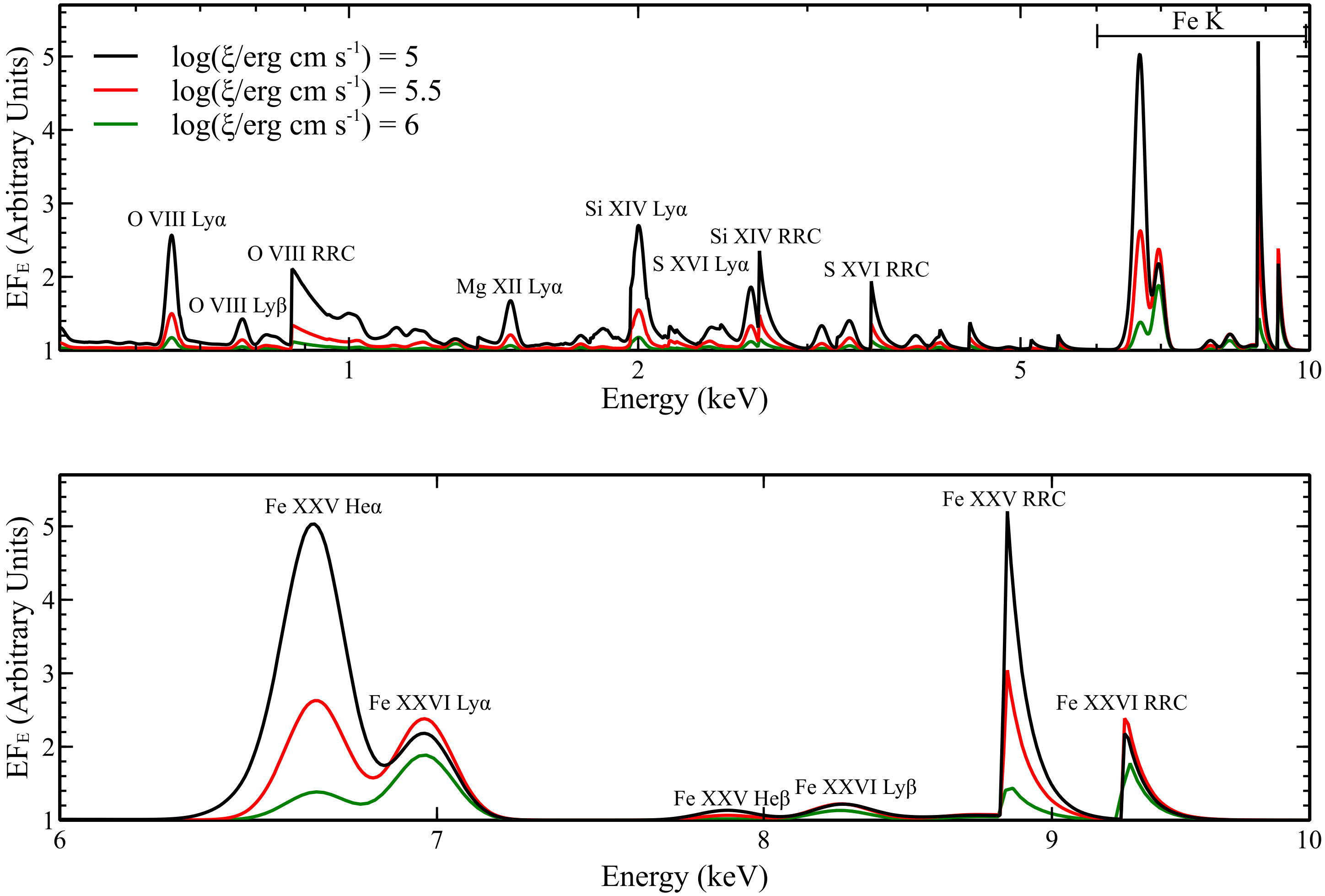

Figure 3.13: XSTAR photoionization model with $v_{\rm turb} = 5000\,{\rm km\,s^{-1}}$ and constant column density $\log(N_{\rm H}/{\rm cm^{-2}}) = 23.8$ where the ionization is varying from $\log(\xi/{\rm erg\,cm\,s^{-1}}) = 5 - 6$ (black to green curves). Top: Plot showing the relative contributions of the photoionized He/H-like emissions from O–Fe and their corresponding RRC emissions across the $0.5 - 10$ keV band, where the most prominent are labelled accordingly. Bottom: Zoomed in plot between the $6 - 10$ keV band showing the contribution of the He/H-like iron including the corresponding RRC emissions. In both plots the relative contribution to the emission of each ion changes as the ionization state varies.

3.7 Table models used in this thesis

Throughout this thesis, multiplicative (absorption) and additive (emission) XSTAR grids that I will adopt have these characteristics:

- The grids are generated with an input $1-1000\,\mathrm{Ryd}$ ionizing luminosity based on the fitting of the unabsorbed SED of PDS 456 which is covered later (in more detail) in § 4.4.2,
- the range of turbulence velocity adopted is between $v_{\mathrm{turb}} = 5000 - 15000\,\mathrm{km\,s^{-1}}$ to model broad spectral lines from the fast wind in PDS 456,
- We adopted a variety of grids depending on the parameter space we wish to cover, for instance in order to model a wide range of absorber properties we would use a 20×20 grid covering the ranges $\log(\xi/\mathrm{erg\,cm\,s^{-1}}) = -1$ to 8 in logarithmic steps of $\Delta(\log\xi) \sim 0.5$ and $\log(N_{\mathrm{H}}/\mathrm{cm^{-2}}) = 21.3 - 24.7$ with steps of $\Delta(\log N_{\mathrm{H}}) \sim 0.2$. If we wish to model a narrower parameter space such as the highly ionized Fe K absorber, we would use a narrower range in $\log(N_{\mathrm{H}})$ and $\log(\xi)$, such as in log increments of 0.1 for both parameters respectively,
- each grid is generated adopting Solar abundances for all abundant elements, based on the values from Grevesse & Sauval (1998), except for Nickel which is set to zero as a default option as the atomic rates are less accurate[10],
- a typical density of $n_{\mathrm{e}} \approx 10^{9}\,\mathrm{cm^{-3}}$ was used, but the output models are not strongly dependent on this parameter,
- each spectrum in each grid of models was generated over the energy range of $0.1 - 20\,\mathrm{keV}$ over 10000 points in energy.

---

[10] https://heasarc.gsfc.nasa.gov/xstar/docs/html/node76.html

4 Broadband X-ray spectral variability of PDS 456[1]

4.1 Chapter content and motivation

In this chapter, I will present a general overview of the relatively recent observations of PDS 456. Here I will present published collaborative work which I contributed either as a main or as a co-author. My contribution includes a comparison between the 2007, 2011 and 2013 *Suzaku* observations and the simultaneous large *XMM-Newton* & *NuSTAR* campaign carried out in late 2013 and early 2014 where evidence for a massive, wide angle disc-wind was established. In particular, I will present the broadband analysis of three *Suzaku* time-averaged (observation) sequences obtained from the long (~ 1 Ms duration) 2013 campaign of PDS 456 as well as an initial comparison with the earlier 2007 and 2011 archival *Suzaku* data. These five *Suzaku* observations from 2007 to 2013, caught PDS 456 in drastically different flux states where in 2013 the quasar flux was unusually low. An analysis of the 2013 dataset has been first presented in Gofford et al.

---

[1] This chapter is partly based on the first part of the published work entitled:
'*Short-term spectral variability of the quasar PDS 456 observed in a low flux state*'; **G. A. Matzeu**; J. N. Reeves; E Nardini; V. Braito; M. T. Costa; F. Tombesi; J. Gofford; 2016, MNRAS, **458**, 1311-1329.

In this chapter I will also present the summary of the published work where I contributed as a co-author:
'*Black hole feedback in the luminous quasar PDS 456*'; E. Nardini; J. N. Reeves; J. Gofford; F. A. Harrison; G. Risaliti; V. Braito; M. T. Costa; **G. A. Matzeu**, G. A.; D. J. Walton; E. Behar; S. E. Boggs; F. E. Christensen; W. W. Craig; C. J. Hailey; G. Matt; J. M. Miller; P. T. O'Brien; D. Stern; T. J. Turner; M. J. Ward; Science, 2015, 347, 860.
'*Variability of the High-velocity Outflow in the Quasar PDS 456*'; J. N. Reeves; V. Braito; J. Gofford; S. A. Sim; E. Behar; M. T. Costa; S. Kaspi; **G. A. Matzeu**; L. Miller; P. T. O'Brien; T. J. Turner; M. J. Ward; 2014, ApJ, 780, 45.
'*Revealing the Location and Structure of the Accretion Disk Wind in PDS 456*'; J. Gofford; J. N. Reeves; V. Braito; E. Nardini; M. T. Costa; **G. A. Matzeu**; P. T. O'Brien; M. J. Ward; T. J. Turner; L. Miller; 2014, ApJ, 784, 77.

All work was conducted by myself unless otherwise stated

(2014), where I also contributed as a co-author, initially focusing on the variability of the iron K absorption feature.

In this chapter I will also investigate in more detail the broadband primary continuum and absorption variability in PDS 456 following on from what I presented in Matzeu et al. (2016). I will subsequently focus on the photoionization modelling of the Fe K profile in *Suzaku* 2013 data, which I extended it to the 2007 and 2011 observations in order to cover a wider flux range. I will then summarize the main results presented in Nardini et al. (2015, N15 hereafter), where I also contributed as a co-author, from the *XMM-Newton* & *NuSTAR* observations. In this collaborative work, my contribution was to re-analyse the properties of the Fe K features from these observations and compare the results to those from *Suzaku*. Thus the overall aim is to give a broadband overview of all the contemporary X-ray observations of PDS 456 from 2007–2014, including how the X-ray absorber varies with changes in flux seen across these observations. More specifically, the aims of this broadband analysis presented in this chapter are to:

(i) construct a UV to hard X-ray spectral energy distribution (SED) of PDS 456 in order to characterize the overall spectral properties of the three 2013 sequences;

(ii) utilise the good energy resolution made available through the *Suzaku* XIS to test for the presence (or absence) of any highly-ionized blueshifted absorption lines in the Fe K band initially focusing on the *Suzaku* 2013 campaign;

(iii) generate a custom made XSTAR photoionization model (defined in § 3.5.2) by applying the above SED as the input continuum for the code;

(iv) perform photoionization modelling of the iron K absorption feature with XSTAR in the 2013 *Suzaku* sequences and subsequently extend to the earlier 2007 and 2011 *Suzaku* observations;

(v) summarise the main results of the later simultaneous *XMM-Newton* & *NuSTAR* campaign in 2013/2014, presented in Nardini et al. (2015) where I contributed by extending the photoionization modelling to both the Fe K absorption and emission profiles, and compare it to the *Suzaku* results;

	2007	2011	2013a	2013b	2013c
Obs. ID	701056010	705041010	707035010	707035020	707035030
Start Date, Time (UT)	2007-02-24, 17:58	2011-03-16, 15:00	2013-02-21, 21:22	2013-03-03, 19:43	2013-03-08, 12:00
End Date, Time (UT)	2007-03-01, 00:51	2011-03-19, 08:33	2013-02-26, 23:51	2013-03-08, 12:00	2013-03-11, 09:00
Duration(ks)	370	240	440.9	404.2	248.4
Exposure(ks)[a]	190.6	125.6	182.3	164.8	108.3
$\mathrm{Flux}^{b}_{(0.5-2)\mathrm{keV}}$	3.46	1.36	0.59	0.30	0.43
$\mathrm{Flux}^{b}_{(2-10)\mathrm{keV}}$	3.55	2.84	2.09	1.59	1.72
$\mathrm{Flux}^{b}_{(15-50)\mathrm{keV}}$	$5.7^{+2.2}_{-2.2}$	< 2.5	< 2.0	< 2.0	< 2.0

Table 4.1: Summary of the three 2013 observations of PDS 456 with Suzaku plus the archival 2007 and 2011 sequences.

[a] Net Exposure time, after background screening and dead-time correction.
[b] Observed fluxes in the $0.5-2$ keV, $2-10$ keV and $15-50$ keV bands in units $\times 10^{-12}$ erg cm^{-2} s^{-1} (1σ upper-limits).

(vi) determine the time-scales through which both the X-ray absorption and continuum variations occur, by directly measuring the absorber's behaviour, on time-scales of days–weeks;

(vii) measure the time-scales at which the Fe K absorber and emitter respond to the hard X-ray continuum variations leading to an estimate of the radial location of the disc-wind in PDS 456 and to subsequently calculate the mass outflow rate.

4.2 Overview of current X-ray observations of PDS 456

The first *Suzaku* (Mitsuda et al. 2007) observation of PDS 456 was carried out in February 24 and March 1 2007 over a total duration of 370 ks through the X-ray Imaging Spectrometer (XIS; Koyama et al. 2007) with a net exposure time of $\sim$ 190 ks. A subsequent follow-up observation of PDS 456 was carried out between the 16-19th of March 2011 for a duration of $\sim$ 240 ks, with a corresponding net (XIS) exposure of 125.6 ks (see Table 4.1 for more of all the exposure details). In a subsequent large campaign, *Suzaku* observed PDS 456 between February and March 2013 through the X-ray Imaging Spectrometer and the Hard X-ray Detector (HXD; Takahashi et al. 2007), although in these observations PDS 456 was not detected in either the PIN or GSO detectors. Due to scheduling reasons the observation is constituted by three sequences: the first (OBSID:707035010, hereafter 2013a), obtained between the 21-26th February 2013, has a duration of $\sim$ 441 ks; the second (OBSID:707035020, hereafter 2013b) and the third (OBSID:707035030, hereafter 2013c) were obtained consecutively between the 3-11th March 2013, and have durations of $\sim$ 404 ks and $\sim$ 248 ks, respectively. The total duration of the 2013 campaign was $\sim$ 1 Ms (after allowing for a scheduling gap between the first and the second sequence), with a total net exposure of 455 ks (Table 4.1).

For all the five *Suzaku* sequences, in order to achieve a further improvement on the constraints on the iron K absorption profile in the XIS-FI spectra, I adopted a spectral binning corresponding to the approximate FWHM resolution of the detector (which is $\sim$ 60 eV at 6 keV), using the `rbnpha` and `rbnrmf` FTOOLS to hardwire this binning into the spectral and response files. An additional grouping corresponding to > 25 counts per spectral bin was subsequently applied to the re-binned spectra, in order to use the χ^2 minimization technique. In the 2007 observation, PDS 456 was marginally detected by the HXD/PIN (Reeves et al. 2009, although subject to background uncertainties discussed in that paper) and has no detection in the 2011 observations (Reeves et al. 2014), thus we did not adopt the HXD data here. Furthermore for the three 2013 *Suzaku* sequences, although not detected at hard X-rays in these observations, I obtained an upper-limit to the HXD/PIN flux in 2013a between $15-50$ keV, i.e. $< 2.0\times10^{-12}$ erg cm^{-2} s^{-1}. The flux was obtained by converting the HXD/PIN count rate upper-limit through WebPIMMS[2], assuming a simple power law with $\Gamma = 2.4$. Thus, in all the subsequent spectral fits, the predicted limits to the hard X-ray flux are consistent with the above value and with subsequent imaging observations by *NuSTAR* which will be presented later in this chapter (§ 4.3.2).

The *XMM-Newton* (Jansen et al. 2001) and *NuSTAR* (Harrison et al. 2013) satellites simultaneously observed PDS 456 on four occasions between the 27th of August to the 21st of September 2013 (hereafter denoted as ObsA–ObsD) with a fifth, and last, observation (hereafter ObsE) performed between the 26–27 of February 2014 (see Table 4.2 for more details of each of the five observations). We also considered the source photometry in the six wide-band V, B, U, UVW1, UVM2 and UVW2 filters of the *XMM-Newton* Optical Monitor (OM) in order to constrain the shape of the optical/UV ionizing continuum, where we applied the appropriate absorption correction based on the standard extinction law with $A_{\rm V} \sim 1.5$ and $E_{\rm B-V} = 0.48$ values appropriate for PDS 456 (Cardelli, Clayton & Mathis 1989). From the fluxes reported in Table 4.1, it is clear that in early 2013 *Suzaku* caught PDS 456 in an extended period of unusually low flux, especially compared to the later (about six months) *XMM-Newton* and *NuSTAR* campaign where the soft X-ray band flux in ObsA, the highest flux to date, is typically a factor of ~ 10 brighter (see Table 4.2). This therefore provided a unique opportunity to study the properties of the intrinsic continuum and the reprocessing material in the low flux state of PDS 456. In the 2007 and 2011 observations, *Suzaku* caught PDS 456 in a high and intermediate flux respectively, when compared to both *Suzaku* 2013 and the *XMM-Newton* & *NuSTAR* observations.

This is shown in Fig. 4.1, which compares the long-term broadband (i.e., $0.5-10$ keV) flux between all the *Suzaku* and *XMM-Newton* & *NuSTAR* observations from 2007 to 2014. The unusually low flux in the 2013 *Suzaku* observations is clear, followed by the drastic factor of 10 increase in the X-ray flux in the first (ObsA) *XMM-Newton* observation just six months later. The flux then declines again during the course of the

---

[2] https://heasarc.gsfc.nasa.gov/cgi-bin/Tools/w3pimms/w3pimms.pl

Obs.	Satellite	Obs. ID	Start Date (UT)	End Date (UT)	Duration(ks)	Exposure(ks)
A	*XMM-Newton*	0721010201	2013-08-27, 04:41	2013-08-28, 11:13	110.0	95.7
	NuSTAR	60002032002	2013-08-27, 03:41	2013-08-28, 11:41	113.9	87.6
B	*XMM-Newton*	0721010301	2013-09-06, 03:24	2013-09-07, 11:13	112.3	95.7
	NuSTAR	60002032004	2013-09-06, 02:56	2013-09-07, 10:51	113.9	85.9
C	*XMM-Newton*	0721010401	2013-09-15, 18:47	2013-09-17, 03:57	119.4	102.0
	NuSTAR	60002032006	2013-09-15, 17:56	2013-09-17, 04:01	119.1	88.0
D	*XMM-Newton*	0721010501	2013-09-20, 02:47	2013-09-21, 09:57	111.0	93.0
	NuSTAR	60002032008	2013-09-20, 03:06	2013-09-21, 11:11	119.1	117.1
E	*XMM-Newton*	0721010601	2014-02-26, 08:03	2014-02-27, 22:51	139.7	100.3
	NuSTAR	60002032010	2014-02-26, 08:16	2013-02-28, 22:56	224.3	219.0

	A	B	C	D	E
Flux$_{(0.5-2)\mathrm{keV}}$	3.78	2.58	2.32	2.25	1.61
Flux$_{(2-10)\mathrm{keV}}$	6.59	2.77	3.49	3.84	2.62
Flux$_{(10-50)\mathrm{keV}}$	5.35	1.35	2.53	2.88	1.73

Table 4.2: Summary of the simultaneous *XMM-Newton* and *NuSTAR* observations of PDS 456 performed from Aug 2013–Feb 2014 . Units of flux are $\times 10^{-12}\,\mathrm{erg\,cm^{-2}\,s^{-1}}$. The net exposure values for *NuSTAR* are for both FPMA + FPMB detectors while *XMM-Newton* net exposures are based on EPIC-pn CCD.

XMM-Newton campaign towards ObsE by a further factor of 2.5 compared to the high flux (ObsA) sequence.

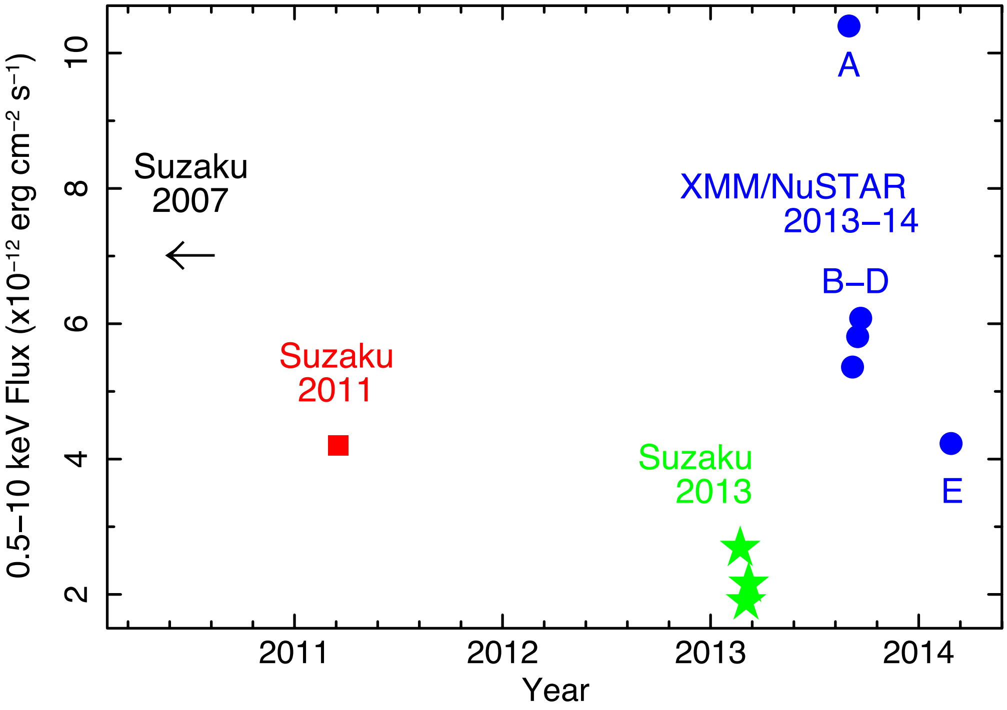

Figure 4.1: Long-term X-ray flux level of the 2007 (black arrow), 2011 (red squares) and 2013 (green stars) *Suzaku* and the simultaneous *XMM-Newton* and *NuSTAR* observations in 2013/2014 (blue dots). This plot shows the wide range of flux variability that characterizes PDS 456 and it also illustrates the unusually low flux state in the *Suzaku* 2013 observations.

4.3 Broadband spectral analysis gof the *Suzaku* observations

I now attempt to model the *Suzaku* spectra for PDS 456. Initially I focus on the 2013 observation, which as I have just shown corresponds to an unusual low flux state for

PDS 456, with a hard spectral form that indicates the presence of substantial X-ray absorption. After I initially concentrate on the Suzaku 2013 observation, the fitting is then extended to incorporate all the Suzaku observations i.e., between 2007, 2011 and 2013, in order to cover a wide range of fluxes and parameter space. Towards the end of this chapter (§ 4.5), I will also summarise the main results from 2013-2014 *XMM-Newton* & *NuSTAR* campaign as presented by N15 and I will characterize how the properties of the outflow in this *XMM-Newton* & *NuSTAR* campaign compare with those of the *Suzaku* observations.

For all the subsequent analysis, the XIS-FI spectra are fitted over the $0.6-10\,\mathrm{keV}$ band, ignoring the $1.7-2.1\,\mathrm{keV}$ interval due to uncertainties with the XIS detector Si edge. Furthermore, all the *Suzaku* spectra included were reduced in accordance to the process outlined in § 3.2. The spectral analysis and model fitting, performed with XSPEC v12.8.2 (Arnaud 1996), were focused on the spectra obtained by the XIS front illuminated (FI) CCDs – XIS 0 and XIS 3 – as they are characterized by a larger effective area and yet a lower background in the iron K band compared to the back illuminated XIS 1 CCD. The XIS 1 spectra, although consistent with those obtained with XIS 0 and 3, are noisier at higher energies in the Fe K band.

4.3.1 Initial comparison between *Suzaku* and *XMM-Newton* & *NuSTAR*

As a preliminary test, the spectral differences between all the five *Suzaku* spectra from 2007–2013 (see Fig. 4.2) were parameterised in the $2-8\,\mathrm{keV}$ rest-frame band (in order to avoid the contribution of the Fe-K absorption lines to the continuum) with a simple power-law model, where the photon indices and normalizations are allowed to vary between all the spectra. The Galactic absorption column towards PDS 456, of $N_{\mathrm{H}} = 2\times10^{21}\,\mathrm{cm}^{-2}$, was included in all the subsequent fits. I find that the 2011, 2013a, 2013b and 2013c sequences are characterized by a harder spectral shape, $\Gamma = 1.94\pm0.04$, $\Gamma = 1.47\pm0.04$, $\Gamma = 1.29\pm0.05$ and $\Gamma = 1.64\pm0.05$ respectively, compared to the 2007 spectrum ($\Gamma = 2.25\pm0.03$). This simple single power-law model provided a statistically very poor

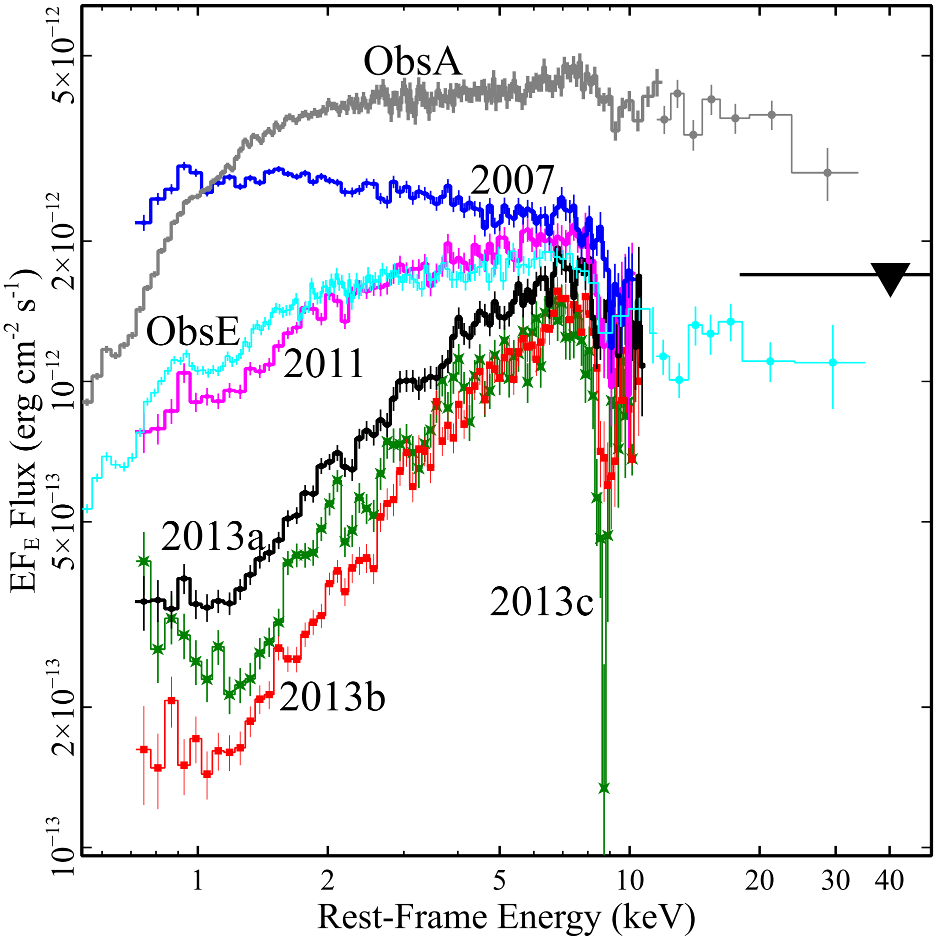

Figure 4.2: Fluxed spectra of the 2013 *Suzaku* observation: Sequence 1 - 2013a (black, including the 15 − 50 keV HXD/PIN upper-limit), Sequence 2 - 2013b (red) and Sequence 3 - 2013c (green). For comparison the 2013 (ObsA, grey) and 2014 (ObsE, cyan) spectra of the *XMM-Newton*/*NuSTAR* campaign and the 2007 (blue) and 2011 (magenta) *Suzaku* spectra are shown. The long term spectral variations in the soft band and in the iron-K region, which characterize this type 1 quasar, are evident. The *Suzaku* observation in 2013 caught PDS 456 in a remarkably low flux state compared to both the earlier *Suzaku* and subsequent *XMM-Newton* observations.

fit to the data, with $\chi^2/\nu = 2125/1318$; such a drastic hardening of the 2013 *Suzaku* spectra may be unphysical if simply attributed to the shape of the intrinsic continuum. On the other hand, what is seen is a series of spectra that may be affected by either complex absorption or reprocessed (reflected/scattered) emission, or the contribution of both.

Furthermore, it is thought that the underlying continuum in PDS 456 is intrinsically steep ($\Gamma \gtrsim 2$), as evident from the 2007 observation, when the continuum was observed through little or no obscuration (R09, also see Chapter 6), as well as from the *NuSTAR* observations, with typically $\Gamma \sim 2.4$ measured above 10 keV (e.g., N15). In addition to the harder shape of the three 2013 sequences, a deeper absorption trough is observed at ~ 9 keV (in the quasar rest-frame) which apparently strengthens as the observation progresses from 2013a to 2013c. This behaviour is shown in Fig. 4.2, where the fluxed spectra are plotted,[3] from the 2013 *Suzaku* sequences to the lowest (ObsE) and the highest (ObsA) of the five *XMM-Newton*/*NuSTAR* sequences (N15). In Table 4.3, the iron K emission and absorption line properties are listed as parameterised by Gaussian profiles. The Fe K variability which I extended to the *Suzaku* 2007, 2011 and 2013 observations will be discussed later in § 4.4.

Generally speaking, it has been suggested that all AGN characterized by a low flux spectrum may be reflection-dominated (e.g., Fabian et al. 2012; Gallo et al. 2013). Nonetheless, there are some clear differences in the PDS 456 spectra, such as the non detection of a 'Compton hump' above 10 keV in *NuSTAR* (see Fig. 4.2), and the lack of a narrow 6.4 keV Fe Kα line, which even in the 2013 low flux state has a low upper-limit on the equivalent width (EW) of < 28 eV (2013a), < 31 eV (2013b) and < 37 eV (2013c). The narrow Fe Kα lines are thought to originate from a parsec scale re-processor e.g., the putative molecular torus (see Chapter 1) and are typically observed with equivalent widths of the order of $100 - 120$ eV (e.g., Yaqoob et al. 2001; Yaqoob & Padmanabhan 2004). Thus the weak detection of the narrow Fe Kα in PDS 456 rules out the presence of a distant Compton-thick re-processor, possibly caused by the X-ray 'Baldwin effect', an apparent anti-correlation between the X-ray luminosity of a source and the equivalent width of the Fe Kα line, which has been well documented in the literature (e.g., Iwasawa

---

[3] The spectra are unfolded through the instrumental response and are compared against a simple $\Gamma = 2$ power law, and not corrected for Galactic absorption

& Taniguchi 1993; Page et al. 2004; Jiang, Wang & Wang 2006; Shu, Yaqoob & Wang 2010; Fukazawa et al. 2011). Neither is a prominent relativistic red wing to any broad iron K emission evident, unlike that claimed in the spectra of other AGN (Fabian et al. 2002). This and the lack of a Compton hump in the *NuSTAR* data above 10 keV (see § 4.5) suggests that PDS 456 is probably not dominated by strong Compton reflection components, from either the disc or distant matter.

4.3.2 Modelling the broadband SED

The spectral variability that characterizes PDS 456 is conspicuous, in particular over a six month/one year time-scale, as shown in Fig. 4.2. In order to gain a better understanding of this pronounced spectral variability, I first need to characterize the broadband intrinsic continuum of PDS 456. I therefore tested whether the broadband SED of PDS 456 could be described by a multi-temperature Comptonised accretion disc model, using the `optxagnf` model (Done et al. 2012) in XSPEC (defined in § 3.4.2). The form of the optical/UV to hard X-ray SED has been defined when the X-ray observations are in the 2013 *Suzaku* low flux state in order to attempt to define the intrinsic continuum in this low flux state[4]. In order to define the hard X-ray spectral shape above 10 keV, I consider only the lowest flux (ObsE) *NuSTAR* spectrum, as it appears closest in flux to the *Suzaku* 2013a observations at 10 keV (i.e., $\sim 2.0 \times 10^{-12}\,\mathrm{erg\,cm^{-2}\,s^{-1}}$) and it is also consistent with the upper-limit obtained for the HXD/PIN (see Tables 4.1, 4.2 and Fig. 4.2). To this end, I also make use of the optical/UV photometry provided by the *XMM-Newton* Optical Monitor also from ObsE, noting that although the optical/UV fluxes are not simultaneous with the *Suzaku* observation one year earlier, there appears to be little variability in this band from all of the *XMM-Newton* observations (to within 5%, see Chapter 5).

---

[4] Note that later in Chapter 5 I will investigate the SED and the spectral variability in the 2007 *Suzaku* observations, which is characterized by a higher X-ray flux and a steep/bare continuum and substantial X-ray flaring.

Component	Parameter	2013a	2013b	2013c
`Tbabs`	$N_{\rm H,Gal}/{\rm cm}^{-2}$	$(2 \times 10^{21})^*$	$(2 \times 10^{21})^*$	$(2 \times 10^{21})^*$
`optxagnf`	$\log(L/L_{\rm Edd})$	-0.08 ± 0.10	-0.08^t	-0.08^t
	$\rm r_{cor}$ ($\rm R_g$)	41^{+58}_{-19}	41^t	41^t
	$a^\star$	0^*	0^*	0^*
	$\rm kT_e$ (eV)	468^{+156}_{-156}	468^t	468^t
	τ	$9.9^{+2.3}_{-2.4}$	$8.9^{+2.5}_{-2.7}$	9.6 ± 2.7
	Γ	2.4 ± 0.1	2.4^t	2.4^t
	$\rm F_{pl}$	$0.09^{+0.07}_{-0.04}$	$0.08^{+0.06}_{-0.03}$	$0.11^{+0.08}_{-0.04}$
$\texttt{pc}_{\rm low}$	$\log(N_{\rm H,low}/{\rm cm}^{-2})$	22.4 ± 0.1	22.4^t	22.4^t
	$\rm f_{\mathit{cov},low}$ (%)	88^{+2}_{-3}	88^t	88^t
$\texttt{pc}_{\rm high}$	$\log(N_{\rm H,high}/{\rm cm}^{-2})$	23.1 ± 0.1	23.1^t	23.1^t
	$\rm f_{\mathit{cov},high}$ (%)	71^{+10}_{-9}	71^t	71^t
$\texttt{zgauss}_{em}$	Energy (keV)	6.9 ± 0.1	6.9^t	6.9^t
	EW (eV)	94^{+32}_{-26}	118^{+33}_{-36}	125^{+43}_{-31}
	σ(eV)	212^t	212^t	212^t
	norm^a	4.6 ± 1.2	4.6^t	4.6^t
$\texttt{zgauss}_{abs}$	Energy (keV)	$8.55^{+0.34}_{-0.26}$	8.88 ± 0.10	8.70 ± 0.07
	EW (eV)	126 ± 63	353 ± 82	530 ± 72
	σ(eV)	$264^{\rm t}$	$264^{\rm t}$	264^{+74}_{-56}
	norm^a	$-3.0^{+1.5}_{-0.76}$	-6.4 ± 1.4	-9.6 ± 1.3
	$(\Delta\chi^2/\Delta\nu)^b$	15/2	61/2	141/2
$\chi^2/\nu = 522/498$				

Table 4.3: `optxagnf` model baseline continuum parameters. ^{t} denotes that the parameter is tied during fitting and * denotes a parameter with a frozen (fixed) value in XSPEC. A cross-normalization factor of 0.98 ± 0.08 has been found between the non simultaneous *Suzaku* 2013a and *NuSTAR* ObsE spectra.

$L/L_{\rm Edd}$: Eddington ratio

$\rm r_{cor}$: radius of the X-ray corona in $\rm R_g$,

$a^\star$: black hole spin parameter,

$\rm F_{pl}$: fraction of the dissipated accretion energy emitted in the hard power law,

$\texttt{pc}_{\rm low}$, $\texttt{pc}_{\rm high}$: low and high column partial covering components with respective column density and covering fraction,

[a] Gaussian emission and absorption profile normalization, in unit of 10^{-6} photons cm^{-2} s^{-1}.

[b] Change in $\Delta\chi^2/\Delta\nu$ when the Gaussian component modelling the iron K absorption profile is removed and the spectra refitted.

Fig. 4.3 shows how the constructed SED appears between the 1 eV − 50 keV range after correcting for any absorption intrinsic to the quasar. The optical/UV fluxes are two order of magnitude higher than the X-ray spectra and they are also rising with energy, as we would expect at the Rayleigh-Jeans tail from the low energy end of the accretion disc. On the contrary, it is quite conspicuous that the X-ray points from the *Suzaku* spectra are drastically falling towards lower energy, starting from below the iron K band (< 7 keV). This spectral behaviour provides a clear indication that the low X-ray flux measured in this *Suzaku* 2013 observation is possibly due to a high level of obscuration. Subsequently the datasets were fitted simultaneously but allowing for a cross-normalization factor between the *Suzaku* 2013 and *NuSTAR* (ObsE) to account for any absolute differences in hard X-ray flux, which is found to be very close to 1.0 (i.e. 0.98 ± 0.08 in this case).

When fitting the SED with `optxagnf`, I found that some absorption is required to account for the spectral curvature above 1 keV, as shown in Fig. 4.4 (top panel). By adding one layer of neutral partial covering (`zpcfabs` model in XSPEC, defined in § 3.5.1) of column density $\log(N_{\rm H}/\rm cm^{-2}) = 22.47^{+0.02}_{-0.04}$ and covering fraction $f_{cov} = 0.97 \pm 0.01$ (tied between the three sequences), the fit improved significantly by $\Delta\chi^2/\Delta\nu = 983/2$ i.e., from $\chi^2/\nu = 1588/502$ to $\chi^2/\nu = 605/500$ without and with including absorption respectively. However, some curvature is still present in the residuals above ~ 3 keV, and the steepness of the spectral slope above 10 keV, observed with the *NuSTAR* data, is not reproduced (Fig. 4.4, middle panel). By adding a second layer of neutral partial covering, the fit improved by a further $\Delta\chi^2/\Delta\nu = 83/2$, yielding $\chi^2/\nu = 522/498$. In this latter case, a lower column zone ($\texttt{zpcfabs}_{\rm low}$) of column density $\log(N_{\rm H,low}/\rm cm^{-2}) = 22.4 \pm 0.1$ and covering fraction $f_{cov,\rm low} = 0.88^{+0.02}_{-0.03}$ is required to account for the absorption present in the soft X-ray band below 2 keV. A higher column zone ($\texttt{zpcfabs}_{\rm high}$), with column density of $\log(N_{\rm H,high}/\rm cm^{-2}) = 23.1 \pm 0.1$ and covering fraction $f_{cov,\rm high} = 0.71^{+0.10}_{-0.09}$, parametrizes the spectral curvature above 2 keV; thus it is the combination of the two zones that reproduces the complex overall spectral curvature below 10 keV.

I initially kept the partial covering column density and covering fractions tied between the three *Suzaku* 2013 sequences; in order to allow for small changes in the

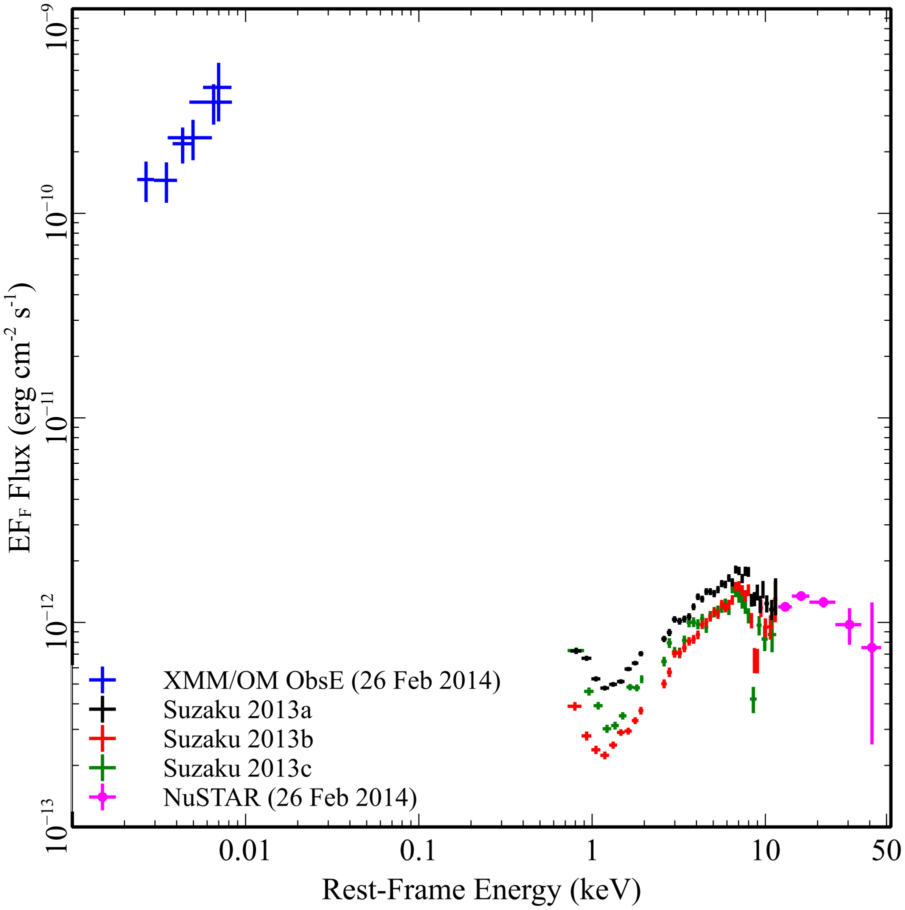

Figure 4.3: 2013/2014 low flux SED over the 1 eV - 50 keV energy range. The spectra correspond to the *XMM-Newton* OM and *NuSTAR* from ObsE in Feb 2014, the latter shown only above 10 keV (blue and magenta respectively), while also plotted are the *Suzaku* 2013a (black), 2013b (red), 2013c (green) sequences. For clarity, the *Suzaku* and *NuSTAR* spectra have been re-binned by a factor of 4 and 15 respectively. The OM points and the X-ray data are de-reddened and thus corrected for Galactic extinction.

continuum level I left the `optxagnf` parameters τ and F$_{\rm pl}$ free to vary. The coronal size was also tied between the sequences, and it is found to be $r_{\rm cor} = 41^{+58}_{-19}\ R_{\rm g}$. Due to the degeneracy between the optical depth and the temperature of the warm electrons

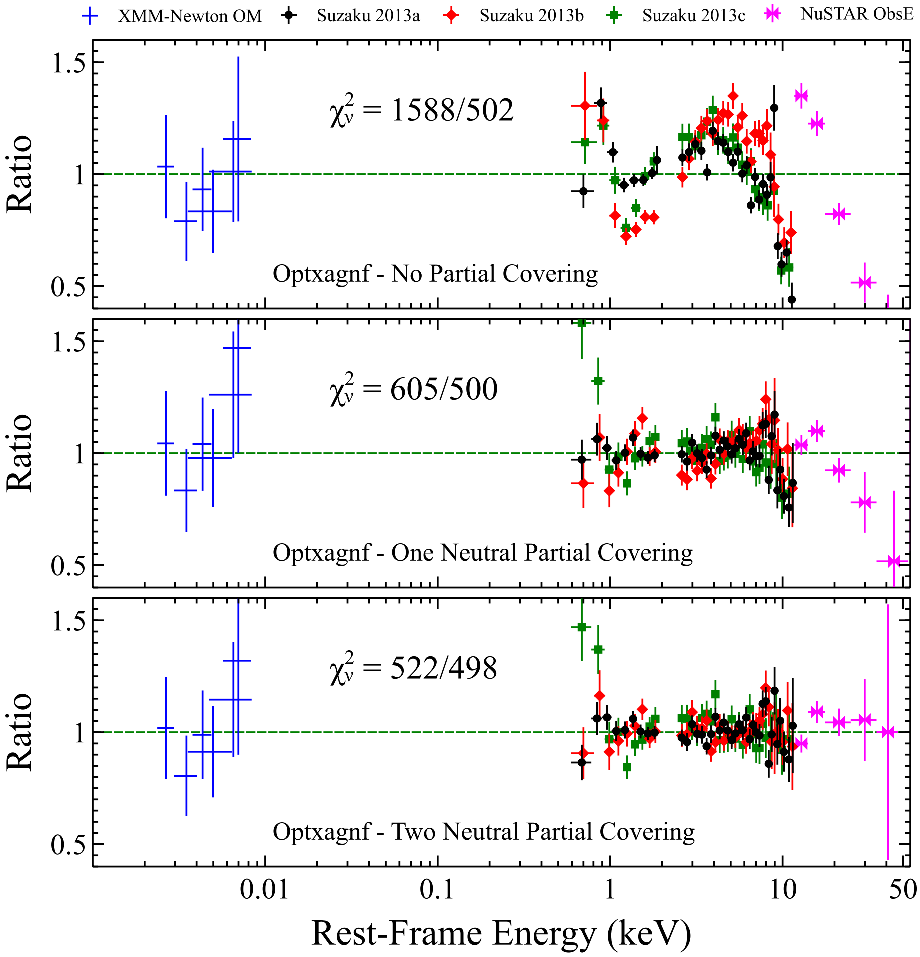

Figure 4.4: Residuals for the different `optxagnf` model fits over the 1 eV - 50 keV energy range, plotted as data/model ratios. The spectra correspond to the *XMM-Newton* OM and *NuSTAR* from ObsE in 2014 shown only above 10 keV (blue and magenta respectively), while also plotted are the *Suzaku* 2013a (black), 2013b (red), 2013c (green) sequences. Top panel: SED fits with `optxagnf` and no partial covering absorption. Middle panel: Same as above but with the addition of one partial covering layer. Bottom panel: Same as above but with two partial covering layers. For extra clarity, the spectra have been re-binned.

responsible for the soft excess, I kept the latter tied between the observations, yielding $kT = 468^{+156}_{-107}$ eV. The Eddington ratio $\log(\mathrm{L}/\mathrm{L}_{\mathrm{Edd}}) = -0.08 \pm 0.10$ implies that PDS 456 radiates close to its Eddington luminosity ($\sim 80\%$ of L_{Edd}). This is consistent with the expectations for PDS 456, given its black hole mass of $M_{\mathrm{BH}} \sim 10^9 M_{\odot}$ and bolometric luminosity $L_{\mathrm{bol}} \sim 10^{47}$ erg s^{-1} (Simpson et al. 1999; Reeves et al. 2000). Hence despite the low flux in the *Suzaku* 2013 X-ray observations, the overall accretion rate is still high and consistent with Eddington. This strongly suggests that the presence of X-ray absorption is suppressing the X-ray continuum below 10 keV in the *Suzaku* 2013 observations. Furthermore, after correcting for this absorption, the overall SED parameters are broadly consistent with the high flux SED that I will present in Chapter 6 from the bare observation with *Suzaku* in 2007. Note that the `optxagnf` best fit values are tabulated in Table 4.3.

When allowing the absorber covering fractions to vary between the three 2013 *Suzaku* sequences, they are typically found to be within $\sim 10\%$ of each other, and the statistical improvement is not too drastic ($\Delta\chi^2/\Delta\nu = 13/2$), at least considering these time-averaged spectra. I note that the value of r_{cor} above is somewhat larger than usually expected (e.g., Risaliti et al. 2009b; Reis & Miller 2013), but given our assumptions (for instance, zero black hole spin) this is regarded as an approximate estimate only. In this work, for simplicity, the spin parameter `a`* was kept fixed to zero in all the `optxagnf` fits. However if I fix $r_{\mathrm{cor}} = 10\ R_{\mathrm{g}}$ an equivalent fit was recovered to that obtained above with $a^\star = 0$ for $a^\star \sim 0.5$. In chapter 5, I will return to consider the spectral variability in the time-sliced spectra on time-scales of ~ 100 ks (corresponding to a light-crossing time of $20\,R_{\mathrm{g}}$ in PDS 456), where more pronounced X-ray variability is present on shorter time-scales.

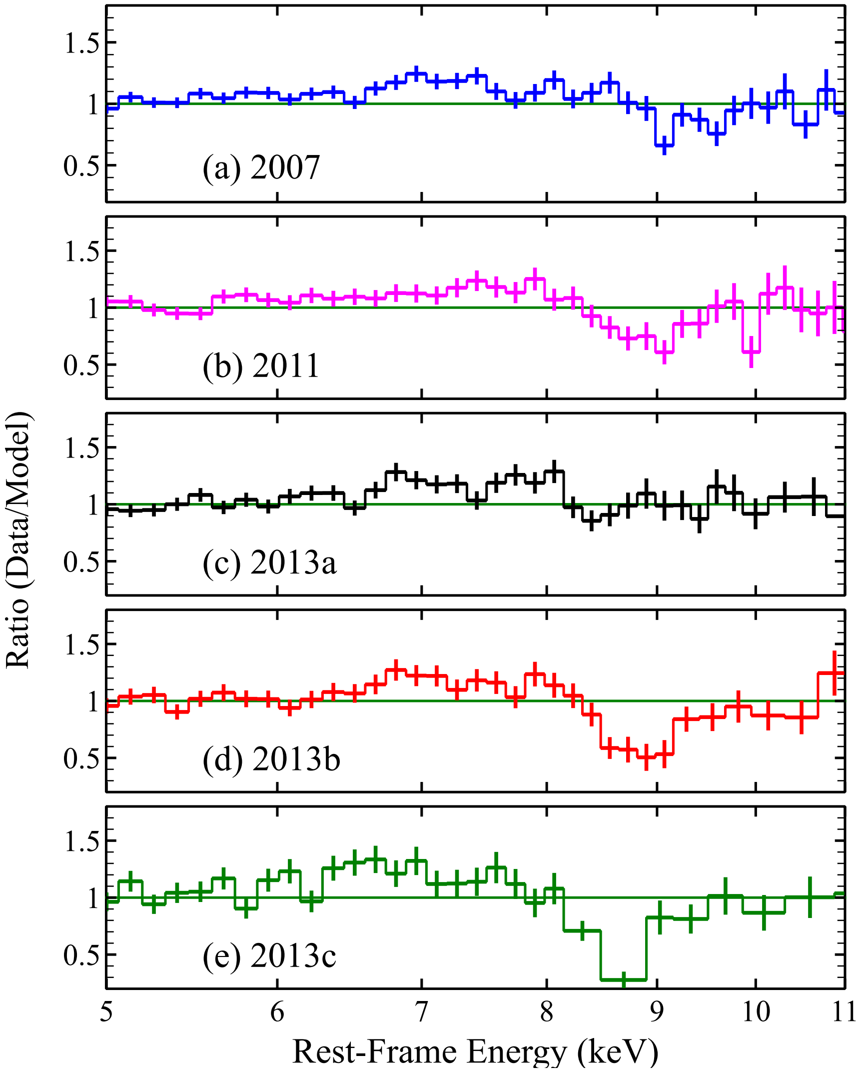

Figure 4.5: Fe K band data of the 2007 (blue), 2011 (magenta), 2013a (black), 2013b (red) and 2013c (green) *Suzaku* observations plotted as a ratio to a phenomenological power-law continuum fitted by excluding the observed $5-8.5\,\mathrm{keV}$ range. It is noticeable how in the 2013 segments, the strength of the absorption feature increases at energies $E \sim 8.5-9\,\mathrm{keV}$ as the observation progresses. The broad iron K emission is rather faint and appears to be centred at $\sim 7\,\mathrm{keV}$, while the narrow Fe Kα line at 6.4 keV is virtually absent from all the five observations.

4.4 The Fe K band modelling: emission and absorption profiles

Here I focus on the analysis of the properties of the iron K emission and absorption profiles and on their variability over the 2013 *Suzaku* observations. When the absorption feature, in the `optxagnf` baseline model, was fitted with a Gaussian profile ($\texttt{zgauss}_{abs}$), the centroid energy at $\sim 8.6-8.8$ keV indicates a large degree of blueshift when compared to the expected laboratory frame energies of the $1s \rightarrow 2p$ lines of He- or H-like Fe at 6.7 and 6.97 keV as shown in Fig. 4.5. The absorption line EW increases by a factor of ~ 5 throughout the observation, from EW $= -126 \pm 63$ eV in the 2013a sequence (improving the fit by $\Delta\chi^2/\Delta\nu = 15/2$) to EW $= -353 \pm 82$ eV in 2013b ($\Delta\chi^2/\Delta\nu = 61/2$), and EW $= -530 \pm 72$ eV in 2013c (improving drastically the fit by $\Delta\chi^2/\Delta\nu = 141/2$; see Table 4.3).

A cosmologically redshifted ($z = 0.184$) Gaussian component ($\texttt{zgauss}_{em}$) parametrizes the ionized emission profile at 6.9 ± 0.1 keV (in the quasar rest frame), likely corresponding to the Fe XXVI Lyα resonance line, although I found that the emission profile (i.e., the width) above is generally difficult to constrain in these 2013 data sets due to the lack of bandpass above 10 keV. As will be discussed later in § 4.5, the nature of the iron K emission might be associated with the P-Cygni-like feature (e.g., see the Fe K profile in 2013b,c from Fig. 4.5) arising from the disc-wind and resolved by N15 in the simultaneous *XMM-Newton* and *NuSTAR* observations carried out in late 2013/early 2014. Similar to the fit adopted in N15, the widths of the emission and the absorption Fe K profiles were tied together with a common velocity broadening of $\sigma = 264^{+74}_{-56}$ eV at the energy of the absorption line corresponding to $E = 8.7$ keV, or $\sigma = 212$ eV at 7 keV (this corresponds to a maximum velocity dispersion of $\sigma_{\rm v} \sim 9100$ km s^{-1} or FWHM ~ 21400 km s^{-1}). In N15 it was found that with *XMM-Newton* & *NuSTAR* both the emission and absorption profiles were well resolved at $\sigma = 380^{+50}_{-30}$ eV corresponding to a velocity dispersion of $\sigma_{\rm v} \sim 13000$ km s^{-1} across the flow (for FWHM ~ 30000 km s^{-1}). This model provided a statistically very good fit ($\chi^2_\nu = 522/498$). Unsurprisingly, if the Fe K absorption feature is not accounted for the model will produce a very poor fit, i.e. $\chi^2_\nu = 717/502$ and a corresponding null-hypothesis probability of 5.4×10^{-9}.

4.4.1 X-ray background

Fig. 4.6 shows the comparison (focused on the Fe K band) between the net source spectra and the averaged background spectrum, where the shaded area indicates its maximal fluctuation during the observation. A strong background emission line, corresponding to Ni Kα, arises at ~ 7.5 keV, which coincides with the observed frame energy of the Fe K absorption profile during the 2013 *Suzaku* observations. Thus it is possible that, if the background is incorrectly subtracted, it could contribute towards the absorption line feature in the source spectrum. The absorption feature is variable by a factor of $\sim 4-5$, whilst the background is almost constant ($\pm 10\%$) across all of the 2013 observations which suggests that the background may be not able to account for the Fe K absorption line variability.

To be conservative, we fitted the background spectrum of 2013c (where the Fe K absorption feature is strongest) between $5-9$ keV with a simple power law and a Gaussian emission profile, centred at 7.49 ± 0.03 keV. We find that by comparing the normalizations of both the Ni Kα background emission ($\sim 1.2 \pm 0.3 \times 10^{-6}$ photons cm^{-2} s^{-1}) and the Fe K absorption ($\sim -9.6 \pm 1.3 \times 10^{-6}$ photons cm^{-2} s^{-1}) lines, the former could only contribute to $\sim 12 \pm 3\%$ of the latter. Consequently, there is no possibility that the background feature can account for both the observed strength and variability of the absorption line, as we would expect similar variability amplitudes from the absorption line and the Ni background line, a trend that we clearly do not observe. Moreover, in the 2007 *Suzaku* observation (R09) the Fe K absorption lines were observed at higher energies (at 7.67 keV and 8.15 keV respectively) and thus were clearly separated from the Ni Kα feature at 7.45 keV (see Fig. 3 in R09). The level of the background relative to the source was much lower in those observations, as the source was much brighter. During the *XMM-Newton* observations of PDS 456 (N15), the overall level of the background is substantially lower ($< 1\%$ compared to the source spectrum), due to the

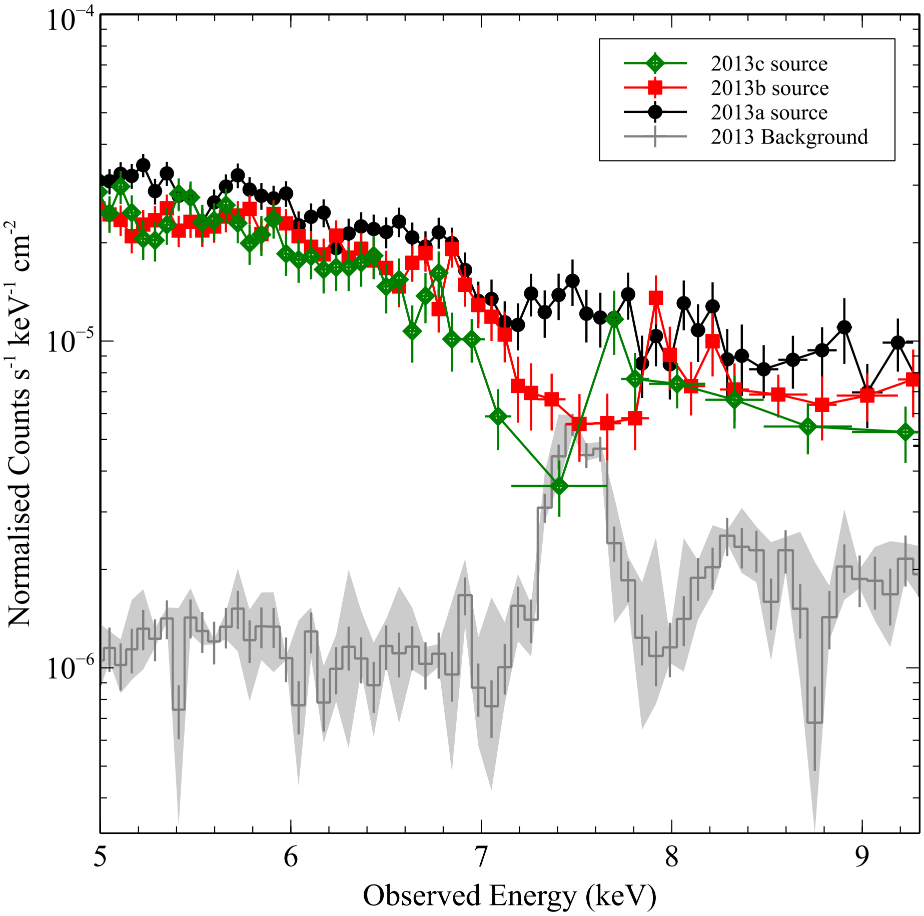

Figure 4.6: 2013 *Suzaku* XIS03 background subtracted source spectra versus the averaged background spectrum. The shaded area indicates the degree of the background fluctuation across the observation. A prominent background line, corresponding to Ni Kα, arises at ~ 7.5 keV; this was also detected by R09 in the 2007 PDS 456 spectrum (see their Fig. 3). Unfortunately, in the 2013 spectra the centroid energy of the Ni Kα in the observed frame, corresponds to that of the Fe K absorption feature, as the latter is shifted to lower energies compared to the 2007 observation. It is important to note the amplitude of the background variability of $\pm 10\%$ is too small to influence the strong increase in strength of the Fe K absorption profile from the 2013a through to the 2013c observation. The source spectra are grouped to a 4σ significance for each energy bin.

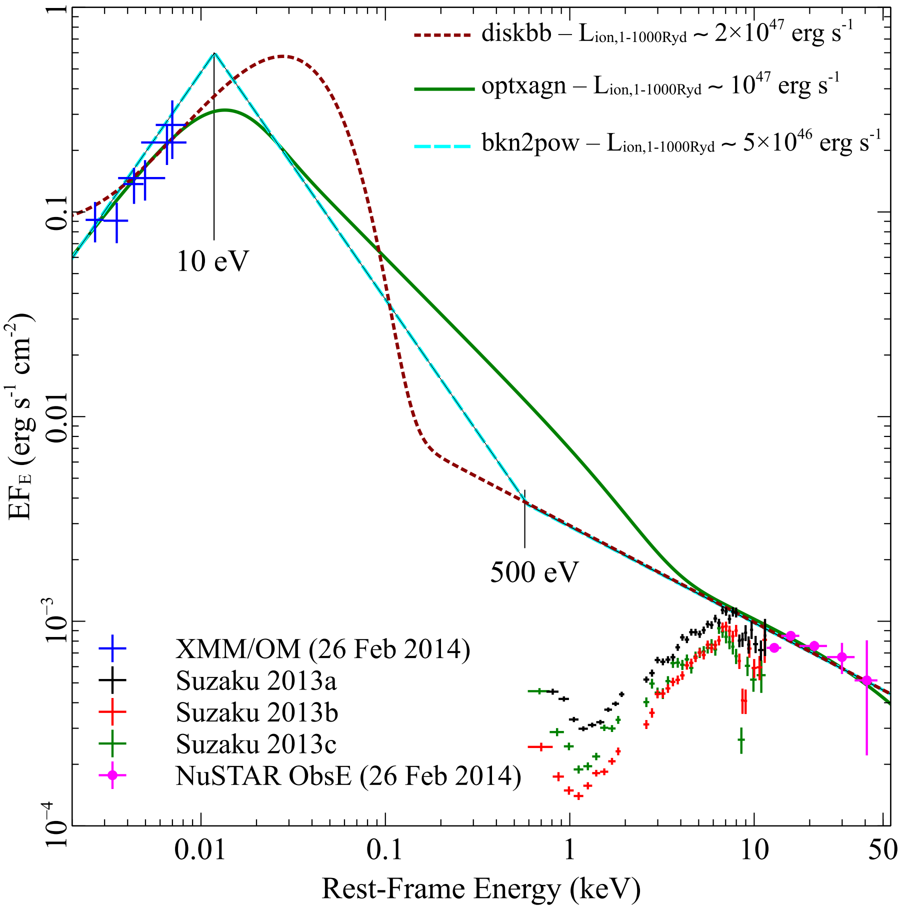

Figure 4.7: Optical to hard X-ray Spectral Energy Distribution (SED) of PDS 456 as first shown in Fig. 4.3. Here the SED was first fitted with the `optxagnf` model (green line), and then approximated with a double broken power-law (dashed cyan line) with break energies of 10 eV and 500 eV as an input for XSTAR. For comparison only, the dotted dark-red curve shows a multi-colour disc blackbody component inner disc ($R_{\rm isco}$) with temperature of 10 eV. Note that the optical/UV and the X-ray data have been de-reddened. Note in addition to the Galactic absorption, all the three models are also corrected for the intrinsic X-ray absorption, in order to visualize the true level of the X-ray continuum.

smaller extraction region used. Thus for either *Suzaku* or *XMM-Newton*, the background subtraction is likely to make a negligible contribution towards the absorption line.

4.4.2 Input SED for XSTAR photoionization models

Having modelled the above SED with the `optxagnf` model, here I need to characterize the input photoionizing continuum in order to generate self-consistent XSTAR grids (v2.21bn13, Bautista & Kallman 2001 defined in § 3.5.2) to be adopted in the subsequent photoionization modelling of the Fe K absorption profile in § 4.4.3. Following the method adopted in N15, I estimated the SED of PDS 456 by using the simultaneous *XMM-Newton* and *NuSTAR* data (including six photometric bands of the Optical Monitor, see section 4.3.2). I found that when accounting for the intrinsic and Galactic absorption towards the AGN, the SED can be approximated with a phenomenological double broken power-law (see Fig. 4.7). This yielded $\Gamma \sim 0.7$ in the optical/UV up to an assumed break energy of 10 eV (typical energy where the disc emission is at its maximum for a black hole of $10^9\, M_{\odot}$), $\Gamma \sim 3.3$ between the optical/UV and the soft X-ray band up to the second break energy fixed at 0.5 keV (the lowest observable energy allowed by the XIS detectors), and $\Gamma = 2.4$ beyond that in the X-ray band (see Fig. 4.7 dashed cyan line). For the SED modelled with the double broken power-law I estimated a total $1 - 1000$ Rydberg ionizing luminosity of $L_{\mathrm{ion,1-1000\,Ryd}} \sim 5 \times 10^{46}$ erg s^{-1}.

I also found that modelling the SED with a multi-colour disc blackbody component with R_{isco} temperature of $kT = 10\,\mathrm{eV}$ (see Fig. 4.7 dotted dark-red line) predicted a total $1 - 1000$ Rydberg ionizing luminosity of $L_{\mathrm{ion,1-1000\,Ryd}} \sim 2 \times 10^{47}$ erg s^{-1}. These estimates are also broadly consistent with the estimate derived earlier for the `optxagnf` model (Fig. 4.7 green line) which predicted $L_{\mathrm{ion,1-1000\,Ryd}} \sim 10^{47}$ erg s^{-1}. The former model over-predicts the ionizing luminosity and although the latter model approximates the overall form of the UV bump and the X-ray continuum/power-law component to a more sophisticated disc plus corona model, I adopted the double broken power-law model as a conservative photoionizing continuum input for XSTAR.

Subsequently, I adopted this SED model as the input continuum for our custom XSTAR grids. I investigated the effects of different velocity broadening by generating various XSTAR grids for a range of turbulence velocity v_{turb} values in order to provide an accurate description of the width of the Fe K absorption profile. It was found that grids with low $v_{\rm turb}$ (e.g., $v_{\rm turb} = 1000 - 3000$ km s^{-1}) resulted in a smaller EW of the absorption lines compared to the data, as the absorption profile saturated too quickly at a relatively lower column density. An adequate fit to the Fe K absorption profile was achieved when I adopted a grid with $v_{\rm turb} = 10000$ km s^{-1}; this is also consistent with the velocity width measured earlier from a simple Gaussian profile i.e., $\sigma = 264^{+74}_{-56}$ eV at 8.7 keV from the `optxagnf` fit in § 4.3.2. Thus I used the $v_{\rm turb} = 10000$ km s^{-1} grid, with the input SED described above, in all the subsequent fits.

4.4.3 Photoionization modelling of the Fe K absorption in the *Suzaku* 2013 observations

In this section I will investigate the physical properties of the iron K absorption feature ubiquitously present in the *Suzaku* 2007, 2011 and 2013 spectra with a physically motivated self-consistent XSTAR photoionization model. Having generated a suitable XSTAR grid, it was used to parameterise the Fe K absorption lines. As an initial test, I first applied the XSTAR absorption model to the 2013c spectrum, where the iron K absorption profile is stronger, in order to investigate any physical degeneracy that may arise in the model by allowing the column density and the ionization parameter to vary along with the absorber's velocity. As defined earlier in § 3.5.2 the ionization parameter is defined as $\xi = L_{\rm ion}/n_{\rm e}R^2$, where $L_{\rm ion}$ is the $1 - 1000$ Rydberg luminosity, n_e is the electron density of the gas and R is the distance of the ionizing source from the absorbing clouds.

In Fig. 4.8 (left panel), the elongated shape of the confidence contours does indeed imply that there is some degeneracy between $N_{\rm H}$ and $\log(\xi)$. This behaviour can be attributed to the fact that most of the iron is in the He- and H-like state. Thus a gradual increase of $\log(\xi)$ would not significantly affect the line centroid energy, but it would instead increase the proportion of fully ionized iron, which produces no absorption, thus requiring an apparent increase in $N_{\rm H}$ to compensate for it. On the other hand, the other two contour plots (centre and right panel) show no apparent degeneracies between either $N_{\rm H}$ or $\log(\xi)$ and the outflow velocity. On this basis, and given the degeneracies

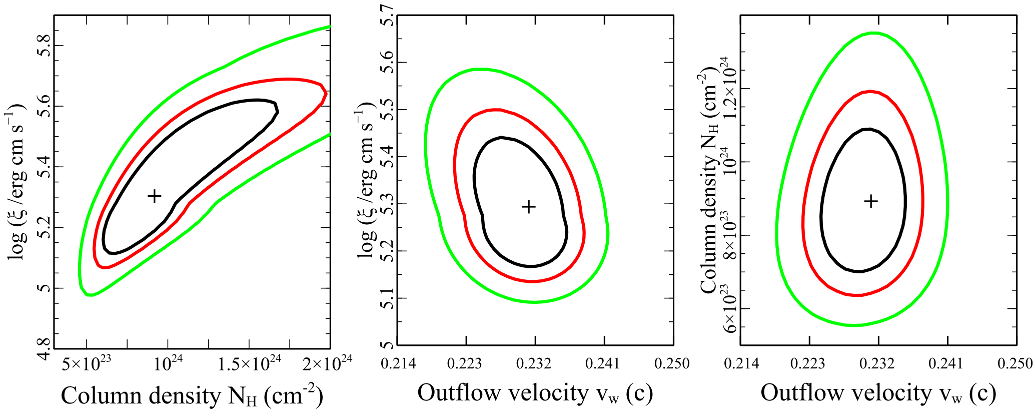

Figure 4.8: Two dimensional contour plots from the XSTAR parameters of the highly ionized wind in the 2013c segment. The solid black, red and green lines correspond to 68 %, 90 % and 99 % confidence levels for two interesting parameters respectively. The elongated contours when plotting the ionization against the column density parameters in the left panel indicate a possible degeneracy. On the other hand, the other two contour plots (centre and right panel) show no apparent degeneracies between either of the former parameters and the outflow velocity.

between N_{H} and $\log(\xi)$, the variability of the iron K absorption feature during the *Suzaku* sequences has been parameterised by either: (i) a *variable ionization*, allowing only $\log(\xi)$ to vary over the course of the observation with constant N_{H}, or (ii) a *variable column density* of the absorber allowing only N_{H} to vary whilst keeping constant $\log(\xi)$. In both cases the outflow velocity v_{w} was allowed to vary between the observations.

4.4.4 Photoionization modelling in *Suzaku* 2007, 2011 and 2013

Here I extend the photoionization modelling over a wider flux range between all the five 2007, 2011, 2013a,b,c *Suzaku* observations where I compare the 2013 observations with the higher flux spectra in 2007 and 2011. In the earlier sections I have used the `optxagnf` model to build an appropriate input SED, however when modelling multiple datasets such as the five *Suzaku* sequences, I choose a simpler two-component model in order to provide a more suitable parametrization of the continuum focusing merely on the X-ray band between $0.6 - 10\,\mathrm{keV}$. Hence I parameterised the continuum with a phenomenological baseline model of the form:

$$\begin{aligned}\texttt{Tbabs} \times [\texttt{zpcfabs}_{\mathrm{low}} \times \texttt{zpcfabs}_{\mathrm{high}} \times (\texttt{powerlaw} + \texttt{bbody}) \\ + \texttt{zgauss}_{\mathrm{Fe\,K\,em}}] \times \texttt{XSTAR}_{\mathrm{Fe\,K\,abs}},\end{aligned} \tag{4.1}$$

where `Tbabs` accounts for the Galactic absorption using the cross sections and ISM abundances of Wilms, Allen & McCray (2000). In this best-fit model, the Gaussian component ($\texttt{zgauss}_{\mathrm{Fe\,K\,em}}$) parametrizes the ionized Fe K emission profile at 6.98 ± 0.10 keV (in the quasar rest frame). We note that in this two-component power-law plus blackbody continuum model, the former is parametrized with a simple (`powerlaw`) component with photon index at $\Gamma = 2.36 \pm 0.04$ (fully consistent with the earlier `optxagnf` findings), whereas the soft excess is now parameterised with a blackbody (`bbody`) component, yielding a temperature of $kT \sim 87^{+13}_{-17}\,\mathrm{eV}$. Here I also retain two neutral partially covering absorbers as required, with column densities of $\log(N_{\mathrm{H,low}}/\mathrm{cm}^{-2}) = 22.20^{+0.05}_{-0.06}$ and $\log(N_{\mathrm{H,high}}/\mathrm{cm}^{-2}) = 23.04^{+0.06}_{-0.05}$.

The properties of the Fe K absorption profiles are now modelled with $\texttt{XSTAR}_{\mathrm{Fe\,K\,abs}}$ generated in § 4.4.2 adopting either the *variable ionization* or *variable column density* scenarios. In the former case, I find that the ionization of the line varies considerably from its maximum value at $\log(\xi/\mathrm{erg\,cm\,s^{-1}}) = 6.05^{+0.18}_{-0.16}$ in 2007 reaching its minimum at $\log(\xi/\mathrm{erg\,cm\,s^{-1}}) = 5.14^{+0.11}_{-0.21}$ in 2013c, thus a factor of 10 difference (in linear space). This large decrease in ionization is also observed within the *Suzaku* 2013 observations where the detection of the Fe K absorption profile is not as strong in the 2013a sequence (see Table 4.3) and result in a lower-limit of $\log(\xi/\mathrm{erg\,cm\,s^{-1}}) > 6.0$. In this case the column density was tied[5] between the five sequences at $\log(N_{\mathrm{H}}/\mathrm{cm}^{2}) = 23.84^{+0.14}_{-0.10}$. The outflow velocity was found to have its largest value also in the 2007 observation at $v_{\mathrm{w}} = 0.293 \pm 0.012c$ and its lowest in 2013c at $v_{\mathrm{w}} = 0.244 \pm 0.008c$. In the latter scenario, the absorbing column density progressively varies by a factor of 10 in the 2013 observation between 2013a and 2013c

---

[5] In this thesis I use the term ‘tied’ when a parameter, during a fit, is only free to vary in one specific data group whilst keeping the parameter of the others groups *tied* to that value.

Model	Parameter	2007	2011	2013a	2013b	2013c
Variable ionization	$\log(N_{\rm H}/{\rm cm}^{-2})^{\rm a}$	$23.84^{+0.14}_{-0.10}$	$23.84^{\rm t}$	$23.84^{\rm t}$	$23.84^{\rm t}$	$23.84^{\rm t}$
	$\log(\xi/{\rm erg\,cm\,s^{-1}})^{\rm b}$	$6.05^{+0.16}_{-0.18}$	$5.64^{+0.33}_{-0.15}$	> 6.0	$5.70^{+0.18}_{-0.21}$	$5.14^{+0.11}_{-0.21}$
	$v_{\rm w}\,/c$ $^{\rm c}$	0.293 ± 0.012	$0.266^{+0.011}_{-0.012}$	< 0.290	0.250 ± 0.011	0.244 ± 0.008
		$\chi^2/\nu = 741/717$				
Variable column density	$\log(N_{\rm H}/{\rm cm}^{-2})$	$23.34^{+0.28}_{-0.14}$	$23.68^{+0.15}_{-0.27}$	$23.16^{+0.28}_{-0.23}$	$23.70^{+0.19}_{-0.21}$	$24.06^{+0.18}_{-0.21}$
	$\log(\xi/{\rm erg\,cm\,s^{-1}})$	$5.45^{+0.18}_{-0.19}$	$5.45^{\rm t}$	$5.45^{\rm t}$	$5.45^{\rm t}$	$5.45^{\rm t}$
	$v_{\rm w}\,/c$	$0.306^{+0.013}_{-0.011}$	0.266 ± 0.011	$0.248^{+0.03}_{-0.02}$	0.255 ± 0.010	0.240 ± 0.010
		$\chi^2/\nu = 739/717$				
$L^{\rm d}_{2-10\,{\rm keV}}$		$4.19^{+0.04}_{-0.05}$	$3.87^{+0.06}_{-0.04}$	$3.43^{+0.04}_{-0.05}$	$2.86^{+0.06}_{-0.04}$	2.68 ± 0.06

Table 4.4: absorption parameters modelled with XSTAR (with $v_{\rm turb} = 10000$ km s^{-1}) for the *variable ionization* and *variable column density* scenarios applied to all five 2007, 2011 and 2013a–c time averaged *Suzaku* spectra. $^{\rm t}$ indicates that a parameter was tied during fitting.

[a] Logarithm of the absorber column density,
[b] logarithm of the ionization parameter,
[c] measured outflow velocity of the highly ionized wind,
[d] intrinsic X-ray continuum luminosity measured in the $2-10\,$keV band in units of $10^{44}\,{\rm erg\,s^{-1}}$.

with $\log(N_{\rm H}/{\rm cm}^{-2}) = 23.16^{+0.28}_{-0.23}$ and $\log(N_{\rm H}/{\rm cm}^{-2}) = 24.06^{+0.18}_{-0.21}$ respectively, while 2007 and 2011 have intermediate values at $\log(N_{\rm H}/{\rm cm}^{-2}) = 23.34^{+0.28}_{-0.14}$ and $\log(N_{\rm H}/{\rm cm}^{-2}) = 23.68^{+0.15}_{-0.27}$ respectively, all for a constant ionization of $\log(\xi/{\rm erg\,cm\,s^{-1}}) = 5.45^{+0.18}_{-0.19}$ (see Table 4.4 for more details). The outflow velocity follows the same trend as the previous scenario, where its maximum value is at $v_{\rm w} = 0.306^{+0.013}_{-0.011}c$ in 2007, whilst its minimum is observed in the 2013c at $v_{\rm w} = 0.240 \pm 0.010c$.

The *variable ionization* case can then be physically described as a scenario where the absorber is observed persistently in the line-of-sight. Therefore the spectral variability may be attributed to a gradual decrease in ionization in response to the decreasing continuum flux from 2007 to 2013c. As a result we can have a gas that exhibits a transition from being fully ionized as Fe XXVII, recombining into Fe XXVI (H-like iron) and subsequently recombining further into Fe XXV (He-like iron) leading to a progressive decrease in ionization. Thus the net result of that drop in ionization is an increase in the opacity of the absorber, which can account for the increase in depth of the absorption profile.

On the other hand, the *variable column density* case can be regarded as an outflow characterized by an inhomogeneous or variable absorber (or wind) with approximately constant ionization with different ejecta or streamlines that can cross the line-of-sight during the observation leading to intrinsic variability in the observed column density. On statistical grounds, both models provided an excellent fit to the Fe K band, with $\chi^2/\nu = 741/717$ and $\chi^2/\nu = 739/717$ for the *variable ionization* and *variable column density* cases respectively (see Table 4.4).

A visual comparison of the two scenarios, applied to the five *Suzaku* sequences, is shown in Fig. 4.9 where the increase in depth of the Fe K profile is clearly apparent between the 2007 and 2013 sequences. Note, these two cases were also discussed in Gofford et al. (2014, where I contributed as co-author), although they focused only on the 2013 *Suzaku* sequences, where it was also found that fitting the iron K profile with two XSTAR models provided a very good description to the data from the time-averaged *Suzaku* sequences (also cf. Fig. 4 from Gofford et al. 2014). From these results, it is evident that the intrinsic $2-10$ keV continuum luminosity is weakly variable, i.e. by a factor less than $\sim 50\%$, between the five time-averaged *Suzaku* sequences (see Table 4.4). On the other hand it was found that the ionization varies considerably (by factor of ~ 10) in particular between the brightest 2007 and faintest 2013c sequences. This may well suggest that the overall absorption variability seen by *Suzaku* is driven by variable column density rather than ionization, given the mismatch between the magnitude of the ionization and luminosity changes over all the *Suzaku* observations.

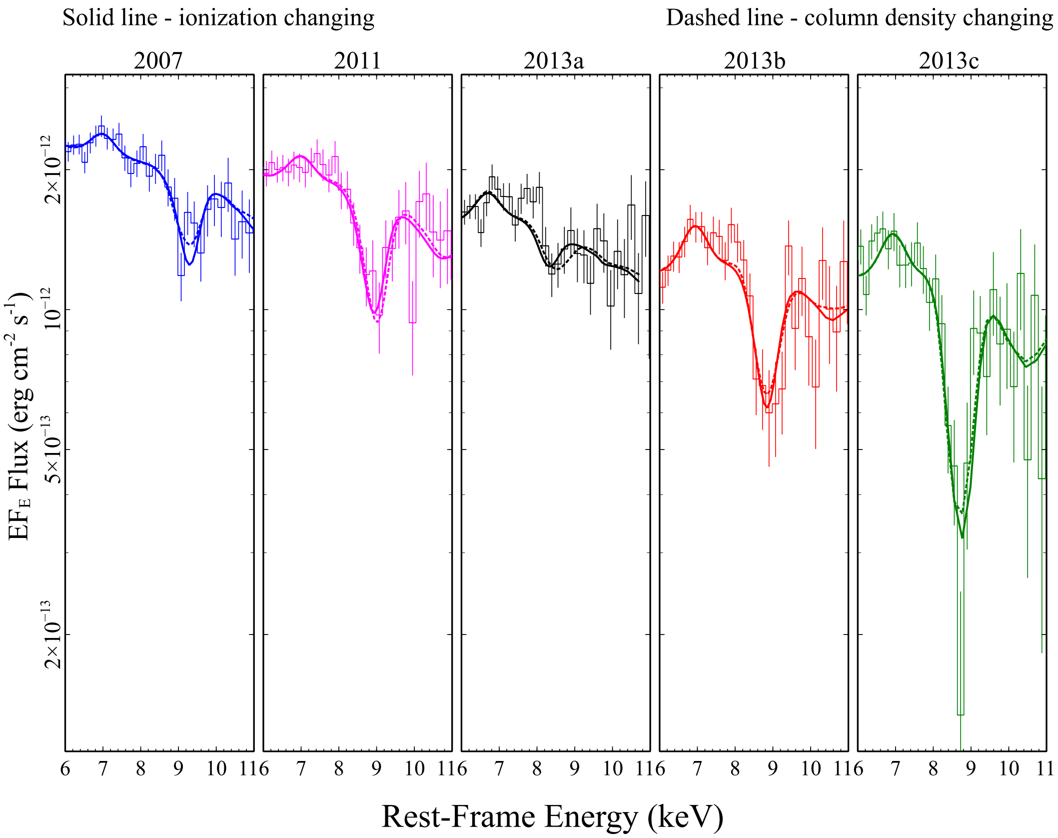

Figure 4.9: Fluxed rest-frame spectra focused on the Fe K absorption feature from the *Suzaku* 2007 (blue), 2011 (magenta), 2013a (black), 2013b (red) and 2013c (green) sequences overlaid with the best XSTAR fitting models corresponding to *variable ionization* (solid lines) and *variable column density* (dashed lines) with parameters tabulated in Table 4.4. Both scenarios describe very well the iron K absorption profile across all spectra. The fluxed spectra have have been unfolded against a simple power-law with $\Gamma = 2$, with the models superimposed afterwards, and not against the best fitting models.

4.5 Results of the *XMM-Newton*/*NuSTAR* campaign on PDS 456

As described earlier in § 4.2, the *XMM-Newton* and *NuSTAR* observations of PDS 456 commenced approximately six months after the *Suzaku* 2013 campaign ended in March

2013. This new campaign was awarded as a large program (PI J Reeves), consisting of 5×100 ks exposures with *XMM-Newton* and with each exposure having simultaneous hard X-ray coverage with *NuSTAR*. The observations were spread over a six month period, with four of the observations performed over a month time-scale in Aug-Sept 2013 and a further observation in February 2014 (see Table 3.2 for details of the exposures).

Indeed the *Suzaku* observations, described in the preceding sections, have revealed the importance of the fast wind in PDS 456 via the presence of the iron K absorber with an outflow velocity of $\sim 0.25c$. The *XMM-Newton* and *NuSTAR* observations were subsequently obtained, with the overall motivation to provide: (i) an accurate description of the shape of the iron K line profile, (ii) a first reliable measurement of the hard X-ray spectrum above 10 keV, bluewards of the absorption profile, (iii) to infer how the outflow varied across the 6 months campaign (and with respect to previous observations) and to build up a physical picture, including the geometry, location and energetics of the wind. In this section I summarise the primary results from this campaign, related to the fast outflow in PDS 456, which are also presented in detail by N15. In my contribution I then apply photoionization modelling, as described in the previous section, to the high velocity absorber measured in these observations and compare the properties of the outflow as measured in these observations to its characteristics during the *Suzaku* campaign.

As I showed earlier in Section 4.2 (see Fig. 4.1 in page 98), substantial X-ray variability was observed both prior to and during the *XMM-Newton* and *NuSTAR* campaign. While six months earlier, the Suzaku 2013 observations caught PDS 456 in a low flux state, in the first observation (ObsA) of the new campaign the X-ray flux had increased by nearly five times. A more gradual decline in flux was then seen towards the remaining exposures during this campaign (with all of the observations brighter than what was observed during the 2013 *Suzaku* observations), making it possible to study the variability of the outflow in response to the continuum, which I will discuss later.

The fluxed spectra plotted in Fig. 4.10 show the presence of substantial spectral variability during this large campaign. As I mentioned earlier, ObsA and ObsE are the highest and lowest flux observations respectively whereas ObsC and ObsD are in an intermediate and comparable flux state. The initial ObsA sequence was not only the brightest, but also showed a harder primary continuum, with $\Gamma = 2.28^{+0.01}_{-0.02}$. One week later, in the following segment (ObsB), the powerlaw continuum softens significantly and has the steepest photon index of all the observations with $\Gamma = 2.68 \pm 0.02$. This change can be clearly seen in the first two panels of Fig. 4.10 and resulted in the hard X-ray (10–50 keV band) flux declining by a factor of 3, from $5.35 \times 10^{-12}\,\mathrm{erg\,cm^{-2}\,s^{-1}}$ to $1.35 \times 10^{-12}\,\mathrm{erg\,cm^{-2}\,s^{-1}}$. In the subsequent C and D sequences (panels 3 and 4) the hard X-ray flux recovered slightly with the photon index now intermediate in slope with $\Gamma = 2.4$ (see Fig. 4.10 and Table 4.5). Then during the ObsE sequence 6 month six months later, the whole spectrum dropped again in flux in both the soft and hard X-ray bands (see panel 5) and is similar in properties to the Suzaku 2011 observation.

From visually inspecting the fluxed spectra in Fig. 4.10, the iron K emission and absorption is apparent in each of the sequences, while the drop in flux due to the aborption near 9 keV becomes deeper following the drop in hard X-ray flux after ObsA. The peak of the emission profile is at $\gtrsim 7$ keV whilst the absorption trough is centred at ~ 9 keV. This is also clear from the data/model residuals for each sequence plotted in Fig. 4.11 as a ratio to the primary power-law continuum in the hard X-ray band, showing the persistence of the iron K features. The average best-fit energies of the peak of the Gaussian emission and absorption profiles at 7.2 keV and 9 keV respectively appear consistent with the *Suzaku* observations presented earlier, where this best-fit Gaussian model returns a very good fit to the spectra ($\chi^2/\nu = 2540.8/2582$). Thus when it is compared to the expected rest energy of the Fe XXVI Lyα line at $E_{\mathrm{rest}} = 6.97$ keV(see Fig. 4.11, magneta dashed line), the absorption is substantially shifted with a velocity of $v_{\mathrm{w}} \sim 0.25c$, while the emission is only required to be moderately blueshifted by $v \sim 0.03c$. Table 4.5 shows the Gaussian parameters and fluxes derived from fitting simple Gaussian emission and absorption profiles to each of the five sequences, as also described in N15 (see supplementary information, Table S2 in that paper). Note that the Gaussian profiles are significantly resolved, with a mean line width of $\sigma = 380^{+50}_{-30}$ eV (with respect to a rest energy of 6.97 keV), which corresponds to a velocity width of $\sigma_{\mathrm{v}} \sim 16000\,\mathrm{km\,s^{-1}}$ (see Table 4.5).

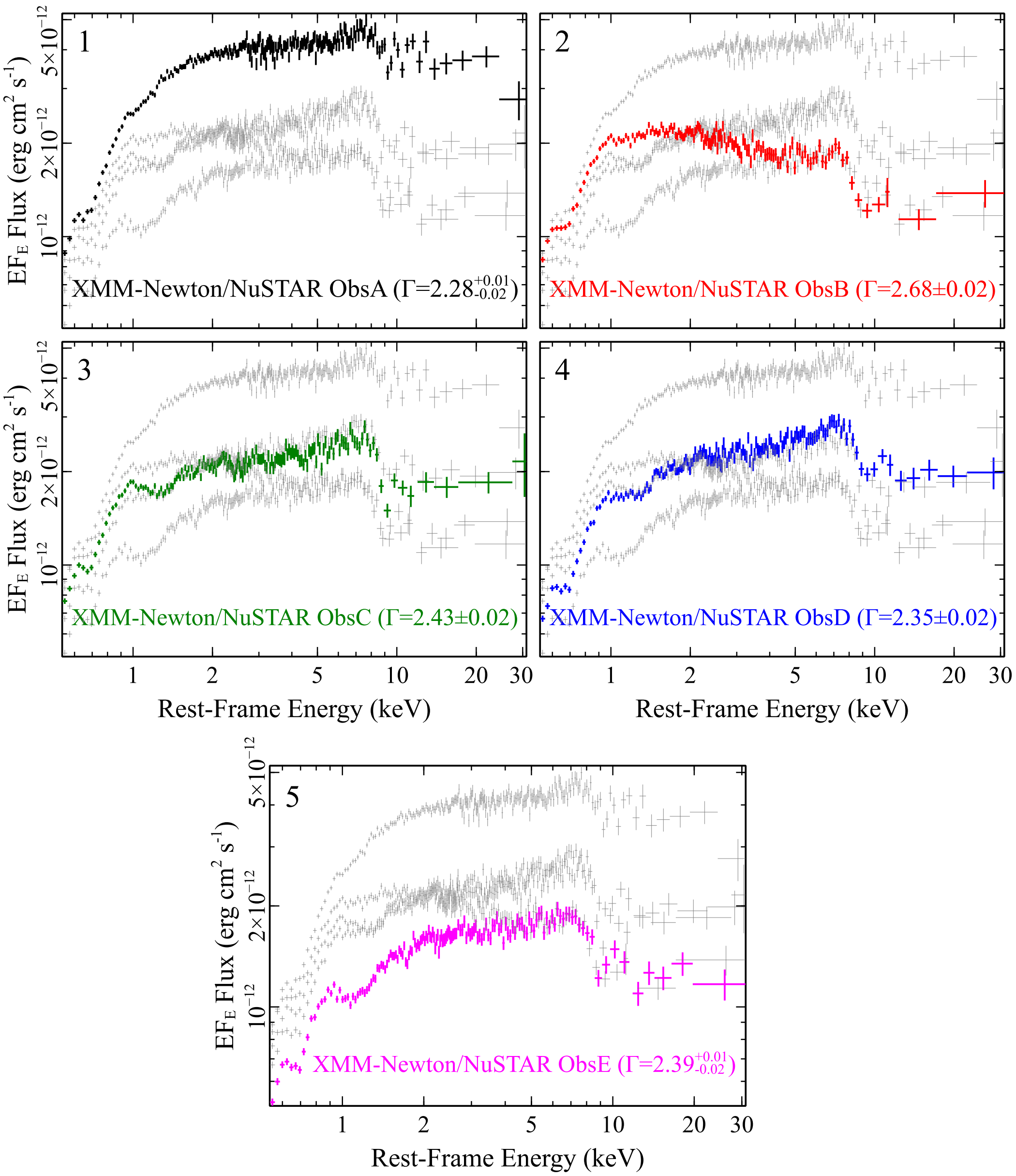

Figure 4.10: Fluxed spectra of the five simultaneous *XMM-Newton*/*NuSTAR* observations plotted between the rest-frame energies of 0.5-30 keV: panel 1 observation A - (ObsA, black), panel 2 observation B - (ObsB, red), panel 3 observation C - (ObsC, green), panel 4 observation D - (ObsD, blue) and panel 5 observation E - (ObsE, magenta). In each panel I purposely included the spectra from the other four observations, plotted in gray, in order to show the extent of the broadband variability during this large campaign. The spectra have been re-binned by a factor of 4 for the *XMM-Newton* and 8 for the *NuSTAR* for clarity. The power-law photon indices corresponding to each spectrum are also noted in each respective panel.

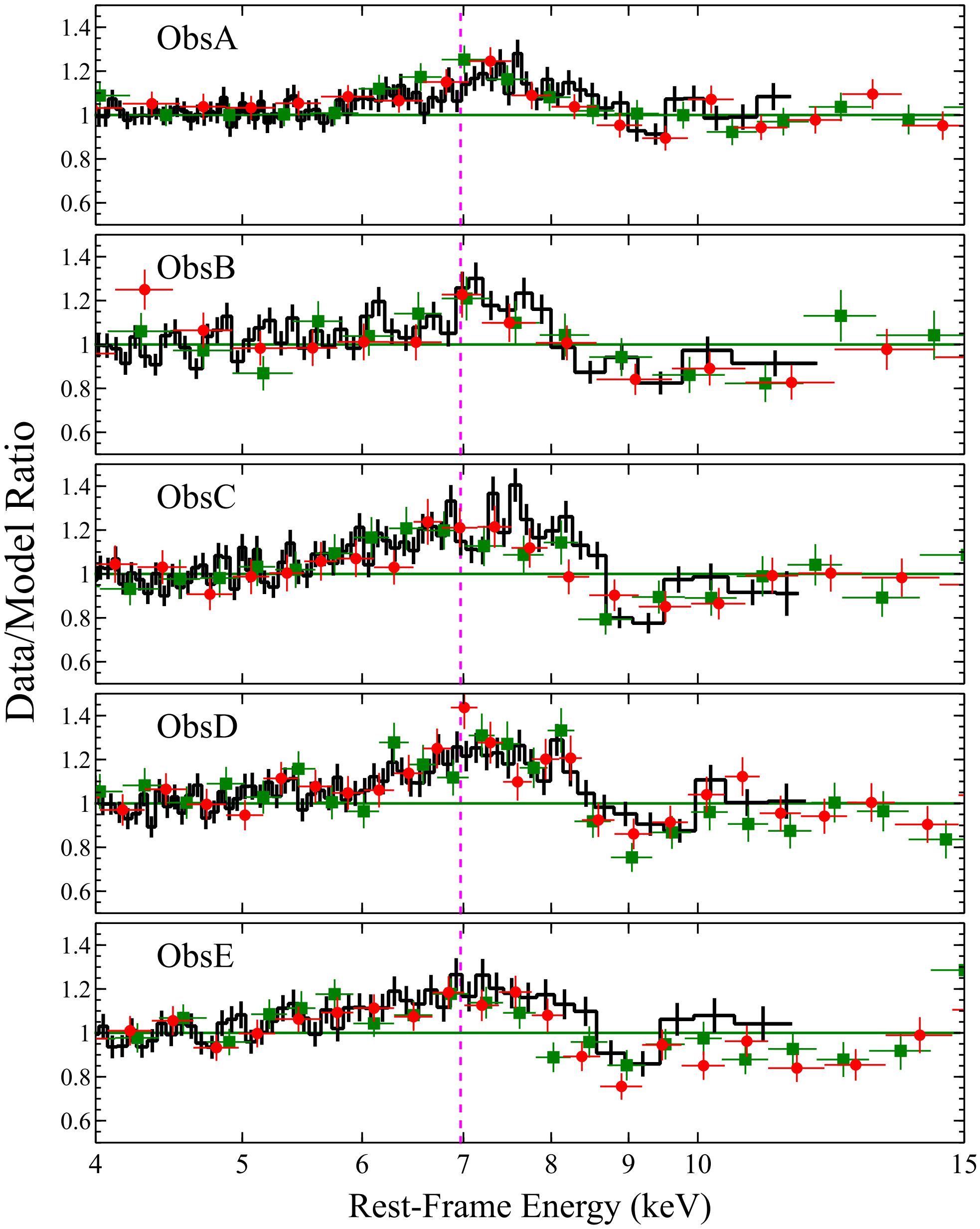

Figure 4.11: The ratio of the observed emission and absorption over the continuum corresponding to all five i.e., ObsA – ObsE simultaneous *XMM-Newton* (black) and *NuSTAR* (red and green) sequences, plotted between the rest-frame energy of 4-15 keV. The presence of a P-Cygni profile is evident in all five observations regardless of the different flux and spectral state of the source where the absorption trough is centred at ∼ 9 keV. The magenta vertical lines correspond to the expected position of the Fe XXVI line at 6.97 keV and in all five observations, the peak of the line lies above 7 keV suggesting a degree of blueshift also for the Fe XXVI emission. The spectra have been re-binned by a factor of 4 for the *XMM-Newton* and 8 for the *NuSTAR* for clarity.

Gaussian	Parameter	ObsA	ObsB	ObsC	ObsD	ObsE
Fe XXVI Lyα emission	Energy (keV)[a]	7.05 ± 0.10	7.05^{t}	7.05^{t}	7.05^{t}	7.05^{t}
	σ^{b}	380^{+50}_{-30}	380^{t}	380^{t}	380^{t}	380^{t}
	Flux[c]	7.2 ± 0.3	4.0 ± 1.3	2.6 ± 1.6	5.1 ± 1.8	1.5 ± 1.3
	EW (eV)	100 ± 30	145 ± 100	< 140	110 ± 80	< 135
Fe XXVI Lyα absorption	Energy (keV)	$8.74^{+0.06}_{-0.05}$	8.74^{t}	8.74^{t}	8.74^{t}	8.74^{t}
	σ	380^{t}	380^{t}	380^{t}	380^{t}	380^{t}
	Flux	$-4.3^{+2.1}_{-2.5}$	$-5.2^{+1.2}_{-1.5}$	$-11.1^{+1.5}_{-1.9}$	$-9.7^{+1.5}_{-2.1}$	$-7.9^{+1.2}_{-1.5}$
	EW (eV)	-75 ± 45	-250 ± 70	-350 ± 60	-280 ± 50	-345 ± 5
P-Cygni	$\tau^{\mathrm{d}}_{\mathrm{tot}}$	0.05 ± 0.01	0.12 ± 0.03	0.13 ± 0.02	0.11 ± 0.02	0.12 ± 0.02
Continuum	Power law Γ	$2.28^{+0.01}_{-0.02}$	2.68 ± 0.02	2.43 ± 0.02	2.35 ± 0.02	$2.39^{+0.01}_{-0.02}$
	$\mathrm{Flux}^{\mathrm{e}}_{(10-50)\,\mathrm{keV}}$	5.51	1.42	2.65	3.01	1.79

Table 4.5: Fe K emission and absorption parameters each modelled with a Gaussian component applied to all five ObsA–ObsE *XMM-Newton* & *NuSTAR* observations. $^{\mathrm{t}}$ indicates that a parameter was tied during fitting.

[a] Rest-frame energy of the Gaussian emission and absorption lines,

[b] Gaussian emission and absorption lines width,

[c] Gaussian emission and absorption flux in units of $10^{-14}\,\mathrm{erg\,s^{-1}\,cm^{-2}}$,

[d] total optical depth of the reprocessing gas with P-Cygni characteristic energy of $E_{\mathrm{c}} = 7.42^{+0.09}_{-0.08}$ keV and terminal velocity of $v_{\infty} = 0.35 \pm 0.02c$,

[e] intrinsic hard X-ray continuum luminosity measured in the $10 - 50$ keV band in units of $10^{44}\,\mathrm{erg\,s^{-1}}$.

Fig. 4.12 shows that with the addition of the *NuSTAR* data, it was possible to reveal the 'true' level of the underlying continuum above 10 keV, making it possible to reliably determine the contribution of both the emission and the absorption to the iron K profile. To illustrate this the ObsC and ObsD spectra have been combined into a single ObsCD spectrum and hence adopted for the subsequent parametrization of the P-Cygni feature below. Note that these two exposures were scheduled close in time to each other (within a gap of just 3 days) and appear very similar in flux and spectral shape (see Fig. 4.10). In panel (a) only the *XMM-Newton* spectrum for ObsCD was fitted at energies below 10 keV in the observed frame (or ~ 12 keV in the AGN rest frame). Without *NuSTAR*, the (incorrect) level and photon index of the continuum could only be defined below the iron K absorption profile at energies < 7 keV, resulting in a substantial spectral drop at higher energies and the appearance of two possible absorption profiles at 9 keV and 11 keV respectively. However in panel (b) it is clear that once the *NuSTAR* data are included, defining the continuum above 10 keV, the actual observed hard X-ray continuum is considerably lower than what is predicted (by a factor of ~ 2) revealing the lack of hard excess at > 10 keV.

Upon allowing a steeper continuum of $\Gamma \sim 2.4$ to fit the *NuSTAR* data (panel c), this revealed the presence both of the broad emission and the main absorption profiles associated with the resonant Fe XXVI Lyα line with the absorption centred at $E \sim 9$ keV (in the quasar rest frame). Indeed the profile can be recognized as a P-Cygni-like profile corresponding to an outflow velocity of $v_{\rm w} \sim 0.25c$, when measured with respect to the centroid of the absorption line. Indeed a P-Cygni-like feature was fitted with a self-consistent P-Cygni profile, using the model of Done et al. (2007) as shown in panel c (red curve). This implies a quasi-spherically symmetric disc-wind with a terminal velocity of $v_{\rm max} = 0.35 \pm 0.02c$ (as measured from the bluewards extent of the absorption profile) and characteristic energy $E_{\rm c} = 7.4 \pm 0.1$ keV (which corresponds to the onset of the absorption component). The final best fit model between $2 - 30$ keV is shown in Fig. 4.12 (d), where the remaining residuals above 10 keV, detected at high significance, were now identified, with self-consistent energies, with the blueshifted Kβ transition (at expected energy of $E_{\rm lab,rest} = 8.25$ keV) observed at quasar rest-frame energy of

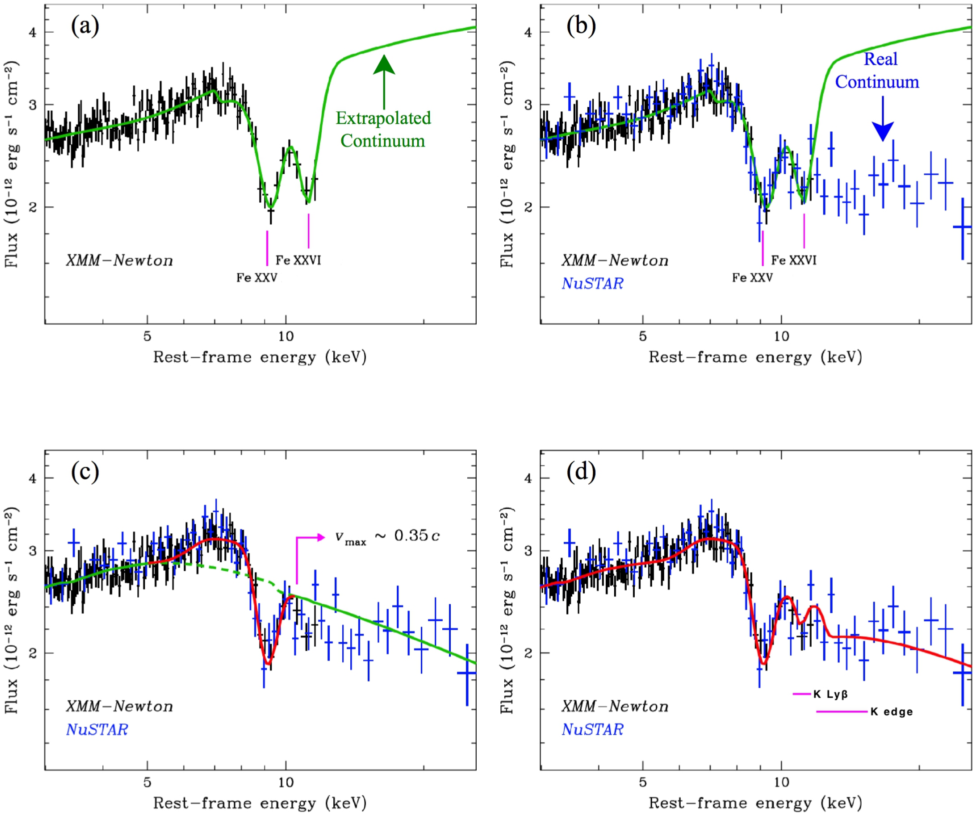

Figure 4.12: The fluxed ObsCD *XMM-Newton* and *NuSTAR* spectra of PDS 456 are shown, with the different models superimposed. Panel (a): the *XMM-Newton* spectrum only showing two absorption troughs at rest frame energies of ~ 9 keV and ~ 11 keV, where the green solid line indicates the extrapolated level of the continuum to hard X-rays from the best fit. panel (b): the combined *XMM-Newton* and *NuSTAR* spectra are shown. Note how the 'true' (factor of ~ 2 lower) level of the hard X-ray continuum above 10 keV is revealed by the *NuSTAR* data. panel (c): the self-consistent P-Cygni model is shown (red solid line) implying a quasi-spherically symmetric disc-wind with terminal velocity of $v_{\rm max} = 0.35 \pm 0.02c$. panel (d): the overall best fit (red line) between $2 - 30$ keV where the remaining residuals above 10 keV are modeled by blueshifted K Lyβ and K edge absorption features at self consistent energies from Fe XXVI. Figure adapted from Nardini et al. (2015).

$E \sim 11.0\,\mathrm{keV}$ and the K-shell absorption edge (the minimum photon energy required to completely ionize Fe XXVI i.e., $E_{\mathrm{lab,rest}} = 9.28\,\mathrm{keV}$) observed at rest-frame energy of $E \sim 12.0\,\mathrm{keV}$ (cf. Nardini et al. 2015 for more details).

Note that in N15 we computed the parameters of the P-Cygni line profile across all 5 observations; it was found that, regardless of the difference in spectral states and flux of the source, the presence of the P-Cygni-like profile is apparent in each sequence of the campaign suggesting a fast outflowing wide angle wind is therefore *persistent* across the entire *XMM-Newton* & *NuSTAR* campaign. Note that the P-Cygni profile parameters are consistent across the five observations, with the only difference being an increase in the optical depth of the profile following the drop in hard X-ray continuum level after ObsA (see Table 4.5).

Thus after resolving the P-Cygni profile and through quantifying the amount of absorbed ionizing radiation that is re-emitted throughout the spectrum, it was possible to compute a direct estimate of the solid-angle (Ω) covered by the wind. To first order this was done in N15 by comparing the luminosity of the absorbed vs re-emitted radiation in the iron K band, which when compared with the fluorescent yield of Fe XXVI (~ 0.5), gave an estimate for the wind solid angle of $\Omega > 2\pi$. A more robust estimate was obtained in N15 by modeling the absorption and emission in XSTAR, where the average estimated value was found to be $\Omega = 3.2 \pm 0.6\,\pi\,\mathrm{sr}$, suggesting that the absorption originates from a wide solid-angle. The breadth of the emission feature also indicates a wide angle outflow, with the emission integrated over a range of angles with respect to the line of sight. On the other hand if the outflowing wind was characterized by a much smaller Ω, while the blueshifted absorption would still be observed if viewed along the line of sight, the amount of emission would be weaker and result in a narrower profile if not integrated over a range of angles.

4.5.1 Photoionization modelling of the *XMM-Newton* & *NuSTAR* observations

In order to characterize the properties and variability of the outflow of PDS 456 and to compare it to what was obtained during the *Suzaku* campaign, photoionization modelling of the *XMM-Newton* and *NuSTAR* spectra with XSTAR was performed. The broadband wind model adopted in N15 included a simple parametrization of the continuum with a soft excess (blackbody) plus power-law (see Fig. 4.10) together with the presence of a low ionisation warm absorber. The latter was allowed to model the soft X-ray absorber below 2 keV, while the overall model allows for one layer of a mildly ionized partial coverer to model the higher energy curvature above 2 keV. The overall mathematical model construction was represented as follows:

$$\begin{split}\texttt{Tbabs} \times \texttt{xstar}_{\rm warmabs}(\texttt{bbody} + \texttt{powerlaw} + \texttt{xstar}_{\rm pc} \times \texttt{powerlaw}\\ + \texttt{xstar}_{\rm Fe\,K\,em}) \times \texttt{xstar}_{\rm Fe\,K\,abs}\end{split} \tag{4.2}$$

where $\texttt{xstar}_{\rm warmabs}$ parametrizes the soft X-ray warm absorption with $v_{\rm turb} = 100\,{\rm km\,s^{-1}}$. As in equation 4.1 the `Tbabs` is the Galactic absorption, `bbody` and `powerlaw` parametrize the soft X-ray excess and the continuum respectively. The mildly ionized partial coverer is modelled with an $\texttt{xstar}_{\rm pc}$ whereas the highly ionized wind emission and absorption are modelled with $\texttt{xstar}_{\rm Fe\,K\,em}$ and $\texttt{xstar}_{\rm Fe\,K\,abs}$ respectively with common ionization and column density (see Table 4.6). All the XSTAR grids for highly ionized wind and partial coverer have a common $v_{\rm turb} = 15000\,{\rm km\,s^{-1}}$. In this observation I find that the Fe K absorption profile was characterized by a larger line width ($\sigma = 380^{+50}_{-30}\,{\rm eV}$), compared to the five *Suzaku* sequences (see Tables 4.3 and 4.5 for comparison). Thus the absorption profile was modelled with the same ionizing SED XSTAR grid adopted in *Suzaku* but generated with a higher velocity broadening of $v_{\rm turb} = 15000\,{\rm km\,s^{-1}}$. Here the emission of the highly ionized wind was also included in the XSTAR photoionization modelling as the re-emission of absorbed photons across the line-of-site is not negligible, leading to the P-Cygni profile discussed above in § 4.5. Thus the Fe K emission component was modelled with an XSTAR emission grid with the same velocity broadening, ionization state and column density of the absorption grid across the five observations. The only free parameters of the Fe K emission are its normalization and the outflow velocity (common to the five epochs).

Table 4.6 reports the best fit values from the XSTAR fits, including the iron K absorber and emitter parameters for each sequence. For the emitter it was assumed that its overall column density and ionisation was equal to that of the high velocity absorber, i.e. it represents the re-emission from the highly ionised wind. The XSTAR normalisation (κ), is directly proportional to the covering fraction of a shell of gas, as a fraction of 4π steradians, as was defined earlier in § 3.6.1 (equation 3.12). Based on the input photoionization model, which used the *XMM-Newton* & *NuSTAR* data from ObsE, the 1–1000 Rydberg ionising luminosity is $5 \times 10^{46}\,\mathrm{erg\,s^{-1}}$, while PDS 456 is at a distance of $\sim 760\,\mathrm{Mpc}$. Thus for the ObsE sequence, the expected normalisation is $\kappa = 9 \times 10^{-4}$ for the above values and hence the estimated covering fraction of a quasi-spherical wind is $f_{\mathrm{cov}} \sim 0.65$. This is consistent with the $\sim 2\pi$ solid angle estimated by N15. Note that the emitter normalisation is correspondingly higher in the brighter ObsA sequence for instance, as the ionising flux is at its highest in this observation.

Here I investigated the same scenarios as in the above *Suzaku* sequences i.e.: (i) *variable ionization* (with constant column density) or (ii) *variable column density* (with constant ionization) and letting the outflow velocity vary in both cases. In the variable ionization scenario, I find that between ObsA–ObsE the ionization is not as variable as in the *Suzaku* 2007–2013c sequences. The Fe K absorption line is most ionized in ObsA at $\log(\xi/\mathrm{erg\,cm\,s^{-1}}) = 6.33^{+0.08}_{-0.19}$ and then progressively decreases to $\log(\xi/\mathrm{erg\,cm\,s^{-1}}) = 5.77^{+0.08}_{-0.12}$ in ObsC and recovers slightly in ObsD and ObsE with $\log(\xi/\mathrm{erg\,cm\,s^{-1}}) = 5.82^{+0.06}_{-0.17}$ and $\log(\xi/\mathrm{erg\,cm\,s^{-1}}) = 5.86^{+0.06}_{-0.13}$ respectively. Here the outflow velocity is found to be at its highest in the ObsA observation at $v_{\mathrm{w}} = 0.293 \pm 0.013c$ when the source is also brightest and at its lowest velocity in ObsE with $v_{\mathrm{w}} = 0.269 \pm 0.008c$ when the flux is at its lowest in this *XMM-Newton* & *NuSTAR* campaign (see Table 4.6). In this case the column density was tied between the five epochs at $\log(N_{\mathrm{H}}/\mathrm{cm^{-2}}) = 23.85^{+0.04}_{-0.11}$.

An equivalent fit can be obtained allowing the column density to vary (with fixed

Model	Parameter	ObsA	ObsB	ObsC	ObsD	ObsE
Variable ionization		**Wind absorption**				
	$\log(\xi/\mathrm{erg\,cm\,s^{-1}})$	$6.33^{+0.08}_{-0.19}$	$6.00^{+0.14}_{-0.13}$	$5.77^{+0.08}_{-0.12}$	$5.82^{+0.06}_{-0.17}$	$5.86^{+0.06}_{-0.13}$
	$\log(N_\mathrm{H}/\mathrm{cm^{-2}})$	$23.85^{+0.04}_{-0.11}$	23.85^t	23.85^t	23.85^t	23.85^t
	v_w/c	0.293 ± 0.013	$0.275^{+0.015}_{-0.017}$	0.290 ± 0.005	$0.292^{+0.007}_{-0.008}$	0.269 ± 0.008
		Wind emission				
	$\log(\xi/\mathrm{erg\,cm\,s^{-1}})$	6.33^t	6.00^t	5.77^t	5.81^t	5.86^t
	$\log(N_\mathrm{H}/\mathrm{cm^{-2}})$	23.9^t	23.9^t	23.9^t	23.9^t	23.9^t
	κ^a	$1.47^{+0.54}_{-0.57}$	0.56 ± 0.22	0.39 ± 0.17	$0.81^{+0.21}_{-0.19}$	$0.59^{+0.16}_{-0.15}$
	v_w/c	$0.009^{+0.009}_{-0.007}$	0.009^t	0.009^t	0.009^t	0.009^t
		$\chi^2/\nu = 4374/4192$				
Variable column density		**Wind absorption**				
	$\log(N_\mathrm{H}/\mathrm{cm^{-2}})$	$23.47^{+0.08}_{-0.11}$	$23.70^{+0.15}_{-0.14}$	$23.92^{+0.08}_{-0.11}$	$23.87^{+0.09}_{-0.10}$	$23.83^{+0.10}_{-0.09}$
	$\log(\xi/\mathrm{erg\,cm\,s^{-1}})$	5.84 ± 0.09	5.84^t	5.84^t	5.84^t	5.84^t
	v_w/c	0.301 ± 0.012	$0.280^{+0.020}_{-0.016}$	0.289 ± 0.050	$0.292^{+0.008}_{-0.007}$	$0.269^{+0.008}_{-0.009}$
		Wind emission				
	$\log(N_\mathrm{H}/\mathrm{cm^{-2}})$	23.5^t	23.7^t	23.9^t	23.9^t	23.8^t
	$\log(\xi/\mathrm{erg\,cm\,s^{-1}})$	5.84^t	5.84^t	5.84^t	5.84^t	5.84^t
	κ^a	$1.38^{+0.63}_{-0.62}$	$0.57^{+0.27}_{-0.26}$	0.39 ± 0.17	$0.81^{+0.21}_{-0.19}$	$0.59^{+0.16}_{-0.15}$
	v_w/c	$0.009^{+0.010}_{-0.008}$	0.009^t	0.009^t	0.009^t	0.009^t
		$\chi^2/\nu = 4375/4192$				
$L^\mathrm{b}_{(2-10)\,\mathrm{keV}}$		8.60 ± 0.14	$4.38^{+0.09}_{-0.11}$	$5.25^{+0.15}_{-0.17}$	$5.39^{+0.16}_{-0.19}$	$3.29^{+0.06}_{-0.08}$
$L^\mathrm{b}_{(10-50)\,\mathrm{keV}}$		$5.57^{+0.16}_{-0.21}$	$1.53^{+0.08}_{-0.06}$	$2.75^{+0.11}_{-0.12}$	$3.09^{+0.11}_{-0.15}$	$1.84^{+0.05}_{-0.16}$
$\mathrm{Flux}^\mathrm{c}_{(2-10)\,\mathrm{keV}}$		6.59	2.78	3.49	3.84	2.62
$\mathrm{Flux}^\mathrm{c}_{(10-50)\,\mathrm{keV}}$		5.35	1.35	2.52	2.89	1.73

Table 4.6: XSTAR parameters of the wind absorption and emission with $v_\mathrm{turb} = 15000\,\mathrm{km\,s^{-1}}$ applied to all five ObsA–ObsE *XMM-Newton* & *NuSTAR* observations. [a] Normalization of the wind XSTAR emission component, in units of $\times 10^{-3} f_\mathrm{cov} \frac{L/10^{38}}{D^2_\mathrm{kpc}}$, [b]intrinsic luminosities in the $2-10\,\mathrm{keV}$ and $10-50\,\mathrm{keV}$ energy bands in units of $10^{44}\,\mathrm{erg\,s^{-1}}$, [c] intrinsic fluxes in the $2-10\,\mathrm{keV}$ and $10-50\,\mathrm{keV}$ bands in units of $10^{-12}\,\mathrm{erg\,cm^{-2}\,s^{-1}}$, [t] indicates that a parameter was tied during fitting.

ionization), see Table 4.6. I find that, as per in the *Suzaku* spectra, both scenarios produced an excellent fit to the data with $\chi^2/\nu = 4374/4192$ and $\chi^2/\nu = 4375/4192$ respectively. However, by analysing the above results it seems that during this *XMM-Newton* & *NuSTAR* campaign, the lack of drastic events in the iron K feature between ObsA–ObsE suggests that the fast outflow is indeed more stable than what observed in the *Suzaku* spectra (particularly in the 2013b and 2013c), perhaps with a modest response of the wind ionization parameters to the hard X-ray continuum level above 10 keV, which decreases subsequent to ObsA. In the next section I will show that investigating these results will give an insight to physical properties and location of the fast outflow.

4.5.2 Comparison of the Fe K variability between the *Suzaku* and *XMM-Newton* & *NuSTAR* observations

The hard X-ray $L_{2-10\,\mathrm{keV}}$ intrinsic luminosity is plotted against the ionization $\log(\xi)$ of the Fe K absorption feature for the *Suzaku* sequences including (for comparison) the brightest (ObsA) and fainter (ObsE) segments of the *XMM-Newton* & *NuSTAR* campaignfdecreasing in Fig. 4.13 panel (i). From this plot it is clear that luminosity and ionization positively correlate with each other, however the latter variability amplitude is far greater than the former. On the other hand, Fig. 4.13 (ii) shows the (now expected) anti-correlation between the absorber's column density with the luminosity, where the former reaches is highest value when the source is fainter i.e., 2013c and progressively decreases with increasing luminosity. Furthermore in Fig. 4.13 (iii) the relationship between the outflow velocity v_{w} and ionization is plotted where they seem to follow a positive correlation. There seems to be also a correlation between v_{w} and the $2-10\,\mathrm{keV}$ intrinsic luminosity and this is shown in Fig. 4.13 (iv) where the outflow velocity is highest (ObsA and 2007) when the source is brightest and conversely in the 2013c observation.

Considering only the *Suzaku* observations on 2007–2013, a factor of 10 change in ionization is required, whereas the intrinsic luminosity changes by less than a factor of ~ 2. This implies that the absorption variability is probably not driven by ionization changes. On the other hand, at least during the *Suzaku* observations, changes in N_{H}

appear more likely the main driver of the variability. More specifically these changes in column density may be associated with:

- an increase in the mass outflow rate ($\dot{M}_{\rm out}$) during the more absorbed phases of the observation,
- an intrinsically variable wind e.g., due to different ejecta being observed at different times where, for instance, the absorption event later in *Suzaku* 2013 mainly occurs after a strong flare in the light curve. This will be investigated later in § 5.8,
- as a result of viewing through different time-variable streamlines in an inhomogeneous wind structure (e.g., Proga & Kallman 2004; Sim et al. 2008, 2010).

Thus by comparing the two extremes, in the higher flux spectra we might observe a part of the outflow closer to the inner launch radius which explains the observed higher ionization (and velocity), while in 2013c we may observe the less ionized streamlines of the outflow that are further out and moving across the line-of-sight resulting in the eclipsing of the source (see § 5.7.1). Note that further implications regarding the Fe K absorption variability will be discussed in greater detail next in Chapter 5, where the variations are investigated on a shorter time-scale of ~ 100 ks (corresponding to a light-crossing time of $\sim 20\,R_{\rm g}$ in PDS 456) across the *Suzaku* 2013 campaign.

4.5.3 A recombining absorber and a variable emitter

Previously in § 4.5.1 I observed that the Fe K line variability could be due to changes in the ionization state of the absorber in high-velocity outflow in PDS 456, whose ionization parameter progressively decreases from ObsA through to ObsB–D by a factor of ~ 3.5. In terms of luminosity, the simultaneous *XMM-Newton* & *NuSTAR* data made it possible to obtain a measure in ionizing luminosity in the $10-50$ keV band, which is a critical energy range as it lies above the ionization threshold of the Fe XXVI K-shell edge (i.e. at $E = 9.28\,\mathrm{keV}$). The most drastic hard continuum variations occurred between ObsA and ObsB where the hard X-ray luminosity dropped by a factor of ~ 3.5. As is shown in the top panel of Fig. 4.14, the ionization and the hard X-ray flux both decline by a factor of ~ 3 (in linear space) across the observation. This suggests that in the *XMM-Newton* & *NuSTAR* campaign, the main driver of the Fe K/wind spectral variability is due to ionization changes, with the absorber responding to the hard X-ray continuum level above 10 keV[6]. This observed drop in ionization may be as a result of recombination within the outflow which is in photoionization equilibrium with the X-ray continuum.

By measuring the approximate time-scale on which the recombination occurs ($t_{\rm rec}$), we can estimate the electron density (n_e) of the absorber. A robust formula for $t_{\rm rec}$ is given in Bottorff, Korista & Shlosman (2000):

$$t_{\rm rec}(X_i) = \left\{ \alpha(X_i, T_e) n_e \left[\frac{f(X_{i+1})}{f(X_i)} - \frac{\alpha(X_{i-1}, T_e)}{\alpha(X_i, T_e)} \right] \right\}^{-1}, \tag{4.3}$$

where $f(X_i)$ is the fraction of ions in the X_i population, $\alpha(X_i, T_e)$ is the recombination co-efficient of the X_i ion for an electron temperature T_e, and n_e is the electron number density. Here the recombination time-scale $t_{\rm rec}$ for the ionic population X_i, depends on the rate at which the X_{i+1} ions recombine into X_i population and the X_i population recombining into the X_{i-1} population. I apply equation (4.3) to the case of Fe XXVI recombining into Fe XXV ions.

Furthermore in equation (4.3), the recombination coefficient $\alpha(X_i, T_e)$ depends on the gas temperature, which Kallman et al. (2004, Fig. 6) estimated to be of the order of $\log(T_e/\mathrm{K}) \simeq 8.0$ for a mean $\log(\xi/\mathrm{erg\,cm\,s^{-1}}) \sim 4.0$ for a flat $\Gamma = 2$ continuum. For the much steeper SED used here, the equivalent ionization parameter is $\log(\xi/\mathrm{erg\,cm\,s^{-1}}) \sim 6$, after accounting for the enhanced opt/UV–soft X-ray luminosity. At this ionization state and gas temperature, the ionic fraction $f(X_i)$ of Fe XXVI is about four times

---

[6] There may be an indication of a slight delay in the response of ionization to the decrease in luminosity, with the former reaching a minimum during ObsC.

that of Fe XXV, whilst the ratio of Fe XXIV to Fe XXV recombination coefficients is around unity (see Nahar, Pradhan & Zhang 2001, Table 2). Equation 4.3 then reduces to $t_{\rm rec}(X_i) \simeq [3\alpha(X_i, T_e)n_e]^{-1}$.

Fig. 4.14 shows that the most dramatic continuum variation (e.g., in the $10-50$ keV band) occurs between ObsA and ObsB, when the hard X-ray luminosity (or flux) decreases by a factor of $\gtrsim 3$. Thus, I take the time separation between these two segments as the observational limit to the recombination time of $t_{\rm rec} < 900$ ks (i.e., within 10 days). The recombination coefficient for Fe XXVI into Fe XXV appropriate for a likely electron temperature of $\log(T_e/{\rm K}) \simeq 8.0$, $\alpha({\rm Fe\,XXV}, 10^8\,{\rm K}) = 1.36 \times 10^{-12}\,{\rm cm^{-3}\,s^{-1}}$, is given in Nahar, Pradhan & Zhang (2001). Adopting these values into the above equation 4.3, gives the lower-limit on the electron density to be $n_e > 3 \times 10^5\,{\rm cm^{-3}}$. From our estimate of n_e and the definition of the ionization parameter $\xi = L_{\rm ion}/n_{\rm H}R^2$, we can estimate a limit on the distance (R) of the absorber from the ionizing continuum source. Thus by taking the ratio factor of $n_e/n_{\rm H}$ to be of the order of unity, an ionization of $\log(\xi/{\rm erg\,cm\,s^{-1}}) = 6.0$ and a photoionizing $1-1000$ Ryd luminosity of $L_{\rm ion} \sim 5 \times 10^{46}\,{\rm erg\,s^{-1}}$ (see § 4.4.2), gives us $R < (L_{\rm ion}/n_{\rm H}\xi)^{1/2} < 4 \times 10^{17}$ cm, or < 0.1 pc. For a $M_{\rm BH} \sim 10^9\,M_\odot$ appropriate for PDS 456, this corresponds to a distance radius of $\lesssim 3000\,R_{\rm g}$ from the black hole. This is comparable with inner regions of the Broad Line Region (BLR), of the order of $\sim 1000\,R_{\rm g}$ (O'Brien et al. 2005, R09) from the black hole. Note that this estimate is likely to be associated to the characteristic typical radius for the responding material as there could still be material over an extended range of radii.

The bottom panel in Fig. 4.14 illustrates that the Fe K emission flux also directly decreases in response to the intrinsic hard X-ray luminosity, where the latter drastically drops by more than a factor of 3, from $L_{10-50\,{\rm keV}} = 5.57^{+0.16}_{-0.21} \times 10^{44}\,{\rm erg\,s^{-1}}$ in ObsA to $L_{10-50\,{\rm keV}} = 1.53^{+0.08}_{-0.06} \times 10^{44}\,{\rm erg\,s^{-1}}$ in ObsB with a slight recovery towards ObsC with $L_{10-50\,{\rm keV}} = 2.75^{+0.11}_{-0.12} \times 10^{44}\,{\rm erg\,s^{-1}}$. The Fe K emitter also declines in response, with initial flux of $F = 7.2 \pm 0.3 \times 10^{-14}\,{\rm erg\,s^{-1}\,cm^{-2}}$ in ObsA, declining to $F = 4.0 \pm 1.3 \times 10^{-14}\,{\rm erg\,s^{-1}\,cm^{-2}}$ in ObsB and $F = 2.6 \pm 1.6 \times 10^{-14}\,{\rm erg\,s^{-1}\,cm^{-2}}$ in ObsC. This is a similar decline, with perhaps the flux slightly delayed (as is still falling in ObsC) in response to such drastic drop of the continuum. By taking the response time of the iron K emitter to be 10 days (from ObsA to ObsB), the reverberation/light-crossing time is $\Delta t \sim 2.6 \times 10^{16}$ cm corresponding to $\sim 170\,R_{\rm g}$ in PDS 456. This estimate is consistent with what will be obtained later in Chapter 5 (§ 5.7.1) by the considerable short term changes that are observed in the depth of the Fe K absorption line over a week long baseline, observed during the *Suzaku* 2013 campaign. These results suggest that the radial distance ranges between $10^2 - 10^3\,R_{\rm g}$ from the X-ray source, which is indeed likely associated with an accretion disc-wind (Tombesi et al. 2013).

4.5.4 Estimating the mass outflow rate

The mass outflow rate can be defined as the amount of matter that expands radially outwards through a thin spherical shell at a specific point in time. A general expression that describes this can be written as:

$$\dot{M}_{\rm w} = \Omega r^2 \rho(r) v(r) \tag{4.4}$$

where Ω is the solid angle, r is the radius of the expanding shell, $\rho(r)$ is defined as the local mass density (at a specific point r in the flow) expressed as $\rho(r) = \mu m_{\rm p} n(r)$ where $\mu \sim 1.2$ is a constant factor for cosmic elemental abundances, $m_{\rm p}$ is the proton mass and $n(r)$ is the number density at a given point r in the outflow, $v(r)$ the velocity of the wind which defines the thickness of the shell of an instantaneous point. By assuming that the wind velocity is approximately within the flow i.e., $v(r) \sim v_{\rm w}$, the mass outflow rate can be also expressed as:

$$\dot{M}_{\rm w} \sim 1.2 \Omega r^2 m_{\rm p} n(r) v_{\rm w} \tag{4.5}$$

hence the column density along the line of sight down to a characteristic wind radius r, for the case of a quasi-spherical flow viewed radially, can be expressed as:

$$N_{\rm H} = \int_{R_{\rm in}}^{\infty} n(r) dr \sim \int_{R_{\rm in}}^{\infty} \left(\frac{\dot{M}_{\rm w}}{1.2 \Omega m_{\rm p} v_{\rm w}} \right) r^{-2} dr \tag{4.6}$$

where the lower bound $R_{\rm in}$ is the inner radius or the starting point of the wind, whilst the upper-bound is taken as a large distance assumed to be $R_{\rm out} >> R_{\rm in}$ which is effectively infinity. Thus a final expression for the mass outflow rate with all the relevant parameters required:

$$\dot{M}_{\rm w} \sim 1.2 \Omega N_{\rm H} m_{\rm p} v_{\rm w} R_{\rm in}. \tag{4.7}$$

Here I adopt $\Omega \sim 2\pi$ sr for a conservative value for the solid angle, the average column density between ObsA and ObsE is taken at $\log(N_{\rm H}/{\rm cm}^{-2}) = 23.78$ and the outflow velocity conservatively is taken as $v_{\rm w} \sim 0.25c$. We have seen from the results discussed earlier in § 4.5.3 that, the typical radial distance of the bulk of matter observed within the wind is $R \lesssim 10^2 - 10^3\, R_{\rm g}$. However the key parameter in equation (4.7) is the starting point radius of the wind $R_{\rm in}$. The minimum likely launch radius, for a wind terminal velocity of $v_{\rm w} \sim 0.25c$, corresponds to the escape radius which is $R_{\rm in} \gtrsim 32 R_{\rm g}$ (see § 4.5.5). On the other hand, the reverberation light-crossing time argument discussed at the end of 4.5.3 gives a plausible upper-limit on the inner radius to be $R_{\rm in} \lesssim 170\, R_{\rm g}$, as we see the iron K emission respond on this time-scale. As a result, a plausible radius for the starting point of the wind can be constrained to be between $32\, R_{\rm g} \lesssim R_{\rm in} \lesssim 170\, R_{\rm g}$.

So by considering the above radial range, the mass outflow rate of the wind is estimated to be of the order of $\dot{M}_{\rm w} \sim (0.27 - 1.5) \times 10^{27}\,{\rm g\,s^{-1}} \sim (4 - 24)\,{\rm M_{\odot}\,yr^{-1}} \sim (0.2 - 1)\,\dot{M}_{\rm edd}$ [7]. This corresponds to a kinetic power of $P_{\rm kin} = \frac{1}{2}\dot{M}_{\rm w} v_{\rm w}^2 \sim (0.8 - 4) \times 10^{46}\,{\rm erg\,s^{-1}} \sim (0.05 - 0.3)\,{\rm L_{Edd}}$. Even for the most conservative values for $R_{\rm in}$, the outflow kinetic power is comparable to typical 5% of $L_{\rm Edd}$ thought necessary for significant feedback to the host galaxy (Di Matteo, Springel & Hernquist 2005; Hopkins & Elvis 2010).

---

[7] Assuming an Eddington mass accretion rate of $20\,M_{\odot}\,{\rm yr}^{-1}$ for PDS 456, corresponding to $L_{\rm Edd} \sim 1.3 \times 10^{47}\,{\rm erg\,s^{-1}}$ and an accretion efficiency of $\eta \sim 0.1$.

4.5.5 What is the wind driving mechanism?

Here I discuss the likely physical mechanisms that might be involved in driving the observed fast outflows. One possibility is that the wind is radiatively driven. Given the high ionization of the wind in PDS 456, the line opacity is small, unless it is boosted by the lower ionization (clumpy) partial covering gas, so the dominant interaction mechanism is probably Thompson scattering (e.g., King & Pounds 2003). Here the photon momentum transfer rate to the wind is:

$$\dot{p}_{\rm w} = \dot{M}_{\rm w} v_{\rm w} \sim \tau L/c, \tag{4.8}$$

where $\dot{p}_{\rm w}$, $\dot{M}_{\rm w}$ and τ are the momentum rate, mass outflow rate and Thompson depth — note that $\tau \sim 1$ for $\log(N_{\rm H}/{\rm cm}^{-2}) \sim 24$ — respectively. Moreover the above definition of the mass outflow rate gives:

$$\dot{M}_{\rm w} \sim 1.2\Omega m_{\rm p} N_{\rm H} v_{\rm w} R_{\rm in}. \tag{4.9}$$

Thus from the above definitions $\dot{M}_{\rm w} v_{\rm w} \propto L$ and $\dot{M}_{\rm w} \propto v_{\rm w}$. Also from the definition of the ionization parameter (see § 3.5.2) we know that $\xi \propto L$ and thus for a radiatively driven wind:

$$v_{\rm w}^2 \propto L \propto \xi. \tag{4.10}$$

Furthermore I now test whether the above correlation is observed in PDS 456, from all the observations. I only concentrate on the correlation between the intrinsic continuum luminosity and the outflow velocity as they are the most model independent quantities. The former can be measured directly from the spectra whereas the latter can be inferred by the energy of the centroid of the absorption line. On the other hand change in the ionization parameter can be degenerate with the column density and as a result it would provide a less reliable test when compared to $v_{\rm w}$.

Fig. 4.15 shows the log-log plot between the outflow velocity and the intrinsic luminosity (in the $2-10$ keV band) where all the five *Suzaku* and the five *XMM-*

Newton & *NuSTAR* sequences are included. The data points were fitted with a standard regression line of the form $\log(v_{\rm w}) = m\log(L_{2-10\,{\rm keV}}) + c$ which produced a gradient of $m = 0.31 \pm 0.06$. This is broadly consistent (if slightly flatter) with the proportionality given in equation (4.10), which predicts a $v_{\rm w} \propto L^{1/2}$ dependence. This may however give an initial indication that the wind in PDS 456 is radiatively driven, although further data will help confirm this and especially whether the relation flattens out towards higher luminosities (i.e. towards ObsA).

On the other hand an alternative launching mechanism of the highly ionized gas is described by MHD processes (e.g., Ohsuga et al. 2009; Fukumura et al. 2010; Kazanas et al. 2012; Fukumura et al. 2015). Although the underlying physical mechanism is still poorly understood, Tombesi et al. (2013) predicted a linear relationship between the outflow velocity and the ionization i.e., $v_{\rm w} \propto \xi$ in the MHD scenario (see their equation 10). These correlations may be an over simplification in the wind and may result from the combination of both radiative and MHD effects. Later in Chapter 5 (§ 5.8.1) I will discuss whether the observed increase in absorption during the *Suzaku* 2013 observation can be purely radiatively powered by a preceding strong flare observed in the light curve.

Another possibility causing the difference in the observed $v_{\rm w}$ can be associated with the discrete streamlines predicted in simulations (e.g., Proga, Stone & Kallman 2000) that characterize the outflow moving across the line-of-sight. In this scenario the streamlines are launched from different escape radii ($R_{\rm esc}$) of the disc, resulting in discrete escape (launch) velocities. The range of velocities observed, i.e. $v_{\rm w} \sim 0.24 - 0.30c$, correspond to escape radii of $R_{\rm esc} \sim 20 - 35\,R_{\rm g}$ in PDS 456. Thus this suggests that the discrete streamlines of the disc-wind may be launched from different portions of the accretion disc, with slower escape velocity streams (of lower ionization) arising from further out in the disc. However this would not easily account from the observed relation between the ionizing luminosity and the velocity.

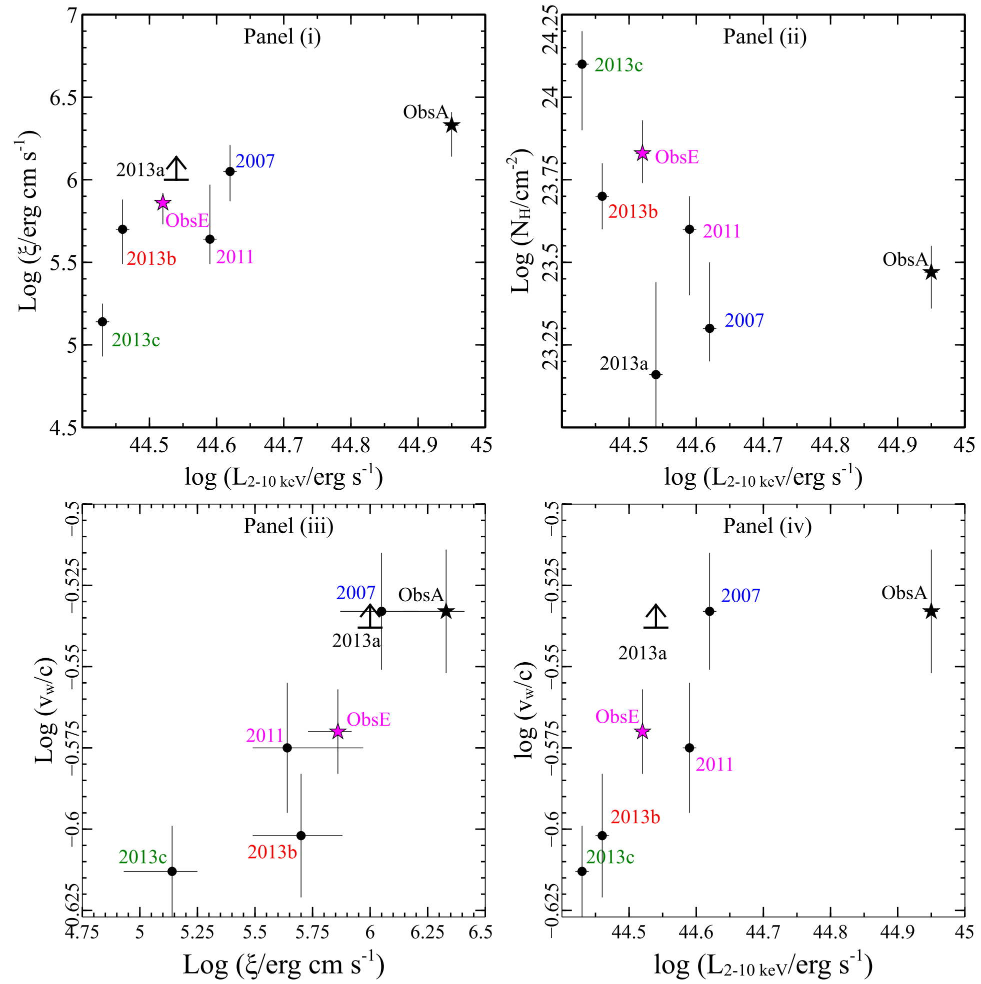

Figure 4.13: Plots showing the comparisons all in log–log space (in order to spot eventual linear correlations) between the XSTAR parameters and the intrinsic hard X-ray luminosities in the $2-10\,$keV band of the five *Suzaku* sequences, where the highest and lowest *XMM-Newton* & *NuSTAR* points respectively are also plotted for comparison. Panel (i): a comparison between ionization and the intrinsic luminosity which seems to show a positive correlation. Panel (ii): a comparison between the behaviour of the absorber's column density against the ionizing luminosity showing the (expected) anti-correlation, where the former reaches its highest value when the source is fainter i.e., during 2013c and progressively decreases with increasing luminosity. Panel (iii): a comparison between the ionization parameter and the outflow velocity which shows a positive correlation suggesting that a higher ionizing luminosity results in a faster outflow. Panel (iv): a comparison between the outflow velocity and luminosity, where the velocity increases with luminosity. At this stage I did not quantify these correlations as I will concentrate later in the text to panel (iv).

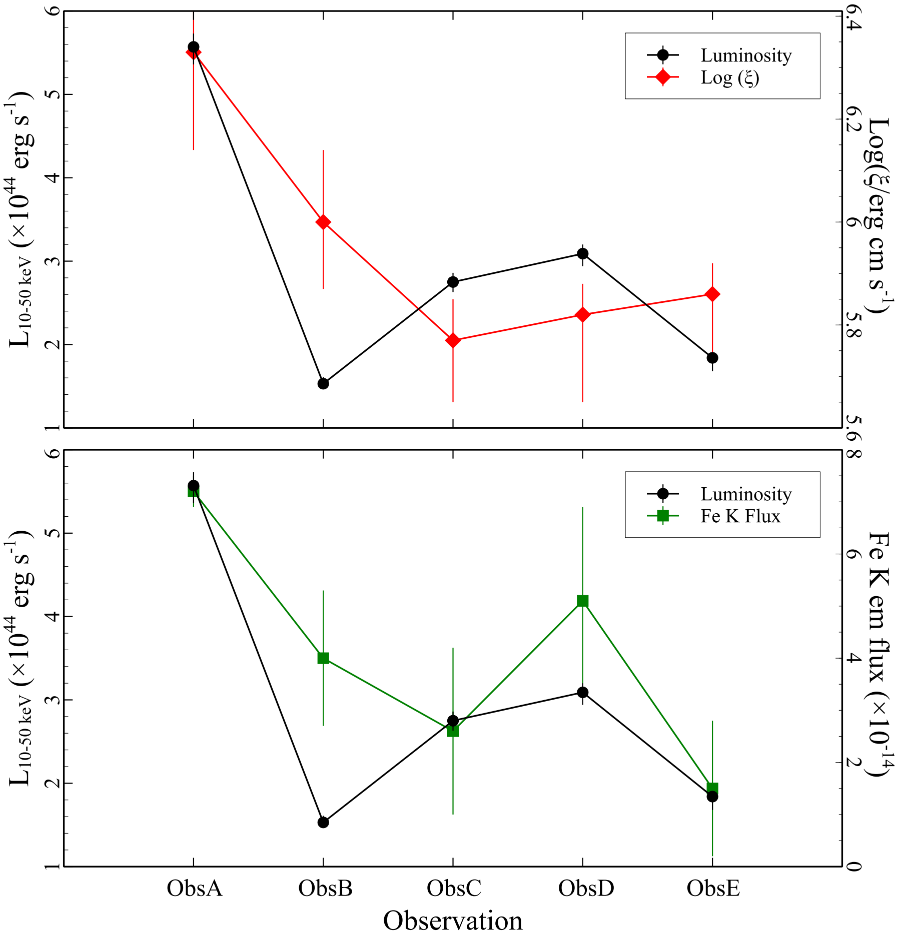

Figure 4.14: Plot showing how both the ionization parameter and iron K emission line flux respond to the change in hard X-ray luminosity during the *XMM-Newton* & *NuSTAR* campaign. Top panel: time behaviour between the intrinsic luminosity in the $10-50$ keV band (left $y-axis$) and ionization parameter (right $y-axis$) across the ObsA–ObsB observations. Bottom panel: same as above but with Fe K emission line flux (right $y-axis$) instead.

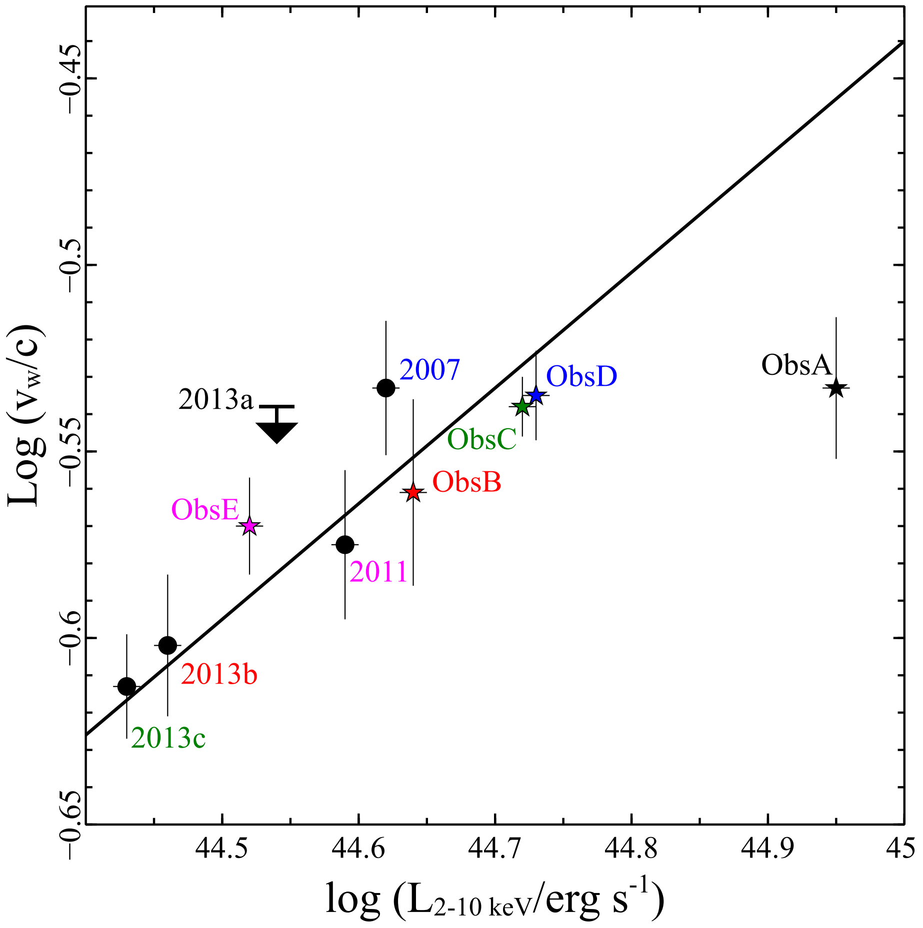

Figure 4.15: Log–log plot showing the linear correlation between the outflow velocity and the intrinsic $2 - 10$ keV continuum luminosity. All the values are adopted from Table 4.6 where *Suzaku* (black dots) and *XMM-Newton* & *NuSTAR* (coloured stars) observations are included. A linear regression was fitted to the data points excluding ObsA (black star) as its high X-ray luminosity is very unusual for PDS 456. The fitted regression line produced a gradient of $m = 0.31 \pm 0.06$ which seems broadly consistent with what would be expected for a radiatively driven wind ($m = 0.5$).

4.6 Chapter Summary

In this chapter I have presented the results from two large observing campaigns of the nearby luminous quasar PDS 456, one carried out with *Suzaku* in early 2013 (~ 1 Ms total duration) while the other was performed simultaneously with *XMM-Newton* and *NuSTAR* between late 2013 and early 2014. I investigated the broadband continuum and the physical properties of the variable Fe K feature present in all the spectra. The main results for this analysis are summarized below:

1. I initially investigated the broadband variability of the 2013 *Suzaku* spectra caught in the lowest flux to date when compared with previous *Suzaku* 2007 and 2011 observations and the later *XMM-Newton* & *NuSTAR* campaign. By modelling the newly constructed optical/UV to hard X-ray SED with a physically motivated accretion disc/X-ray corona model like `optxagnf`, I find that this was able to account very well for the optical/UV to X-ray brightness ratio with sensible values of the accretion rate, $\log(\mathrm{L}/\mathrm{L}_{\mathrm{Edd}}) = -0.08 \pm 0.10$ suggesting that the source is radiating close to the Eddington luminosity ($\sim 80\%$). The X-ray portion of the SED was dominated by a prominent spectral curvature that could only be accounted for by including two zones of partial covering absorption, which supported the evidence that the 2013 *Suzaku* spectra were modified by obscuration.

2. While modelling the broadband SED with the `optxagnf` baseline model, the Fe K absorption profile was fitted with a Gaussian profile. It was found that its centroid energy at $\sim 8.6-8.8$ keV suggested a large degree of blueshift if associated to the expected lab-frame energies of the $1s \rightarrow 2p$ lines of He- or H-like Fe. It was also found that the equivalent width was variable with an increase by a factor of ~ 5 throughout the observation. This was an initial indication of a significant Fe K profile variability in a relatively short time-scale of the order of ~ 100 ks.

3. A custom made XSTAR grid to parameterise the Fe K absorption profile was used on all five *Suzaku* observations including the 2007, 2011 and 2013a,b,c sequences in order

to investigate the Fe K physical properties over a wider flux range. By parametrizing the variability of the Fe K absorption feature with either *variable ionization* or *variable column density* I find that both cases equally produce a very good description of all the five *Suzaku* (time-averaged) spectra of PDS 456. However given the relatively large change in ionization during all the *Suzaku* sequences I ruled it out in favour of the variable column density (and a small change in luminosity) as the principle driver of the observed variability.

4. In a series of five simultaneous observations with *XMM-Newton* & *NuSTAR* campaign, was resolved a fast ($\sim 0.25c$) P-Cygni like profile at Fe K, showing that the absorption originates from a wide angle (i.e., $\Omega \gtrsim 2\pi$) and persistent accretion disc-wind across the entire observation campaign. This implied a quasi-spherically symmetric disc-wind with terminal velocity of $v_{\mathrm{max}} = 0.35 \pm 0.02c$ and a mass outflow rate of $\sim 10\,M_{\odot}\,\mathrm{yr}^{-1}$, capable of causing significant feedback between the black hole and its host galaxy (e.g., King 2003).

5. The photoionization modelling of the Fe K emission and absorption profiles of the *XMM-Newton* & *NuSTAR* spectra was also performed with the aim to compare it to the earlier *Suzaku* observations. In this campaign the ionization parameter of the absorber and the flux level of the emitter follow the flux variability of the hard X-ray continuum. This is consistent with the absorber becoming less ionized (via recombination) for a decrease in the hard X-ray continuum above 10 keV. This gave an estimated upper-limit on the location of the absorber, which is found to be < 0.1 pc from the black hole, whereas from the reverberation time-scale, at which the Fe K emitter responds to the hard X-ray flux, I obtained an upper-limit for the radial distance to be $< 170\,R_{\mathrm{g}}$.

6. I also find that there is a positive correlation, over all the observations, between the outflow velocity and the intrinsic luminosity. This may be a consequence of a radiatively driven wind favouring a $v_{\mathrm{w}} \propto L^{1/2}$ relation.

5 Short-term X-ray spectral variability of the quasar PDS 456[1]

5.1 Chapter content and motivation

In the previous chapter I showed that the *Suzaku* and *XMM-Newton* & *NuSTAR* sequences in PDS 456 present broadband X-ray continuum variability together with changes in the Fe K absorption profile. I observed that the variability of the latter was more pronounced in the *Suzaku* time-averaged sequences, and in particular between the three 2013 segments. This gave a strong indication that the X-ray spectral variability of the iron K absorption feature might be observed on a shorter time-scale of $\sim 50-100\,\mathrm{ks}$ (corresponding to a light-crossing distance of $10-20\,R_{\mathrm{g}}$ in PDS 456). In this chapter, I will present a time-dependent spectral analysis of the *Suzaku* 2013 campaign, where I initially focused on the short-term variability Fe K region and then extended to the broadband X-ray continuum. More specifically, the aim of the time-dependent spectral analysis presented in this chapter was to:

(i) determine the timescales through which both the X-ray absorption and continuum variations occur, by directly measuring the absorber's behaviour, on timescales down to tens of ks,

(ii) investigate in detail the physical properties of the highly ionized absorber affecting the Fe K region by first parametrizing the profile with a simple Gaussian and then modelling with the XSTAR photoionization grid,

---

[1] This chapter is based on the published work entitled:
'*Short-term spectral variability of the quasar PDS456 observed in a low flux state*'; **G. A. Matzeu**; J. N. Reeves; E Nardini; V. Braito; M. T. Costa; F. Tombesi; J. Gofford; 2016, MNRAS, **458**, 1311-1329.

All work was conducted by myself unless otherwise stated.

(iii) explore the short-term spectral X-ray continuum changes in PDS 456 which are interpreted in terms of variable partial covering absorption and/or changes in the intrinsic continuum,

(iv) to investigate the properties and location of the partial covering absorbers, within the outflow, by characterizing its short-term variability over the course of the observation,

(v) analysing the behaviour of the soft ($0.5 - 1$ keV) and hard ($2 - 5$ keV) band light curves during the course of a strong flare,

(vi) explore whether the radiation pressure imparted by the strong flare could deposit enough kinetic power in the outflowing material to drive the wind.

As I already mentioned previously in Chapter 4, it is clear that in 2013 *Suzaku* caught PDS 456 in an extended period of unusually low flux, especially compared to the earlier *Suzaku* 2007 and 2011 (and the later *XMM-Newton* & *NuSTAR*) observations. This is also seen in Fig. 5.1, which compares the long-term broadband (i.e., $0.5 - 10$ keV) light curves between all the five *Suzaku* observations from 2007 to 2013. The temporal behaviour of these light curves indeed shows that PDS 456 presents variability on both long and short timescales and also reveals the presence of X-ray flares of variable intensities across most of the five *Suzaku* observations. Thus in this chapter I will focus on the short-term spectral properties of the three (low flux) 2013 observations, whereas later in Chapter 6 I will investigate the flaring observed in the (high flux) 2007 observations that is apparent in the light-curve and the implications to the observed short-term variability. No spectral variability was observed during the shorter 2011 observations.

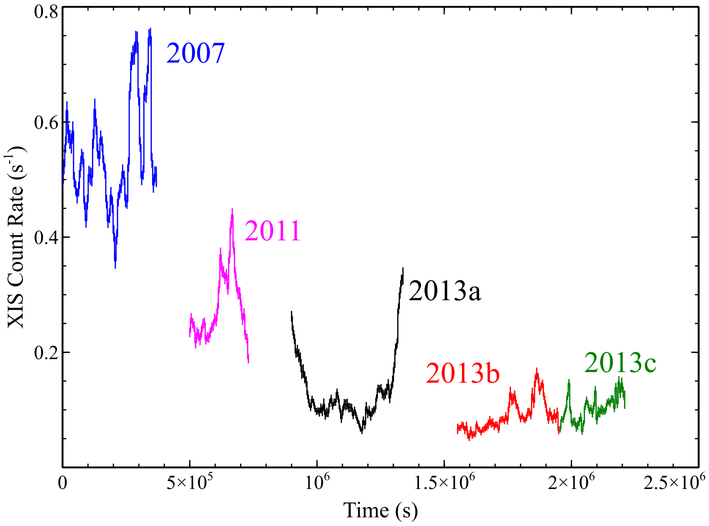

Figure 5.1: Long-term behaviour of the broadband X-ray light curves of all the five *Suzaku* observations: 2007 (blue), 2011 (magenta), 2013a (black), 2013b (red) and 2013c (green). This plot shows the wide range of variability that characterizes PDS 456 and it also illustrates the unusually low count rate in the *Suzaku* 2013b and 2013c observations. Note that the gap between the observations is arbitrary, although the 2013b and 2013c are contiguous.

5.2 Time-dependent spectral analysis in *Suzaku* 2013

In this section I will investigate the properties and behaviour of the light curves extracted in different energy bands across the *Suzaku* 2013 long observations. More specifically Fig. 5.2 shows the overall light curves of the 2013 *Suzaku* campaign in different energy bands, strongly indicating variability of the X-ray flux in PDS 456 on short-time scales. A prominent flare is detected, with the flux increasing by a factor of 4 between $400-450$ ks in sequence 2013a, followed by smaller flares towards the second half of sequence 2013b. Guided by the visual properties of the overall light curve and softness ratio (between the $0.5-1$ and $2-5$ keV bands), the spectra were divided into a total of eight slices (see panel 1 in Fig. 5.2); this was done by taking into consideration the width of each slice and the number of counts in it. Note that for PDS 456, with $M_{\rm BH} \sim 10^9 M_\odot$, a

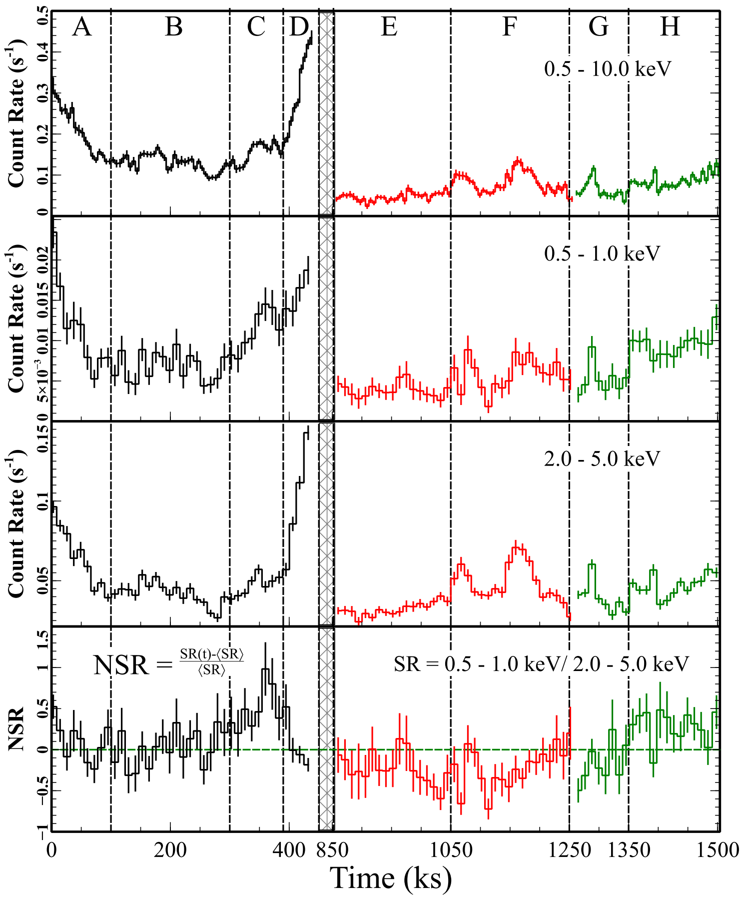

Figure 5.2: light curves and normalized softness ratio (0.5 – 1/2 – 5 keV) for sequences 2013a (black), 2013b (red) and 2013c (green). The dashed vertical lines identify the boundaries of the eight slices.

Panel 1: XIS-FI (X-ray Imaging Spectrometer-Front Illuminated) 0.5 – 10.0 keV light curve of the overall *Suzaku* observation. Note the strong flare between 400 – 450 ks in segment D.

Panel 2: 0.5 – 1 keV soft band light curve.

Panel 3: 2 – 5 keV hard band light curve.

Panel 4: Fractional change in the softness ratio (see the text for the definition). Positive (negative) values correspond to the softening (hardening) of the source with respect to the average spectral state. The bin size of the light curves is 5760 s, corresponding to one satellite orbit.

variability timescale of $\sim 100\,\mathrm{ks}$ corresponds to a light-crossing distance of $\sim 20\,R_{\mathrm{g}}$. A slice of at least 100 ks in duration was usually required to obtain enough counts to accurately characterize the spectrum, whilst, on the other hand, I had enough counts to isolate the much brighter flare between $400 - 450\,\mathrm{ks}$ into the observation. The plots of the fluxed $\mathrm{EF_E}$ spectra and the Fe K band data to model ratios (obtained as in Fig. 4.5) of the eight slices are shown in the top and bottom panels of Fig. 5.3. The first four spectra (A–D), correspond to the 2013a sequence, tracing the decline of an initial flare (A) followed by a quiescent period (B) together with the initial onset of the large flare (C) and the subsequent flare itself (D). In the remaining four spectra (E–H), corresponding to the 2013b and 2013c sequences, the Fe K absorption feature becomes very noticeable (E), progressing in strength (F) to reach a maximum depth in slice G and tentatively recovering in slice H. The timing periods for each of the slices are noted in Table 5.1.

In section 4.3.2 I used the `optxagnf` model to account for the optical/UV to hard X-ray SED of PDS 456. However, in order to describe the lower S/N time-sliced spectra over the $0.6 - 10$ keV band, I used a simpler two-component model to provide a more convenient parameterisation of the intrinsic continuum. I therefore parameterised the continuum with a phenomenological baseline model of the form:

$$\mathtt{Tbabs} \times [\mathtt{zpcfabs}_{\mathrm{low}} \times \mathtt{zpcfabs}_{\mathrm{high}} \times (\mathtt{po} + \mathtt{bbody}) + \mathtt{zgauss}_{\mathrm{em}} + \mathtt{zgauss}_{\mathrm{abs}}], \quad (5.1)$$

where `Tbabs` accounts for the Galactic absorption using the cross sections and ISM abundances of Wilms, Allen & McCray (2000). The Gaussian component $\mathtt{zgauss}_{\mathrm{em}}$ of the best-fit parameterises the ionized emission profile at 6.9 ± 0.1 keV (in the quasar rest-frame). I note that this two component (power law plus blackbody) continuum model, when applied to the parent sequences, is fully consistent with the earlier `optxagnf` findings. Again, the model requires two neutral partially covering absorbers, with column densities of $\log(N_{\mathrm{H,low}}/\mathrm{cm}^{-2}) = 22.3 \pm 0.1$ and $\log(N_{\mathrm{H,high}}/\mathrm{cm}^{-2}) = 23.2 \pm 0.1$. The soft excess, now parameterised with a blackbody (`bbody`), yields a temperature of $kT \sim 82^{+21}_{-20}\,\mathrm{eV}$, while the properties of the Fe K emission and absorption profiles, as expected, are not modified compared to Table 4.3.

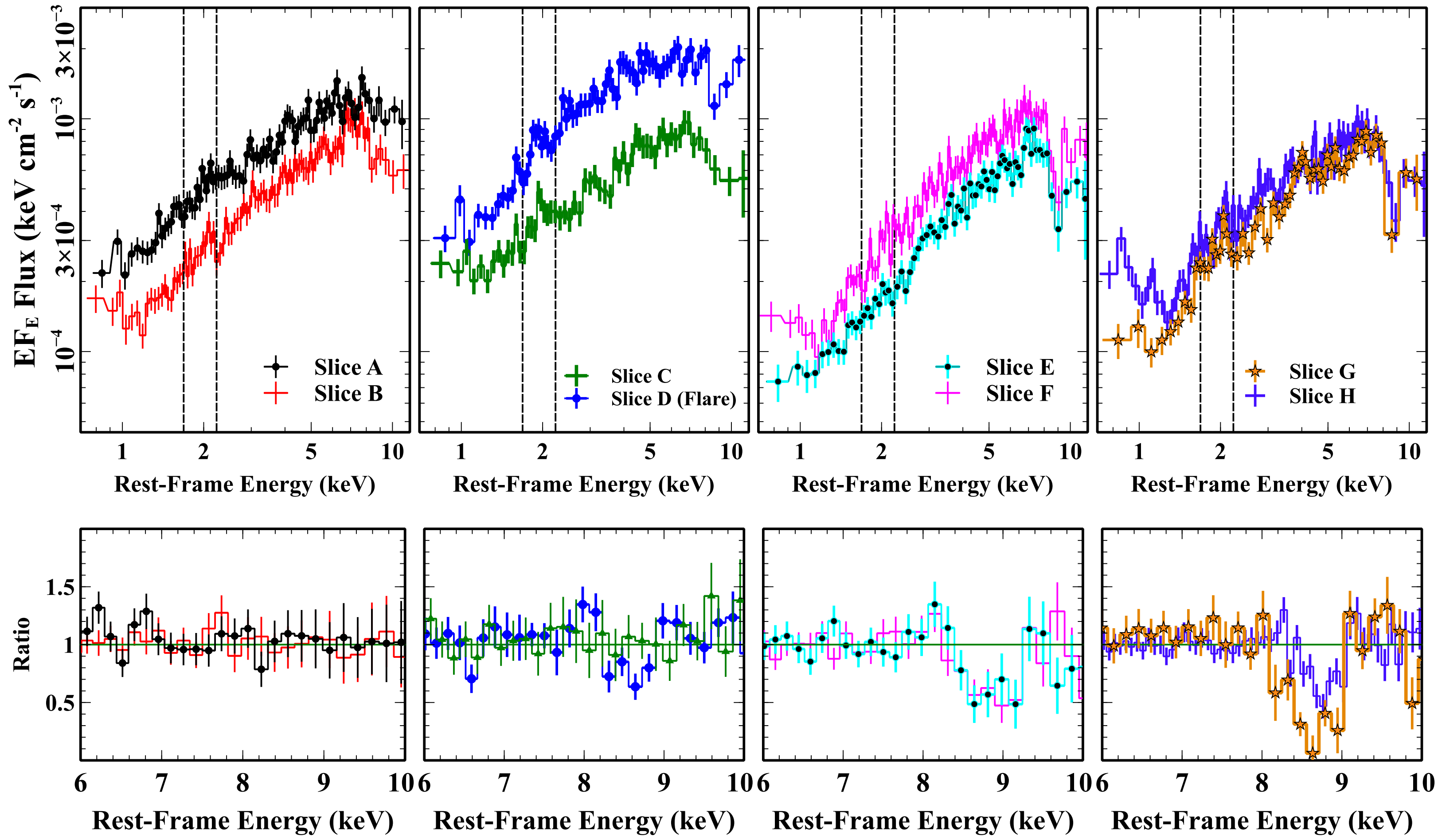

Figure 5.3: Top panels: Fluxed spectra of the slices A (black), B (red), C (green), D (blue), E (cyan), F (magenta), G (orange) and H (violet). What is noticeable is the absence of a clear Fe K absorption feature in the first three spectra, and its possible onset in slice D (corresponding to the flare). The dotted rectangular areas represent the XIS Si edge calibration uncertainty range between 1.7-2.1 keV, ignored during fitting. The depth of the Fe K absorption feature ($\sim$ 7.4 keV in the observed frame, $\sim$ 8.7 keV in the quasar rest frame) gradually increases after the flare between slice E and slice G, when the absorption trough becomes very prominent. The fluxed spectra have been plotted against a simple power-law with $\Gamma = 2$ with minimum 50 cts per bin. Bottom Panels: Ratio spectra of the slices to the best fit partial covering continuum model as defined by Equation 5.1, without including the Fe K emission or absorption lines.

5.3 The iron K short-term absorption variability

Here I investigate the variability of the iron K absorption when applied to the short spectral slices. To provide an acceptable fit to the baseline continuum, I applied the baseline model introduced above over the $0.6-10$ keV band. The high and low column covering fractions ($f_{\rm cov,low}$ and $f_{\rm cov,high}$) are allowed to vary between the eight slices, together with the power-law and blackbody normalizations. The high and low column densities of the partial covering absorbers were tied between the slices.

5.3.1 Gaussian modelling

To characterize the behaviour of the Fe K absorption line across all the eight slices, this has been initially parameterised using a simple Gaussian profile. I found that the Fe K absorption is not significant (at $> 99\%$ confidence level) in the first three slices (A–C). As the observation progresses the absorption feature becomes significant, through slices E ($\Delta\chi^2/\Delta\nu = 24/2$, equivalent to $\sim 5\sigma$ confidence level) and F ($\Delta\chi^2/\Delta\nu = 40/2$ $\sim 6\sigma$), reaching its maximum depth during slice G ($\Delta\chi^2/\Delta\nu = 77/2 > 8\sigma$), with $EW = -537^{+121}_{-131}$ eV, when the count rate becomes almost null at the centroid of the absorption line ($E = 8.63 \pm 0.11$ keV; see Fig. 5.3). Assuming a common velocity width between all the slices as in § 4.4, I obtained $\sigma = 282^{+69}_{-56}$ eV for the width of the absorption line, thus corresponding to a velocity dispersion of $\sim 9900\,{\rm km\,s^{-1}}$. The baseline model provided a very good fit to the slices, with $\chi^2_\nu = 1554/1681$. The parameter details of the Gaussian absorption line, for each of the eight slices, are listed in Table 5.1 and plotted in Fig. 5.4 (a).

5.3.2 XSTAR modelling

I then replaced the Gaussian absorption line profile in the baseline model above with a multiplicative XSTAR absorption grid, generated as described earlier in Chapter 4 (Equation 4.1; hereafter this is referred to as 'XSTAR baseline model'). Three scenarios

Slice	Time	E (keV)^a	EW (eV)^b	$(\Delta\chi^2/\Delta\nu)^c$
A	0-100	8.55^t	< 105	–
B	100-300	8.55^t	< 156	–
C	300-400	8.55^t	< 145	–
D	400-450	8.55 ± 0.15	254^{+116}_{-89}	15/2
E	850-1050	8.84 ± 0.14	341^{+112}_{-121}	24/2
F	1050-1250	$8.85^{+0.12}_{-0.11}$	350^{+100}_{-90}	40/2
G	1250-1350	8.63 ± 0.11	537^{+121}_{-131}	77/2
H	1350-1510	8.69 ± 0.11	396^{+99}_{-113}	46/2

Table 5.1: Fe K Gaussian absorption profile components for Suzaku XIS 2013 data from the best fit baseline model. ^{t} denotes that the parameter is tied over the entire sequence 2013a (slices A–D).

[a] Rest-frame energy of the Gaussian absorption line,

[b] equivalent width for a width tided at $\sigma = 282^{+69}_{-56}$ eV,

[c] change in $\Delta\chi^2/\Delta\nu$ when the Gaussian component modelling the iron K absorption profile is removed.

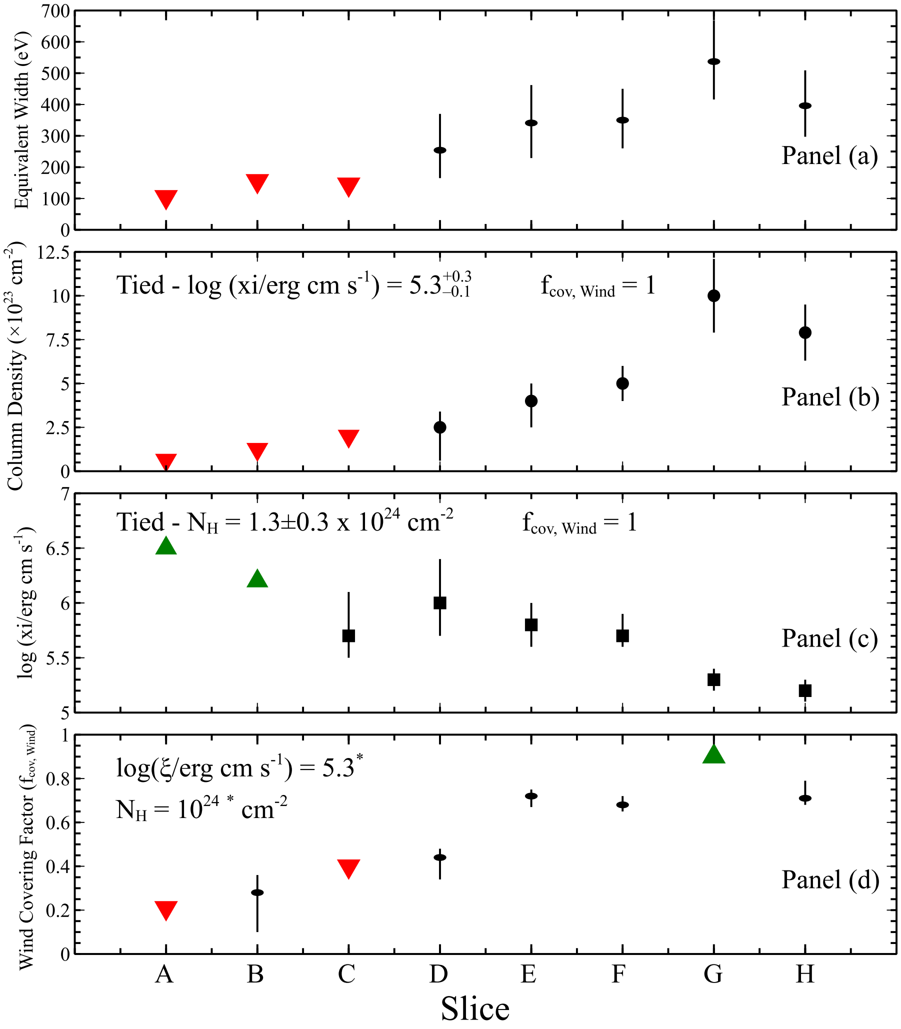

Figure 5.4: Fe K absorption short-term variability across the observation when modelled with either a Gaussian profile (panel a) or XSTAR (panels b - d). (a) EW evolution with time. (b) Column density variability assuming constant ionization and $f_{\rm cov,Wind} = 1$. (c) Ionization variability assuming constant column density and $f_{\rm cov,Wind} = 1$. (d) Variability of $f_{\rm cov,Wind}$ by assuming fixed ionization and column density. The red triangles represent upper-bound measurements, while green triangles indicate lower-bound measurements.

were investigated to explain the iron K short-term variability: (i) *variable column density*, where the column density of the fully covering wind is allowed to vary, while the ionization parameter is tied between the slices; (ii) *variable ionization*, where the ionization parameter of the fully covering wind is allowed to vary, while the column density is tied; (iii) *transiting absorber*, where the wind covering factor ($f_{\mathrm{cov,Wind}}$) across the line of sight is allowed to vary, while both the column density and ionization are fixed across the whole observation. In this case, the increase in Fe K absorption could occur if the absorber covers an increasing geometric fraction of the X-ray source over time. All the XSTAR parameters in modelling the Fe K absorption profile are summarised in Table 5.2.

Fig. 5.4 (panel a) plots the variability of the equivalent width of the absorption profile versus slice, where the EW clearly increases through the observations and reaches a maximum depth in slice G. Fig. 5.4(b) shows the *variable column density* case above, by keeping the ionization tied between the slices at $\log(\xi/\mathrm{erg\,cm\,s^{-1}}) = 5.3^{+0.3}_{-0.1}$. Remarkably, when I compare two adjacent slices the variability is consistent within the errors, but overall the column density of the highly ionized wind increases by a factor of ~ 10 as the observation progresses – i.e. from $\log(N_{\mathrm{H}}/\mathrm{cm^{-2}}) < 22.8$ in slice A to $\log(N_{\mathrm{H}}/\mathrm{cm^{-2}}) = 24.0 \pm 0.1$ in slice G. In the *variable ionization* case, Fig. 5.4(c), with the column density tied between the slices at $\log(N_{\mathrm{H}}/\mathrm{cm^{-2}}) = 24.1 \pm 0.1$, I find that instead the ionization parameter of the wind decreases during the observation reaching its lowest value in slice H, $\log(\xi/\mathrm{erg\,cm\,s^{-1}}) = 5.2 \pm 0.1$, compared to a lower limit of $\log(\xi/\mathrm{erg\,cm\,s^{-1}}) > 6.5$ in slice A. Thus in this scenario the ionization varies by a factor of ~ 10 or more between the two ends of the observation. In physical terms, however, for the ionization to follow such a trend, the ionizing flux has to vary by a factor of ~ 10, unless the density and/or distance of the gas from the source also varies.[2] While both *variable column density* and *variable ionization* cases provided an excellent fit to the data, yielding $\chi^2_\nu = 1552/1685$ and $\chi^2_\nu = 1543/1682$ respectively, the latter appears to be physically ruled out, as such drastic ionization changes do not occur in response to

---

[2] This former case is not easily distinguishable from a simple column density change, which is already considered in the *variable column density* case.

similar changes of the hard X-ray continuum.

I explored the *transiting absorber* case in Fig. 5.4(d) where, by assuming a fixed column density and ionization at $\log(N_{\rm H}/{\rm cm}^{-2}) = 24.0$ and $\log(\xi/{\rm erg\,cm\,s}^{-1}) = 5.3$, the variability of the absorption profile is instead accounted for by changes in the covering fraction of the iron K absorber. In this model, in order to compensate for the loss of flexibility as both $N_{\rm H}$ and $\log(\xi)$ are now constant, I also allowed the wind velocity to vary over the single slices. This better accounts for the moderate redwards shift of the line energy in the second part of the observation (see also Table 5.1). I find that the X-ray source is virtually unobscured in slice A (as the ionized absorber is covering $< 21\%$), and as the observation progresses the gas moves across the line of sight almost fully covering the source in slice G ($> 89\%$ covering); by the end of the observation, the X-ray source may begin to uncover again in slice H ($71^{+8}_{-3}\%$). Thus either $N_{\rm H}$ or $f_{\rm cov,Wind}$ changes may account for the variability of the iron K absorption feature. The physical implications will be examined in detail in the discussion.

	A	B	C	D	E	F	G	H
variable column density ($\log(\xi/$ erg cm s$^{-1}) = 5.3^{+0.3}_{-0.1}$), $f_{\rm cov,Wind} = 1$,$v_{\rm w} = 0.245^{+0.003}_{-0.005}c$								
$\log(N_{\rm H}/{\rm cm}^{-2})$	< 22.8	< 23.1	< 23.3	$23.4^{+0.2}_{-0.6}$	$23.6^{+0.1}_{-0.2}$	23.7 ± 0.1	24.0 ± 0.1	23.9 ± 0.1
variable ionization ($\log(N_{\rm H}/{\rm cm}^{-2}) = 24.1 \pm 0.1$), $f_{\rm cov,Wind} = 1$,$v_{\rm w} = 0.257^{+0.011}_{-0.010}c$								
$\log(\xi/$ erg cm s$^{-1})$	> 6.5	> 6.2	$5.7^{+0.4}_{-0.2}$	$6.0^{+0.4}_{-0.3}$	5.8 ± 0.2	$5.7^{+0.2}_{-0.1}$	5.3 ± 0.1	5.2 ± 0.1
transiting absorber ($\log(N_{\rm H}/{\rm cm}^{-2}) = 24.0^*$, $\log(\xi/$ erg cm s$^{-1}) = 5.3^*$)								
Wind $f_{\rm cov}$	< 0.21	$0.28^{+0.08}_{-0.18}$	< 0.40	$0.44^{+0.04}_{-0.10}$	$0.72^{+0.03}_{-0.07}$	$0.68^{+0.04}_{-0.03}$	> 0.89	$0.71^{+0.08}_{-0.03}$
$v_{\rm w}(c)$	0.24^t	0.24^t	0.24^t	0.24 ± 0.02	0.27 ± 0.02	0.27 ± 0.01	0.24 ± 0.01	0.25 ± 0.02

Table 5.2: XSTAR photoionization model components of the Fe K absorption profile for Suzaku XIS 2013 data. * denotes that the parameter has being fixed, ^{t} denotes that the parameter is tied to the first segment value. See the text for the details of the three different cases.

5.4 What causes the continuum short-term spectral variability?

In addition to the iron K absorption changes, the 2013 observations also show a significant broadband continuum spectral variability. Fig. 5.2 (bottom panel) shows the normalized softness ratio (NSR), computed as the difference between the $0.5 - 1$ keV over $2 - 5$ keV softness ratio (as a function of time) and its mean value, divided by the mean itself. This was defined mathematically as $\mathrm{NSR} = \frac{\mathrm{SR(t)} - \langle \mathrm{SR} \rangle}{\langle \mathrm{SR} \rangle}$, and shows the fractional change in the softness ratio (see Fig. 5.2 lower panel). This can be seen in particular prior to and during the course of the flare (slices C and D). This variability can also be appreciated from the spectral shape of the individual slices plotted in Fig 5.3 (top panels).

In particular, I want to test whether the broadband spectral variability is mainly produced by either (i) rapidly varying partial covering absorption or (ii) variations in the intrinsic shape of the continuum, such as the power law and soft excess, while the partial covering parameters ($N_{\mathrm{H}}, f_{\mathrm{cov}}$) are assumed to remain constant between the slices. I adopt the 'XSTAR baseline model' above (which includes the XSTAR modelling of the iron K absorption) as our baseline continuum model to test both scenarios.

5.4.1 Partial covering variability

In this scenario, the X-ray photons are reprocessed due to the presence of compact clouds of gas, that partially absorb the AGN emission allowing a fraction $(1 - f_{\mathrm{cov}})$ to emerge unattenuated. The size-scale of these clouds is typically similar to the X-ray emitting region, of the order of a few tens of R_{g} (e.g., Risaliti et al. 2007). For simplicity, the column densities of the two required partial covering zones are not allowed to vary between the slices, so that the spectral changes over the course of the observation are only due to variations in the covering fractions. Note that I would obtain equivalent results by letting the column densities, rather than the covering fractions, vary between the slices. The relative flux normalizations of the blackbody and the power-law continuum are *only* allowed to vary together by the same factor, i.e. I assumed that there is no intrinsic continuum spectral variability (hereafter *variable partial covering* model).

For the partial coverer, the column densities of the two regions are found again to be $\log(N_{\rm H,high}/{\rm cm}^{-2}) = 23.2 \pm 0.1$ and $\log(N_{\rm H,low}/{\rm cm}^{-2}) = 22.3 \pm 0.1$. For the high column zone, the covering fraction reaches its minimum during the flare (slice D) at $f_{cov,\rm high} = 0.47^{+0.09}_{-0.11}$, and increases to its maximum value $f_{cov,\rm high} = 0.72^{+0.04}_{-0.05}$ in slice E. Thus slice D is the highest flux/least absorbed spectrum overall, while slice E is the lowest flux/most absorbed spectrum. Conversely, the variations in the covering fractions for the low column partial coverer are smaller, simply ranging from $f_{cov,\rm low} = 0.72^{+0.05}_{-0.07}$ in slice C to $f_{cov,\rm low} = 0.85 \pm 0.03$ in slice D (see Table 5.3).

This suggests that the high column covering fractions account for most of the spectral variability, and tend to vary by ±15% around the mean ($\sim 60\%$) but never reaching zero. The range of variability of $f_{cov,\rm high}$ can give us an idea of the possible number of clouds (N) crossing our line of sight at any time, as in first approximation it is related to $1/\sqrt{\rm N}$. This suggests that a large number of clouds ($\rm N \gtrsim 25$) are needed along the line of sight to produce small ($\sim 20\%$) variations in covering. However, $\rm N > 25$ would imply that the size of each cloud is $\sim 1\,R_{\rm g}$, thus favouring an alternative scenario where the clouds are just a few but have an irregular or filamentary shape. The temperature of the blackbody component is $kT = 69^{+24}_{-21}\,$eV, slightly lower but still consistent with the values previously obtained. Overall, the variable partial covering model provided an excellent fit to the data, with $\chi^2_\nu = 1581/1689$.

		power law		**bbody**		$\mathrm{pc_{low}}$	$\mathrm{pc_{high}}$	**Model Statistic**	
		$\Gamma = 2.5 \pm 0.2$		$\mathrm{kT} = 69^{+24}_{-21}$ eV		$\log(N_{\mathrm{H,low}}/\mathrm{cm}^{-2})$	$\log(N_{\mathrm{H,high}}/\mathrm{cm}^{-2})$		
						22.3 ± 0.1	23.2 ± 0.1		
Slice	Time (ks)	$\mathrm{norm}^{a}_{\mathrm{po}}$	F^{b}_{2-10}	$\mathrm{norm}^{c}_{\mathrm{bb}}$	$\mathrm{F}^{d}_{0.5-2}$	$f_{cov,\mathrm{low}(\%)}$	$f_{cov,\mathrm{high}(\%)}$	$(\chi^2/\nu)^e$	N.P.^{e}
A	0-100	$3.3^{+1.2}_{-0.8}$	2.3	6.0	0.33	75^{+4}_{-6}	59^{+6}_{-7}	218/224	0.59
B	100-300	$2.4^{+0.9}_{-0.5}$	1.6	4.3	0.18	78^{+4}_{-5}	66^{+5}_{-6}	241/255	0.73
C	300-400	$2.5^{+1.0}_{-0.6}$	1.8	4.6	0.28	72^{+5}_{-7}	60^{+7}_{-8}	139/143	0.58
D	400-450	$5.1^{+1.9}_{-1.1}$	3.9	9.1	0.41	85 ± 3	47^{+9}_{-11}	148/160	0.75
E	850-1050	$2.1^{+0.8}_{-0.5}$	1.3	3.8	0.10	82^{+4}_{-5}	72^{+4}_{-5}	168/193	0.90
F	1050-1250	$3.0^{+1.2}_{-0.7}$	1.9	5.4	0.14	84^{+3}_{-4}	69 ± 5	283/278	0.41
G	1250-1350	$2.2^{+0.9}_{-0.5}$	1.6	4.0	0.14	84^{+3}_{-4}	61^{+6}_{-8}	128/123	0.36
H	1350-1510	$2.4^{+0.9}_{-0.5}$	1.8	4.4	0.21	80^{+3}_{-4}	55^{+7}_{-8}	256/243	0.27
					$\chi^2/\nu = 1581/1689$				

Table 5.3: Variable partial covering model parameters for *Suzaku* XIS 2013 slices where the spectral changes are accounted for by variability of the partial covering fraction. The blackbody and power-law normalizations are varying together through the same scale factor throughout the eight slices.

[a] Power-law normalization, in units of 10^{-3} photons keV^{-1} cm^{-2} s^{-1} at 1 keV,

[b] observed (non absorption corrected) power-law flux between $2-10$ keV, in units of 10^{-12} erg cm^{-2} s^{-1},

[c] blackbody normalization in units of 10^{-4} (L_{39}/D^2_{10}), where L_{39} is source luminosity in units of 10^{39} erg s^{-1} and D_{10} is the distance to the source in units of 10 kpc

[d] observed blackbody (soft excess) flux between $0.5-2$ keV, in units of 10^{-12} erg cm^{-2} s^{-1},

[e] χ^2, degrees of freedom and null hypothesis probability (N.P.) calculated in each individual slice.

		power law ($\Gamma = 2.5 \pm 0.1$)		**bbody** (kT= 69 eV)		**Model Statistic**		
Slice	Time (ks)	$\mathrm{norm_{po}}$	$\mathrm{F_{2-10,po}}$	$\mathrm{norm_{bb}}$	$\mathrm{F_{0.5-2,bb}}$	(χ^2/ν)	N.P.	$(\Delta\chi^2/\Delta\nu)$
A	0-100	$3.6^{+1.2}_{-0.9}$	2.5	$9.5^{+4.5}_{-3.9}$	0.38	271/226	2.0×10^{-2}	53/2
B	100-300	$2.3^{+0.7}_{-0.6}$	1.6	$5.1^{+2.3}_{-2.9}$	0.21	244/257	7.2×10^{-1}	3/2
C	300-400	$2.8^{+0.9}_{-0.7}$	1.9	$17.0^{+7.1}_{-5.5}$	0.69	177/145	3.5×10^{-2}	38/2
D	400-450	$6.0^{+1.9}_{-1.5}$	4.1	< 14.0	< 0.25	170/162	3.0×10^{-1}	22/2
E	850-1050	$1.4^{+0.5}_{-0.4}$	1.1	< 1.4	< 0.06	224/195	7.9×10^{-2}	56/2
F	1050-1250	$2.5^{+0.8}_{-0.6}$	1.7	< 3.6	< 0.15	372/280	1.9×10^{-4}	89/2
G	1250-1350	$2.2^{+0.7}_{-0.6}$	1.5	< 4.5	< 0.18	133/125	3.0×10^{-1}	5/2
H	1350-1510	$2.6^{+0.8}_{-0.6}$	1.8	$13.0^{+4.9}_{-3.8}$	0.53	257/245	2.9×10^{-1}	1/2
				χ^2/ν =1848/1697				

Table 5.4: Variable intrinsic continuum model parameters for Suzaku XIS 2013 slices. Here the power-law and blackbody components are allowed to vary independently, while N_{H} and f_{cov} are constant for both absorbers. The temperature of the blackbody component was fixed to the best value found in the earlier XSTAR baseline model, i.e. $kT = 69\,\mathrm{eV}$, in order to avoid physically unrealistically high values to model the curvature present at higher energies. All the quantities and units are the same as in Table 5.3. The last column shows the difference in χ^2 and degrees of freedom compared to the variable partial covering model.

5.4.2 Intrinsic spectral variability

Alternatively, I tested if the main driver of the short-term spectral variability is actually a change in the intrinsic continuum via independently variable normalizations of the blackbody and power-law components. The partial covering fractions $f_{cov,\mathrm{low}} = 81^{+3}_{-4}\%$ and $f_{cov,\mathrm{high}} = 63^{+5}_{-6}\%$ and column densities $\log(N_{\mathrm{H,low}}/\mathrm{cm}^{-2}) = 22.3\pm0.1$ and $\log(N_{\mathrm{H,high}}/\mathrm{cm}^{-2}) = 23.2 \pm 0.1$ are assumed to be constant between the slices (See Table 5.4). Notably, the values of both $f_{cov,\mathrm{low}}$ and $f_{cov,\mathrm{high}}$ are almost coincident with the average values found in the previous case. Statistically, this model (hereafter *variable intrinsic continuum* model) gives an overall worse fit ($\chi^2/\nu = 1848/1697$) compared to the variable partial covering scenario, by $\Delta\chi^2/\Delta\nu \sim 270/8$. On this basis, I investigated these differences through the inspection of the residuals in each of the eight slices (see Fig. 5.5).

Generally speaking, when the partial covering absorption is constant the χ^2 is worse in all of the slices, in particular in some of the pre- and post-flare spectra (e.g., C, E, and F). Without allowing the absorber covering fractions to vary, there is in fact an additional curvature present in the residuals as shown in the right panels of Fig. 5.5. The variable intrinsic continuum model seems to account for some of the slices (i.e., slice B, G, and H), although a caveat is that the blackbody normalizations are strongly varying between the slices (e.g., from slice C to E and from slice G to H) and not always in sync with the power-law changes, possibly indicating that such extreme intrinsic changes are physically unrealistic (see Table 5.4 for values).

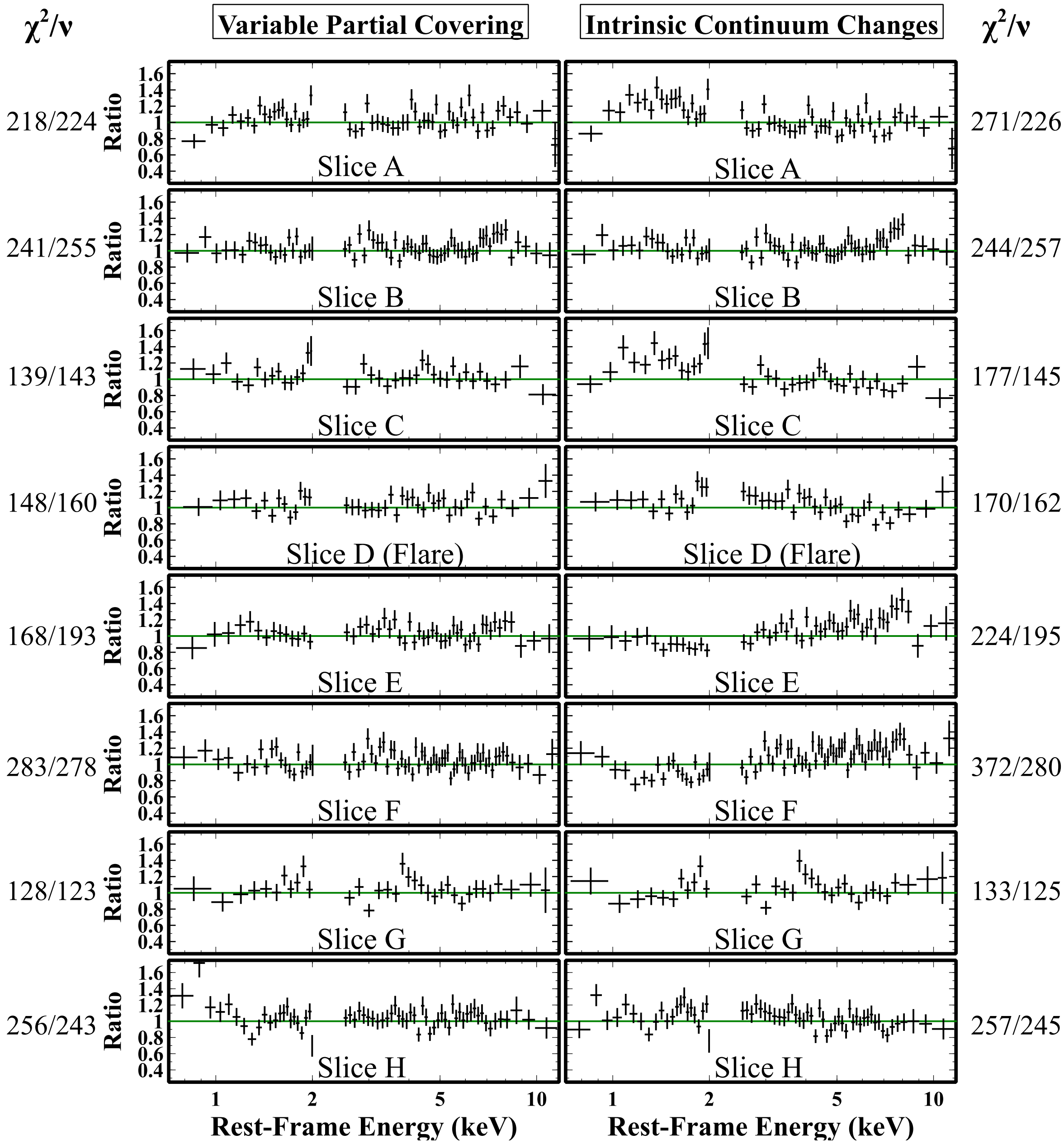

Figure 5.5: Plots comparing the data/model residuals of each individual slice fitted with a variable partial covering model (left) or intrinsic spectral variability (right). The χ^2/ν values of the variable partial covering model are equal or lower in all the eight slices compared to the intrinsic variability fit (see Tables 5.3 and 5.4). This is due to the extra curvature present in the residuals when the covering fraction is not allowed to vary.

5.5 Fractional variability

In order to further quantify the spectral variability, I also calculated the fractional variability (F_{var}; e.g., Rodríguez-Pascual et al. 1997) defined as:

$$F_{\mathrm{var}} = \frac{\sqrt{S^2 - \overline{\sigma^2_{\mathrm{err}}}}}{\bar{x_i}} \tag{5.2}$$

where S^2 is the total variance about the mean, $\overline{\sigma^2_{\mathrm{err}}}$ is the contribution towards the total variance from the individual measurement errors and $\bar{x_i}$ is the arithmetic mean of the light curves comprising of a series of fluxes x_i measured at discrete times $t_i\,(t = 1, 2, \cdots N)$. Thus the F_{var} was computed in different energy bands, adopting a time binning of 5760 s (i.e. one *Suzaku* orbit) and using the method described in Vaughan et al. (2003). The overall shape of the broadband F_{var} spectrum (plotted in Fig. 5.6) appears broadly consistent with the results of either the *variable partial covering* model (see Table 5.3) or the *variable intrinsic continuum* model (see Table 5.4). Indeed if, the continuum were variable without any spectral variability, which would be the case if the power-law and soft excess components varied in proportion together, then the F_{var} spectrum would, in principle, appear to be constant across all energies. Here instead the variability in the softer band is enhanced with respect to the hard X-ray band. This behaviour could be naturally attributed to: (i) absorption variability seen as partial covering fraction changes across the observation and/or (ii) a two component continuum, where the soft X-ray band component is more variable compared to the hard one. In either case, the soft X-rays would be more affected with respect to the harder X-rays, resulting in an enhanced F_{var} towards lower energies.

To test the F_{var} spectrum against the actual spectral models, I simulated 2000 light curves based on the spectral parameters obtained for the slices from the previous section. I used as an input for the simulations the best-fitting spectral model of Table 5.3 (variable partial covering), where the spectral variability is produced by the partial covering absorber. Informed by the best fit parameters from the individual spectral slices, the partial covering fractions ($f_{\mathrm{cov,low}}$ and $f_{\mathrm{cov,high}}$) were allowed to vary within the ranges from $0.70 < f_{\rm cov,low} < 0.85$ and $0.4 < f_{\rm cov,high} < 0.8$. The soft (blackbody) and hard X-ray (power-law) components of the continuum were allowed to vary together (as per variable partial covering model) by a factor of $0.5 - 2$ in respect to the average normalization, which represents the expected range of intrinsic continuum variability (see Fig. 5.2). Each simulated light curve was then randomly generated by varying the spectral parameters within these ranges and the subsequent $F_{\rm var}$ calculated versus energy from averaging over all 2000 simulated curves.

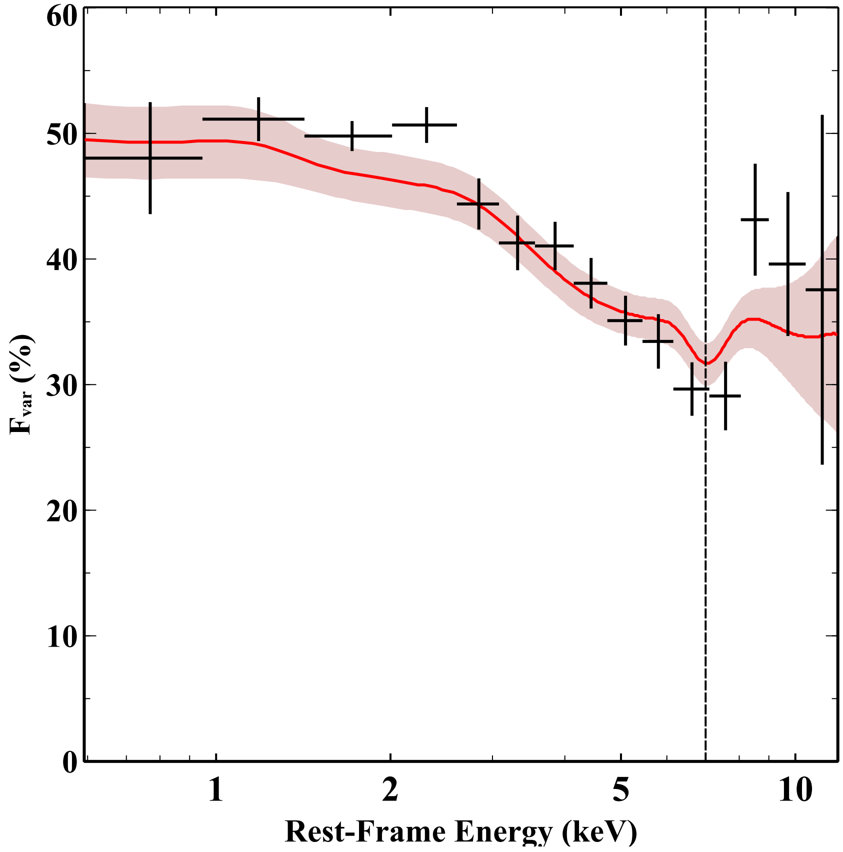

Figure 5.6: X-ray fractional variability from the 2013 *Suzaku* observations (in black). The iron K emission band centred at 7 keV (dashed black line) appears to be less variable than the rest of the spectrum. This may be associated with the reprocessed emission arising from the more distant material within the wind. The solid red line corresponds to the simulated $F_{\rm var}$ shape based on the *variable partial covering* model (see text for details). The curve has been smoothed with a spline function, and the shaded area indicates the 1σ dispersion for 2000 simulated light curves.

The result is also shown in Fig. 5.6, where the red solid line corresponds to the simulated $F_{\rm var}$ model (and associated 1σ dispersion shown as the shaded area), compared to the actual $F_{\rm var}$ spectrum measured from the observations. The overall observed shape and normalization of the $F_{\rm var}$ spectrum is generally well reproduced by the simulations, with the variable partial covering model not only accounting for the rising shape of the $F_{\rm var}$ spectrum towards lower energies, but also for the overall curvature. In contrast, the *variable intrinsic continuum* model, where the power-law and blackbody components were allowed to vary independently (with the partial covering absorption held constant), estimated to under-predicts the $F_{\rm var}$ spectrum in the $1-3$ keV range. This is likely due to the fact that the soft X-ray blackbody component only adds sufficient variability below 1 keV and thus the simulated $F_{\rm var}$ spectrum is then flatter compared to the observations. Thus the overall shape of the $F_{\rm var}$ spectrum appears consistent with the variable partial covering scenario presented in the previous section.

Furthermore, looking at Fig. 5.6, there is a minimum in $F_{\rm var}$ in the $6.5-7.5$ keV energy band, which is centred on the ionized Fe K emission. This may also suggest that the iron line is less variable compared to the continuum, or at least is not varying on the same short timescale of the X-ray continuum (of the order of ~ 100 ks). In this light, I investigated from the spectral slices whether the iron K emission line responded to the variability of the continuum. Two opposite scenarios were investigated; first, I kept the Fe K emission line flux fixed between the slices, then I let the emission line flux vary in sync with the continuum, so that the line equivalent width is constant. As indicated from the $F_{\rm var}$ spectrum, I can achieve a very good fit in the constant flux scenario. In the second case, a constant equivalent width produced a significantly worse fit by $\Delta\chi^2/\Delta\nu = 100/8$, thus indicating that there is no apparent short timescale correlation between the Fe K line and the continuum flux between the slices. These results imply that on $\gtrsim 100$ ks timescales ($\gtrsim 20\,R_{\rm g}$), the iron K emission is less variable than the continuum; this suggests that the iron K emitting region is larger than the typical continuum size inferred, which is of the order of $\sim 6-20\,R_{\rm g}$ (see below). The line may then originate from the outer regions of the disc or, alternatively, if it is associated with the wind as suggested by Nardini et al. (2015), its lack of variability would be consistent with an origin at distances $\gtrsim 100\,R_{\rm g}$ from the black hole. Indeed as was observed earlier in § 4.5.1 the Fe K emission does appear to vary on longer timescales of a week or longer, between different *XMM-Newton* & *NuSTAR* observations.

I finally note that, above $7-8\,$keV, the observed variability reaches again a larger value $F_{\rm var} \sim 45\%$ value between $8-9\,$keV, coincident with the energy of the iron K absorption feature. This suggests that the iron K absorption variability, discussed earlier in § 5.3, may be responsible for this increase in $F_{\rm var}$. For simplicity, however the properties of the highly ionized wind were not allowed to vary when generating the simulated light curves.

5.6 Properties of the partial covering absorber

From the previous sections I conclude that I cannot explain the overall short-term spectral variability without invoking a variable partial coverer. Therefore there is a natural question of what the partial covering is associated with.

One possibility is that it is the less ionized and more dense (or clumpy) part of the outflow. To test this, I investigated the outflow velocity of the partial covering absorber(s) ($v_{\rm pc}$) by allowing it to vary independently from the wind's outflow velocity ($v_{\rm w}$). The resulting fit (applied to the eight slices) suggested that this component is indeed outflowing with a velocity comparable to the velocity of the highly ionized gas. Fig. 5.7 (left) shows the contour plot of the χ^2 against the partial covering redshift parameter tied between all the slices (but allowing the other spectral parameters to vary). A local minimum at about the quasar's rest frame (i.e. $z = 0.184$) is clearly visible, however by assuming a systemic velocity for the partial coverer the fit statistic is worse by $\Delta\chi^2/\Delta\nu = 11/1$ compared to the best-fit case. The global minimum in Fig. 5.7 indicates that the partial covering gas prefers an outflow velocity of $v_{\rm pc} \sim 0.25c$ over a null velocity at the $\sigma = 3.29$ (99.9%) confidence level. This indicates that the two partially covering zones might be the least ionized component of the *same* fast ($v_{\rm pc} \sim v_{\rm w} \sim 0.25c$) wind.

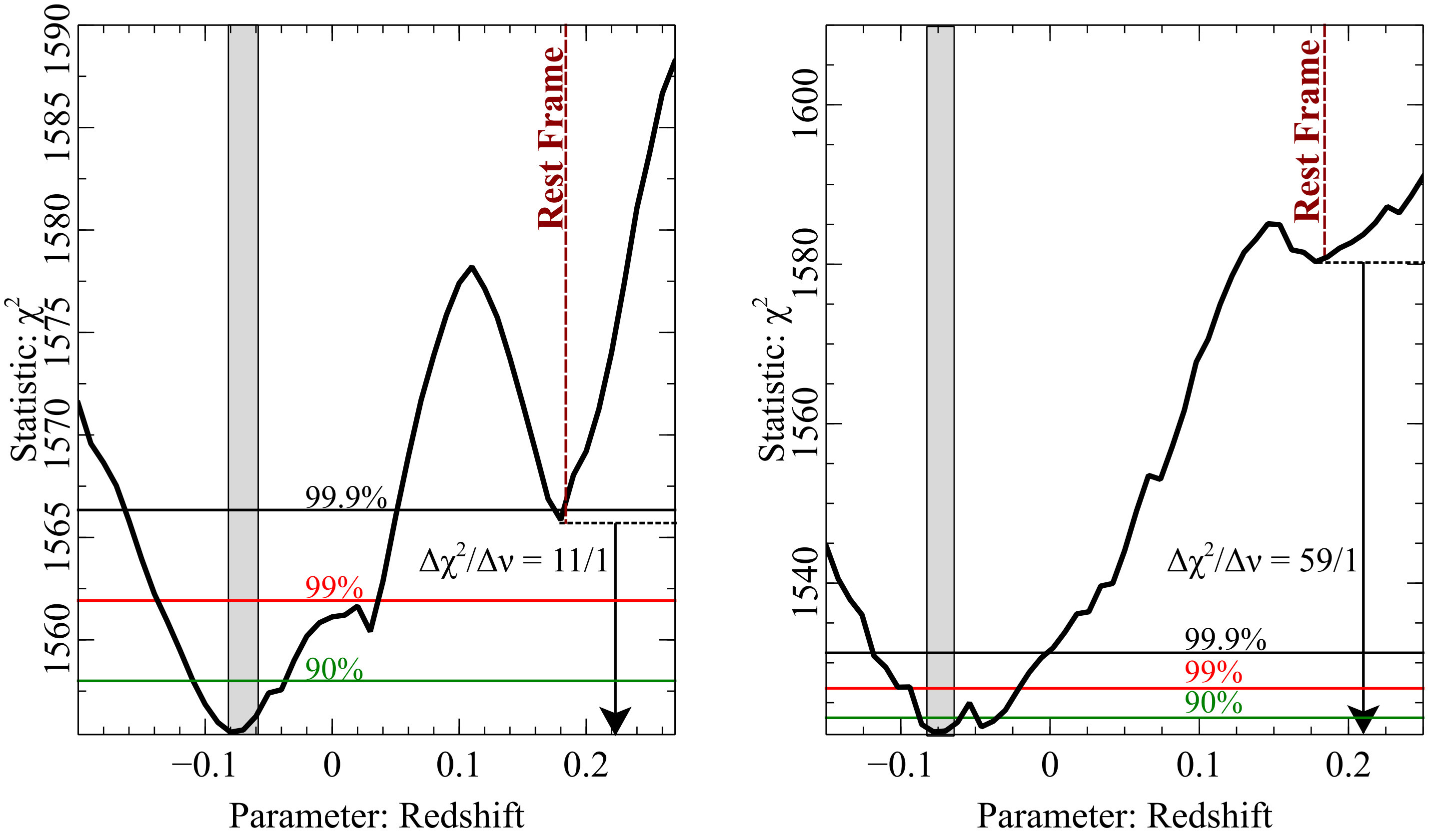

Figure 5.7: Left: Contour plot of the χ^2 against the partial covering redshift parameter (used as proxy for the velocity) in all the slices. A local minimum at about the quasar rest frame (i.e. $z = 0.184$) is clearly visible, but the global minimum indicates that the partial covering layers are possibly outflowing with velocity comparable to that of the fully covering ionized wind, i.e. $v_{\rm pc} \sim \ v_{\rm w} \sim 0.25c$. This suggests that the two partially covering zones may correspond to the less ionized component of the same ultra fast wind. Right: as for left panel, but with a mildly ionized partial covering absorber. The global minimum corresponds to a statistical improvement, with respect to the rest-frame velocity, of $\Delta\chi^2/\Delta\nu = 59/1$. The vertical shaded area correspond to the range of $v_{\rm w}$ across the slices given in Table 5.2.

As a consistency check, I also tested the above result by replacing the two neutral partial covering components with two mildly ionized absorbers, modelled through the same absorption grid responsible for the absorption line at Fe K. I therefore constructed a *'mildly ionized partial covering model'* expressed as:

$$\begin{aligned} & \texttt{Tbabs} \times \texttt{xstar}_{\rm Fe\,K} \times \{[(C_{\rm high} \times \texttt{xstar}_{\rm pc,high}) \\ & +(C_{\rm low} \times \texttt{xstar}_{\rm pc,low}) + (1 - C_{\rm high} - C_{\rm low})] \times \texttt{po} + \texttt{bbody} + \texttt{zgauss}\}, \end{aligned} \tag{5.3}$$

where $C_{\rm high}$ and $C_{\rm low}$ are multiplicative constants such that $C_{\rm high} + C_{\rm low} < 1$, $\texttt{xstar}_{\rm Fe\,K}$ represents the fully covering highly ionized wind, while $\texttt{xstar}_{\rm pc,low}$ and $\texttt{xstar}_{\rm pc,high}$ represent the low and high column, mildly ionized partial covering zones respectively. The Gaussian component `zgauss` again parametrizes the ionized emission profile, while the soft excess is described by the `bbody` component. Note that the model structure is slightly different compared to the previous models, so that $C_{\rm high}$ and $C_{\rm low}$ are not immediately comparable to the previous $f_{\rm cov,high}$ and $f_{\rm cov,low}$. Here the constants $C_{\rm high}$ and $C_{\rm low}$ physically represent the mutual covering fractions of the high and low column absorbers, so that the remaining fraction $1 - C_{\rm high} - C_{\rm low}$ of the continuum is not absorbed by either layer and passes through the partial coverer unattenuated. Also, for simplicity, the blackbody component is assumed to be unobscured. For this reason, its temperature is somewhat larger ($kT = 110^{+8}_{-11}$ eV).[3]

Overall, the column densities $\log(N_{\rm H,high}/{\rm cm}^{-2}) = 23.6^{+0.3}_{-0.4}$ and $\log(N_{\rm H,low}/{\rm cm}^{-2}) = 22.5 \pm 0.3$ are marginally larger (but fully consistent) than in the neutral absorber case, as the gas here is more transparent to the illuminating radiation. I get $\log(\xi/\ {\rm erg\ cm\ s}^{-1}) = 2.5 \pm 0.2$ for the high column partial coverer and $\log(\xi/\ {\rm erg\ cm\ s}^{-1}) = 0.62^{+0.18}_{-0.08}$ for the low column one. Notably, the high column zone is confirmed to be the main source of the observed continuum variability, and its behaviour is very similar to the one previously described, ranging from $\sim 50\%$ (slice D) to $\sim 80\%$ (slice E). The fraction of the intrinsic continuum that is not affected by any absorber (apart from the fully covering highly

---

[3] However, by letting the blackbody component vary together with the power law and experience exactly the same absorption, I still achieve a very good fit ($\chi^2_\nu \simeq 0.94$) and the results do not change.

ionized one) is always of the order of a few percent, and never exceeds 10%. Note that as the uncovered fraction (i.e., $1 - C_{\mathrm{high}} - C_{\mathrm{low}}$) is $< 10\%$, it might be that the unattenuated continuum represents the fraction of radiation that is scattered back into the observed line-of-sight. The confidence contour plotted in Fig. 5.7 (right) suggests a very similar behaviour in χ^2 space for the velocity of the partial coverer. Indeed, the statistical improvement with respect to a systemic velocity is much larger ($\Delta\chi^2/\Delta\nu = 59/1$). Thus I conclude that the partial covering absorbers' outflow velocity, $v_{\mathrm{pc}} = 0.25^{+0.01}_{-0.05}c$, is consistent with that of the iron K absorber.

This result was later confirmed in an extensive high-resolution analysis performed on PDS 456 by Reeves et al. (2016). From resolving the absorption troughs from the RGS/EPIC-MOS spectra on some of the low flux states such as the ObsE from the *XMM-Newton* & *NuSTAR* campaign, it was found that the spectrum required two fast soft X-ray absorption zones as shown in Fig. 5.8. Reeves et al. (2016) also found that both zones formally required an outflow velocity at a $> 99.99\%$ confidence level, where the absorbers located in zone 1 was lower at $v_{\mathrm{w}} = 0.064 \pm 0.012c$ compared to $v_{\mathrm{w}} = 0.17 \pm 0.01c$ in zone 2. Thus the result from this work and Reeves et al. (2016), confirm that indeed PDS 456 presents fast outflowing absorbing gas detected in both the hard and soft X-rays and possibly from a range of ionization parameters. The physical implications in terms of the structure and geometry of the wind will be discussed in the next section.

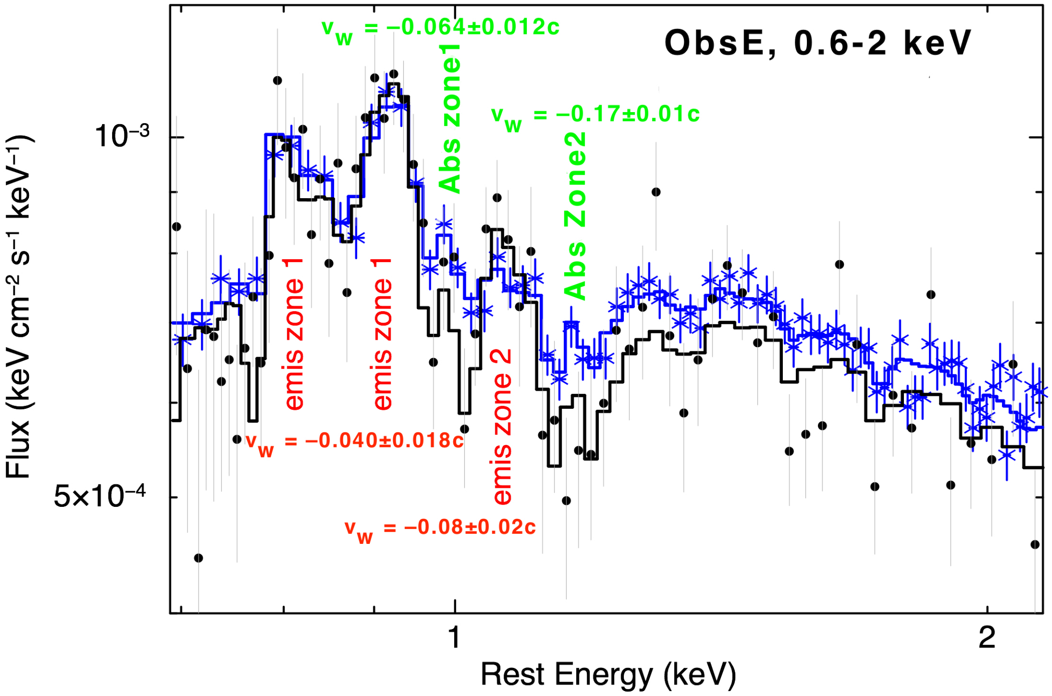

Figure 5.8: XSTAR photoionization model fitted simultaneously with RGS (black dots) and MOS (blue stars) data from the ObsE observation, between $0.6 - 2$ keV where the solid lines are the best-fit models fitted to the corresponding instruments. This model is able to account for two fast zone of outflowing absorbing material and the corresponding emissions. Figure adapted from Reeves et al. (2016).

5.7 Discussion

In the previous section I found that the observed short-term spectral variability can be explained by the combination of partial covering absorption and intrinsic continuum variability, although the former effect may be the dominant cause in this observation. Furthermore, by investigating in more detail the properties of the partial covering absorbers, I found that their outflow velocity is comparable to that of the highly ionized

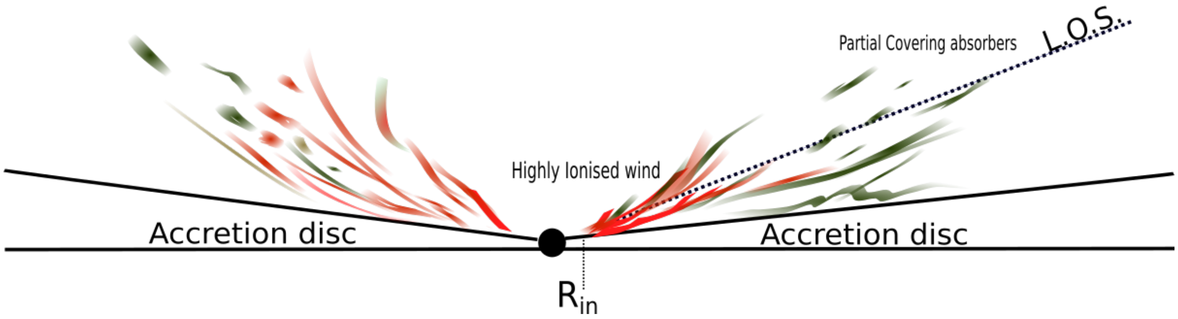

Figure 5.9: A schematic representation of a possible structure of the outflow and the relative locations of the highly ionized wind (red) and less ionized partial covering absorbers (green) within the outflow. The dashed line represents a possible line of sight. The highly ionized absorber is located in the vicinity of the black hole whilst the less ionized partial covering material is possibly situated further out, both being part of the same outflow.

wind (i.e. $v_{\rm pc} \sim v_{\rm w} \sim 0.25c$) for both the neutral and mildly ionized case. This suggests that the partial covering absorber may be the less ionized but clumpier component of the disc wind, as also supported by the analysis of the soft X-ray absorption features in the high-resolution *XMM-Newton* RGS spectra (Reeves et al. 2016). A schematic representation of the possible location and structure of the highly ionized wind and partial covering absorbers in the context of the outflowing material from the neighbourhood of the accreting supermassive black hole is shown in Fig. 5.9.

5.7.1 Properties of the clumpy wind and constraints on the X-ray emitting region

During the observation, the column density $N_{\rm H}$, or equivalently the EW of the Fe K absorption feature, increased by a factor of ~ 10, from $\log(N_{\rm H}/{\rm cm}^{-2}) < 22.8$ in slice A to $\log(N_{\rm H}/{\rm cm}^{-2}) = 24.0^{+0.1}_{-0.3}$ in slice G. Alternatively, these variations may be accounted for by a change in the wind covering factor ($f_{\rm cov,Wind}$), where initially the absorber is not covering the X-ray source but progresses to almost fully covering ($> 89\%$) at the time of slice G. These changes could be caused by the transit of a cloud or stream of highly ionized material moving across the line of sight as part of an inhomogeneous outflow (see Fig. 5.4 panel d). The linear size of the transiting clump can be estimated as $\Delta R_c \sim v_{\rm w}\Delta t$, assuming that the transverse velocity is comparable to the outflow velocity (i.e., $v_{\rm K} \sim v_{\rm w}$), and that ΔR_c is similar to the size of the X-ray source. The putative cloud, in fact, cannot be much smaller than the X-ray emitting region in PDS 456 since an almost complete covering is reached in slice G (see Fig. 5.10). At the same time it cannot even be much larger, given that in slice H the covering seems to decrease instead of remaining close to $f_{\rm cov,Wind} \sim 1$. I choose $\Delta t = 400$ ks, corresponding to the time between the initial (statistically significant, $\sim 3\sigma$) onset of the absorption profile in slice E and its completion at maximum depth in slice G ($> 5\sigma$). By adopting $v_{\rm w} \simeq 0.25c$, I estimate $\Delta R_c \approx 3 \times 10^{15}$ cm $\sim 20\ R_g$ for $M_{\rm BH} \sim 10^9 M_\odot$. This can also be seen as a constraint on the size of the X-ray emitting region, which therefore cannot be larger than $\sim 20\ R_g$ in order for the absorber to reach full covering during slice G.

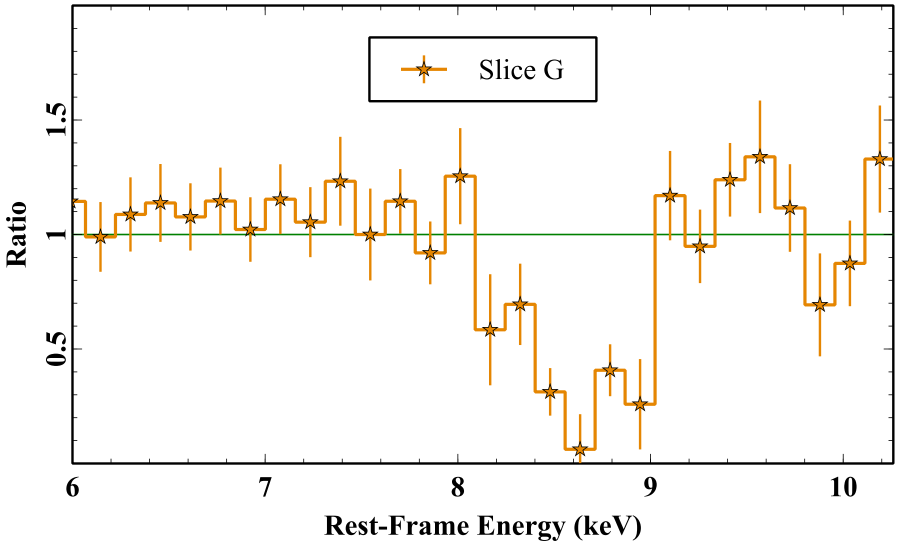

Figure 5.10: Zoom in of ratio plot of slice G binned at FWHM resolution. The continuum flux reaches almost zero flux at ~ 8.6 keV, indicating the highly ionized absorber is fully covering the X-ray emitter.

For an ionizing luminosity of $L_{ion} \sim 5 \times 10^{46}\,\mathrm{erg\,s^{-1}}$, and taking the average column density between slices E and H of $\log(N_{\mathrm{H}}/\mathrm{cm^{-2}}) \sim 24$, as well as the average ionization parameter of $\log(\xi/\mathrm{erg\,cm\,s^{-1}}) \sim 5.3$, the distance of the absorber from the ionizing continuum can be estimated. Considering an average hydrogen number density of $n_{\mathrm{H}} \sim N_{\mathrm{H}}/\Delta R \sim 3.3 \times 10^{8}\,\mathrm{cm^{-3}}$, then from the definition of the ionization parameter $R = (L_{ion}/n_{\mathrm{H}}\xi)^{\frac{1}{2}} \sim 2.8 \times 10^{16}\,\mathrm{cm}$, or $R \sim 180\,R_{\mathrm{g}}$. This radial estimate is of the same order of that measured by Nardini et al. (2015) and also consistent with what was estimated in Chapter 4. These results suggest that we are viewing through a clumpy wind at typical distance of few $100\,R_{\mathrm{g}}$ from the black hole.

5.7.2 Estimate of the wind radial distance from its Keplerian velocity

In estimating the radial distance of the wind from the black hole above, I assumed that $v_{\mathrm{K}} \sim v_{\mathrm{w}}$. Relaxing this assumption, I now instead express the Keplerian velocity as $v_{\mathrm{K}}^2 = \frac{c^2}{r_{\mathrm{g}}}$, where $r_{\mathrm{g}} = \frac{R}{R_{\mathrm{g}}}$ is the distance in units of gravitational radii.
The hydrogen number density in terms of r_{g} is expressed as

$$n_{\mathrm{H}} \sim \frac{\Delta N_{\mathrm{H}}}{\Delta R_c} \sim \frac{\Delta N_{\mathrm{H}}}{\Delta R_{\mathrm{x}}} \sim \frac{\Delta N_{\mathrm{H}} r_{\mathrm{g}}^{1/2}}{c\Delta t}, \tag{5.4}$$

where ΔR_{x} is the size of the X-ray source. As I practically observe an eclipsing event of the X-ray source, I again assume that $\Delta R_{\mathrm{x}} \sim \Delta R_{\mathrm{c}}$ (Risaliti et al. 2007). ΔN_{H} is the change in column density between slices E and H of the passing clump as shown in Fig. 5.4b. $\Delta R_c = c\Delta t/r_{\mathrm{g}}^{1/2}$ is the transverse radial distance covered by the passing clump between slices E–H.

By substituting the definition of the ionization parameter I can therefore obtain an expression for the radial distance (in gravitational units) as,

$$r_{\mathrm{g}}^{5/2} = \frac{L_{\mathrm{ion}}}{\xi} \frac{\Delta t\ c^5}{\Delta N_{\mathrm{H}}} \left(G M_{\mathrm{BH}}\right)^{-2}. \tag{5.5}$$

From the known variables then $R \sim 3 \times 10^{16}$ cm $\sim 200 R_{\mathrm{g}}$, which is of the same order of the previous estimate. The fast variability likely implies that the wind is not uniform but inhomogeneous. What I see in this observation may be therefore described as a ~ 20 day long "picture" of a complex time-dependent AGN accretion disc-wind (Proga, Stone & Kallman 2000; Proga & Kallman 2004), where the line of sight absorption varies over a timescale of days to weeks. On the other hand, Gofford et al. (2014) investigated whether the increase in depth of the Fe K absorption profile could be attributed to changes in the ionization state due to recombination within a smooth (constant column density over time) outflow in photo-ionization equilibrium. In this case, the estimate of the radial extent of the outflow was found to be $R \sim 1000\ R_{\mathrm{g}}$. Note, however, that a smooth wind without denser clumps would require another explanation to account for the variable partial covering absorber.

5.8 Origin and energetics of the flare

In order to analyse the remarkable flare, I focused on the soft $(0.5-1\,\mathrm{keV})$ and the hard $(2-5\,\mathrm{keV})$ light curves corresponding to the first 450 ks of the observation (sequence 2013a, slices A - D) plotted in Fig. 5.11 (top panel). These are plotted together with the corresponding softness ratio $(0.5-1/2-5\,\mathrm{keV})$ as shown in Fig. 5.11 (bottom panel). Here, I observe a steady increase of the soft X-ray flux by a factor of ~ 4 between $t \sim 250-430$ ks. In contrast, the hard X-ray flux shows a sharp increase, by a factor ~ 2.5, between $t \sim 390-430$ ks. Therefore the doubling time for the soft flux is ~ 90 ks, whilst the doubling time for the hard flux is ~ 2 times shorter (i.e. ~ 40 ks), implying from the light-crossing time argument that the approximate extent of the soft and hard X-ray emission regions in PDS 456 is $\sim 15-20\,R_{\mathrm{g}}$ and $\sim 6-8\,R_{\mathrm{g}}$ respectively. This suggests a corona characterized by an extended region of "warm" electrons combined with a more compact region of "hot" electrons contributing to the rapid hard flare. This would overall be consistent with the earlier representation with the `optxagnf` disc plus corona model (see section 4.3.2).

The soft X-ray (0.5 – 1 keV) flux appears to increase prior to the onset of the hard flare (see Fig 5.11). This suggests that the hard photons lag behind the softer band, as might be expected in coronal models whereby the softer photons act as “seeds” for the hard X-ray emission. However without coverage of the decline of the flare, it is not possible to test this qualitatively. Whatever the physical explanation, this is consistent with the most recent results from micro-lensing studies, which hint at soft and hard X-ray coronal components of different size (Mosquera et al. 2013).

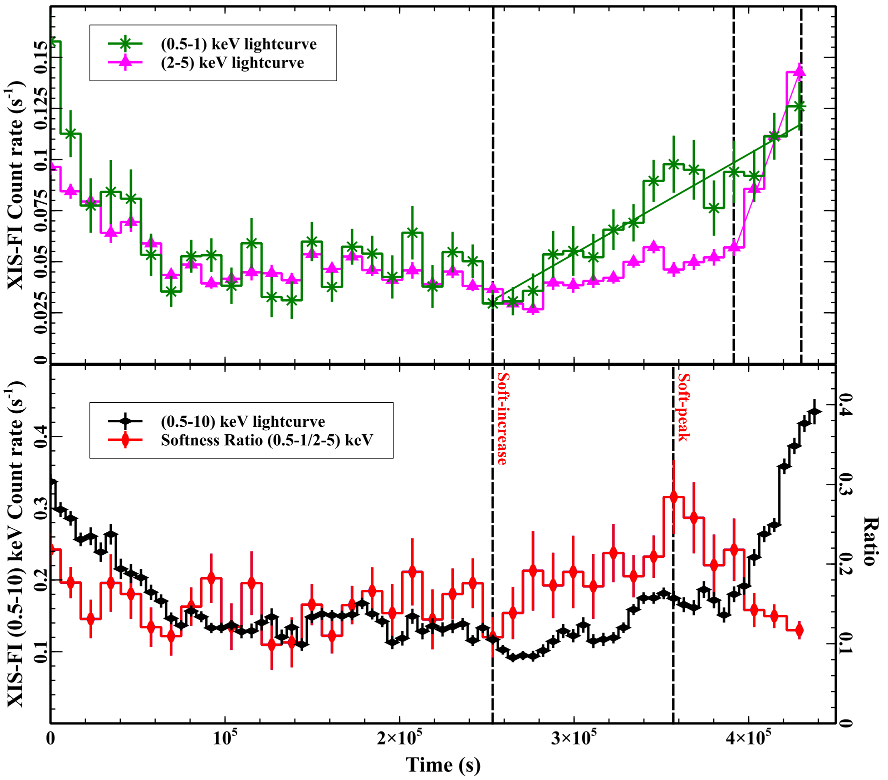

Figure 5.11: light curves of the first 450 ks of the 2013 *Suzaku* observation (corresponding to the 2013a sequence). Top panel: the soft (0.5 – 1 keV, green) and hard (2 – 5 keV, magenta) light curves. The soft light curve shows a gradual increase in flux (by a factor of 4 in ∼ 180 ks) in the latter part of the observation, while the hard band increases abruptly by a factor of 2.5 in ∼ 40 ks. Lower panel: The softness ratio overlaid on the full band light curve. This shows that the X-ray emission become softer just prior the strong flare (i.e., slice D) at ∼ 400 ks and subsequently hardens during the flare.

One open question involves the origin of the flare itself. A possible scenario is whether the observed flare (in slice D) can be simply due to a “hole” in the partial coverer, rather than due to an intrinsically variable X-ray continuum. On this basis, I tested a model where *only* the covering fractions $f_{\mathrm{cov,low}}$ and $f_{\mathrm{cov,high}}$ were allowed to vary between the eight slices, whereas the normalizations of blackbody and power law components were not. The overall fit statistic was substantially worse, $\Delta\chi^2/\Delta\nu = 333/14$, in the case where no intrinsic continuum variations were allowed. Thus it is likely that the flare is produced intrinsically.

5.8.1 Can the flare drive the outflow ?

Another question arising is whether the strong flare emission could radiatively power the outflow in the latter part of the observation, as the outflow at iron K is more clearly detected after the occurrence of the flare in the light curve. From the transfer of photon momentum to the wind it follows that:

$$\dot{p}_{\mathrm{w}} = \dot{M}_{\mathrm{w}} v_{\mathrm{w}} \sim \tau \frac{L_{\mathrm{flare}}}{c}, \tag{5.6}$$

where $\dot{p}_{\mathrm{w}}, \dot{M}_{\mathrm{w}}$ and v_{w} are the momentum rate, mass outflow rate and outflow velocity of the wind, while the Thomson depth is $\tau \sim 1$ for $N_{\mathrm{H}} \sim 10^{24}\,\mathrm{cm}^{-2}$, as observed in the highly ionized wind.

Thus the kinetic power (luminosity) of the wind is,

$$\dot{E}_{\mathrm{w}} = \frac{1}{2}\dot{M}_{\mathrm{w}} v_{\mathrm{w}}^2 \sim \left(\frac{v_{\mathrm{w}}}{2c}\right) L_{\mathrm{flare}}, \tag{5.7}$$

or, integrating over time for the total energy:

$$E_{\mathrm{w}} \sim \left(\frac{v_{\mathrm{w}}}{2c}\right) E_{\mathrm{flare}}. \tag{5.8}$$

For an outflow velocity of $v_{\rm w} \sim 0.25c$, then $\dot{E}_{\rm w} \sim \dot{E}_{\rm flare}/8$, hence implying that I would expect only $\sim 10-15\%$ of the radiative power in the flare to be directly transferred to the wind.

From the best fit to the eight slices, I estimated the $1-1000\,$Ryd luminosity of the flare to be $L_{\rm Flare} \sim 2\times10^{46}\,{\rm erg\,s^{-1}}$ (corrected for absorption).

Now, the mass outflow rate of the wind, derived earlier in § 4.5.4, is given by:

$$\dot{M}_{\rm w} \sim \mu\Omega m_p N_{\rm H} v_{\rm w} R_{\rm in}, \tag{5.9}$$

and, based on the discussion in Chapter 4 I, have adopted the following variables: $\mu \sim 1$, $\Omega \sim 2\pi$ sr for the solid angle, the average column density between slices E and H is $N_{\rm H} > 5\times10^{23}\,{\rm cm^{-2}}$, $v_{\rm w} \sim 0.25c$ and $R_{\rm in} > 100\ R_{\rm g} \sim 1.5\times10^{16}$ cm. Hence, I estimated $\dot{M}_{\rm w} \gtrsim 9\,M_{\odot}\ {\rm yr^{-1}} \sim 0.4\dot{M}_{\rm edd}$ (in good agreement with Nardini et al. 2015 and with what was estimated in Chapter 4). The kinetic luminosity of the outflow is $\gtrsim 1.5\times10^{46}\,{\rm erg\,s^{-1}}$, or $\sim 0.1\,L_{\rm Edd}$ for $M_{\rm BH} = 10^9 M_{\odot}$.

The duration of the wind in slices E to H is at least $\sim 600\,$ks, thus the mechanical energy carried by the wind post-flare is at least $\sim 10^{52}\,$erg. To be conservative, I can assume that the flare is symmetric and persists at its maximum observed luminosity ($L_{\rm Flare} \sim 2\times10^{46}\,{\rm erg\,s^{-1}}$) for the entire duration of the observational gap, i.e. for 450 ks in total. This would impart a total radiative energy of up to $\sim 10^{52}\,$erg. Indeed, this value represents a maximum upper limit for the total energy radiated during the flare as: (i) it is assumed that the full band $1-1000\,$Ryd ionizing luminosity has risen in proportion to the X-ray luminosity, which is unlikely be the case; (ii) the flare luminosity is assumed to remain constant for an extended period, contrary to the usual flaring behaviour. Thus the energy radiated during the flare may be an order of magnitude lower if the flare is short lived, which is likely given its rapid rise during slice D. Even for this maximum case, however, given that only $\sim 10-15\%$ of the radiative energy is deposited in the wind, it is not possible for the subsequent outflow to be purely driven by the radiation pressure provided by the flare alone. The discrepancy between the observed wind kinetic power and the estimated flare contribution is at least an order of magnitude, and probably even larger. Magnetically driven outflows may instead provide an alternative mechanism for the initial driving for such a powerful wind (Ohsuga et al. 2009; Ohsuga & Mineshige 2011; Kazanas et al. 2012; Fukumura et al. 2010, 2015). Alternatively the increased opacity through line driving may also be important in PDS 456 (Hagino et al. 2015) which effectively boosts the transfer of momentum to the wind beyond that expected from Thomson scattering. Thus lower ionization gas within the wind may also play a role in helping to accelerate the outflow.

5.9 Chapter summary

In this chapter I have presented the results based on the initial analysis carried out in Chapter 4. Here I performed a time-dependent spectral analysis focused on the 2013 *Suzaku* observing campaign where I investigated the short-term spectral variability on timescales of $\sim 50-100$ ks observed in the X-ray continuum as well as in the Fe K energy band. The main results for this analysis are summarized below:

1. I have shown that the short term variability of the iron K absorption feature may be attributed to the line of sight variations in the column density (or covering fraction in an X-ray eclipse scenario). It was possible, to infer the size of the absorber to be $\sim 20\,R_{\mathrm{g}}$. Furthermore the size of the X-ray emitting region cannot be larger than this value, given the almost complete obscuration at Fe K seen later in the observation (slice G).

2. Most of the spectral variability during the 2013 low-flux observations can be accounted for by variations in the partially covering (or clumpy) absorber in the line-of-sight. However the strong flare at ~ 400 ks into the observation can only be accounted for by rapid continuum variability.

3. By investigating the properties of the partial covering absorbers, I have found that these absorbers may be the least ionized denser clumpy component of the fast wind detected through the Fe K absorption feature, with typical outflow velocity of $v_{\mathrm{pc}} \sim 0.25c$.

4. By analysing the behaviour of the soft ($0.5 - 1\,\mathrm{keV}$) and hard ($2 - 5\,\mathrm{keV}$) band light curves during the course of the flare. I find that the X-ray emitting corona may be characterized by two components. These consist of "warm", more extended ($\sim 15 - 20\,R_\mathrm{g}$) soft X-ray emitter and a "hot". more compact ($\sim 6 - 8\,R_\mathrm{g}$) corona, where the latter might be responsible for the rapid rise in the hard ($2 - 5\,\mathrm{keV}$) band light curve.

5. I have explored whether the radiation pressure imparted by the flare could deposit enough kinetic power in the outflowing material to drive the wind. I find that the estimated radiative power of the flare was less than the mechanical power measured for the outflow by at least one order of magnitude. This lead to the conclusion that another physical launching mechanism (e.g., magneto-hydrodynamic) is likely to be contributing as well.

6 X-ray flaring in PDS 456 observed in a high-flux state[1]

6.1 Introduction and content of this chapter

In this chapter I present a detailed analysis of the 190 ks (net exposure) *Suzaku* 2007 observation where the intrinsically bare continuum is revealed compared to the subsequent more absorbed *Suzaku* observations carried out in 2011 and 2013 (see Chapter 4 and 5). The rapid variability that is exhibited by PDS 456 during this observation, as well as the relatively clean determination of the primary continuum form, provides an opportunity to study the intrinsic variability mechanism in a high luminosity AGN. The importance of this work lies in the fact that the exact origin of the rapid X-ray variability and coronal changes are not generally well understood in AGN at present, but may be related to magnetic flaring activity in the corona (e.g., Leighly & O'Brien 1997; Di Matteo 1998; Merloni & Fabian 2001; Reeves et al. 2002).

For instance, Legg et al. (2012) measured the different responses of the continuum over broad energy bands to short time-scale flares seen in lower mass Narrow Line Seyfert 1 Galaxies, which were found to show contrasting and complex behaviour. In addition several authors have also parametrized the delayed responses between different energy bands in the form of lag spectra, which may be the result of reverberation delays on short time-scales (e.g., Zoghbi et al. 2010; Kara et al. 2013), but whose exact interpretation is subject to debate (e.g Miller et al. 2010). In PDS 456, the high black hole mass is especially advantageous, as it makes it possible to directly measure the changes in the X-ray spectrum in response to flares over time-scales of tens of ks, which in lower mass AGN are confined to very short time-scales of < 1 ks, precluding a direct spectral analysis.

---

[1] This chapter is partly based on the published work entitled:
'*X-ray flaring and Compton cooling in PDS 456 observed in a high-flux state*'; **G. A. Matzeu**; J. N. Reeves; E Nardini; V. Braito; T. J. Turner; M. T. Costa; 2017, MNRAS, **465**, 2804-2819

All work was conducted by myself unless otherwise stated.

Furthermore, as I introduced in Chapter 1, it is also known that the broadband X-ray spectra of AGN consist of multiple continuum components, being dominated by a soft X-ray excess at energies below 1 keV and a harder power-law like component that emerges at higher energies from a hot corona, possibly via thermal Comptonization (e.g., Haardt & Maraschi 1993). The nature of this two component continuum is still under debate, particularly the form of the soft excess which has been accounted for via Comptonization of UV disc photons by a cooler population of electrons in a multi-temperature corona (e.g Done et al. 2012), but also in terms of relativistically blurred ionized reflection from the inner accretion disc (e.g., Crummy et al. 2006; Nardini et al. 2011; Gallo et al. 2013). In these PDS 456 observations, a further motivation is to study how these soft and hard continuum components evolve across a long observation, where pronounced short-term variability is present.

In this chapter I focus on the broadband spectral variability of PDS 456 on short time-scales, as the 2007 *Suzaku* observation exhibits substantial short-term variability, which for brevity I will refer to as 'flares' hereafter. In this observation several strong individual flares in both the soft and hard X-ray bands are detected. The previous results on this 2007 data set, which focused on the Fe K feature and fast ($\sim 0.3c$) wind, were presented in Reeves et al. (2009). As I will show, the time-sliced spectra from PDS 456 present an overall spectral evolution from hard to soft during the observation, which may be intrinsically associated with Comptonization in a compact corona of $\lesssim 10\,R_{\rm g}$ in extent. Note that I also checked whether the *Suzaku* 2011 observation (which is in the intermediate flux state and shorter in duration) presented a similar short-term spectral variability. The resultant 2011 time-slices did not show any significant short-term spectral variability (they only slightly varied up and down in normalization without any intrinsic changes).

This chapter is organized as follows; in § 6.2 I summarize the data reduction, while in § 6.3 I model the overall optical to hard X-ray SED during the high-flux 2007 *Suzaku* observation, utilizing simultaneous *XMM-Newton* & *NuSTAR* observations at a similar flux level. In § 6.4 I present an initial variability analysis and quantify the overall spectral evolution, while in § 6.5 I present a detailed time-dependent spectral analysis. § 6.6

Parameter	*Suzaku* 2007	*Suzaku* 2013c	*XMM*/ObsB	*NuSTAR*/ObsB
Obs. ID	701056010	707035030	0721010301	60002032004
Start Date, Time (UT)	2007-02-24, 17:58	2013-03-08, 12:00	2013-09-06, 03:24	2013-09-06, 02:56
End Date, Time (UT)	2007-03-01, 00:51	2013-03-11, 09:00	2013-09-07, 10:36	2013-09-07, 10:51
Duration(ks)	370	248.4	112.3	113.9
Exposure(ks)$^{\mathrm{a}}$	190.6	108.3	92.2	85.9
$\mathrm{Flux}^{b}_{(0.5-2)\mathrm{keV}}$	3.46	0.43	2.6	–
$\mathrm{Flux}^{b}_{(2-10)\mathrm{keV}}$	3.55	1.72	2.8	2.9
$\mathrm{Flux}^{b}_{(15-50)\mathrm{keV}}$	5.7 ± 2.2	< 1.97	–	0.89

Table 6.1: Summary of the 2007 and the third 2013 (2013c) *Suzaku* observations of PDS 456 plus the second 2013 (ObsB) *XMM-Newton* & *NuSTAR* observation which are similar in spectral form to the 2007 *Suzaku* observation, for comparison purposes.

[a] Net Exposure time, after background screening and dead-time correction.
[b] Observed fluxes in the 0.5–2 keV, 2–10 keV and 15–50 keV bands in units $\times 10^{-12}$ erg cm^{-2} s^{-1} (1σ upper limits).

discusses the origin of the spectral variability, which is most likely to be the result of changes in the coronal X-ray emission of PDS 456.

6.2 Data reduction

The *Suzaku* 2007 data have been reduced in accordance with the process outlined in § 3.2.4 and the observational details are introduced earlier in § 4.2. The observation is constituted by a single continuous sequence (see Table 6.1 OBSID:701056010, hereafter

2007), with a duration of ~ 370 ks. The details for the 2007 observation are listed in Table 6.1. Reeves et al. (2009) found that the front illuminated XIS-FI CCDs (XIS 0, XIS 3) and the back illuminated XIS-BI XIS 1 spectra are consistent with each other; however in this chapter I focus, for simplicity, on the XIS-FI spectra. They were subsequently merged into a single XIS-FI 03 spectrum, where for the combined spectrum I adopted a minimum grouping of 50 counts per spectral bin in order to adopt the χ^2 minimisation technique. For all subsequent spectral fitting in this chapter, I consider the XIS-FI spectrum between 0.6–10 keV and I remove the 1.7–2.1 keV band when fitting to avoid uncertainties associated with the detector Si K edge.

6.3 Broadband spectral analysis

All the spectral analysis and model fitting were carried out with XSPEC v12.9.0 (Arnaud 1996). Initially I compare the *Suzaku* 2007 spectrum to some of the more recent *XMM-Newton* & *NuSTAR* data that captured the source in a similar flux state. More specifically, Fig. 6.1 shows this comparison where the 2007 *Suzaku* observation and the second sequence (ObsB, hereafter) from the simultaneous *XMM-Newton* & *NuSTAR* campaign, carried out in late 2013 (see Nardini et al. 2015 for details), are shown in black and red respectively. Although the *XMM-Newton* & *NuSTAR* campaign consists of five sequences, the second observation is very similar in flux and photon index to the 2007 *Suzaku* observation, as measured in the 2–8 keV rest-frame band (e.g., *XMM-Newton* & *NuSTAR* ObsB $\Gamma_{2-8} = 2.24 \pm 0.03$ versus *Suzaku*, $\Gamma_{2-8} = 2.25 \pm 0.03$). Indeed the only difference is a slight offset of $\sim 20\%$ in flux, due to the *Suzaku* observation being slightly brighter. In Fig. 6.1 I also show for comparison the last *Suzaku* sequence from the large campaign consisting of three observations in 2013 (as discussed in detail in Chapter 5), carried out approximately six months prior to the *XMM-Newton* & *NuSTAR* observation. In contrast to the 2007 *Suzaku* observation, in 2013 *Suzaku* caught PDS 456 at a considerably lower flux, where the third sequence (2013c hereafter) has the lowest flux state to date and is much harder in shape (see Chapter 4). The relative fluxes for these 2007 and 2013c

Suzaku observations, as well as the *XMM-Newton* & *NuSTAR* (ObsB) observation are also summarized in Table 6.1.

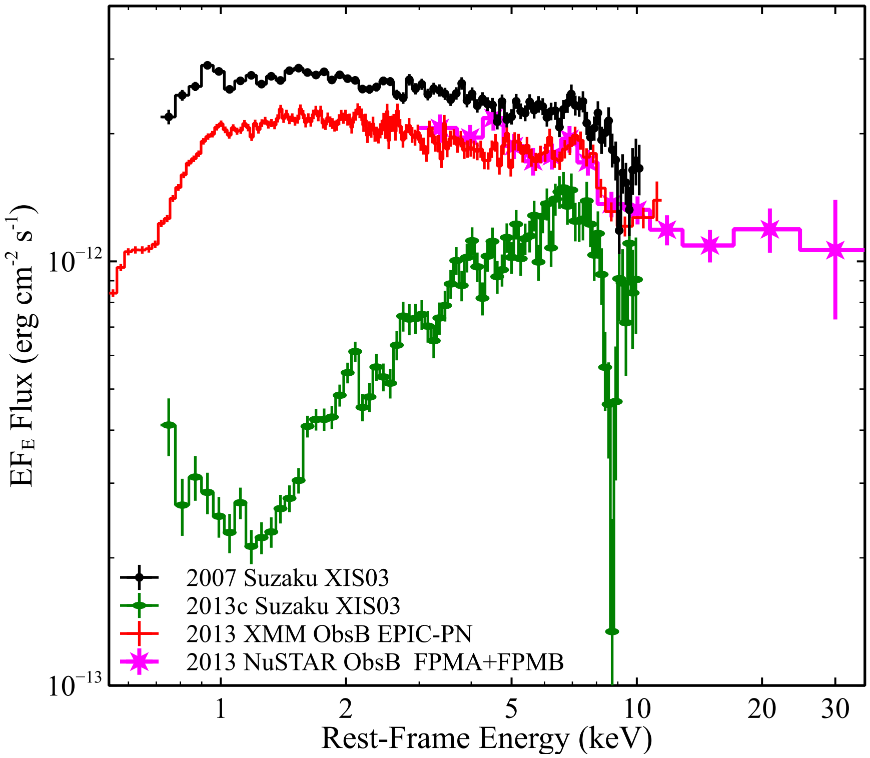

Figure 6.1: XIS spectra of the 2007 *Suzaku* observation (black). For comparison, the 2013 ObsB spectra of the *XMM-Newton* & *NuSTAR* campaign (red and magenta respectively), together with the 2013c (green) *Suzaku* spectrum, are also shown. Through a visual inspection, the 2007 and ObsB spectra are remarkably similar in shape. Overall, the long-term spectral variations in the soft band and in the iron-K region, which characterize this type 1 quasar, are conspicuous. Note that the spectrum becomes harder and more absorbed during the lower flux 2013 *Suzaku* observation. The spectra were unfolded against a simple $\Gamma = 2$ power law and are not corrected for Galactic absorption.

During the 2007 *Suzaku* observation (Reeves et al. 2009), PDS 456 was observed with little obscuration, which revealed a steep intrinsic continuum ($\Gamma > 2$) as evident in Fig. 6.1. The comparable characteristics between the 2007 *Suzaku* and ObsB spectra are also illustrated in Fig. 6.1. Note that as the HXD detection gives a large uncertainty on the hard X-ray ($> 10\,\mathrm{keV}$) flux, due to the large systematics of the HXD/PIN background subtraction (Reeves et al. 2009), I adopted the *NuSTAR* data instead in order to characterize the broadband spectrum. The imaging characteristics of the FPMA and FPMB detectors provide a much more reliable measurement of the spectrum above 10 keV. Thus, the *NuSTAR* observations do not show any evidence of a strong hard X-ray excess (also see Nardini et al. 2015) and are consistent with a simple extrapolation of the steep power-law to high energies.

6.3.1 Modelling the broadband SED

I now attempt to characterize the broadband SED of PDS 456 in this high-flux (unabsorbed) state. In particular, I tested whether the broadband SED could be described by a multi-temperature Comptonized accretion disc model, using the `optxagnf` model (Done et al. 2012, also described in § 3.4.2) in XSPEC. In this analysis, for simplicity, the spin parameter `a`* was kept fixed at zero in all the `optxagnf` fits, noting that the subsequent spectral parameters are not strongly dependent on the black hole spin.

The form of the optical/UV to hard X-ray SED has been defined by using a combination of both *XMM-Newton* & *NuSTAR* ObsB spectra, as previously shown in Fig. 6.1, which are in a similar form in the X-ray band to the *Suzaku* 2007 spectrum. Thus I adopted the optical/UV *XMM-Newton* optical monitor (OM) and the *NuSTAR* data (above 10 keV) associated with ObsB sequence together with the *Suzaku* data. I also included a cross-normalization constant between the *NuSTAR* and *Suzaku* spectra, to allow for a small offset in flux, which was found to be 0.80 ± 0.10. It is important to note that when I make use of the optical/UV photometry, although the optical/UV fluxes are not simultaneous, there appears to be little variability in this band as observed from all the *XMM-Newton* OM observations from 2007 to 2014 inclusive (to $\lesssim 20\%$), as shown in Fig. 6.2.

In order to fit the SED with the `optxagnf` model, I included the effect of Galactic absorption in the X-ray band and also corrected the OM data points for reddening based on the standard Cardelli, Clayton & Mathis (1989) extinction law, with A(V) and

Component	Parameter	*Suzaku* XIS03 2007
`Tbabs`*	$N_{\rm H,Gal}/{\rm cm}^{-2}$	2.0×10^{21}
`optxagnf`	$\log(L/L_{\rm Edd})$	$-0.13^{+0.11}_{-0.12}$
	${\rm r_{cor}}$ (${\rm R_g}$)	38^{+43}_{-28}
	${\rm kT_e}$ (eV)	292^{+32}_{-20}
	τ	$12.4^{+1.2}_{-1.4}$
	Γ	$2.31^{+0.06}_{-0.04}$
	${\rm F_{pl}}$	$0.08^{+0.02}_{-0.03}$
`pc`	$\log(N_{\rm H,low}/{\rm cm}^{-2})$	$23.1^{+0.1}_{-0.3}$
	${\rm f_{cov}}$	0.15 ± 0.07
${\rm Gaussian_{em,Fe\,K}}$	Energy (keV)$^{\rm a}$	$7.07^{+0.15}_{-0.14}$
	norm^b	3.89 ± 1.84
	σ (eV)	260^{+239}_{-118}
	EW (eV)	88^{+41}_{-42}
${\rm Gaussian_{abs,Fe\,K}1}$	Energy (keV)$^{\rm a}$	$9.07^{+0.05}_{-0.06}$
	norm^b	$-2.48^{+1.21}_{-0.93}$
	σ (eV)	< 160
	EW (eV)	105^{+51}_{-40}
${\rm Gaussian_{abs,Fe\,K}2}$	Energy (keV)$^{\rm a}$	$9.54^{+0.09}_{-0.08}$
	norm^b	$-1.88^{+0.89}_{-1.03}$
	σ (eV)	$< 160^{\rm t}$
	EW (eV)	94^{+45}_{-52}
${\rm Gaussian_{em,soft}}$ 1	Energy (keV)$^{\rm a}$	$0.93^{+0.02}_{-0.03}$
	norm^b	$125.7^{+101.5}_{-54.6}$
	σ (eV)	45^{+27}_{-25}
	EW (eV)	24^{+8}_{-7}
${\rm Gaussian_{em,soft}}$ 2	Energy (keV)$^{\rm a}$	1.15 ± 0.02
	norm^b	$18.8^{+0.9}_{-1.0}$
	σ (eV)	10^*
	EW (eV)	7^{+4}_{-3}
	$\chi^2_\nu = 910/802$	

Table 6.2: `optxagnf` best-fit parameters for the *Suzaku* 2007 observation. $^{\rm t}$ denotes that the parameter is tied during fitting, * indicates a parameter fixed during fitting.

${\rm L/L_{Edd}}$: Eddington ratio,
${\rm r_{cor}}$ radius of the X-ray corona in ${\rm R_g}$,
${\rm F_{pl}}$: fraction of the dissipated accretion energy emitted in the hard power-law,
`pc`: partial covering component with respective column density and covering fraction,

[a] rest-frame energy of the emission and absorption Gaussian profiles,
[b] Gaussian emission and absorption profile normalization, in units of 10^{-6} photons cm^{-2} s^{-1}. Note that here, for simplicity, the spin parameter `a`* was kept fixed to zero in all the `optxagnf` fits.

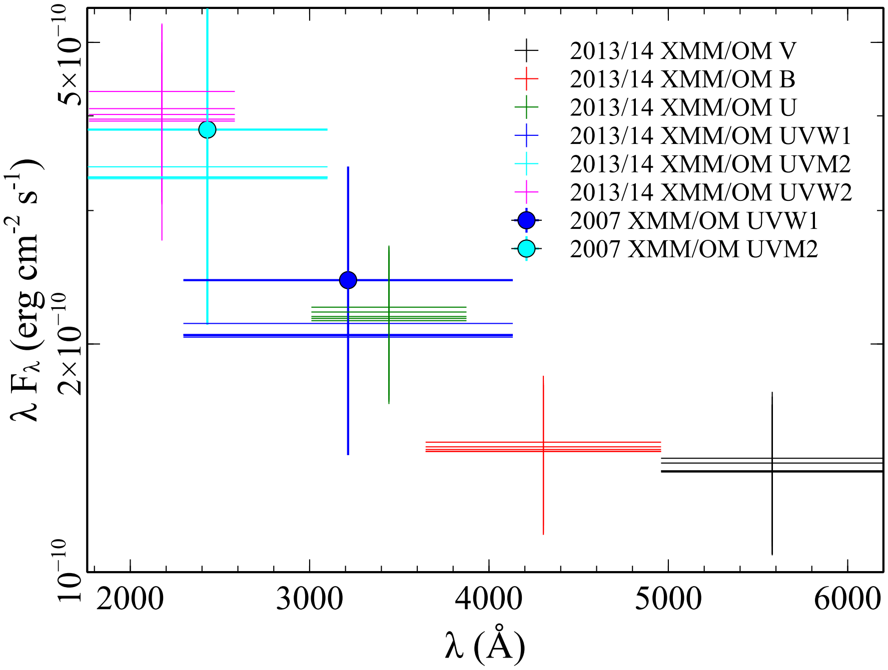

Figure 6.2: The *XMM-Newton* OM photometric data of PDS 456 taken between 2007 and 2014. Overall only small changes are observed in the optical/UV band, typically of the order of 5–20% and are consistent within the uncertainties. Thus, when constructing the optical to hard X-ray SED, I can adopt the OM data from ObsB regardless of the fact that they are non simultaneous with the 2007 *Suzaku* observation.

E(B–V) values relevant to the source (Simpson et al. 1999; O'Brien et al. 2005). Overall, the `optxagnf` model reproduced well the shape of the UV bump, the soft excess and the hard X-ray power-law component. The overall SED and best fit `optxagnf` model are shown in Fig. 6.3. I note that, in contrast to the 2013 *Suzaku* campaign where PDS 456 appeared highly absorbed (see Chapter 4), there is no prominent spectral curvature above 1 keV (see Fig. 6.4 top panel). Thus, it was possible to achieve an acceptable fit, with $\chi^2/\nu = 916/804$, without the inclusion of any absorbers. Adding some absorption to the broadband SED leads to a very marginal improvement, $\Delta\chi^2/\Delta\nu = 6/2$ to the fit, shown in Fig. 6.4 (bottom panel). Thus in 2007, the degree of absorption is minimal when parametrized with one layer of a neutral partial coverer (`zpcfabs`) of column density $\log(N_{\rm H}/{\rm cm}^{-2}) = 23.1^{+0.1}_{-0.3}$, as then the covering fraction is very low with $f_{cov} = 0.15 \pm 0.07$.

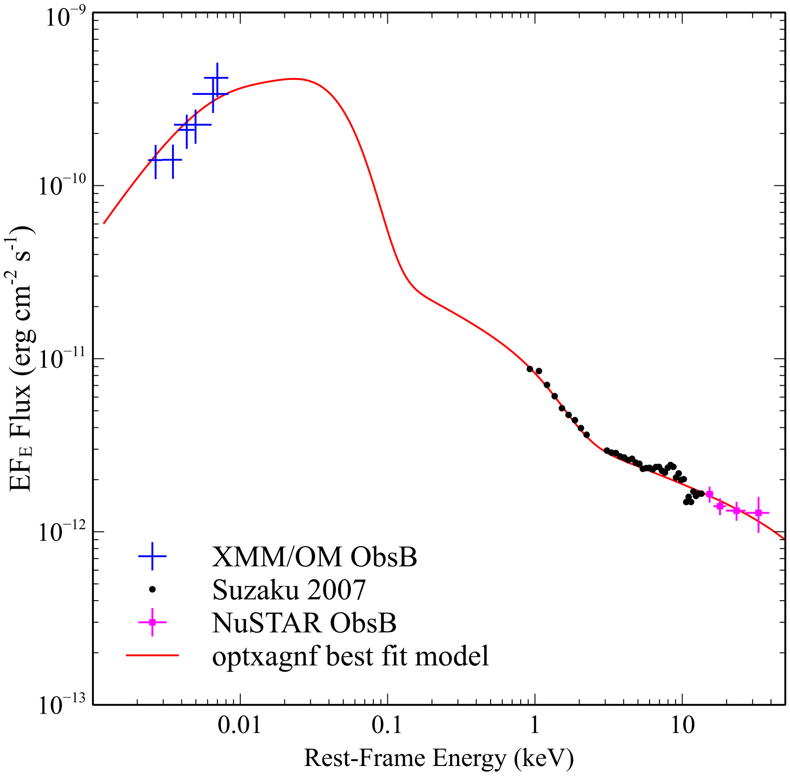

Figure 6.3: Optical to hard X-ray spectral energy distribution (SED) of PDS 456 obtained by combining the OM and *NuSTAR* data (blue and magenta respectively) from the *XMM-Newton/NuSTAR* observation in 2013 (ObsB) and the 2007 time-averaged spectrum from the *Suzaku* campaign (black). For clarity, the NuSTAR data is only plotted above 10 keV. The SED was fitted with the `optxagnf` model (red solid line). Note that the model is corrected for absorption (either Galactic or local to the source), the OM data has been dereddened as is described in § 6.3.1 while the X-ray data have been corrected for a Galactic absorption column of $2.0 \times 10^{21}\,{\rm cm}^{-2}$.

Nonetheless, the `optxagnf` best-fit parameters of the 2007 data are similar to what was found in the highly absorbed 2013 *Suzaku* spectrum, once the latter is corrected for absorption. In the 2007 data, the coronal size is found to be $r_{\rm cor} = 38^{+43}_{-28}\,R_{\rm g}$ and the optical depth is $\tau = 12.4^{+1.2}_{-1.4}$. The temperature of the warm electrons, responsible for the

Comptonized soft excess, is $kT = 292^{+32}_{-20}$ eV, whilst the fraction of energy released in the power-law is found to be $\mathrm{F_{pl}} = 0.08^{+0.02}_{-0.03}$. The Eddington ratio of $\log(\mathrm{L/L_{Edd}}) = -0.13^{+0.11}_{-0.12}$ implies that PDS 456 radiates close to its Eddington luminosity ($\sim$ 80% of $L_{\rm Edd}$). This is consistent with what was found in Chapter 4 and with the expectation of a high accretion rate for PDS 456, given its black hole mass ($\sim 10^9\,M_\odot$) and high bolometric luminosity of $L_{\rm bol} \sim 10^{47}\,\mathrm{erg\ s^{-1}}$ (Simpson et al. 1999; Reeves et al. 2000). The X-ray spectral shape is also consistent with what was found in Reeves et al. (2009) and previously in Chapter 4 with a best fit photon index of $\Gamma = 2.31^{+0.06}_{-0.04}$ (see Table 6.2 for more details). Thus, the high-flux 2007 SED of PDS 456 reveals the bare AGN continuum, which can be consistently fitted by disc/coronal models.

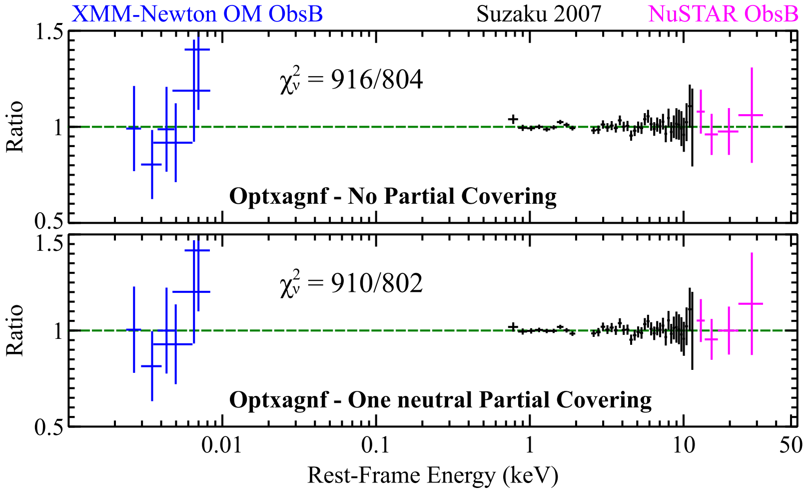

Figure 6.4: Residuals for the different `optxagnf` model fits over the 1 eV–50 keV rest-frame energy range, plotted as data/model ratios. The spectra correspond to the *XMM-Newton* OM (blue) and *NuSTAR* from ObsB in 2013 (magenta) respectively, while also plotted is the *Suzaku* 2007 (black) time-averaged spectrum with the Galactic absorption included. The various Gaussian emission and absorption lines, as described in § 6.3.1, have been included in the model. Top panel: SED fits with `optxagnf` and no partial covering absorption. Bottom panel: Same as above but with the addition of one neutral partial covering layer. There is no apparent difference between the two cases, with little intrinsic absorption required in the high-flux data. For extra clarity, the *Suzaku* and *NuSTAR* spectra have been re-binned by a factor of 4 and 8 respectively.

In Reeves et al. (2009), the Fe K absorption profile was resolved into two components at $E \sim 9.1$ keV and $E \sim 9.6$ keV that could be associated with He and H-like iron with two offset outflow velocities. Here, as I changed the parametrization of the underlying continuum, I checked the consistency of these absorption features. Following the same approach as in Reeves et al. (2009), the Fe K absorption is fitted with two (cosmologically redshifted) Gaussian components at rest-frame energies of $E = 9.07^{+0.05}_{-0.06}$ keV and $E = 9.54^{+0.09}_{-0.08}$ keV. As per Reeves et al. (2009), I also adopted three further Gaussian components to parameterise the ionized emission profile at $7.07^{+0.15}_{-0.14}$ keV (in the quasar rest frame), and two soft X-ray emission lines with the stronger at $E = 0.93^{+0.02}_{-0.03}$ keV and the weaker at $E = 1.15 \pm 0.02$ keV. These five lines are consistent with what was found in Reeves et al. (2009) and Reeves et al. (2014) and for completeness I tabulate them in Table 6.2. The residuals of the emission (square/red arrows) and absorption (circle/blue arrows) lines are shown in Fig. 6.5 where the *Suzaku* 2007 time-averaged spectrum was plotted as a ratio to the `optxagnf` model. As discussed earlier in Chapter 4 and in Reeves et al. (2016), the emission lines may represent the re-emission that occurs from the outflow in PDS 456, as seen in the Fe K band and measured in the soft X-ray grating spectra with the *XMM-Newton* Reflection Grating Spectrometer (RGS). Indeed Reeves et al. (2016) identified the above soft X-ray line features with a blend of recombination emission from primarily O VIII, Ne IX and Ne X. These emission lines were especially prominent in the lower flux observations when the AGN was more absorbed and also when the broad absorption profiles from the wind were revealed near to 1 keV.

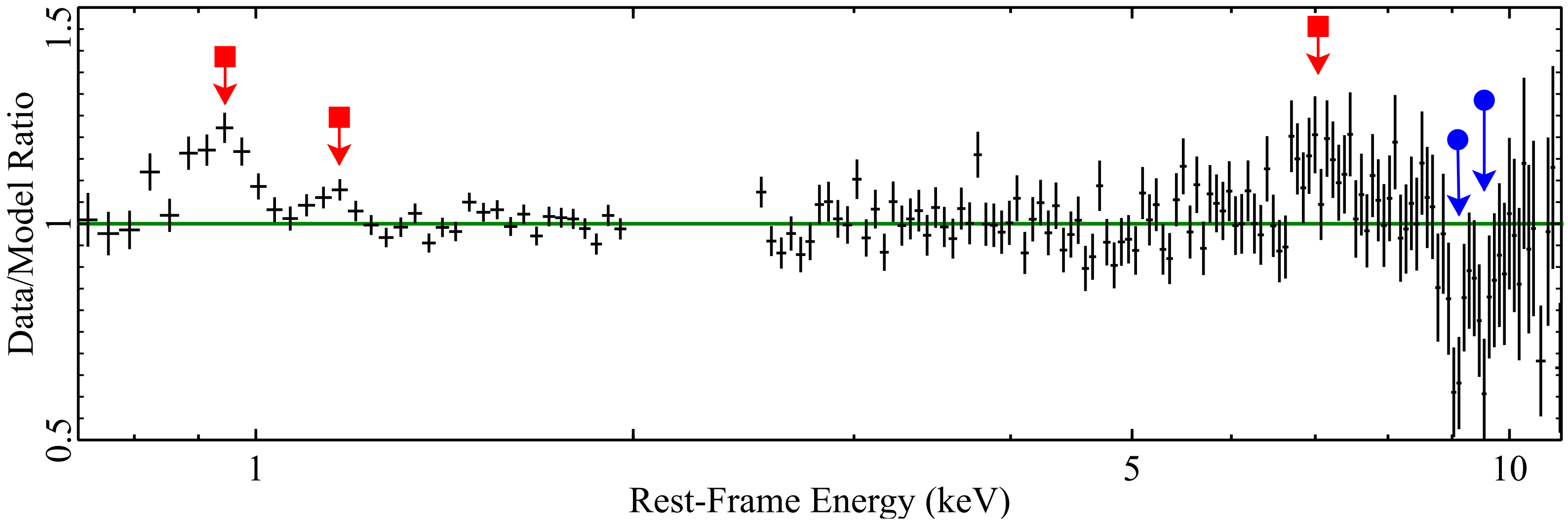

Figure 6.5: Data to model ratio, compared to the best-fit `optxagnf` model, plotted for the time-averaged *Suzaku* 2007 XIS03 spectrum between the rest-frame energy of 0.7–11 keV showing the residual emission and absorption lines where their positions are indicated by the square/red and circle/blue arrows respectively. The positions of these lines features are consistent with those originally reported in Reeves et al. (2009).

6.4 Temporal behaviour

Having parametrized the broadband 2007 high-flux spectrum of PDS 456, here our primary aim is to characterize the variability of PDS 456 during this observation. Initially, I extracted the light curves corresponding to different energy bands, and their behaviour was subsequently compared.

6.4.1 Description of the light curves and softness ratios

In Fig. 6.6 (Panel 1) I plot the overall broadband light curve between 0.5–10 keV of the 2007 *Suzaku* observation of PDS 456, and according to the overall behaviour, I define six distinct slices. Slice A, between 0–45 ks, corresponds to a first minor flare, which is followed by a quiescent period, between 45–120 ks, denoted as slice B. Between 120–170 ks into the observation, a second minor flare is detected (slice C), followed again by a quiescent state (slice D), between 170–255 ks, where the observation reaches its lowest flux at ~ 210 ks. Towards the end of the observation, a first major flare of ~ 55 ks in duration is detected between 255–310 ks (slice E), followed by a second major flare of ~ 60 ks, between 310–370 ks (slice F). Moving to narrower energy bands, the 0.5–1 keV soft band light curve plotted in Fig. 6.6 (P.2) is completely dominated by two flares at the end of the observation; whereas in the 5–10 keV hard band light curve (Fig. 6.6 P.4) I detect two prominent flares only in the first half of the observation. Thus the soft band flares (slices E and F) are not evident at all in the hardest 5–10 keV band and likewise, the hard band flares (slices A and C) are not present in the softest 0.5–1 keV band. On this basis, I can differentiate between two soft and two hard events across the entire observation. Interestingly in the 2–5 keV band light curve (Fig. 6.6 P.3) I observe both sets of these separate (soft and hard) events. This indicates a two component behaviour with distinct variability in the soft and hard bands, the physical implications of which will be discussed later in § 6.5.3.

After extracting the light curves in the above energy bands, I computed the corresponding normalized softness ratios (NSR hereafter) defined mathematically as

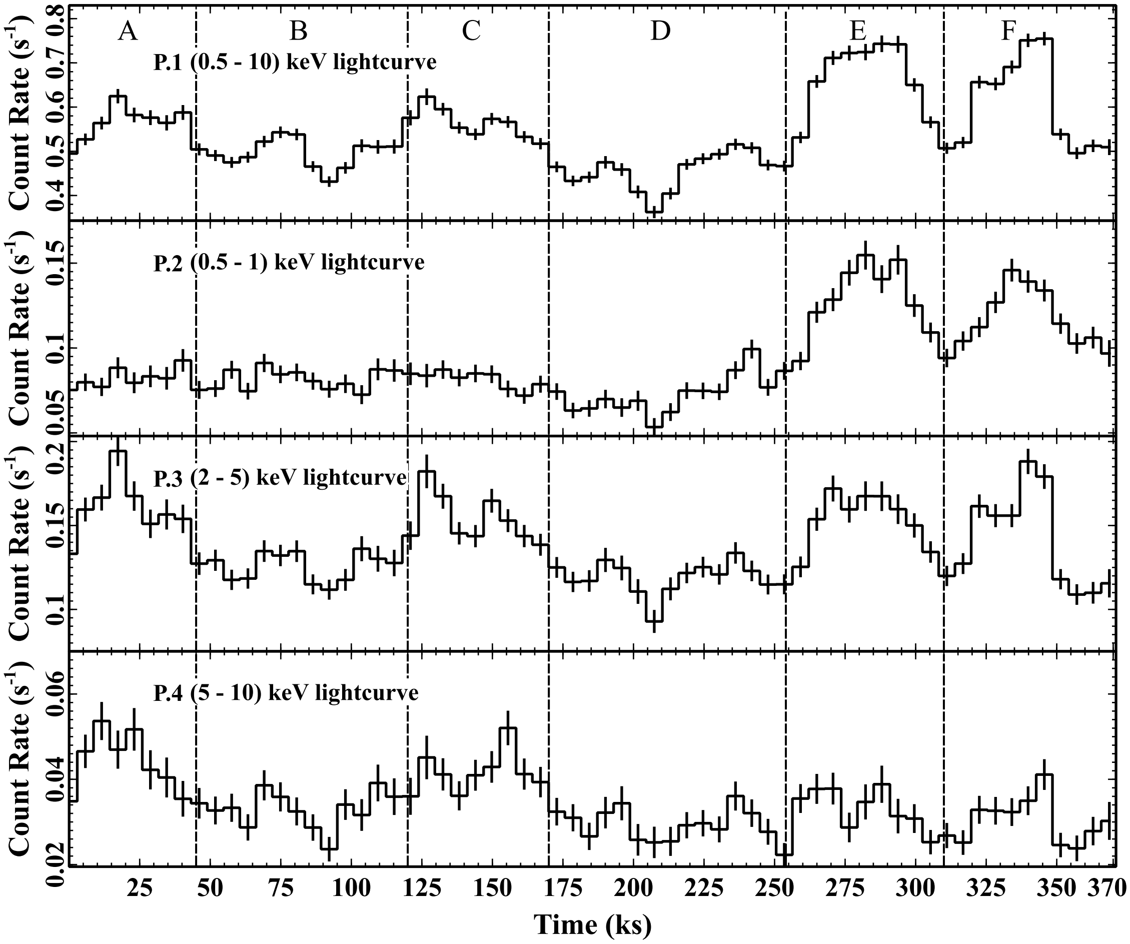

Figure 6.6: Plots showing the light curves extracted in different energy bands revealing some distinct behaviours. The two extremes are seen in the soft band (0.5–1 keV) and in the hard band (5–10 keV) where in the former I see two prominent flares only detected towards the end of the observation, whereas in the latter I observe two distinct flares confined to the first half of the observation. In the broadband (0.5–10 keV) and in particular the middle band (2–5 keV) both sets of events are visible (see text for more details). The bin size of the light curves are 5760 s, corresponding to one satellite orbit.

NSR = $\frac{\mathrm{SR(t)}-\langle\mathrm{SR}\rangle}{\langle\mathrm{SR}\rangle}$, showing the fractional change in the softness ratio between two energy bands when compared to the mean value. The 0.5–1 /2–5 keV, the 0.5–1 /5–10 keV and the 2–5 /5–10 keV NSRs are plotted in Fig. 6.7. By inspecting all the three NSRs it is revealed, particularly in Fig. 6.7 (P.1) and (P.2), that in the first half of the observation the source is dominated by hard photon counts. On the other hand, at ~ 170 ks into the observation, the source becomes progressively softer, reaching its peak towards the end. Thus these three NSR plots confirm that the hardening of the spectrum coincides with the hard events, seen earlier in Fig. 6.6 (P.4), and also indicate that the gradual softening of the source starts before the soft flares are detected (see Fig. 6.6 P.2).

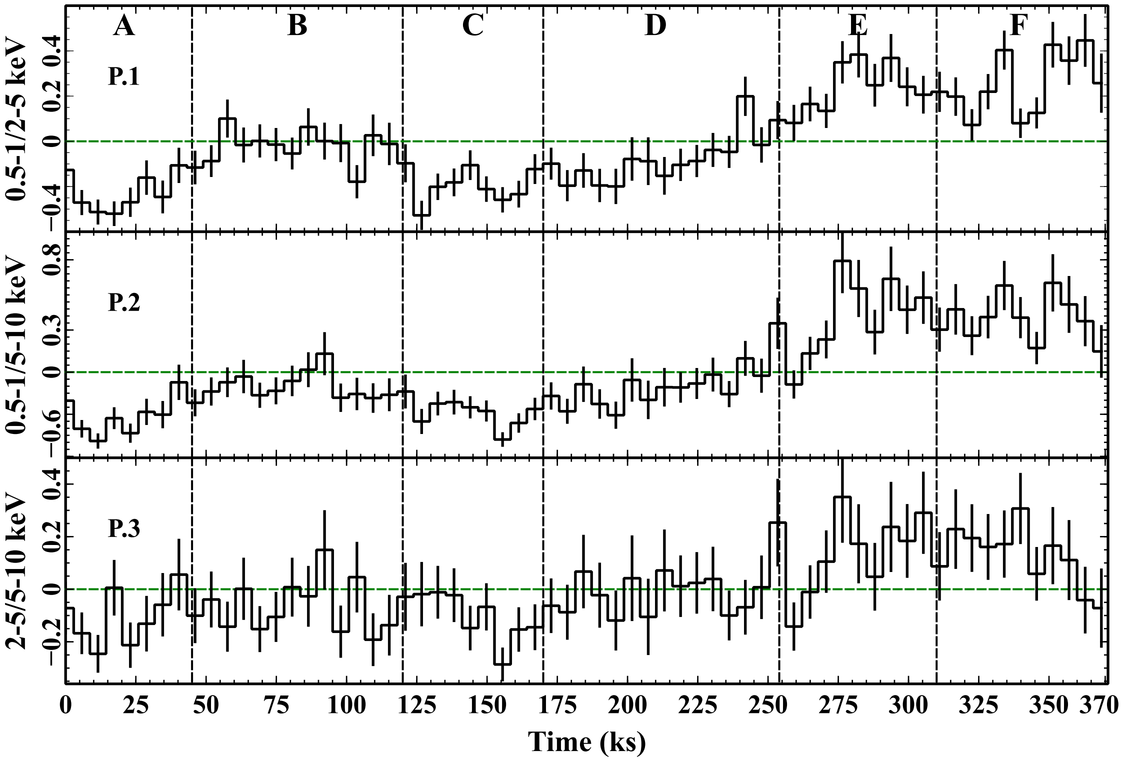

Figure 6.7: The normalized softness ratios (NSR) defined mathematically as NSR $= \frac{\mathrm{SR(t)} - \langle \mathrm{SR} \rangle}{\langle \mathrm{SR} \rangle}$, where SR is the softness ratio between the respective energy bands. Note that positive and negative values correspond to the respective softening and hardening of the source with respect to the average spectral state. The dashed vertical lines identify the boundaries of the six individual slices.

In order to analyse the flares observed in both the hard and soft bands, I focused on the corresponding 0.5–1 keV and 5–10 keV light curves. As described above, during the latter part of the observation I detect an increase of the soft X-ray flux by a factor of ~ 3.5, starting at $\sim 200\,\mathrm{ks}$ into the observation and peaking during the flare in slice E over a duration of $\Delta t_{\mathrm{soft}} \sim 90\,\mathrm{ks}$. On the other hand, the hard X-ray flux shows an increase by a factor ~ 2.5 between $\sim$ 90–160 ks ($\Delta t_{\mathrm{hard}} \sim 70\,\mathrm{ks}$). The doubling time for both the soft and the hard band is $t_{\mathrm{double}} \sim 50\,\mathrm{ks}$. This corresponds to an X-ray emission region size of about $\sim 10\,R_{\mathrm{g}}$ for PDS 456. Note that this is also consistent with the earlier `optxagnf` disc plus corona model representation, where the lower limit of the coronal size was found to be $r_{\mathrm{cor}} \gtrsim 10\,R_{\mathrm{g}}$ (see § 6.3.1 and the estimates of coronal sizes in § 5.8).

6.4.2 Flux-flux analysis

In order to examine further how the different energy bands interact with one another, I specifically investigated the correlation between the flux (in terms of count rate) in the soft and the hard bands. On the basis of what I observed in the light curves and NSRs, I initially investigated the flux-flux distribution between the 0.5–1 keV and 5–10 keV bands (plotted in Fig. 6.8) where the corresponding spectral states are clearly labelled. Within this distribution, I note that the soft flares (E, F), hard flares (A, C) and quiescent periods (B, D), lie in three distinct areas of the plots, with substantial overlap between each of the companion slices, e.g. between the soft flares E and F slices. Therefore given the similar behaviour between the hard flares, soft flares and quiescent periods, the A + C, E + F and B + D segments were separately combined to form single hard flare, soft flare and quiescent spectra respectively. This additional grouping was also done in order to achieve a higher signal-to-noise ratio (S/N) and it was adopted in the subsequent time-sliced spectral fitting in § 6.5.

In Fig. 6.9, I show three flux-flux plots corresponding to: 0.5–1 keV (soft band) versus 2–5 keV (mid-flux) in panel (a), 0.5–1 keV versus 5–10 keV (hard band) in panel (b) and 2–5 keV versus 5–10 keV in panel (c). Here as above the respective data were grouped into the hard flare (black), soft flare (green) and quiescent periods (red). Furthermore in order to increase the S/N, the data were binned to two-orbital size (11520 s). Subsequently, I computed the linear regression fits (in the form of $y = mx + C$) to the respective

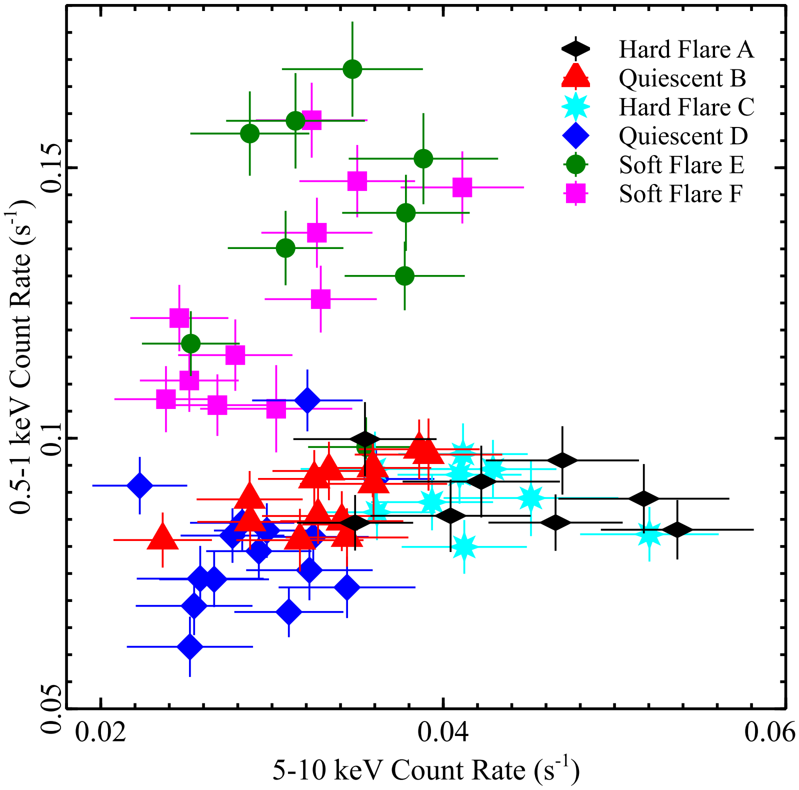

Figure 6.8: Flux-Flux plot for PDS 456 between 5–10 keV and 0.5–1 keV where the distributions of the individual six slices are clearly labelled. The hard flare (A + C), soft flare (E + F) and quiescent (B + D) slices fall on distinct portions of the flux-flux plot, with little overlap between them. Each point on the plot corresponds to one orbital bin (5760 s) during the observation.

segments performed through the bivariate correlated errors and intrinsic scatter algorithm (BCES, Akritas & Bershady 1996)[2] and tabulated in Table 6.3. What emerges from all three flux-flux plots is that the three individual segments behave rather distinctively when compared with one another. In particular, Fig. 6.9 (a) and (b) emphasize how the flux-flux distribution in the hard flares largely follows an almost constant relation with a very small gradient (see Table 6.3 for values), with little rise in the soft flux compared to the mid and hard flux bands, strongly suggesting that the increase in flux is completely

---

[2] This is one of the most common methods that takes into account errors in both x and y values.

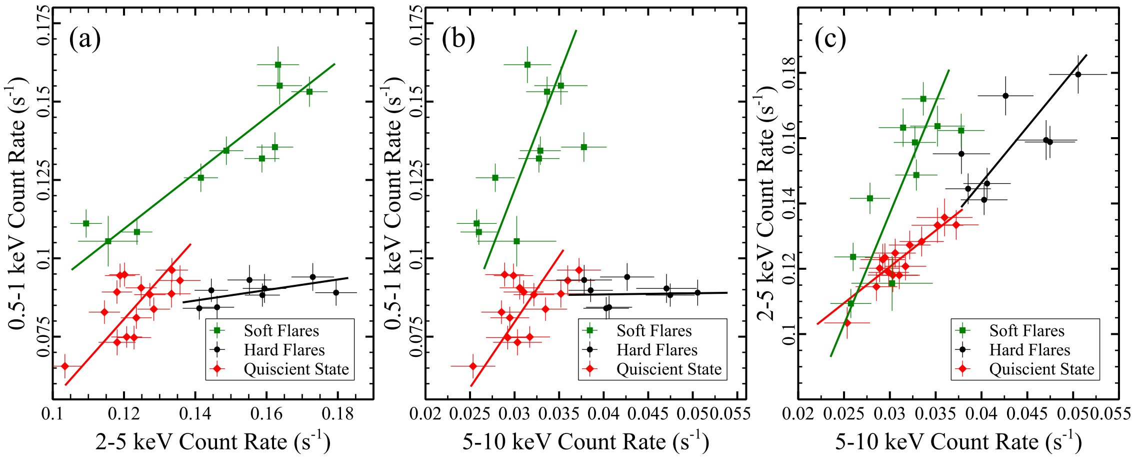

Figure 6.9: Flux-flux plots for PDS 456 showing how the behaviour of the three segments are remarkably distinct. Panel (a): soft flux (0.5–1 keV) against the mid flux (2–5 keV). Panel (b): the soft flux against the hard flux (5–10 keV). Panel (c): mid-flux flux against the hard flux. The three distinct grouped segments are plotted together in each panel showing the hard flares (black), quiescent (red) and the soft flares (green) where the corresponding best fit linear regression lines obtained separately are shown as solid lines respectively. The overall binning of the data is 2× the orbital time (i.e., 11520 s) in order to improve the S/N ratio. The results of the linear correlations are listed in Table 6.3.

dominated by the hard band. On the other hand, the soft flares distribution shows the opposite behaviour, with a very steep relation between the 0.5–1 keV vs 5–10 keV flux. This reaffirms the behaviour seen in the light curves, where there is a considerably greater increase in soft flux compared to the hard band in the last part of the *Suzaku* observation at $t > 250$ ks. The behaviour of the quiescent period is intermediate between the soft and hard flares.

The behaviour of the three segments in the flux-flux plot between the 2–5 and 5–10 keV energy band is not immediately apparent. Fig. 6.9 (c) reveals that the hard flares distribution appears to be an extension of the quiescent, as they are characterized by a comparable gradient ($m_{\text{hard flare}} = 3.4 \pm 0.9$ and $m_{\text{quiescent state}} = 2.2 \pm 0.4$), whereas the soft portion distribution is again steeper ($m_{\text{soft flare}} = 6.8 \pm 1.6$). Furthermore, these energy ranges provide more of a description of the behaviour of the power-law photon

Panel	(x, y)	BCES Linear regression	Grouped segments		
		$y = mx + C$	Soft Flares	Quiescent	Hard Flares
(a)	2–5 keV vs 0.5–1 keV	m	0.89 ± 0.14	1.28 ± 0.32	0.168 ± 0.096
		C	0.0026 ± 0.0019	-0.073 ± 0.039	0.063 ± 0.015
(b)	5–10 keV vs 0.5–1 keV	m	7.36 ± 2.59	4.19 ± 1.50	0.037 ± 0.014
		C	-0.099 ± 0.081	-0.046 ± 0.045	0.087 ± 0.023
(c)	5–10 keV vs 2–5 keV	m	6.80 ± 1.63	2.22 ± 0.38	3.41 ± 0.91
		C	-0.067 ± 0.051	0.054 ± 0.012	0.010 ± 0.038

Table 6.3: Gradients and intercepts evaluated from the BCES linear regression fits corresponding to each segment plotted in Fig. 6.9 (a)–(c). From these values it is evident that the three segments behave distinctively. See text for more details.

index, where a steeper Γ would correspond to a higher 2–5/5–10 keV ratio. The steepness of the soft flare portion of the flux-flux plot compared to the other two, is consistent with an increase in photon index corresponding to the soft flares. The origin of the contrasting spectral behaviour of the soft, hard and quiescent segments will be discussed in detail in the next section.

6.5 Time dependent spectral analysis

Previously in § 6.3.1 I used the `optxagnf` model to account for the broadband optical/UV to hard X-ray SED of PDS 456. In order to describe the lower S/N time-sliced 2007 *Suzaku* spectra over the 0.6–10 keV band, I adopted a simpler two component model, in the form of a low energy blackbody plus a power law, to provide a more convenient parametrization of the intrinsic continuum. Although not physically motivated, the blackbody component here is a proxy for the cooler Comptonized emission responsible for the soft excess, as described by the `optxagnf` model. In particular, and similar to

Chapter 5, I want to test whether the broadband spectral variability is mainly produced by either (i) rapidly varying partial covering absorption, while the intrinsic continuum parameters are assumed to vary together in normalization, through the same scale factor, throughout the segments, or (ii) variations in the intrinsic shape of the continuum, such as the power law and soft excess.

6.5.1 Partial covering changes

In the first scenario, the presence of compact clouds of gas reprocess the X-ray photons by partially absorbing the AGN emission, allowing a fraction $(1 - f_{\mathrm{cov}})$ to emerge unattenuated. Previous studies of other AGN have found that these clouds can have a typical size-scale comparable to the X-ray emitting region, i.e. of the order of few tens of R_{g} (e.g., Risaliti et al. 2007). The motivation behind this model is testing whether the observed change in flux (see Figs. 6.8 and 6.9) that defines the three main spectral portions is the direct result of the presence of variable absorbers crossing the line-of-sight. The partial covering variability successfully explained the changes observed in the *Suzaku* 2013 campaign of PDS 456, when the source spectrum was much harder, although substantial intrinsic variability was also present (see § 5.4.1 and § 5.6). One interesting possibility is whether the harder portions of the 2007 observations could be explained by an increase in the absorber's covering fraction. Thus I constructed a *partial covering changes* model of the form:

$$\begin{aligned} \texttt{Tbabs} \times [\texttt{zpcfabs}_{\mathrm{low}} \times \texttt{zpcfabs}_{\mathrm{high}} \times (\texttt{po} + \texttt{bbody}) + \texttt{zgauss}_{\mathrm{em,soft}} \\ + \texttt{zgauss}_{\mathrm{em,FeK}} + \texttt{zgauss}_{\mathrm{abs,FeK}}] \end{aligned} \tag{6.1}$$

where `Tbabs` (Wilms, Allen & McCray 2000) accounts for the Galactic absorption column density $N_{\mathrm{H}} = 2 \times 10^{21}$ cm^{-2}. I apply this model to the three combined segments (A + C, B + D and E + F). For completeness, I adopted a Gaussian component ($\texttt{zgauss}_{\mathrm{abs,FeK}}$) to parametrize a single (due to the lower S/N present in the segments) iron K absorption profile with best-fit centroid rest-frame energy at $E = 9.26^{+0.16}_{-0.14}$ keV and with equivalent

		Slice A + C	Slice B + D	Slice E + F
power law	Γ	$2.45^{+0.05}_{-0.04}$	2.45^{t}	2.45^{t}
	$\mathrm{norm}^{\mathrm{a}}_{\mathrm{po}}$	$4.14^{+0.42}_{-0.38}$	2.85 ± 0.16	$2.87^{+0.23}_{-0.29}$
Blackbody	kT (eV)	100^{*}	100^{t}	100^{t}
	$\mathrm{norm}^{\mathrm{b}}_{\mathrm{bb}}$	8.42	5.80	5.85
`pc`$_{\mathrm{low}}$	$\log(N_{\mathrm{H,low}}/\mathrm{cm}^{-2})$	21.5 ± 0.2	21.5^{t}	21.5^{t}
	$\mathrm{f}_{\mathrm{cov,low}}$	$0.57^{+0.18}_{-0.09}$	$0.37^{+0.13}_{-0.07}$	< 0.12
`pc`$_{\mathrm{high}}$	$\log(N_{\mathrm{H,high}}/\mathrm{cm}^{-2})$	$23.2^{+0.3}_{-0.1}$	23.2^{t}	23.2^{t}
	$\mathrm{f}_{\mathrm{cov,high}}$	0.34 ± 0.05	0.22 ± 0.06	< 0.17
	$\mathrm{Flux}^{\mathrm{c}}_{0.5-2}$	3.09	2.84	4.18
	$\mathrm{Flux}^{\mathrm{d}}_{2-10}$	4.19	3.16	3.56
Model Statistic	$(\chi^2/\nu)^{\mathrm{e}}$	334/349	514/485	471/449
	$\mathrm{N.P.}^{\mathrm{f}}$	0.71	0.17	0.22
	Best Fit Statistic	$\chi^2/\nu = 1320/1313$		

Table 6.4: *Partial covering changes* parameters for the three *Suzaku* XIS 2007 combined segments. Here the spectral changes are accounted by the variability of the partial coverer covering fractions. The power-law and blackbody are varying together by the same scale factor throughout the segments. $^{\mathrm{t}}$ denotes that the parameter is tied during fitting, * indicates a parameter fixed during fitting.

[a] Power-law normalization, in units of 10^{-3} ph keV^{-1} cm^{-2} s^{-1},
[b] blackbody normalization in units of 10^{-5} (L_{39}/D_{10}^2), where L_{39} is source luminosity in units of 10^{39} erg s^{-1} and D_{10} is the distance to the source in units of 10 kpc,
[c] overall absorbed flux, between 0.5–2 keV, in units of 10^{-12} erg cm^{-2} s^{-1},
[d] overall absorbed flux between 2–10 keV in units of 10^{-12} erg cm^{-2} s^{-1},
[e] χ^2 and degrees of freedom calculated in each individual slice.
[f] null hypothesis probability (N.P.) calculated in each individual slice.

width $EW = -179^{+56}_{-70}$ eV in A + C, $EW = -255^{+80}_{-100}$ eV in B + D and $EW = -246^{+96}_{-78}$ eV in E + F. The iron K absorption feature is almost constant throughout the three segments, which is in contrast to what was observed in the 2013 *Suzaku* spectra previously in Chapter 5, where the equivalent width of the iron K absorption line increased by a factor of ∼ 10 through the observation. As before I also included a Gaussian component ($\texttt{zgauss}_{\rm em,FeK}$) to model the iron K emission best-fitted at slightly blueshifted energy of $E = 7.08^{+0.18}_{-0.16}$ keV with $EW = 52^{+30}_{-27}$ eV in A + C, $EW = 73^{+43}_{-37}$ eV in B + D and $EW = 69^{+40}_{-35}$ eV in E + F. I adopted a common line broadening of $\sigma = 202^{+92}_{-64}$ eV at the energy of the Fe K emission line, or $\sigma = 265$ eV at the energy of the Fe K absorption profile. From the time-averaged spectrum, I retained the two soft emission lines at $E = 0.94^{+0.1}_{-0.2}$ keV and $E = 1.17 \pm 0.2$ keV that are parametrized with two Gaussian components ($\texttt{zgauss}_{\rm em,soft}$), with equivalent width and velocity broadening values consistent to the earlier broadband SED fit (see Table 6.2).

When modelling the broadband SED in § 6.3.1, the time-averaged 2007 spectrum required only a single thin layer of partial covering (see Table 6.2). However, when fitting the three segments the model prefers an additional layer improving the fit by $\Delta\chi^2/\Delta\nu = 70/5$ ($\sim 7.4\sigma$ confidence level). This additional layer is required in this case to account for the hard to soft spectral changes. For simplicity, the $N_{\rm H}$ of the two partial covering zones are not allowed to vary between the three segments, so that the spectral changes over the course of the observation are only due to variations in the covering fractions[3]. Similar to the *Suzaku* 2013 observation, the partial covering absorbers consist of a low ($\texttt{zpcfabs}_{\rm low}$) and high ($\texttt{zpcfabs}_{\rm high}$) column zone with column densities of $\log(N_{\rm H,low}/{\rm cm}^{-2}) = 21.5 \pm 0.2$ and $\log(N_{\rm H,high}/{\rm cm}^{-2}) = 23.2^{+0.3}_{-0.1}$ respectively. In this scenario I assume that there is no intrinsic continuum spectral variability, thus the relative flux normalizations of the blackbody and the power-law continuum were allowed to vary together by the same scale factor. The temperature of the blackbody component was fixed at $kT = 100$ eV, however a value of $kT = 94^{+18}_{-22}$ eV was found when

---

[3] Note that I would obtain equivalent results by letting the column densities, rather then covering fractions, vary between the segments.

the temperature was allowed to vary.

For the low column zone, the covering fraction is substantially variable between the segments, reaching its highest value at $f_{cov,\rm low} = 0.57^{+0.18}_{-0.09}$, while its minimum value was reached during the soft flares at $f_{cov,\rm low} < 0.12$ (See Table 6.4). For the high column the covering fraction ranges from its maximum value during the hard flares with $f_{cov,\rm high} = 0.34 \pm 0.05$ to its minimum value during the soft flares with $f_{cov,\rm high} < 0.17$. The high column zone is less variable than the low column zone, but the behaviour is similar. Nonetheless in order to compensate for the higher absorption, the intrinsic normalization of the continuum is required to be $\sim 50\%$ higher during the hard flares, compared to either the soft and quiescent periods (see Table 6.4). Overall, the *partial covering changes* model provided an excellent fit to the data, with $\chi^2_\nu = 1320/1313$ (see Fig. 6.10).

6.5.2 Intrinsic continuum changes

Alternatively, I test whether the observed short-term spectral variability is purely driven by intrinsic continuum changes. In this case, I assumed that the overall continuum is unabsorbed, with no modification by any partial covering absorbers. The parametrization of both the iron K absorption and emission profiles, together with the two soft emissions lines are perfectly consistent with the previous model. In order to account for the variability between the three segments, I parametrized the spectra with a baseline model of the form:

$$\begin{aligned}\texttt{Tbabs} \times \big(&\texttt{bbody} + \texttt{powerlaw} + \texttt{zgauss}_{\rm em,soft} \\ &+\texttt{zgauss}_{\rm em,Fe\,K} + \texttt{zgauss}_{\rm abs,Fe\,K}\big).\end{aligned} \tag{6.2}$$

Here, the power-law photon index (Γ) and the corresponding power-law and blackbody normalizations were allowed to vary independently between the three segments. The photon indices were indeed variable, yielding $\Gamma = 2.14 \pm 0.02$, $\Gamma = 2.27 \pm 0.02$ and $\Gamma = 2.44 \pm 0.03$, for the hard flare, quiescent and soft flare portions respectively. The

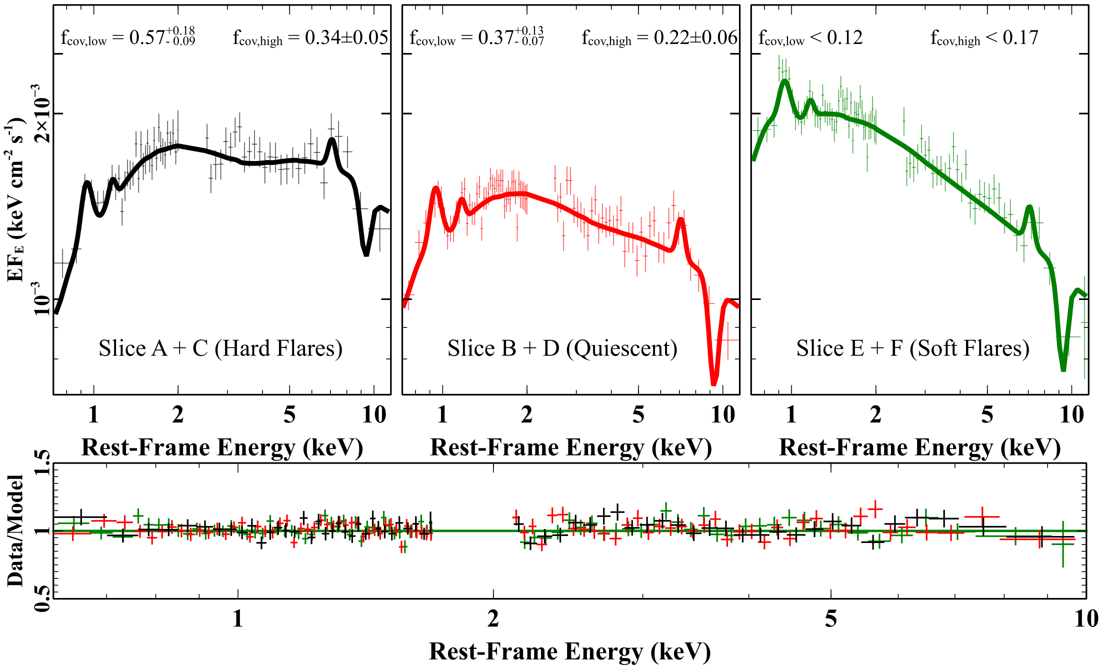

Figure 6.10: Plots of the XIS03 spectra from the *Suzaku* 2007 observation, showing the evolution from the hard flare (A + C) to the quiescent (B + D) and to the soft flare (E + F). Top panels: unfolded spectra for each of the three segments and their corresponding best-fit model corresponding to *partial covering changes* model. In this scenario the spectral variability is caused by changes in the covering fractions of two absorbing zones ($f_{\mathrm{cov,low}}$ and $f_{\mathrm{cov,high}}$), where the rapid softening of the spectrum of slice E + F is caused by an uncovering of the X-ray emitting region. Bottom panel: the data/model residuals compared to the continuum for all three segments.

resulting model is plotted in Fig. 6.11 and clearly shows that the power-law photon index generally increases as the observation progresses, being flatter during the hard segment and becoming steeper during the soft segment and intermediate in slope between the two in the quiescent segment. The spectral shape is therefore largely consistent to what was observed in the flux-flux plots in Fig. 6.8 and Fig. 6.9, presented earlier in § 6.4.2.

As with the previous model, for consistency, the soft excess was also parametrized with a blackbody component where its temperature was fixed at $kT = 100\,\mathrm{eV}$ (which if allowed to vary was found to be $kT = 98 \pm 16\,\mathrm{eV}$). In this fit, the blackbody normalization

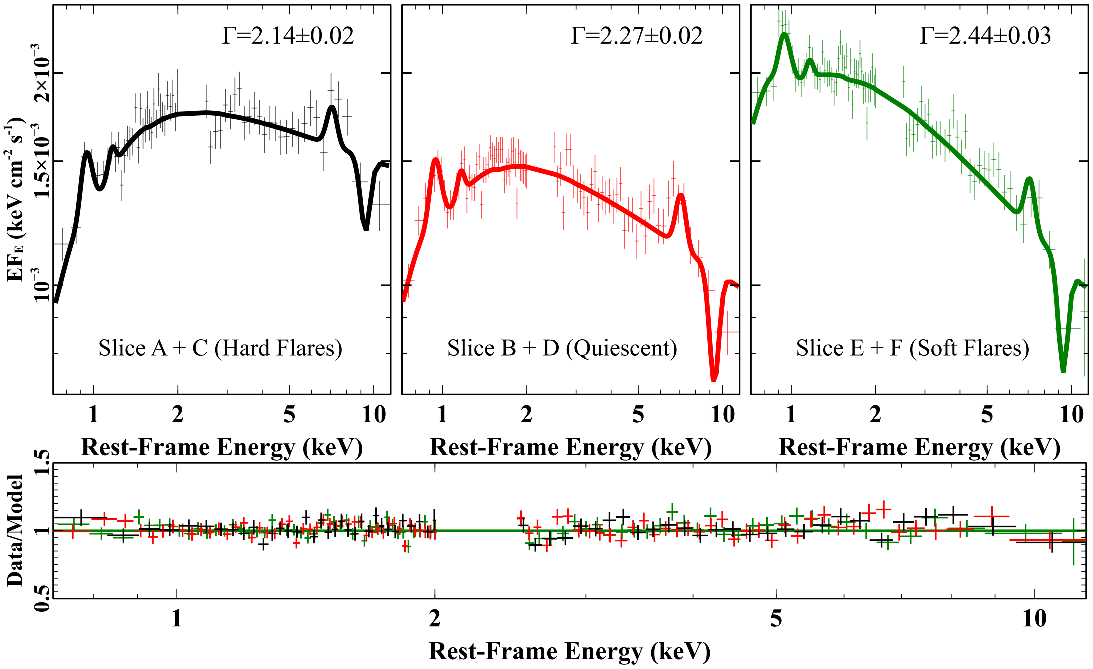

Figure 6.11: As per Fig. 6.10, but instead the spectral evolution compared to the *intrinsic continuum changes* model. Note how the spectra soften during slice E + F which is mainly caused by an increase of the photon index together with the blackbody normalization (see Table 6.5).

increased by a factor of ~ 3.5 across the three segments (i.e., from A + C to E + F) as the overall observation increasingly became softer. Overall in this scenario (as well as in the partial covering changes case) I obtained an excellent fit to the data i.e., $\chi^2/\nu = 1328/1316$. This suggests that the spectral variability in this 2007 *Suzaku* observation of PDS 456 can be equally well explained by both scenarios.

6.5.3 Difference spectrum analysis

I have established that the spectral variations during the 2007 *Suzaku* observation are characterized by two prominent hard and soft events. In order to characterize the properties of the variability in the different soft versus hard segments, I calculated the corresponding difference spectra. This was accomplished by simply subtracting (in turn)

		Slice A + C	Slice B + D	Slice E + F
power law	Γ	2.14 ± 0.02	2.27 ± 0.02	2.44 ± 0.03
	norm^{a}_{po}	2.06 ± 0.05	1.86 ± 0.03	2.60 ± 0.05
Blackbody	kT (eV)	100^{*}	100^{t}	100^{t}
	norm^{b}_{bb}	< 1.76	1.69 ± 0.80	$5.92^{+1.14}_{-1.11}$
	$\mathrm{Flux}^{c}_{0.5-2}$	3.09	2.84	4.18
	Flux^{d}_{2-10}	4.19	3.16	3.56
Model Statistic	$(\chi^2/\nu)^{e}$	338/353	516/490	474/454
	N.P.^{f}	0.71	0.20	0.25
	Best Fit Statistic	$\chi^2/\nu = 1328/1317$		

Table 6.5: *Intrinsic continuum changes* best-fit parameters for *Suzaku* XIS 2007 three combined segments. Here the power-law and blackbody components are allowed to vary independently accounting for the short-term spectral variability. ^{t} denotes that the parameter is tied during fitting, * indicates a parameter fixed during fitting

[a] Power-law normalization, in units of 10^{-3} ph keV^{-1} cm^{-2} s^{-1},

[b] blackbody normalization in units of 10^{-5} (L_{39}/D_{10}^2), where L_{39} is source luminosity in units of 10^{39} erg s^{-1} and D_{10} is the distance to the source in units of 10 kpc,

[c] overall absorbed flux, between 0.5–2 keV, in units of 10^{-12} erg cm^{-2} s^{-1},

[d] overall absorbed flux between 2–10 keV in units of 10^{-12} erg cm^{-2} s^{-1},

[e] χ^2 and degrees of freedom calculated in each individual slice.

[f] null hypothesis probability (N.P.) calculated in each individual slice.

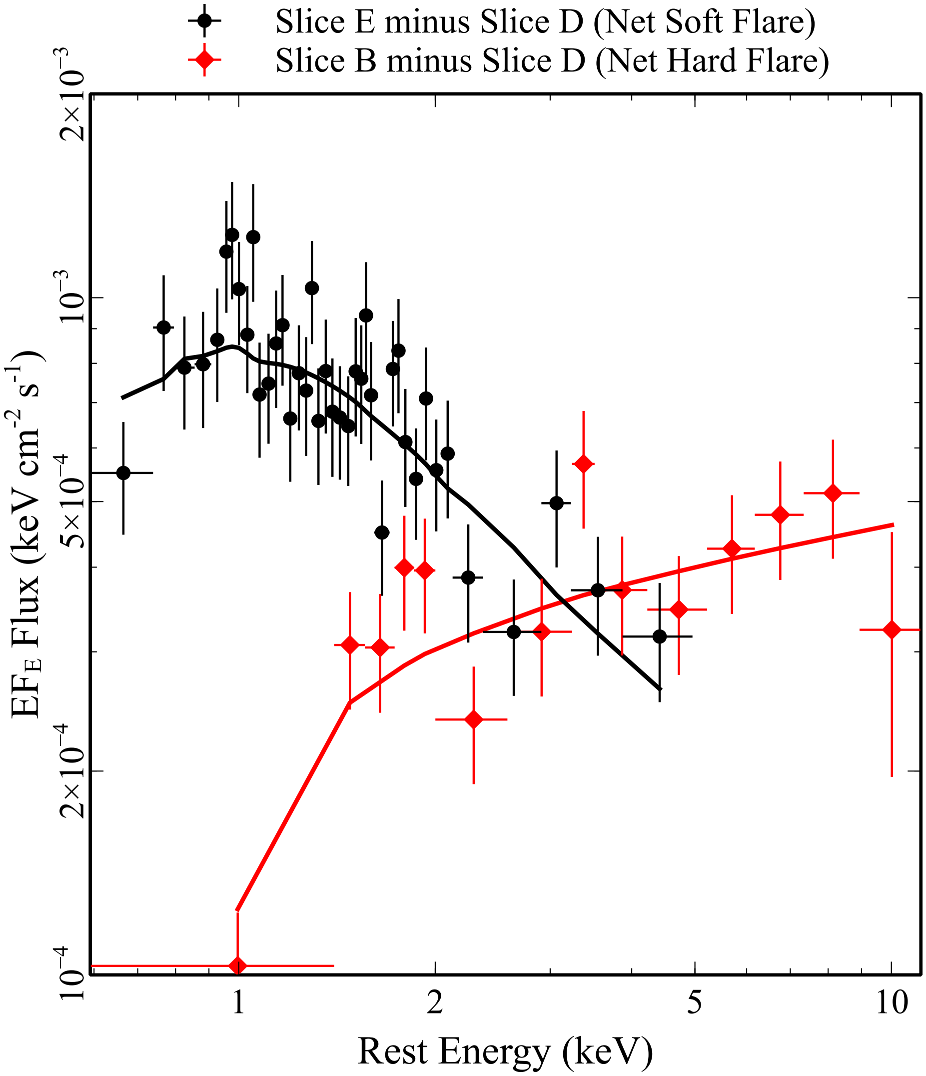

Figure 6.12: The net soft flare (E – D, black) and the net hard flare (C – D, red) difference spectra. The solid black and red lines correspond to the dual power law model which in the net soft spectrum is characterized by a soft photon index $\Gamma \sim 3.8$ with a weak 'harder' tail at $\Gamma \sim 2.3$; while the net hard spectrum is characterized by a hard photon index of $\Gamma \sim 1.8$. It is evident that the observation is characterized by the variability of two distinct continuum components. Both net spectra were grouped to a 5σ detection per bin.

the individual slice D spectrum (the quiescent portion of the observation lowest in flux) from the adjacent slice C (hard flare) and likewise from slice E (soft flare). Thus these subtracted spectra are now referred to as net hard flare (C – D) and net soft flare (E – D). I found that the net hard flare spectrum could be fitted with a simple power-law model component with a relatively hard photon index (in the context of PDS 456) of $\Gamma = 1.8 \pm 0.2$. The net soft flare spectrum required a power-law component consisting of a very steep photon index at $\Gamma = 3.8 \pm 0.5$ dominating below 2 keV, together with a weak 'harder' tail[4] ($\Gamma \sim 2.3$) mainly affecting the 2–5 keV band. Both cases produce an acceptable fit with $\chi^2/\nu = 51.6/48$ and the resulting difference spectra with their corresponding power-law components are plotted in Fig. 6.12.

I find that both the net soft and net hard flare spectra could have been equally fitted with a single `compTT` model (Titarchuk 1994), each characterized by a distinct Comptonizing region. The net soft flare portion can be reproduced by an optically thick (with $\tau = 2.0 \pm 0.2$) 'warm' Comptonizing region with temperature of $kT = 4.7^{+0.5}_{-0.4}$ keV. On the other hand, an optically thin ($\tau = 0.34^{+0.05}_{-0.04}$) 'hot' Comptonizing region with temperature fixed at $kT \sim 100$ keV, characterizes the net hard flare. This produces an overall acceptable fit with $\chi^2/\nu = 55.7/50$. This result suggests that the overall spectral variability of PDS 456 in 2007 is likely to be characterized by the superposition of two different variable continuum components; (i) variable soft flares (or 'warm' coronal component) and (ii) variable hard flares (or 'hot' coronal component).

6.5.4 Fractional variability

To further quantify the spectral changes, I computed the fractional variability ($F_{\rm var}$ hereafter) in different energy bands, adopting a time binning of 5760 s (i.e. one *Suzaku* orbit) and using the method described in Vaughan et al. (2003) as described earlier in § 5.5. The $F_{\rm var}$ spectrum computed over the entire observation is plotted in the top

---

[4] The presence of a weak 'harder' tail is consistent with the behaviour of the 2–5 keV band light curve in Fig. 6.6 (P.3) where the two prominent soft flares in the second half of the observation, that dominate the 0.5–1 keV band, are also still detected in the 2–5 keV band.

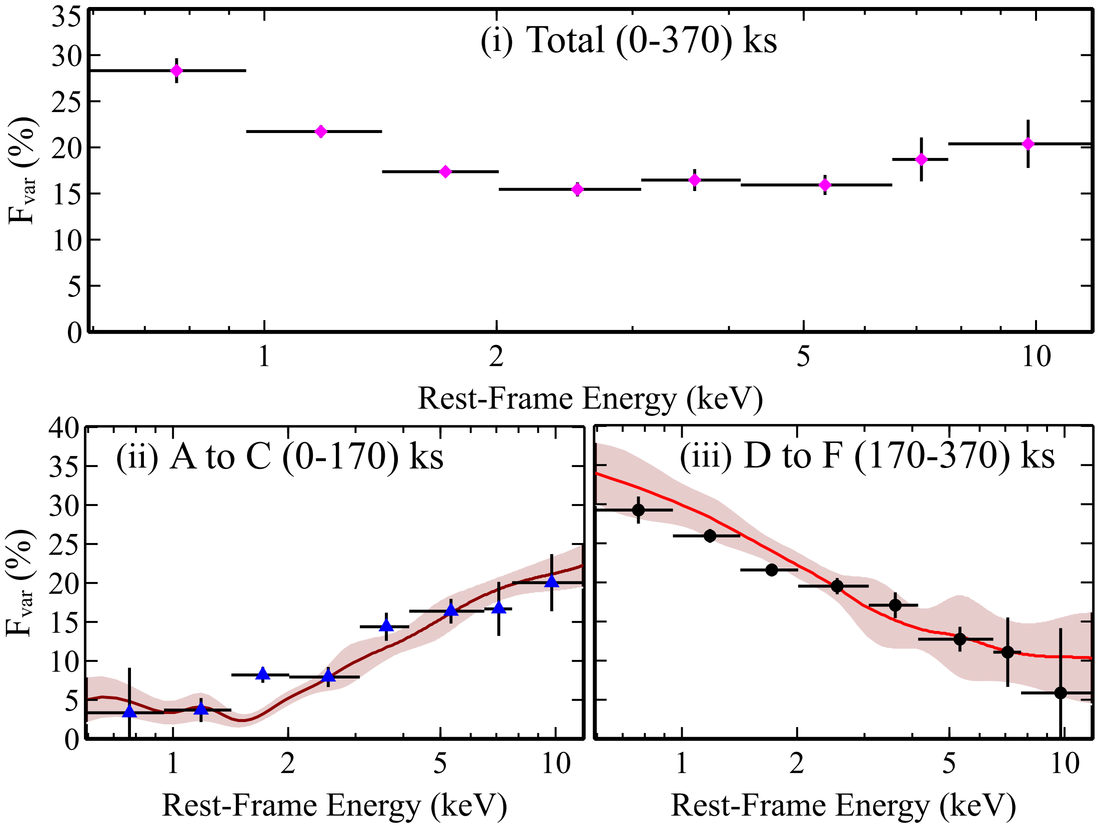

Figure 6.13: Fractional X-ray variability ($F_{\rm var}$) from the 2007 *Suzaku* observation where panel (i) shows the total $F_{\rm var}$ spectrum, panel (ii) shows the $F_{\rm var}$ computed only in the first half of the observation while panel (iii) the $F_{\rm var}$ from only the second half of the observation. It is clear that the total $F_{\rm var}$ (i) is the superposition of (ii) and (iii) strongly suggesting that the observation is dominated by distinct variable hard and soft components. The solid red lines correspond to the simulated $F_{\rm var}$ shape based on the *intrinsic continuum changes* model (see text for details). The curves have been smoothed with a spline function, and the shaded area indicates the 1σ dispersion for 3000 mock light curves.

panel of Fig. 6.13 (i). However a striking difference in the $F_{\rm var}$ spectrum was found when comparing the two halves of the 2007 observation.

The $F_{\rm var}$ spectra computed over the first (0–170 ks between A to C) and the second part (170–370 ks between D to F) of the observation, are plotted in Fig. 6.13 (ii) and Fig. 6.13 (iii) respectively. Their resulting shapes were remarkably similar to the difference spectra plotted in Fig. 6.12, where in panel (ii) the variability was most prevalent in the hard energy band (hard flare portion) and conversely in panel (iii), most of the variability occurred in the soft band (soft flare portion) of the observation. This confirms the two component behaviour represented by different soft and hard emission components. The resultant shape of the total $F_{\rm var}$ spectrum, in panel (i), is therefore consistent with the contribution of both components superimposed. One possibility is that the first half of the observation is dominated by changes in the intrinsic power-law flux and slope, resulting in enhanced variability above 2 keV, while the behaviour of the second half of the observation is dominated by a drastic rise in the soft X-ray emission below 2 keV.

In order to test more quantitatively what I have found above, simulations were used to test the possible variability mechanism that produced both $F_{\rm var}$ shapes in Fig. 6.13 (ii) and (iii). This was achieved by computing two separate $F_{\rm var}$ spectra, each representing one half of the observation, from 3000 simulated light curves. More specifically, each light curve in the observation has 65 data points (see Fig. 6.6), which is effectively produced by having 65 separate spectra per each simulated light curve; in other words $3000 * 65 = 195000$ spectra were randomly generated within the input ranges extrapolated from the earlier best fit *intrinsic continuum changes* model. I computed two sets of simulations by adopting for simplicity a simple dual power-law component, described earlier in § 6.5.3, as the input model. For the first half of the observation (simulation A hereafter) only the hard power-law photon index, corresponding to the hard variable component, was allowed to vary within the range from $2.0 \leq \Gamma \leq 2.5$. This is consistent with the observed Γ changes in § 6.5.2, with no change required in the soft component. For the second half of the observation (simulation B hereafter), I only allowed the normalization of the soft power-law component (of photon index $\Gamma = 4.0$ consistent with the difference analysis) to vary between 1–$9 \times 10^{-4}\,{\rm ph\,keV^{-1}\,cm^{-2}\,s^{-1}}$. This can be seen in Fig. 6.12 from the respective photon fluxes at 1 keV in the difference spectra.

The resulting simulations are overlaid on the $F_{\rm var}$ spectra in Fig. 6.13 (ii) and (iii), where the red solid lines correspond to the simulated $F_{\rm var}$ model and associated 1σ dispersion, shown as the shaded area, compared to the actual $F_{\rm var}$ spectrum measured from the observations. I found that the observed shape of the $F_{\rm var}$ spectrum plotted in

Fig. 6.13 (ii) is well reproduced by simulation A with a moderate pivoting of the photon index. The rising shape of the $F_{\rm var}$ spectrum towards higher energies can be pictured as a variable photon index due to the hardening of the spectrum. On the other hand, simulation B largely reproduced the $F_{\rm var}$ shape of the second half of the observation, plotted in Fig. 6.13 (iii), achieved by a variable normalization of the 'soft' component. Therefore a change in normalization of the soft component in the 2007 D to F segments, would have been mainly responsible for an $F_{\rm var}$ spectrum dominated by variability in the soft band rather than at higher energies. The overall behaviour is consistent with a two component variable continuum where the soft is dominated by a rapid increase in the normalization of the soft component, causing the overall steepening of the spectrum, whereas during the first part of the observation, when the soft component is less prevalent, the photon index of the power law tail tends towards harder values.

On the other hand it may be difficult to reconcile the distinct behaviour in the $F_{\rm var}$ spectra in Fig. 6.13, from the two halves of the observation, with the variable *partial covering changes* model. Although I do not test this explicitly here, the only way for this bimodal behaviour to be reproduced might be for the first half of the observation to be dominated only by the variability of the high column absorption zone, which then would primarily enhance the variability in the harder band. Then in the second half of the observation, the variability would need to be dominated only by the lower column partial coverer, enhancing the variability in the soft band. Nonetheless such a distinct behaviour of the two absorption zones may seem somewhat contrived and furthermore, as discussed in the next section, such rapid absorption variability is likely to be on too short time-scales to be physically plausible. Finally, during the 2013 *Suzaku* observations, when PDS 456 was in low-flux state dominated by absorption, the $F_{\rm var}$ spectrum did not show this simple power-law like variability behaviour from either of two distinct continuum components (see Fig. 5.6 in § 5.5); in those observations the $F_{\rm var}$ spectrum had pronounced curvature and showed enhanced variability in the iron K band due to the variability of the outflow.

6.6 Discussion

In the previous sections I found that the observed short-term spectral variability can be statistically well explained by either: (i) the presence of variable partial covering absorption, or (ii) an intrinsically variable continuum. In scenario (i), the X-ray spectral variability may be caused by an uncovering of the intrinsically steep continuum. This is due to changes in the covering factors from two zones of partial covering absorbers, characterized by the same physical properties observed in the 2013 *Suzaku* campaign (see Chapter 5). On the other hand in scenario (ii), such a rapid spectral variability may be caused by intrinsic flaring, with some episodes (A + C) intrinsically harder and others (E + F) intrinsically softer. The latter scenario can also reproduce the $F_{\rm var}$ spectra discussed above. In this section I will discuss the feasibility and physical implications of these two scenarios.

6.6.1 Variable partial covering

In § 6.5.1 I described a scenario where the short-term spectral variability can be well explained by variable a partial covering model. However, there are some physical implications that need to be addressed. First of all, when modelling the broadband SED in § 6.3.1, the time-averaged 2007 spectrum is not strongly absorbed as it allows only a weak single layer of partial covering with column density $\log(N_{\rm H}/{\rm cm}^{-2}) = 23.1^{+0.1}_{-0.3}$ and $\sim 15\%$ covering fraction (see Table 6.2). Yet when fitting the three segments, two zones of partial covering are required in order to account for the observed spectral variability; where the low column is mainly affecting the soft energy band, whilst the high column is changing the spectral shape above 2 keV. Furthermore despite being more absorbed, the hard flare segment is required to have an intrinsically higher continuum level (by a factor of $\sim 50\%$, see § 6.5.1) compared to the less absorbed soft and quiescent periods. This may seem somewhat contrived, as the most absorbed portion of the observation is required to be at the highest flux level.

A physical issue that makes the partial covering scenario unfeasible is the variability time-scale being too short. To determine whether the time-scale of the partial covering changes are realistic, an estimate of the absorber velocity is required. Reeves et al. (2016) presented a high resolution soft X-ray analysis of all PDS 456 RGS spectra to date. By measuring the discrete features in the RGS spectra, they found the presence of X-ray absorbers moving at a typical outflow velocity of $v \sim 0.20$–$0.25c$. Furthermore in Chapter 5, by fitting the 2013 broadband spectra of PDS 456, the high column partial coverer was also suggested to be outflowing at velocity of the order of $v_{\rm pc} \sim 0.25c$. Therefore I argue that the partial coverer could be considered as a plausible, less ionized, component of the same fast wind. From adopting a transverse velocity (comparable to the outflow velocity i.e., $v_{\rm T} \sim v_{\rm pc} \sim 0.20$–$0.25c$) for the partial covering absorber, I can determine the absorber size-scale. Assuming that a partial eclipsing event may be responsible for the observed flux drop between the two (fully unobscured) soft flares, in slice E and F (see Fig. 6.6 P.2), the time-scale at which this event occurs would be of the order of $\sim 50\,$ks, suggesting a typical size-scale of the eclipsing clump to be $\Delta R_{\rm clump} \sim v_{\rm pc}\Delta t \sim 3$–$4 \times 10^{14}\,{\rm cm} \sim 2$–$3\,R_{\rm g}$. Note this is also similar to the time-scale of the 'hard' events, where in the partial covering model the quasar becomes more obscured. Taking the column density of the variable absorber to be $N_{\rm H} \sim 10^{22}\,{\rm cm}^{-2}$, I obtain a value for the average hydrogen number density of $n_{\rm H} \sim N_{\rm H}/\Delta R \sim 2 \times 10^{7}\,{\rm cm}^{-3}$. To be conservative, I can also assume that these partial coverers are partially ionized, rather than neutral, with the ionization parameter required to be at most $\log(\xi/{\rm erg\,cm\,s^{-1}}) \lesssim 2.5$ (see § 5.6) in order to remain opaque at soft X-rays [5].

From the definition of the ionization parameter and taking the ionizing luminosity of PDS 456 consistent with the results in Chapter 4 (and Nardini et al. 2015) to be $L_{\rm ion} \sim 5 \times 10^{46}\,{\rm erg\,s^{-1}}$, I estimate the radial location of these absorbers to be at $R = (L_{\rm ion}/n_{\rm H}\xi)^{\frac{1}{2}} \gtrsim 10^{18}\,{\rm cm} \gtrsim 10^{4}\,R_{\rm g}$. This would place these clumps at parsec-scale distances from the black hole in PDS 456. In contrast Reeves et al. (2016) found, in the RGS spectra, that these absorbers were located at least one order of magnitude

---

[5] Note that in § 5.6 the ionization parameter of the low and high column partially ionized partial covering absorbers was found to be $\log(\xi/{\rm erg\,cm\,s^{-1}}) = 0.62^{+0.18}_{-0.08}$ and $\log(\xi/{\rm erg\,cm\,s^{-1}}) = 2.5 \pm 0.2$.

closer (at BLR scale). Therefore the time-scales at which I observe the uncovering of the X-ray source would lead to rather compact clumps (of a few $R_{\rm g}$ in extent) with typical size-scales physically too small to be located at such large (parsec-scale) distances. On the other hand, by assuming that the Keplerian velocity across the source is comparable to the outflow velocity i.e., $v_{\rm pc} \sim v_{\rm K}$, I estimate the radial distance of these absorbers to be $r_{\rm clump} \sim \frac{c^2}{v_{\rm K}^2} R_{\rm g} \sim 20\,R_{\rm g}$. Thus if these clumps were located at such a small distance from the inner accretion disc, with a typical density of $n_{\rm H} \sim N_{\rm H}/\Delta R \sim 2 \times 10^{7}\,{\rm cm}^{-3}$, the ionization derived would be unrealistically high i.e., $\xi \sim L_{\rm ion}/n_{\rm H}{\rm R}^2 \sim 10^{8}\,{\rm erg\,cm\,s}^{-1}$. Indeed this would be two orders of magnitude higher even than the high ionization absorber at iron K (Nardini et al. 2015). Thus given the compactness of the absorbing clouds and the high degree of ionization required to place them at a reasonable distance from the black hole, the partial covering scenario seems less plausible to explain the rapid spectral changes in PDS 456. Thus the rapid variability in these high-flux observations is more likely to be intrinsic in origin. In contrast the prolonged (~ 1 Ms) low-flux periods observed in 2013 with *Suzaku* are likely to be due to enhanced absorption, as it is also required to explain the hard spectral shape during those observations as well as the prominent increase in depth of the iron K absorption profile (as discussed in earlier in Chapter 5).

6.6.2 Variable intrinsic continuum

All the observational evidence in this work suggests there are two sources of variability present in this 2007 *Suzaku* observation of PDS 456 in the form of hard and soft variable components. Note that this two-component variability has also been detected in other AGN by means of principal component analysis (e.g., Miller et al. 2007; Parker et al. 2015). In the PDS 456 observation the spectrum is initially hard, becoming softer as the observation progresses. A possible explanation can be attributed to a large increase of the soft photon flux, detected below ~ 2 keV, towards the end of the observation, which may act as the 'seed' photons that produce the hard power-law component. In particular an increase in soft photon flux could lead to the cooling of the 'hot' coronal electrons, which are responsible for producing the hard X-ray power-law via Compton up-scattering. Thus an increase in soft photon flux may lead to a steepening of the power-law photon index (from $\Gamma \sim 2$ to $\Gamma \sim 2.5$), as seen in the later E + F segment of the observation.

6.6.3 Compton cooling of the corona

Here I investigate whether any Compton cooling of the corona could occur on a similar time-scale to the spectral changes seen in the 2007 *Suzaku* observation. In § 6.5.2, I determined that the softening of the spectrum occurs on a typical time-scale of $\sim 50\,\mathrm{ks}$. In comparison, the cooling rate (i.e., the rate of energy loss) per electron from inverse Compton scattering (IC) can be expressed as:

$$\left(\frac{\mathrm{d}E}{\mathrm{d}t}\right)_{\mathrm{IC}} = \frac{4}{3}\sigma_{\mathrm{T}} c \left(\frac{v_{\mathrm{e}}}{c}\right)^2 \gamma^2 U_{\mathrm{rad}} \tag{6.3}$$

where $\sigma_{\mathrm{T}} \sim 6.65 \times 10^{-25}$ cm^2 is the Thomson cross section of an electron, v_{e} is its velocity, γ is the Lorentz factor where $\gamma = (1 - v^2/c^2)^{-1/2}$, and $U_{\mathrm{rad}} = \frac{L}{4\pi r^2 c}$ is the energy density of the incident radiation. From recent studies performed on Type 1 AGN samples I can assume a typical coronal temperature of the order $\sim 100\,\mathrm{keV}$, based on their high energy roll over (e.g., de Rosa et al. 2012; Ursini et al. 2015). It follows that a Lorentz factor of $\gamma \sim 1.2$ is required in order to produce such kinetic energies, and thus $\left(\frac{v_{\mathrm{e}}}{c}\right)^2 \sim 1/3$.

The radiation field (U_{rad} hereafter) is estimated in terms of the intrinsic soft X-ray luminosity, in the 0.5–2 keV band, assuming that the soft X-ray component acts as the input 'seed' photons for the hard power-law. The soft X-ray luminosity extrapolated from soft flare segment is $L_{0.5-2} \sim 10^{45}$ erg s^{-1}, which may be a factor of a few higher if the soft component extends below the 0.5 keV low-energy bandpass. Thus, our choice of energy range provides a conservative estimate of U_{rad}. From the observed time-scale of the variability of $\Delta t \sim 50\,\mathrm{ks}$, I can deduce the typical size of the X-ray emitting region to be $r \sim 10\,R_{\mathrm{g}} \sim 1.5 \times 10^{15}$ cm in PDS 456. This yields an energy density of the radiation field in the order of $U_{\mathrm{rad}} \sim 1000$ erg cm^{-3}. Thus the cooling rate, of a single electron, can be estimated due to inverse Compton scattering (Longair 2011) to be:

$$\left(\frac{\mathrm{d}E}{\mathrm{d}t}\right)_{\mathrm{IC}} \sim 1.3 \times 10^{-11}\,\mathrm{erg\,s^{-1}}. \qquad (6.4)$$

As noted above, the most popular models predict that the high-energy cut-off (E_{cut}) of the electron population in the corona is of the order of $kT_{\mathrm{e}} \sim 100\,\mathrm{keV}$ (e.g., Marinucci et al. 2014). On this basis I am able to estimate the corona Compton cooling time, i.e., $t_{\mathrm{cool}} = \frac{E_{\mathrm{kin}}}{\left(\frac{\mathrm{d}E}{\mathrm{d}t}\right)_{\mathrm{IC}}}$, where $E_{\mathrm{kin}} \sim 2$–$3\,kT_{\mathrm{e}}$ is the typical energy of the coronal electrons. Thus I estimate that the cooling time to be of the order of $t_{\mathrm{cool}} \sim 40\,\mathrm{ks}$. Indeed this is on a similar time-scale on which I observe the spectrum (segment E + F) becoming softer during the two flares. Thus the increase in photon index of the primary power-law continuum may occur as a result of the strong soft X-ray flares in the latter half of the 2007 observation.

6.6.4 Energetics and reprocessing

Although it is not possible to determine the coronal geometry, one possibility is that it is characterized by a thick ‘warm’ atmosphere blanketing the inner region of the disc, responsible for the soft excess and by a compact, but thin, ‘hot’ coronal region located above the accretion disc which is responsible for the high-energy power-law (Done et al. 2012). This configuration is shown schematically in Fig. 6.14. However, due to the rapid soft band variability observed here, the soft (as well as the hard) variable component cannot be overly extended (see § 6.4.1).

What might occur in this ‘dual-layered’ configuration, is a build up of energy stored in the ‘hot’ corona, previously estimated to be in the order of $\sim 10^{51}$ erg over time-scales of $\sim 10^{5}$ s from the duty cycle of the X-ray flares (Reeves et al. 2002). This is followed by some ‘triggering’ factors, perhaps in the form of ‘cascade of events’ (Merloni & Fabian 2001; Reeves et al. 2002), which would eventually dissipate the energy stored, leading to the hard X-ray flares as seen during segment A + C. Note that similar hard X-ray flares were also found in earlier *RXTE* and *BeppoSAX* observations of PDS 456 (Reeves et al. 2000; Reeves et al. 2002). In turn these hard photons may illuminate the outer layers of

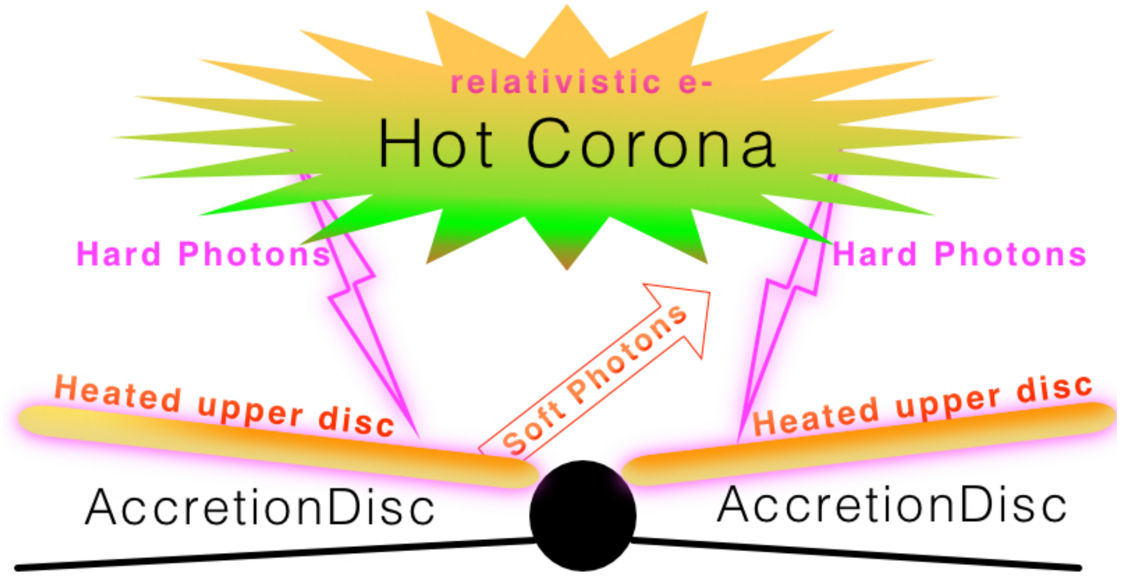

Figure 6.14: Schematic of a possible coronal-heated disc geometry in accreting systems of AGN. Hard events are triggered in the hot coronal regions, producing the observed hard X-ray photons that are also heating the upper atmosphere of the accretion disc. Furthermore the lower energy disc photons are Compton up-scattered to the observed soft X-ray band when they interact with the heated electrons. An increase in soft X-ray flux might cool the hot corona.

the disc, leading to an increase in temperature of the 'warm' scattering region. By doing so, the 'heated' electrons would, effectively, impart more energy to the EUV disc-photons undergoing Compton up-scattering into the observable soft X-ray domain as seen during the soft flares (segment E + F). Therefore a relatively small increase in temperature can in principle lead to a large increase in the soft X-ray flux as the Comptonized tail of the disc is shifted into the observable band above $\sim 0.5\,\mathrm{keV}$.

As an example I simulated the warm/soft Comptonizing region with a `compTT` model where, at first, I assumed a disc blackbody component with an input temperature of $kT = 20\,\mathrm{eV}$ (UV input photons, see equation 1.9 in § 1.2.1). This is a reasonable value for a $10^9\,M_\odot$ black hole accreting near $L_{\rm Edd}$. The parameter space adopted was based upon the difference spectrum analysis in § 6.5.3 Fig. 6.12. Thus we have a 'warm' Comptonizing layer in the upper disc atmosphere to have a temperature of $kT_{\rm e} = 2\,\mathrm{keV}$ and optical depth of $\tau = 4$. In this example, by increasing the plasma temperature, from $kT_{\rm e} = 2\,\mathrm{keV}$ to $kT_{\rm e} = 4\,\mathrm{keV}$, resulted in an increase in the 0.5–2 keV soft band flux by more than one order of magnitude as shown in Fig. 6.15. Thus, the drastic increase observed in the 0.5–2 keV band luminosity in the segments E + F may be the result of this process, where the emission from the Comptonized 'warm' component is 'pushed' up in the observable soft X-ray band by an increase in its temperature. In turn, the increased soft photon flux could cool the 'hot' coronal electrons leading, as a result, to an increase in Γ observed towards the end of the observation.

This may be regarded as an over simplification of a more complex physical scenario; nonetheless the underlying idea is that the hard events are responsible for the energy injection into the corona, whereas the soft events contribute to its energy loss as an increasing flux of soft photons is supplied into it. Subsequently, the hot electrons give up their energies via inverse Compton scattering to the soft photons. Eventually what I may expect is that further hard events would re-inject energy into the system (i.e., coronal heating) resulting in the hardening of the spectra defining a possible onset of a new cycle.

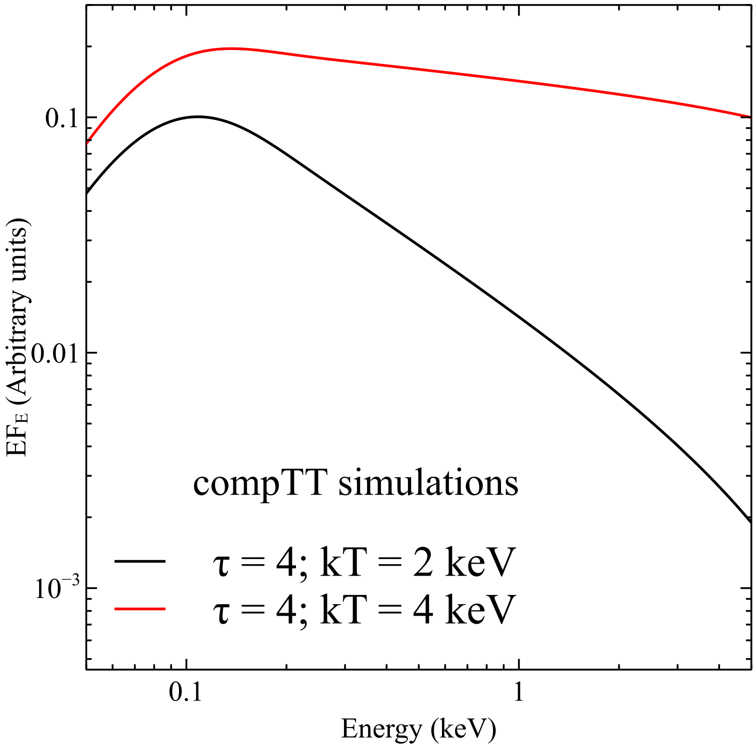

Figure 6.15: `compTT` simulation of the warm/soft Comptonizing region based upon values observed in the difference spectra. For the “warm” Comptonizing layer in the upper disc atmosphere, a temperature of $kT_{\rm e} = 2$ keV and an optical depth of $\tau = 4$ was used. Here, by increasing the plasma temperature, from $kT_{\rm e} = 2$ keV to $kT_{\rm e} = 4$ keV, resulted in an increase in the 0.5–2 keV soft band flux by more than one order of magnitude.

6.7 Chapter summary

In this chapter, I have presented the results from a *Suzaku* observation carried out in 2007 when PDS 456 was in an unabsorbed state. I have detected the presence of strong hard and soft band X-ray flaring on time-scales of ~ 50 ks, confined in the first and second half of the observation respectively. The main results are summarised below:

1. I have found that after constructing an optical/UV to hard X-ray SED, the `optxagnf` model was able to explain it successfully with values consistent with what was found

in the earlier analysis of *Suzaku* 2013 campaign of PDS 456 in § 4.3.2. However, in contrast to the 2013 sequences, in this 2007 *Suzaku* observation I appear to observe the bare continuum from PDS 456, with little intrinsic absorption.

2. Rapid variability is observed from PDS 456 in 2007, with hard (> 2 keV) flares occuring in the first half of the observation and soft flares events occurs in the latter half, on time-scales of ~ 50 ks. The variability was interpreted in terms of either, (i) partial covering changes or (ii) intrinsic continuum variability. However the partial covering scenario implies that such short time-scale variability ($\Delta t \sim 50$ ks) would result in very compact clumps ($\Delta R \sim 2$–$3\,R_{\mathrm{g}}$) located far away from the source (at parsec-scales) which appears an implausible scenario.

3. Instead the X-ray spectral variability is likely due to variations in a two-component continuum. A variable soft component dominates the variability below 2 keV and may arise from a cool Comptonized spectrum. The hard variability may be explained by changes in the hot coronal emission, where the photon-index steepens as the observation progresses. The two-component model can subsequently account for the fractional/rms spectral variability of PDS 456 over the two halves of the observation.

4. I find that the overall X-ray spectral variability of PDS 456 may be accounted for by coronal changes, whereby an increase in soft photons from the Comptonized Wien-tail of the disc emission Compton cools the hot coronal electrons. This subsequently leads to a steepening of the primary power-law during the soft flaring episodes.

7 Conclusions and future work

The body of work presented in this thesis was aimed at the understanding of the physical properties and the nature of the ultra fast outflows in AGN by studying one of the prototype examples that are currently known, the luminous radio-quiet quasar PDS 456. The number of X-ray observations conducted over the years, provided a unique opportunity to study its properties and variability, thus PDS 456 can be considered the test case in understanding accretion disc-winds in general. A summary of results from this study has already been included in the prior Chapters 4–6. Below I discuss the main results of this work and I attempt to place them into a broader context in terms of our current understanding of disc-winds in general.

7.1 The key findings of this thesis and comparison with previous work

The spectra obtained from the contemporary *Suzaku* and *XMM-Newton* & *NuSTAR* campaigns have confirmed that PDS 456 presents in its spectrum a strong and blueshifted Fe K absorption feature, which results from a fast wind inferred to be on the scale of the accretion disc. Photoionization modelling has shown that the fast wind has an ionization ranging between $\log(\xi/\mathrm{erg\,cm\,s^{-1}}) \sim 5-6$ and column densities from $\log(N_{\mathrm{H}}/\mathrm{cm^{-2}}) \sim 23-24$. The outflow velocity also ranges from $v_{\mathrm{w}} \sim 0.24-0.30c$ and as I showed in § 4.5.5, the velocity appears to correlate with the X-ray luminosity of PDS 456 varying as $v_{\mathrm{w}} \propto L^{1/2}$. This appears consistent with what may be expected from a radiatively driven wind.

In earlier work on a sample of AGN (which included PDS 456), Gofford et al. (2013) found that Fe K absorption lines (associated with Fe XXV Heα and / or Fe XXVI Lyα) were robustly detected in $\sim 40\%$ of the sample (confirming their common detection). These outflows were found to have a distribution of velocities ranging between $v_{\mathrm{w}} < 1500\,\mathrm{km\,s^{-1}}$ in the least luminous AGN up to $v_{\mathrm{w}} \sim 100,000\,\mathrm{km\,s^{-1}}$ in the most luminous

AGN, with a median velocity of 0.056c. Also photoionization modelling revealed that the gas is characterized by column densities and ionization parameters which ranged between $21.5 < \log(N_{\rm H}/{\rm cm}^{-2}) \leq 24$ and $2.5 < \log(\xi/{\rm erg\,cm\,s}^{-1}) \leq 6$, with means of $\log(N_{\rm H}/{\rm cm}^{-2}) \sim 23$ and $\log(\xi/{\rm erg\,cm\,s}^{-1}) \sim 4.5$, respectively. Thus by comparing these mean values to what has been measured in this work (and previously in Tombesi et al. (2010)), PDS 456 represents one of the most extreme cases of the so-called Ultra Fast Outflows (UFOs, i.e. where $v_{\rm w} \geq 10000\,{\rm km\,s}^{-1}$; Tombesi et al. 2010). Indeed a similar, but high redshift, counterpart to PDS 456 occurs in the luminous gravitationally lensed BAL quasar, APM 08279+5255 at $z = 3.91$, which has a similar fast outflow velocity (Chartas et al. 2002; Chartas, Brandt & Gallagher 2003; Chartas et al. 2009; Hagino et al. 2016a). This may be what is expected from luminous quasars with high black hole masses $> 10^9\,M_\odot$ and which accrete at a considerable Eddington fraction (Tombesi et al. 2010; Gofford et al. 2013). Furthermore the common detection of ultra fast outflows in the X-ray spectra of AGN ($\sim 40\%$) is an indication that their geometry might be characterized by a relatively wide solid angle. This is confirmed in the PDS 456 *XMM-Newton* & *NuSTAR* observations, where a fast P-Cygni like profile at Fe K is resolved (see Chapter 4) and which shows that a considerable fraction of the absorbed X-ray radiation is also re-emitted over different line-of-sights, in the form of a broad Fe K line.

Another physical property of the Fe K absorption feature in PDS 456 is its short-term variability (of the order of $\Delta t \sim 100$ ks corresponding to $\sim 20\,R_{\rm g}$ in PDS 456), which I discuss in detail in § 5.7.1. Here one interpretation can be attributed to part of the wind that moves through the line-of-sight, eclipsing the emission that we see from the X-ray source, which suggests that a transiting substructure of the wind is observed on scale sizes of $\sim 10 - 20\,R_{\rm g}$. This also implies that the X-ray emission is produced from a compact region not larger than $\sim 10 - 20\,R_{\rm g}$ as the eclipsing of the X-ray source occurs at similar time-scales. In addition to the Fe K variability I also observed the effect of variable absorption on the rest of the X-ray spectrum where part of the X-ray emission has been covered by obscuring less ionized ("colder") and more dense material.

Thus we have "hot" gas that is detected in the Fe K band as well as cooler gas which affects the softer X-ray band too. This was later confirmed in an RGS analysis of all of the soft X-ray spectra of PDS 456, where broad absorption troughs were detected in the more absorbed *XMM-Newton* epochs (Reeves et al. 2016). Furthermore lower ionization soft X-ray absorption components associated to fast outflows have also been observed in the nearby NLS1s, IRAS 17020+4544 (Longinotti et al. 2015) and PG 1211+143 (Pounds et al. 2016). In both of these cases the soft X-ray wind components were confirmed with a velocity of $v_{\rm w} \sim 0.1c$. This suggests that like their slower counterparts – the warm absorbers – the disc-winds may also consist of a multi-phase medium.

One key property that connects these absorbers is that they appear to be outflowing at comparable velocity to the highly ionized wind. These findings seem consistent with the earlier work by Tombesi et al. (2013), where the possibility was discussed of absorbers that are sometimes considered of different types, which can be part of a single stratified outflow observed at different locations along the line-of-sight. The spectral signature of a fast outflow detected in the softer X-ray band was also predicted in multidimensional disc-wind modelling by Sim et al. (2008, 2010); where highly blueshifted, but less ionized, absorption lines from L-shell iron as well as the K-shell lines of lighter elements are predicted to be observed along many line-of-sight angles through the outflow.

The apparent correlation between the wind velocity and the hard X-ray luminosity found in PDS 456 may appear to favour a radiatively driven wind. However in § 5.8.1 it was shown that the outflow observed in the latter part of the *Suzaku* 2013 observation could not be powered purely by the radiation pressure imparted by the strong flare which occurred just prior to the onset of the wind (at ~ 450 ks into the observation). Indeed the radiation force imparted as a result of Thomson scattering was found to be at least an order of magnitude lower than what would be required in order to reproduce the observed wind kinetic power. This observed discrepancy suggests that there may be more than one physical mechanism involved in the launching and/or subsequently driving of the wind; e.g., magnetically driven outflows (Ohsuga et al. 2009; Kazanas et al. 2012; Fukumura et al. 2015).

Alternatively, instead of being driven by continuum radiation pressure, the wind could be line driven, which acts to amplify the radiation force imparted on the wind. Indeed in recent work, Hagino et al. (2015) explored the physical conditions in the wind through a 3-D Monte-Carlo code (MONACO, Odaka et al. 2011) for radiation transport. The authors show that the increased gas opacity through line-driving may also be very important in PDS 456, especially as its SED is likely to peak towards lower energies in the UV. Generally speaking, line-driven winds are prevalent when relatively low–moderate ionization gas interacts with UV radiation. As a consequence the opacity due to the bound-bound absorption cross section can considerably exceed that due to continuum scattering by several orders of magnitude (i.e., $\sigma_{\rm line} \gg \sigma_{\rm T}$), where the relative contribution to the total opacity is called the *force multiplier* (Castor, Abbott & Klein 1975). Thus Hagino et al. (2015) found that their simulation predicted the observed mass-loss rate in PDS 456 to be $\dot{M}_{\rm w} \sim 7 - 10\, M_{\odot}$ (corresponding to $\sim 30\%$ of the total mass inflow rate) which is also within the range that I find in this work (see § 4.5.4). This result is consistent with what is expected from a purely line-driven system (e.g., Laor & Davis 2014) and matches the properties of UV line driven disc-wind models.

Within this framework, the wind in PDS 456 may be initially accelerated vertically by UV radiation at its launch point on the inner accretion disc, where the line driving force is likely to be greatest, before it becomes highly ionized by the continuum X-ray emission and eventually follows a more radial trajectory at large radii. An example of such a line disc driven wind is shown in Figure 7.2, calculated from the 2D hydrodynamical simulations of Nomura & Ohsuga (2016). It is generally found that this process works at its best for high mass sources like PDS 456 as their disc emission peaks in the UV band. Furthermore observations also show that as a source approaches Eddington (i.e., high $L/L_{\rm Edd}$), the fraction of the X-ray luminosity compared to bolometric decreases (e.g., Done et al. 2012; Jin et al. 2012; Gofford et al. 2015). This may help prevent the wind being over-ionized, as well as giving extra acceleration to the wind from line driving compared to Thompson/Compton scattering (see § 4.5.5). Thus the most powerful radiatively driven winds are more likely to be produced via the combination of UV line and continuum driving. In Chapter 4 I discussed the SED of PDS 456, fitted with the `optxagnf` model (Done et al. 2012), where the latter was able to account very well for the optical/UV to hard X-ray flux ratio. Furthermore the source was found to be radiating to a considerable fraction ($\sim 80\%$) of is Eddington luminosity. Overall the SED of PDS 456 is steep, both in terms of the the UV to X-ray spectral index and the hard X-ray photon index (where $\Gamma > 2$). The steepness (and enhanced UV versus X-ray emission) of the ionizing SED is likely to play a key role in preventing the wind becoming too highly ionized, while the lower ionization gas may further help to shield some of the wind.

Some of the most extreme outflows are predicted to be observed in high Eddington fraction AGN like PDS 456. Recently Hagino et al. (2016b) managed to fit successfully the NLSy1 1H 0707–495 with MONACO code (also used for PDS 456), which has a very steep X-ray spectrum ($\Gamma > 2.6$) and as PDS 456, likely accretes near Eddington. Thus it is natural to expect fast winds from this class of AGN. Fig. 7.1 shows a comparison between the PDS 456 (*Suzaku* 2013c; blue), APM 08279+5255 (*Chandra* 2002; grey) and 1H 0707–495 (*XMM-Newton* 2011; red) spectra, where the Fe K absorption feature is strongest. Here it is clear that the signature of an ultra fast outflow is present in all three spectra, where their degrees of blueshift suggest a similar outflow velocity of $v_{\rm w} \sim 0.3c$.

This result is important in context of what was presented in recent work by Nomura & Ohsuga (2016) from their two-dimensional radiative hydrodynamical simulations. In their model, Nomura & Ohsuga (2016) were able to reproduce the correlations involving mass outflow rate, wind momentum rate and kinetic power versus luminosity, which were originally found from the sample of outflows measured by Gofford et al. (2015). They also showed that a minimum Eddington rate of $\eta > 0.025$ was required to launch a fast, line driven disc-wind for AGN black hole masses of $< 10^8 M_\odot$. An even higher Eddington rate is likely to be needed in the higher black hole mass regime, of up to 30-50% of Eddington, which appears consistent with the observations of powerful winds in highly luminous and massive quasars like PDS 456 and APM 08279+5255.

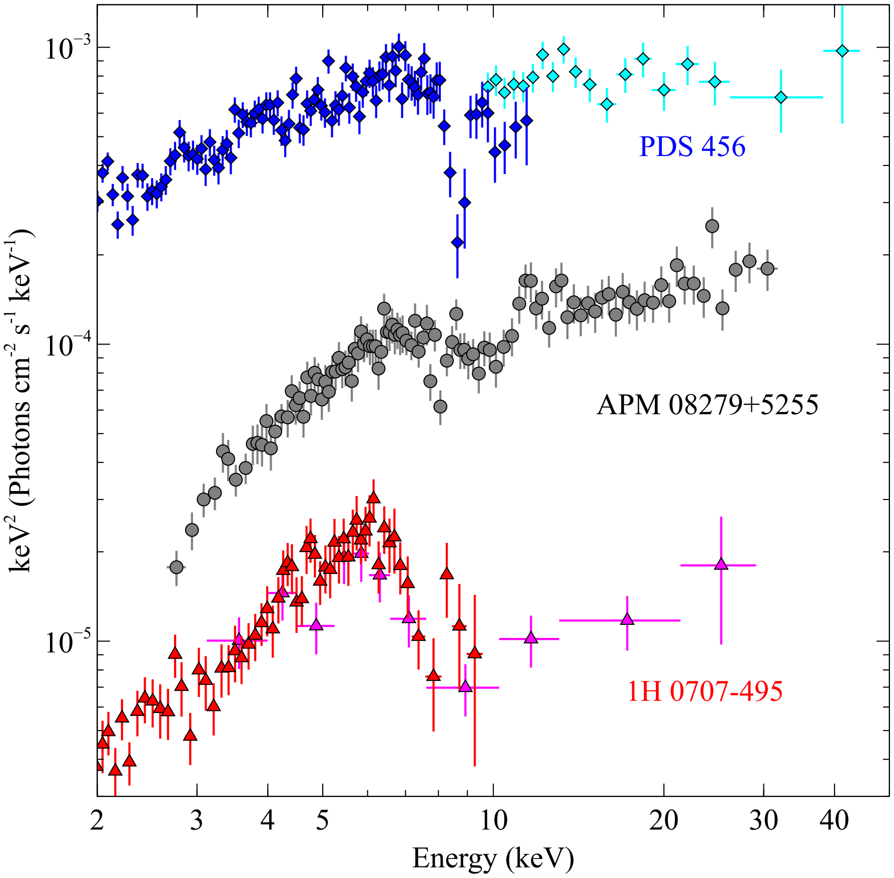

Figure 7.1: Plot showing the comparison between PDS 456 (blue / cyan), APM 08279+5255 (grey) and 1H 0707-495 (red / magenta) observed with *Suzaku*, *Chandra* and *XMM-Newton* respectively plotted in their rest-frame energies. The additional *NuSTAR* spectra used in PDS 456 and 1H 0707-495 are not simultaneous but are observed at similar flux levels, while the flux for 1H 0707-495 is scaled down by a factor of 10 for clarity. It is evident that the Fe K absorption features have a similar degree of blueshift, suggesting that the outflow velocities of each source are indeed comparable. Figure taken directly from Hagino et al. (2016a)

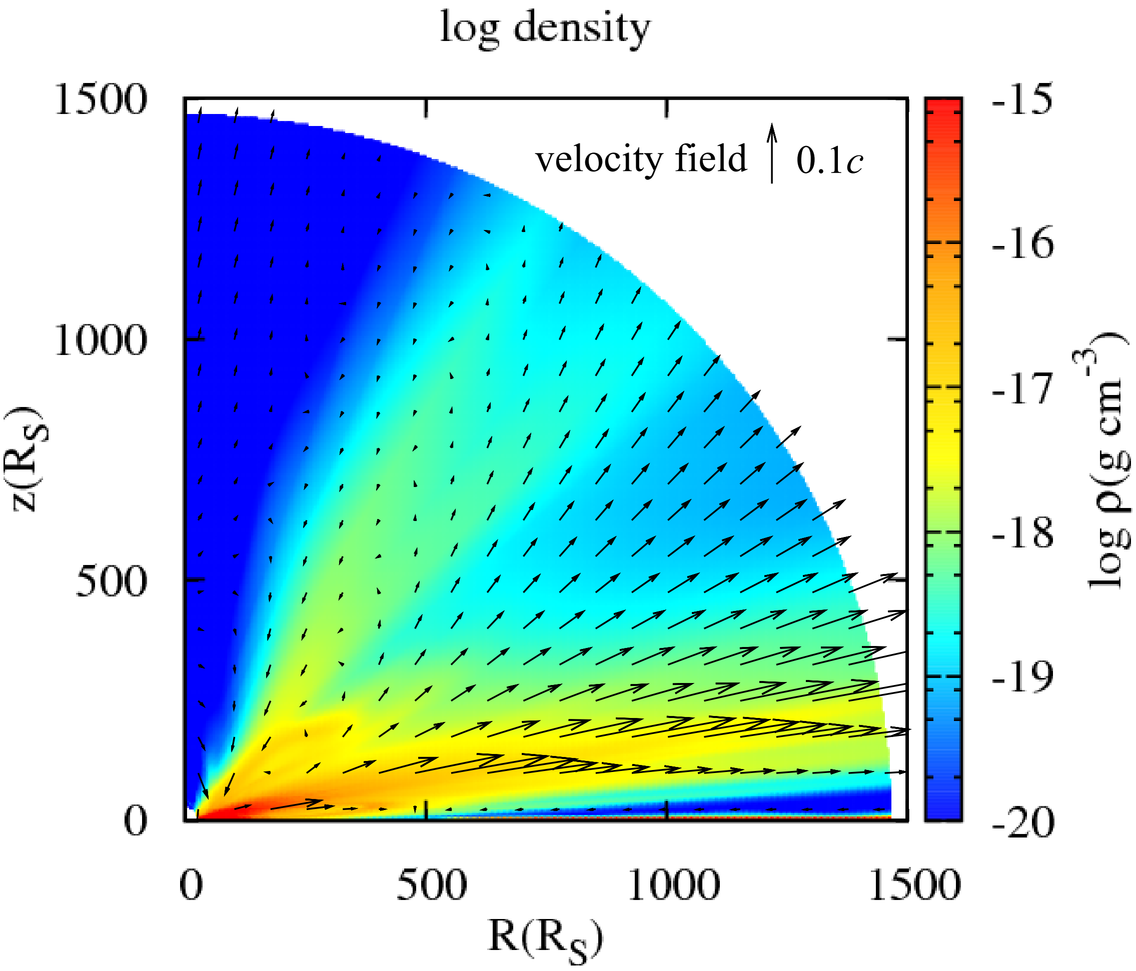

Figure 7.2: Time-averaged color density map of the line-driven disc-wind structure for a black hole mass of $M_{\rm BH} = 10^8\,M_\odot$ and Eddington ratio of $L/L_{\rm Edd} = 0.1$ where the vectors represent the velocity field and the strength. The x-axis (radial direction) corresponds to the accretion disc surface and the z-axis is the rotational axis of the accretion disc and the colour bar shows the density of the material. This plot is showing that the gas is launched vertically from the inner disc surface $(30 - 40\,R_{\rm s})$ relatively close to the black hole. Subsequently, the direction of the acceleration bends towards the radial direction where the outflow is driven with an opening angle of $\sim 80°$. Figure taken directly from Nomura & Ohsuga (2016)

7.2 PDS 456 in context of AGN–host-galaxy feedback

Although SMBHs are a 1000 times less massive and have a scale scale up to 10^9 times smaller than their host galaxies, it is established that there is a tight correlation between the two (see Chapter 1). This is seen in terms of the relation between the black hole mass and the velocity dispersion of the stars in the galaxy bulge (Ferrarese & Merritt 2000; Gebhardt et al. 2000). Due to the high accretion efficiency of many SMBHs, the total bolometric output of AGN can potentially act as a source of mechanical feedback regulating the host galaxy evolution (e.g., Silk & Rees 1998; Fabian 1999). A plausible link that can provide the mechanical feedback between the AGN and their host galaxies are in fact "AGN winds", which are theoretically expected to have a direct impact on the surrounding galactic environment (e.g., King 2003). In this work we have seen that AGN outflows can be observed through absorption (or emission) signatures in their spectra. Accurate spectroscopic measurements in the X-ray band have established the presence of complex absorbers with distinct physical properties, such as ionization, column density and outflow velocities. The relatively low density and *slow* warm absorbers, outflowing typically at hundreds of $\mathrm{km\,s^{-1}}$ (e.g., Kaspi et al. 2002; Blustin et al. 2005), generally do not provide enough kinetic power ($< 0.5\%$ of L_{Edd}) to impart sufficient mechanical feedback upon the host galactic environment (e.g., Hopkins & Elvis 2010). On the other hand the highly ionized *fast winds* may well produce enough mechanical power to have a significant effect on their host galaxies. As we have seen with PDS 456, a mass outflow rate of $10 M_{\odot}\,\mathrm{yr}^{-1}$ results in the wind having a kinetic power which is a significant fraction of L_{bol}, likely reaching up to $10^{46}\,\mathrm{erg\,s^{-1}}$. Integrating over the lifetime of the AGN, of at least 10^8 years, the total mechanical wind energy can plausibly exceed the gravitational binding energy of its host galaxy bulge of $\sim M_{\mathrm{bulge}}\sigma^2 \sim 10^{60}\,\mathrm{erg}$ (Nardini et al. 2015).

These fast, highly ionized outflows, as observed in PDS 456, might be launched from the inner regions of the accretion disc provided that the radiation and/or magnetic force (or the contribution of both) overcomes the gravitational force due to the SMBH. However outflows of distinct properties can be detected across the entire electromagnetic spectrum. The observation in a specific energy band might probe an outflow component in a distinct phase, such as fast, ionized (mainly Fe XXV–Fe XXVI) gas observed very close to the black hole, to cold molecular gas observed on kpc scales (e.g. observed as blueshifted OH$\lambda 119\mu$m Sturm et al. 2011; CO(1–0)$\lambda 2.6$ mm Feruglio et al. 2010). In the latter phase, the molecular outflow is characterized by a much higher mass outflow rate, (theoretically predicted to be up to $\sim 1000\,M_{\odot}\,\mathrm{yr}^{-1}$ Zubovas & King 2012) and can have typical outflow velocities of up to $v_{\mathrm{w}} \sim 1000 - 1500$ km s^{-1} on kpc scales. In comparison the mass outflow rates of the innermost AGN winds are much smaller, of the order of solar masses per year, although the kinetic power can be similar given their faster velocities.

In two recent observations of the ULIRGs IRAS–F11119+3257 (Tombesi et al. 2015) and Mrk231 (Feruglio et al. 2015) it was possible to simultaneously observe the highly ionized X-ray wind together with a massive galactic molecular outflow. Furthermore these fast highly ionized disc-winds, as observed here in PDS 456, may be the initial stage of the sweeping process that leads to *energy–driven* molecular mass outflows of hundreds to thousands $M_{\odot}\,\mathrm{yr}^{-1}$ out on the larger scales of the AGN host galaxy. A comparison between the momentum rate to the radiation force ($\dot{p}_{\mathrm{w}}/(L_{\mathrm{AGN}}/c)$) of the inner fast winds observed in quasars (including PDS 456: Gofford et al. 2014, PG 1211+143:Pounds & Reeves 2009 and APM 08279+4244:Chartas et al. 2009) and the molecular outflows observed in ULIRG (e.g., Feruglio et al. 2010; Cicone et al. 2014; Tombesi et al. 2015) is shown in Fig. 7.3. Here Tombesi et al. (2015) found that on large scales, the molecular outflow has to receive a substantial momentum boost (by a factor of up to a ×100), when compared to the much lower momentum rates seen on the scale of the inner black hole wind which are of the order $\sim L/c$. This work showed that the large scale molecular outflows are required to be *energy–driven* and directly supports the idea that winds in AGN provide an efficient way of directly imparting energy to the galaxy interstellar medium, which might then explain the observed large-scale outflows in many ULIRGs (e.g., Feruglio et al. 2010; Sturm et al. 2011; Cicone et al. 2014; Tombesi et al. 2015).

The two cases of *momentum–driven* and *energy–driven* outflows correspond to how efficiently the initial wind energy is transmitted to the outflow. In the former case the flows are able to cool efficiently, e.g. via Compton cooling in the quasar radiation field. The shocked wind gas is compressed to high density and hence forms a geometrically thin shell, as shown in Fig. 7.4 (top panel) and radiates away almost all of the wind kinetic energy so that $\dot{E}_{\rm flow} \ll \dot{E}_{\rm w} = L_{\rm Edd}(\eta/2)$. On small scales the momentum rate of the outflows remain of the order $\dot{p}_{\rm w} \sim L_{\rm Edd}/c$ and require a continuous injection to be pushed outwards without stalling (e.g., Fabian 1999; King 2003; McQuillin & McLaughlin 2012).

On the other hand the energy–driven flows are not efficiently cooled, leading to a geometrically thick shell (see Fig. 7.4 bottom panel) that expands adiabatically as a hot bubble by thermal pressure exerted by the hot gas (King 2010). The adiabatic hot bubbles' thermal expansion drives the wind into the host interstellar medium more vigorously than in the momentum–driven scenario as the flow rate is $\dot{E}_{\rm flow} \sim \dot{E}_{\rm w} = L_{\rm Edd}(\eta/2) \sim 0.05 L_{\rm Edd}$ and as a result it receives a momentum boost. This is why the observed galaxy-wide molecular outflows must be energy–driven and subsequently can become efficient at removing gas and dust from the central regions of the galaxy. Thus momentum–driven shells are Compton cooled which implies that initially a momentum–driven shell of gas will undergo a transition to an energy–driven phase when the rate of incident X-ray photons is no longer sufficient to enable efficient cooling. This can occur on distances of the order $\simeq 10\,{\rm pc}$ from the SMBH for a typical $M_{\rm BH} = 10^8\,M_\odot$ black hole with a $v_{\rm w} \sim 0.03c$ wind (McQuillin & McLaughlin 2013). Potentially at larger scales the initial fast outflow launched from the accretion disc can drive material out from the galaxy and as a consequence limit the growth of the bulge by quenching star formation by clearing out the surrounding medium.

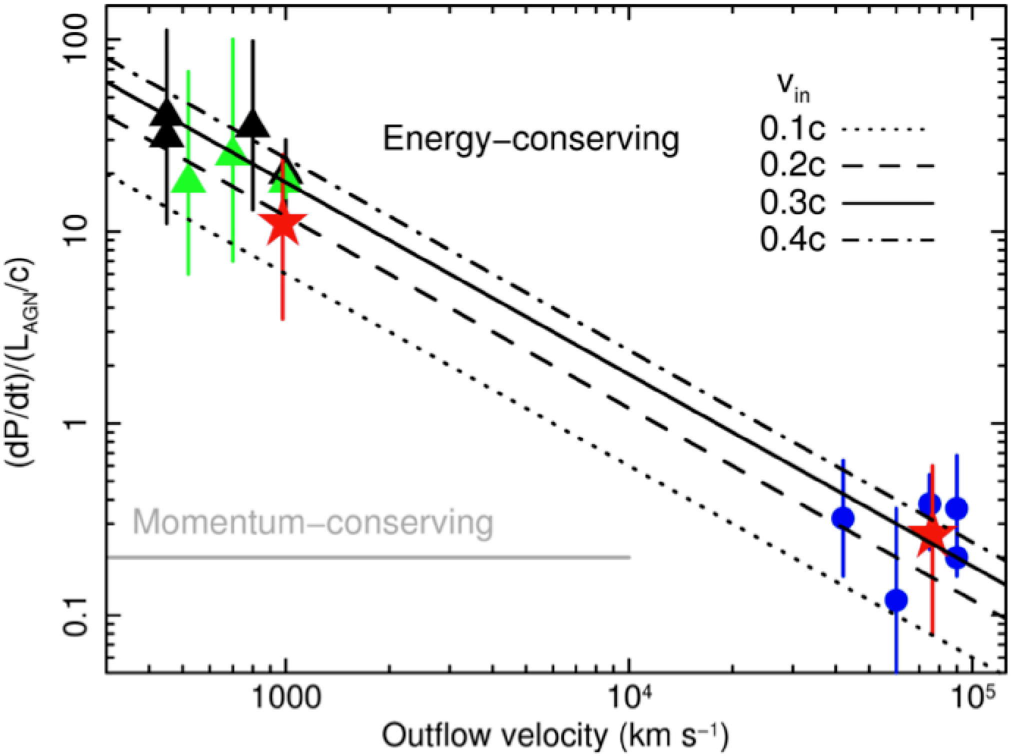

Figure 7.3: Comparison between the fast and molecular outflow in IRAS–F11119+3257 (red filled stars), with the disc-winds observed in other quasars, including PDS 456, (blue filled circles) and the molecular outflows of other ULIRGs (OH green and CO black filled triangles) are shown. Uncertainties are at the 1σ confidence level. The black curves represent the energy-conserving trends (e.g., Zubovas & King 2012), whereas the horizontal gray line indicates the momentum-conserving case. Figure taken directly from Tombesi et al. (2015)

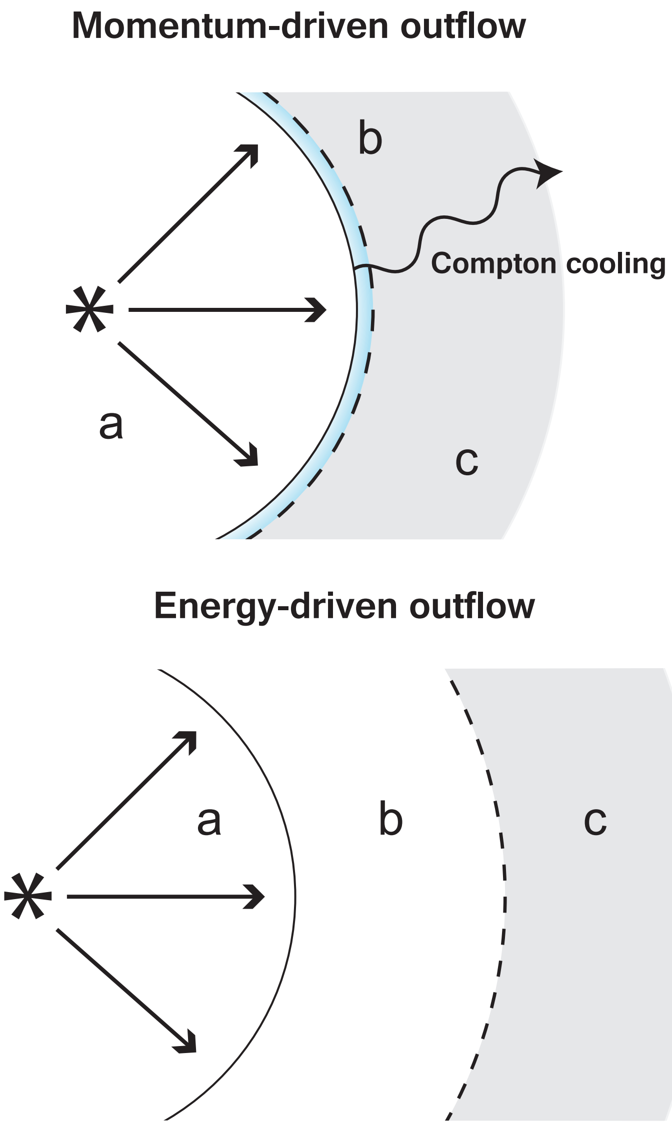

Momentum-driven outflow

Energy-driven outflow

Figure 7.4: Schematic representation of the difference between momentum and energy–driven AGN outflows. Top panel: A momentum–driven outflow which occurs when the inner-flow (region a) is able to cool efficiently (as it passes region b), e.g. via Compton cooling in the quasar radiation field. The shocked wind gas is compressed to high density and hence forms a geometrically thin shell (shown in light blue), and radiates away almost all of the wind kinetic energy. Bottom panel: Energy–driven flows (region a) are not efficiently cooled, leading to a geometrically thick shell (region b) that expands adiabatically as a hot bubble by thermal pressure exerted by the hot gas (region c). Figure taken directly from Costa, Sijacki & Haehnelt (2014)

7.3 Future prospects for PDS 456 and beyond

Throughout this work, I discussed the importance of AGN accretion disc-winds in shaping their host galaxy and how PDS 456, in particular, is considered the "Rosetta Stone" of black hole winds due to its vicinity and the powerful outflow detected across the X-ray spectrum. In AGN studies, X-ray spectroscopy is indeed one of the best methods to investigate the complex physical processes occurring in the inner regions of the black hole accretion disc. However the understanding of the underlying physical systems through this method relies on the sophistication of the applied theoretical models. Earlier in § 4.4 I discussed, for instance, that an initial step for investigating an absorption feature in AGN is to measure their individual line properties (such energy, equivalent width and line broadening) using Gaussian fitting. This is followed by adopting a phenomenological model which is generated from photo-ionization codes such as XSTAR in order to deduce ionization / density structure of the absorber (see § 4.4.3). However a limitation associated with the XSTAR code is that it does not take into account the effects of Compton scattering in the outflow and hence the full physics of the system. XSTAR is essentially a 1D radiative transfer code, assuming spherical symmetry around an illuminated shell of gas (or part thereof). Nonetheless we have seen that in the analysis in Chapter 4, I included the XSTAR emission as well as the absorption which provided a simplified 1D parametrization of the wind.

7.3.1 Disc-wind models

A more sophisticated model with the aim to tackle those limitations has been developed by Sim et al. (2008, 2010) through a 3D Monte Carlo radiative transfer code for calculating Compton-thick disc-wind spectra. The model calculates the spectra over grid points in the $x-z$ plane and is assumed to be symmetric about the polar (z) axis in the azimuthal direction (see Fig. 7.5)

The model creates tables of simulated wind-spectra which take into account the effects of the radiation transmitted through the wind, including scattering and reflected emission (Fe Kα included) from the flow. An interesting outcome from this model is that the disc-wind itself can give rise to Fe K emission, with line widths of the order FWHM ~ 1 keV obtained by the combination of both velocity-shear in the flow, its rotation around the polar axis and from the Compton scattering of the Fe Kα line photons in the wind. Thus disc-wind models can provide a physically motivated self-consistent treatment of both the absorption and emission that is produced in the wind as well as computing the ionization state and velocity field within the flow, which can be applied to spectra within XSPEC. Note that the Sim et al. model calculates the ionization at each point in the wind over a wide range of ionization states. For iron, this covers charge states from Fe X-XXVII and the output spectra include not just the absorption and emission at Fe K, but also from L-shell iron and the K-shell lines of lighter elements in the soft X-ray band.

In the disc-wind model, the resulting spectra are strongly dependent on the line-of-sight orientation, which is specified by $\mu = \cos\theta$, where θ is measured with respect to the polar axis. Thus Fig. 7.5 shows that increasing the inclination towards the equatorial, the line-of-sight will intercept a greater column of less ionized gas. The effect of the inclination imprinted in the output simulated spectra for three cases i.e., $\mu = 0.875$ (face-on, red), $\mu = 0.575$ (intermediate, green), $\mu = 0.275$ (equatorial, blue), are illustrated in Fig. 7.6 (left). This plot shows that at low values of θ, where the line-of-sight points towards the disc plane (i.e., high values of μ), the resulting spectra will have little absorption imprinted as the primary continuum radiation can reach the observer without being absorbed by the bi-conical wind structure, while reflection (or scattering) of X-rays off material on the wind outer surface can still produce broad Fe K emission features superimposed on the direct continuum. At the other extreme, at highest equatorial inclination (i.e., low values of μ) the primary continuum radiation becomes increasingly suppressed by Compton thick absorption and scattering processes. Here the line-of-sight passes through the least ionized material located towards the base of the flow, where the resulting spectrum becomes highly absorbed and reflection dominated. At intermediate inclinations, the resulting spectrum is characterized by strong blue-shifted absorption lines in the Fe K band, produced by highly ionized iron such as Fe XXV and Fe XXVI

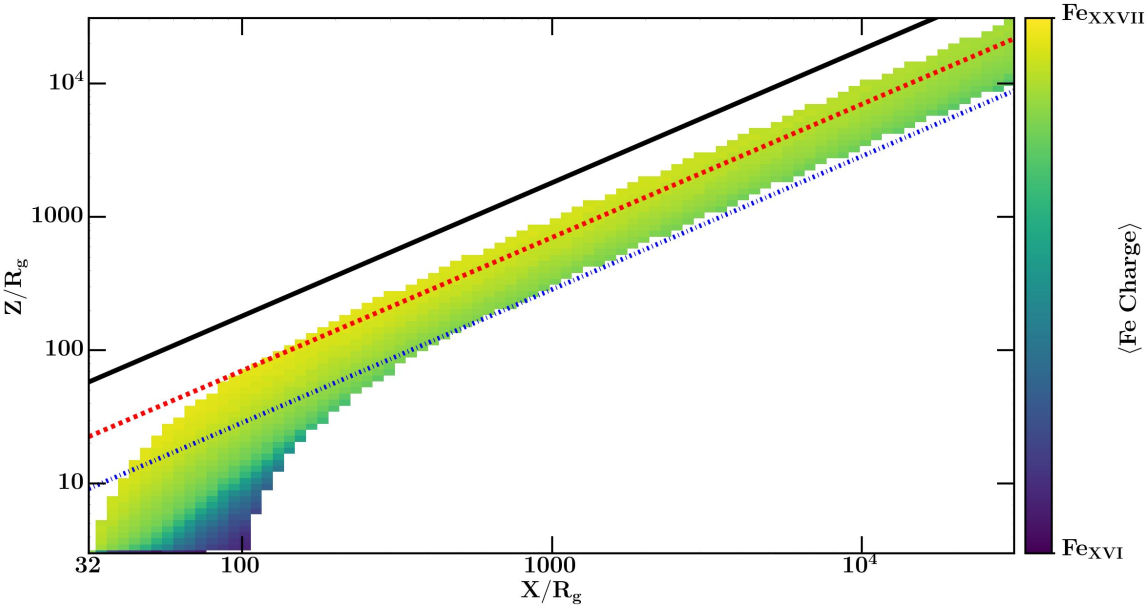

Figure 7.5: An illustration of a disc-wind model obtained using the radiative transfer code of Sim et al. (2010). The plot shows the distribution of Fe ionization states throughout the wind (the darker shades are less ionized). The inner surface of the wind is less ionized than the outer surface due to the effects of shielding from the central X-ray source.The three diagonal lines correspond to different line-of-sight inclinations through the flow, from face-on ($\mu = \cos\theta = 0.875$, black solid line) to equatorial inclination ($\mu = \cos\theta = 0.275$ blue dashed line). Note the inclination is measured with respect to the polar z axis. By increasing the inclination towards the equatorial direction, the line-of-sight will intercept a greater column of less ionized gas and the output spectra will be more absorbed. The units on both axis are given in gravitational radii ($R_{\rm g}$) from the black hole. In this example the wind is launched between $32 - 100\,R_{\rm g}$ from the black hole.

that intercept the line-of-sight.

The right panel in Fig. 7.6 shows that the change in the overall mass outflow rate $\dot{M}_{\rm w}$ has a strong impact on the emergent simulated spectra, where in this model it is normalized to the Eddington accretion rate $\dot{M}_{\rm Edd}$, giving $\dot{M} = \dot{M}_{\rm w}/\dot{M}_{\rm Edd}$. This plot illustrates three simulated spectra (for a given inclination $\mu = 0.4$) corresponding to three different mass outflow rates, $\dot{M} = 0.1$ (red), $\dot{M} = 0.4$ (green) and $\dot{M} = 1.0$ (blue). Thus for low $\dot{M}$ the spectrum presents a weak Fe K absorption line, which becomes stronger as $\dot{M}$ increases towards the Eddington rate. Furthermore as $\dot{M}$ increases, the gas becomes denser and hence less ionized resulting in a harder spectral shape with absorption lines becoming apparent in the soft X-ray band. With this model it is therefore possible to directly measure the mass outflow rate, rather than estimate it through the many geometrical assumptions resulting from ad-hoc spectral fitting of 1D photoionization models.

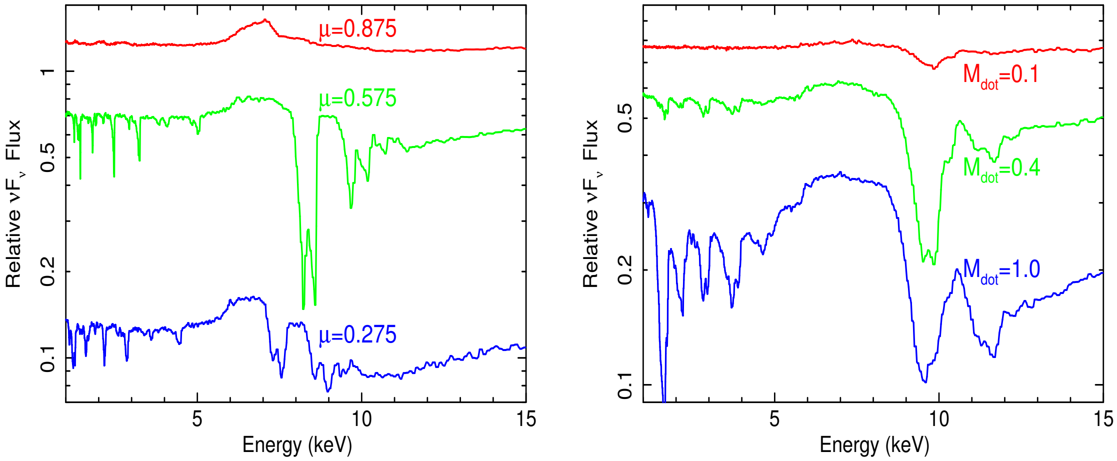

Figure 7.6: Plots showing six examples of simulated spectra generated from the disc-wind model of Sim et al. (2008, 2010). Left panel: spectra generated for three different inclinations, changing from face-on (red, $\mu = \cos\theta = 0.875$), intermediate (green, $\mu = 0.575$) and equatorial (blue, $\mu = 0.275$). For face-on inclinations, as line-of-sight does not directly intercept the flow, the resulting spectrum present very little absorption, although a weak emission line from scattering off the surface of the wind is imprinted on it. At the other extreme (equatorial inclinations), the line-of-sight becomes Compton thick, thus the resulting spectrum is dominated by scattering processes off the wind surface, while the direct continuum is suppressed. At intermediate inclinations, the spectrum is characterized by strong absorption lines in the Fe K band, produced by highly ionized iron such as Fe XXV and Fe XXVI that intercept the line-of-sight. Right panel: three spectra generated from different mass outflow rates $\dot{M}$, changing from 10% (red) to 100% of Eddington (blue), for a given inclination ($\mu = 0.4$). Note how the output spectra are sensitive to the wind outflow rate, where the absorption becomes deeper (denser and least ionized) as the $\dot{M}$ increases towards the Eddington outflow rate value.

Investigating the disc-wind modelling is indeed a possible future direction for PDS 456, where a suitable grid for PDS 456 has been already generated and originally applied by Reeves et al. (2014) to the 2007 and 2011 *Suzaku* spectra. Therefore one possible future aim would be to apply the disc-wind modelling to all the available PDS 456 spectra over all epochs, where it will be possible to explain the causes of the observed wind variability with a physically realistic model. For instance we can differentiate between: (i) changes in the ionization/photoionizing continuum, (ii) changes in the mass outflow rate and/or (iii) changes in the launch radius. Fig. 7.7 shows an example of disc-wind modelling applied to the low-flux *Suzaku* 2013c observation of PDS 456, where the Fe K absorption feature is very strong.

Here it was possible to replicate well the fast $v_{\rm w} \sim 0.25c$ outflow in the spectrum, requiring a mass outlow rate of $\dot{M}_{\rm w} \sim 0.4\dot{M}_{\rm Edd}$ ($\sim 10\,M_{\odot}\,{\rm yr}^{-1}$) and an inclination angle of $\theta \sim 75^{\circ}$ ($\mu = 0.375$). At this low inclination, the line-of-sight will intercept the thick part of the wind, with a total column of $N_{\rm H} \sim 10^{24}\,{\rm cm}^{-2}$, resulting in a strong iron K absorption line. The wind is launched from an inner radius of $32\,R_{\rm g}$, with a corresponding terminal velocity of $0.25c$, although the latter can be fine tuned as required in the model. The relative level of X-ray illumination is also low, with a ratio of the 2-10 keV X-ray luminosity to Eddington luminosity of 0.5%, together with a steep X-ray photon index of $\Gamma = 2.4$. As discussed earlier in the chapter, the relative X-ray weakness of AGN like PDS 456 is favourable to the production of disc-winds and in preventing the absorbing matter from becoming too highly ionized.

These preliminary results suggest that the disc-wind spectral signatures are indeed observed across the X-ray spectrum, where the re-processing of the incident X-ray photons might produce, self-consistently, broad Fe Kα features and highly ionized absorption lines. These results are promising and for this reason disc-wind models are currently not only being developed for PDS 456, but also for other AGN with fast winds such as PG 1211+143 and other NLSy1 (e.g., 1H 0707–495, Mrk 766) where strong Fe K features are observed. Furthermore a study from Tatum et al. (2012) has demonstrated that the broad Fe Kα profile and Compton hump observed in several "bare" (i.e., un-absorbed) Seyfert galaxies can be modelled as the face-on scattered emission from the surface of a

Compton-thick wind. This also raises the possibility of studying winds indirectly through their scattered spectra.

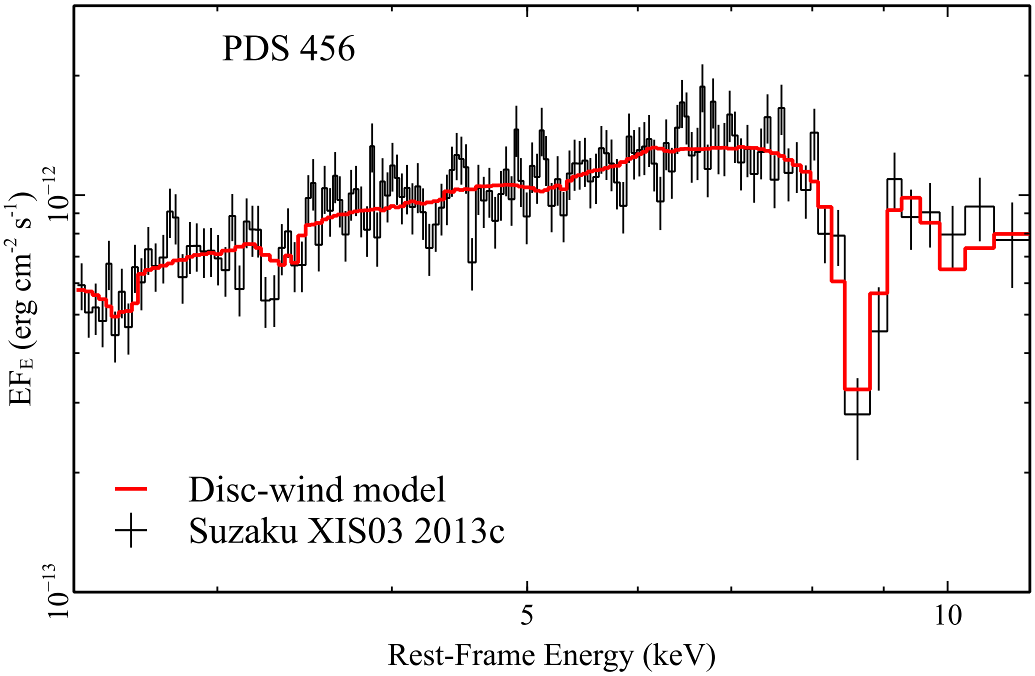

Figure 7.7: The Sim et al. (2010) wind model applied to the PDS 456 *Suzaku* 2013c observation. The data and model are shown in black and red, respectively. It is clear that the model is able to replicate very well the absorption centred at ~ 8.7 keV (rest-frame), from a relatively equatorial wind (with $\mu \sim 0.4$) and a mass outflow rate of $\dot{M} = 0.4$.

7.3.2 Future multiwavelength observations of PDS 456

Sub-millimeter signatures of a large scale outflow

Revealing the nature of the powerful outflow in this nearby quasar PDS 456 might be key in understanding the correlation between the quasar wind and the galactic scale feedback processes, which is thought to be common in the early Universe at $z = 2 - 3$

(Di Matteo, Springel & Hernquist 2005). Thus it will be important to establish a direct connection between the inner AGN wind, via the fast outflow, and the wider scale molecular outflow, as shown earlier in the work of Tombesi et al. (2015). This can be investigated through observations with the ground-based Atacama Large Millimetre Array *ALMA* radio interferometer, where it will be possible to probe the larger scale colder gas content and its kinematics. Indeed follow-up *ALMA* observations of PDS 456 have been already approved (PI Piconcelli). On the other hand, another approach is to search for signatures of an X-ray wind in AGN which have known large scale molecular outflows in order to establish the possible correlation in the outflow momentum rate shown by Tombesi et al. (2015).

Optical/UV and X-ray Monitoring

Earlier in § 2.2 I estimated the UV to X-ray spectral index $\alpha_{\rm ox}$ corresponding to the two extremities (in flux) in PDS 456. In the case when PDS 456 is at its lowest flux, during the *Suzaku* 2013 campaign (i.e., 2013b) I measured $\alpha_{\rm ox} = 2.1$, which suggests that in this flux-state PDS 456 might present some characteristics which are recognized in BALQSOs, i.e. a low X-ray to UV flux ratio due to enhanced X-ray absorption. The characteristic spectral signature imprinted on BALQSOs are the blueshifted broad absorption line (BAL) troughs due to resonant transitions of ionized metals e.g., C IV, N V, O VI, Si IV, from a fast UV wind.

While classic BAL features in PDS 456 were not observed in the earlier HST observation, it did have some BAL like characteristics (see Chapter 2). Therefore a subsequent campaign has been approved with *XMM-Newton* & *NuSTAR* and the *HST* Cosmic Origins Spectrograph (COS) to simultaneously measure the X-ray and UV components of the wind (PI Reeves), which will commence in March 2017. From this it will be possible to measure any change in the UV line profiles between epochs and determine how they may react to changes in the X-ray absorber. Furthermore if PDS 456 is caught in a highly absorbed state, like the one observed during the Suzaku 2013 campaign, this might reveal the presence of the above broad absorption lines. Indeed the archetypal Sy1 galaxy, NGC 5548, showed a similar behaviour with the UV BAL profiles from an outflow emerging during an extended period of high X-ray obscuation (Kaastra et al. 2014).

Furthermore to supplement this, our group has also had approved a monitoring campaign with *Swift* (PI Braito), which will consist of approximately 40×3 ks snapshots over weekly intervals during 2017. The aim will be to simultaneously monitor PDS 456 both in the optical/UV band (with V and UVW1 band photometry with *Swift/UVOT*) and in X-rays. As I have discussed in earlier chapters, PDS 456 shows drastic variability in the X-ray band and it will be important to understand how the whole SED varies during the course of the campaign and especially during any prolonged low or flaring states.

Future X-ray Observatories

In early 2016 the long awaited *HITOMI* X-ray satellite (*ASTRO-H*) was launched. The Soft X-ray Spectrometer (SXS) on board *Astro-H*/*HITOMI* (Takahashi et al. 2010) was the primary instrument, which consists of a micro calorimeter array capable of achieving high spectral resolution of ~ 5 eV (FWHM) at 6 keV. This instrument would have proven critical for our understandimg of outflows from AGN at Fe K, with a resolution 25 times better than that of the CCDs on board *XMM-Newton* or *Suzaku*. Indeed AGN like PDS 456 were among the early list of targets to be observed within the first year of the mission. As shown by the *HITOMI* observation of the Perseus cluster of galaxies (Hitomi Collaboration et al. 2016), the SXS achieved its goal of high resolution X-ray spectroscopy, resolving a wealth of ionized Fe K emission lines from this cluster. Unfortunately within a couple of months it became non-operational due to an anomaly on the on-board computer software[1]. Although yet to be formally announced, NASA and JAXA are attempting a replacement mission, which hopefully will be launched within a 5-6 year time-scale.

---

[1] http://global.jaxa.jp/projects/sat/astro-h

Going to the next decade what will be critical to the success of this research field will be the forthcoming ESA mission Advanced Telescope for High ENergy Astrophysics or *ATHENA* (Nandra et al. 2013), which is scheduled to be launched on 2028. It is planned to house a single X-ray telescope with a collecting area of $2\,\mathrm{m}^2$ together with a payload of two interchangeable scientific instruments in the focal plane which are:

- the Wide Field Imager (WFI), which is a solid-state spectrometer with a large $40'$ FOV operating between $\sim 0.1-15\,\mathrm{keV}$,
- X-ray Integral Field Unit (X-IFU), consisting of a micro-calorimeter which has a very high effective area ($\simeq 0.65\,\mathrm{m}^2$ at $6\,\mathrm{keV}$) coupled with a minimum (expected) energy resolution of FWHM $\simeq 2.5\,\mathrm{eV}$ ($\simeq 1.5\,\mathrm{eV}$) from $\sim 0.1\,\mathrm{keV}$ through to $\sim 12-13\,\mathrm{keV}$. This will provide an unprecedented sensitivity, $3-5$ times greater than the SXS that hopefully will be on board of *ASTRO-H2*. This will represent a huge advance in the high resolution spectroscopy from the soft X-rays to the Fe K band.

These specifications will provide an unprecedented understanding of iron K winds as it will be possible to investigate individual line profiles in greater detail, where the velocity broadening can be measured down to $\sim 50-100\,\mathrm{km\,s^{-1}}$ at $\sim 6\,\mathrm{keV}$. Such high spectral resolution will make it possible to reveal the fine substructures of the Fe lines, such as for instance the components of the He-like triplet of Fe XXV. The X-IFU will be able to resolve the multi-phase and likely blended (at CCD resolution) absorber in PDS 456 (e.g., Reeves, O'Brien & Ward 2003; Reeves et al. 2009) into its constituent lines as shown in a 100 ks simulation of PDS 456 in Fig. 7.8). It will also be possible to perform a sensitive time-resolved analysis of the wind, due to the much shorter exposures that will be required.

Very importantly, the synergy between the large effective area and high spectral resolution means that not only we will be able to study in exquisite detail the nearest and the brightest examples of these quasar winds, but it will be possible to carry out detailed spectroscopy on relatively faint, high redshift quasars. This is one of the key science goals of *ATHENA*, as this is where black hole accretion was at its peak (i.e. at $z \sim 2$) and where powerful winds, like the one in PDS 456, may be more common place. Thus *ATHENA* may have the potential to reveal the impact of winds in AGN and their host galaxies in the high redshift Universe, which is currently limited to only the nearest and brightest AGN.

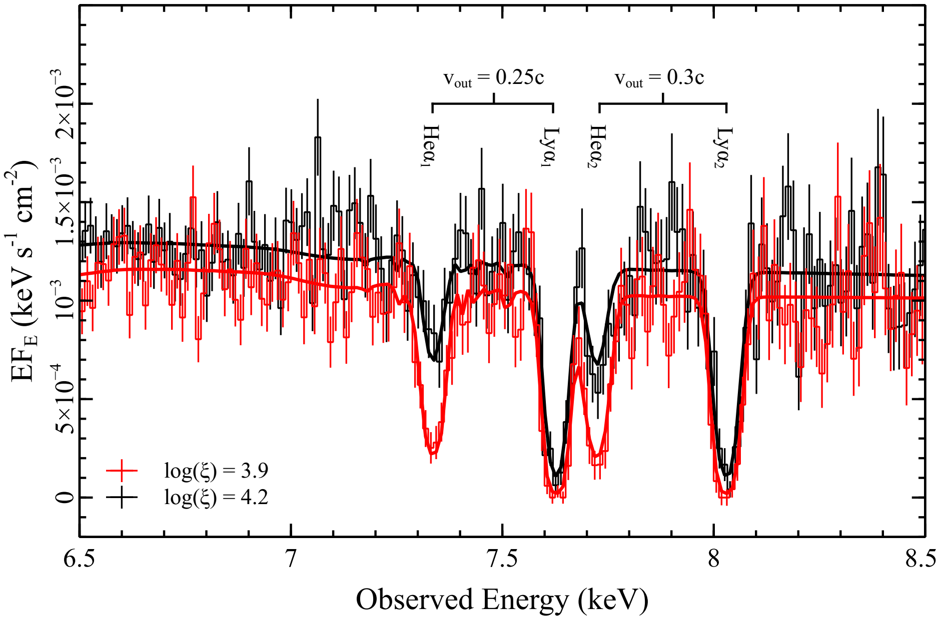

Figure 7.8: Simulation of how the *Suzaku* spectra of PDS 456 will look in a 100 ks *ATHENA* X-IFU observation. The black and red spectra correspond to the 2007 and 2011 observations respectively, whilst the best-fitting spectral models to both datasets are shown in black and red solid lines respectively. The simulation was assuming an X-IFU energy resolution of $\Delta E = 2.5\,\mathrm{eV}$, which corresponds to the minimum specification of the detector, whereas the mission resolution goal of $\Delta E = 1.5\,\mathrm{eV}$ will provide even more precise results. These simulated spectra were made available by J. Reeves and V. Braito on behalf of the *ATHENA* science group.

7.3.3 The "bare" AGN sample

Another aspect that I studied in Chapter 6 is the X-ray continuum variability in PDS 456 when it was observed with virtually no absorption (or "bare") in 2007 with *Suzaku*. The rapid variability present during this observation provided an opportunity to investigate the intrinsic variability mechanism in a high luminosity AGN as a "clean" view of the primary continuum was allowed to be observed. In addition to this, regardless of being in a "bare" state, the ultra fast outflow was still present.

On this basis, one of the key aspects to investigate, in order to understand the physical mechanism involved in powering the winds, are the fundamental properties of the accretion processes in luminous AGN. Thus with this in mind, I selected a sub-sample of nine of the brightest *"bare" AGN* where the term "bare" refers to a subclass of AGN characterized by a notable lack of intrinsic absorption resulting in a prominent soft X-ray excess and an intense broad Fe K emission line (originating from the inner disc in the vicinity of the black hole) present in the X-ray spectrum. Thus the "clean" spectrum of these "bare" objects unimpeded by any absorption will allow us to study directly the intrinsic properties of the central engine close to the black hole.

TON S180 the benchmark AGN

From this sub sample, I have been awarded recently a simultaneous *XMM-Newton* & *NuSTAR* observation of the "bare" NLSy1 TON S180, where for the first time it will be possible to simultaneously reveal the broad-band UV to hard X-ray emission, giving unique insight into the nature of the X-ray continuum and central engine. In all the past observations up to $\sim 10\,\mathrm{keV}$ (like e.g., *XMM-Newton* observation alone) TON S180 presents a pronounced and smooth soft excess, which without the hard X-ray band can be equally modelled by either Comptonized accretion disc emission or by relativistic reflection arising off the very inner accretion disc around a maximally spinning black hole. However, the same can be said if the modelling is based only on the hard X-ray data above 3 keV, indeed without the soft X-ray band information several solutions will be degenerate. Furthermore, like many other NLSy1, TON S180 is highly variable, thus a simultaneous fitting of single-epoch spectra alone would not provide any strong constraint on the origin of the intrinsic X-ray emission without accounting for the spectral variability of the AGN.

With the simultaneous *NuSTAR* & *XMM-Newton* data, covering the optical/UV to hard X-ray band, I will discriminate between models and determine the origin of both the soft and hard excesses. More specifically I will:

(i) determine the **true shape** of the primary X-ray continuum. This can be achieved by applying self-consistent Comptonised accretion disc models, e.g. `optxagnf` and taking advantage of the simultaneous optical/UV photometry that is provided by the OM, yielding the SED from the optical to hard X-rays.

(ii) test if either a dual Comptonisation model (warm disc plus hot corona) or a highly blurred reflection model, can simultaneously reproduce both the soft excess and hard X-ray emission.

In Figure 7.9, I show a preliminary example of how the broadband SED of TON S180 can be constructed from the optical/UV to hard X-ray. For informative purposes only the SED was modelled with a baseline self-consistent disc/coronal model `optxagnf` and I find that it reproduces well the shape of the UV bump, the soft excess and the hard X-ray power-law component in TON S180. As a preliminary result we find that it is radiating at near the ($\sim 70\%$) Eddington luminosity. This may confirm the nature of the NLSy1s, which are thought to have high accretion rates but low black hole masses ($10^6 - 10^7\, M_\odot$).

The bright "bare" Seyfert sample

In addition to the recent TON S180 data, this project will undertake a study of a sample of archival *XMM-Newton* and *NuSTAR* data. The selection of this bright "bare" sample is based on the precise scope of exploiting their high quality *XMM-Newton* EPIC-pn spectra, (of the order of $\gtrsim 10^6$ counts) making it possible to define the X-ray continuum and any accretion disc emission precisely. The sources included in the sample are: 3C 120, 3C 390.3, Ark 120, Ark 564, Fairall 9, Mrk 509, PKS 0558-504 and TON S180. The combination of the *XMM-Newton* and *NuSTAR* data will make possible to obtain unprecedented

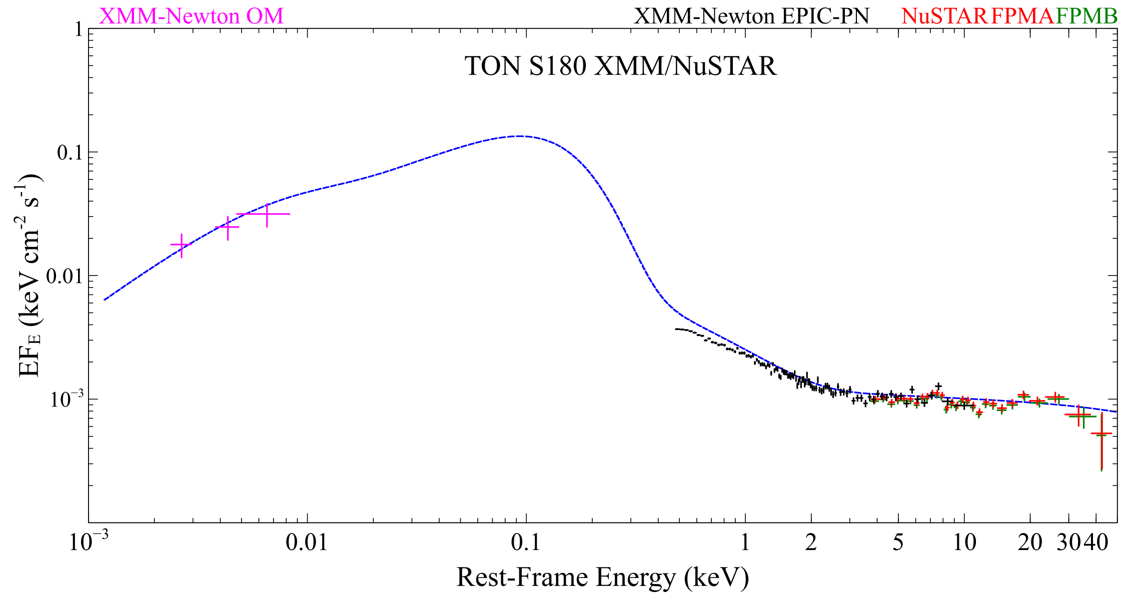

Figure 7.9: Optical to hard X-ray spectral energy distribution (SED) of TON S180 obtained by including the OM (magenta), *XMM-Newton* EPIC-pn (black) and *NuSTAR* FMPA (red) and FPMB (green) data from the *XMM-Newton/NuSTAR* observation in June 2016 (PI Gabriele Matzeu). The SED was fitted with the disc/corona model (blue dashed line). The slight roll-over below 1 keV in the EPIC-pn spectra can be accounted for by a Galactic absorption column of $1.36 \times 10^{20}\,\mathrm{cm}^{-2}$. The entire SED can be accounted for by thermal emission from the disc (UV) plus Comptonized emission from the corona at a high fraction ($\sim 70\%$) of the Eddington limit.

information on the hard X-rays above 10 keV and hence with the synergy of these two X-ray telescopes it will be possible to obtain high quality broadband spectra from the optical band to hard X-rays and hence investigate important questions such as:

(i) are these “bare” AGN truly intrinsically unabsorbed or their appearance is possibly due to a ‘favourable’ (e.g., face-on) line-of-sight?

(ii) is there any material out of the line-of-sight, and if so can it be characterized by how much of the distant (i.e. neutral Fe Kα line) reflection component is detected in the X-ray spectra (thought to arise from the pc-scale torus) and by the flux of any photoionized emission lines in the soft X-ray spectrum (measured with the *XMM-Newton* RGS) such as from O, Ne and Mg?

(iii) can we get more information on the inner most stable circular orbit (R_{ISCO}) and potentially the black hole spin by analysing the degree of broadening of the Fe K line and Compton reflection spectrum?

(iv) can we infer the properties of the central engine, corona, accretion disc geometry and origin of the, still disputed, soft excess from modelling the broadband UV to hard X-ray emission?

Eventually in a more distant future this pilot sample of "bare" AGN will be extended to a wider sample of AGN (~ 30) with little intrinsic absorption. I plan to utilize the template broadband (optical/UV to X-ray) spectra from the core nine AGN and apply these models to a wider sample from the *XMM-Newton* archives. Here I will investigate the broader picture of the physical properties of the "bare" AGN by achieving a more accurate description of the disc/corona interaction and hence further our understanding of the origin of the illusive hard and soft X-ray excess. The insight that will be gained from the study of accretion onto these "bare" AGN will make it possible to gain insight into the nature of wider AGN population as a whole and the origin of the fast wind, from a better understanding of the intrinsic continuum process.

Bibliography

Akritas M. G., Bershady M. A., 1996, ApJ, 470, 706

Aller M. C., Richstone D. O., 2007, ApJ, 665, 120

Antonucci R., 1993, Annu. Rev. Astron. Astrophys., 31, 473

Arnaud K., Smith R., Siemiginowska A., 2011, Handbook of X-ray Astronomy, Cambridge Observing Handbooks for Research Astronomers. Cambridge University Press

Arnaud K. A., 1996, in Astronomical Society of the Pacific Conference Series, Vol. 101, Astronomical Data Analysis Software and Systems V, Jacoby G. H., Barnes J., eds., p. 17

Bautista M. A., Kallman T. R., 2001, ApJS, 134, 139

Behar E., Kaspi S., Reeves J., Turner T. J., Mushotzky R., O'Brien P. T., 2010, ApJ, 712, 26

Behar E., Netzer H., 2002, ApJ, 570, 165

Behar E., Sako M., Kahn S. M., 2001, ApJ, 563, 497

Bennert V. N., Auger M. W., Treu T., Woo J.-H., Malkan M. A., 2011, ApJ, 742, 107

Bentz M. C. et al., 2013, ApJ, 767, 149

Bianchi S., Maiolino R., Risaliti G., 2012, Advances in Astronomy, 2012, 782030

Blustin A. J., Page M. J., Fuerst S. V., Branduardi-Raymont G., Ashton C. E., 2005, A&A, 431, 111

Boller T., Brandt W. N., Fink H., 1996, A&A, 305, 53

Boroson T. A., Green R. F., 1992, ApJS, 80, 109

Bottorff M. C., Korista K. T., Shlosman I., 2000, ApJ, 537, 134

Braito V. et al., 2007, ApJ, 670, 978

Brandt W. N., Alexander D. M., 2010, Proceedings of the National Academy of Sciences, 107, 7184

Brenneman L. W., Reynolds C. S., 2006, ApJ, 652, 1028

Canizares C. R. et al., 2005, PASP, 117, 1144

Cappi M. et al., 2009, A&A, 504, 401

Cardelli J. A., Clayton G. C., Mathis J. S., 1989, ApJ, 345, 245

Cash W., 1979, ApJ, 228, 939

Castor J. I., Abbott D. C., Klein R. I., 1975, ApJ, 195, 157

Chartas G., Brandt W. N., Gallagher S. C., 2003, ApJ, 595, 85

Chartas G., Brandt W. N., Gallagher S. C., Garmire G. P., 2002, ApJ, 579, 169

Chartas G., Kochanek C. S., Dai X., Poindexter S., Garmire G., 2009, ApJ, 693, 174

Cicone C. et al., 2014, A&A, 562, A21

Collin S., Kawaguchi T., 2004, A&A, 426, 797

Condon J. J., Cotton W. D., Greisen E. W., Yin Q. F., Perley R. A., Taylor G. B., Broderick J. J., 1998, AJ, 115, 1693

Costa T., Sijacki D., Haehnelt M. G., 2014, MNRAS, 444, 2355

Crummy J., Fabian A. C., Gallo L., Ross R. R., 2006, MNRAS, 365, 1067

Czerny B., Nikołajuk M., Różańska A., Dumont A.-M., Loska Z., Zycki P. T., 2003, A&A, 412, 317

de Rosa A. et al., 2012, MNRAS, 420, 2087

den Herder J. W. et al., 2001, A&A, 365, L7

Di Matteo T., 1998, MNRAS, 299, L15

Di Matteo T., Springel V., Hernquist L., 2005, Nature, 433, 604

Done C., 2010, ArXiv e-prints

Done C., Davis S. W., Jin C., Blaes O., Ward M., 2012, MNRAS, 420, 1848

Done C., Sobolewska M. A., Gierliński M., Schurch N. J., 2007, MNRAS, 374, L15

Elitzur M., 2012, ApJL, 747, L33

Fabian A. C., 1999, MNRAS, 308, L39

Fabian A. C., Lohfink A., Kara E., Parker M. L., Vasudevan R., Reynolds C. S., 2015, MNRAS, 451, 4375

Fabian A. C., Rees M. J., Stella L., White N. E., 1989, MNRAS, 238, 729

Fabian A. C. et al., 2002, MNRAS, 335, L1

Fabian A. C. et al., 2012, MNRAS, 419, 116

Ferland G. J., Rees M. J., 1988, ApJ, 332, 141

Ferrarese L., Ford H., 2005, SSRv, 116, 523

Ferrarese L., Merritt D., 2000, ApJL, 539, L9

Feruglio C. et al., 2015, A&A, 583, A99

Feruglio C., Maiolino R., Piconcelli E., Menci N., Aussel H., Lamastra A., Fiore F., 2010, A&A, 518, L155

Fukazawa Y. et al., 2011, ApJ, 727, 19

Fukumura K., Kazanas D., Contopoulos I., Behar E., 2010, ApJ, 715, 636

Fukumura K., Tombesi F., Kazanas D., Shrader C., Behar E., Contopoulos I., 2015, ApJ, 805, 17

Gallo L. C. et al., 2013, MNRAS, 428, 1191

Gebhardt K. et al., 2000, ApJL, 539, L13

George I. M., Turner T. J., Netzer H., Nandra K., Mushotzky R. F., Yaqoob T., 1998, ApJS, 114, 73

Ghisellini G., Haardt F., Matt G., 2004, A&A, 413, 535

Gierliński M., Done C., 2004, MNRAS, 349, L7

Giustini M. et al., 2011, A&A, 536, A49

Giustini M., Turner T. J., Reeves J. N., Miller L., Legg E., Kraemer S. B., George I. M., 2015, A&A, 577, A8

Gofford J. et al., 2014, ApJ, 784, 77

Gofford J., Reeves J. N., McLaughlin D. E., Braito V., Turner T. J., Tombesi F., Cappi M., 2015, MNRAS, 451, 4169

Gofford J., Reeves J. N., Tombesi F., Braito V., Turner T. J., Miller L., Cappi M., 2013, MNRAS, 430, 60

Goodrich R. W., 1989, ApJ, 342, 224

Grevesse N., Sauval A. J., 1998, SSRv, 85, 161

Guilbert P. W., Rees M. J., 1988, MNRAS, 233, 475

Gültekin K., Cackett E. M., Miller J. M., Di Matteo T., Markoff S., Richstone D. O., 2009, ApJ, 706, 404

Haardt F., Maraschi L., 1991, ApJL, 380, L51

Haardt F., Maraschi L., 1993, Astrophysical Journal, 413, 507

Hagino K., Done C., Odaka H., Watanabe S., Takahashi T., 2016a, ArXiv e-prints

Hagino K., Odaka H., Done C., Gandhi P., Watanabe S., Sako M., Takahashi T., 2015, MNRAS, 446, 663

Hagino K., Odaka H., Done C., Tomaru R., Watanabe S., Takahashi T., 2016b, MNRAS, 461, 3954

Hainline K. N., Hickox R., Greene J. E., Myers A. D., Zakamska N. L., 2013, ApJ, 774, 145

Halpern J. P., 1984, ApJ, 281, 90

Hamann F., Sabra B., 2004, in Astronomical Society of the Pacific Conference Series, Vol. 311, AGN Physics with the Sloan Digital Sky Survey, Richards G. T., Hall P. B., eds., p. 203

Häring N., Rix H.-W., 2004, ApJL, 604, L89

Harrison F., Cook W., Miyasaka H., McLean R., 2010, in Devices, Circuits, and Systems, CRC Press, pp. 67–82

Harrison F. A. et al., 2013, ApJ, 770, 103

Hitomi Collaboration et al., 2016, Nature, 535, 117

Holczer T., Behar E., 2012, ApJ, 747, 71

Holczer T., Behar E., Arav N., 2010, ApJ, 708, 981

Hopkins P. F., Elvis M., 2010, MNRAS, 401, 7

Iwasawa K., Taniguchi Y., 1993, ApJL, 413, L15

Jansen F. et al., 2001, A&A, 365, L1

Jiang P., Wang J. X., Wang T. G., 2006, ApJ, 644, 725

Jin C., Ward M., Done C., Gelbord J., 2012, MNRAS, 420, 1825

Kaastra J. S. et al., 2012, A&A, 539, A117

Kaastra J. S. et al., 2014, Science, 345, 64

Kaastra J. S., Mewe R., Liedahl D. A., Komossa S., Brinkman A. C., 2000, A&A, 354, L83

Kallman T. R., Palmeri P., Bautista M. A., Mendoza C., Krolik J. H., 2004, ApJS, 155, 675

Kara E., Fabian A. C., Cackett E. M., Uttley P., Wilkins D. R., Zoghbi A., 2013, MNRAS, 434, 1129

Kaspi S. et al., 2002, ApJ, 574, 643

Kaspi S., Brandt W. N., Netzer H., Sambruna R., Chartas G., Garmire G. P., Nousek J. A., 2000, ApJL, 535, L17

Kaspi S., Maoz D., Netzer H., Peterson B. M., Vestergaard M., Jannuzi B. T., 2005, ApJ, 629, 61

Kazanas D., Fukumura K., Behar E., Contopoulos I., Shrader C., 2012, The Astronomical Review, 7, 92

Kellermann K. I., Sramek R., Schmidt M., Shaffer D. B., Green R., 1989, AJ, 98, 1195

Kelley R. L. et al., 2007, PASJ, 59, 77

Kerr R. P., 1963, Phys. Rev. Lett., 11, 237

Khachikian E. Y., Weedman D. W., 1974, ApJ, 192, 581

King A., 2003, ApJL, 596, L27

King A. R., 2010, MNRAS, 402, 1516

King A. R., Pounds K. A., 2003, MNRAS, 345, 657

Kollatschny W., Zetzl M., 2013, A&A, 558, A26

Kormendy J., Ho L. C., 2013, Annu. Rev. Astron. Astrophys., 51, 511

Kormendy J., Richstone D., 1995, Annu. Rev. Astron. Astrophys., 33, 581

Koyama K. et al., 2007, PASJ, 59, 23

Krause M. O., 1979, Journal of Physical and Chemical Reference Data, 8

Krolik J. H., Begelman M. C., 1988, ApJ, 329, 702

Krolik J. H., Kallman T. R., 1987, ApJL, 320, L5

Laha S., Guainazzi M., Dewangan G. C., Chakravorty S., Kembhavi A. K., 2014, MNRAS, 441, 2613

Laor A., 1991, ApJ, 376, 90

Laor A., Davis S. W., 2014, MNRAS, 438, 3024

Laor A., Fiore F., Elvis M., Wilkes B. J., McDowell J. C., 1994, ApJ, 435, 611

Larkin A. C., McLaughlin D. E., 2016, MNRAS, 462, 1864

Legg E., Miller L., Turner T. J., Giustini M., Reeves J. N., Kraemer S. B., 2012, ApJ, 760, 73

Leighly K. M., O'Brien P. T., 1997, ApJL, 481, L15

Lightman A. P., White T. R., 1988, ApJ, 335, 57

Lobban A. P., Reeves J. N., Miller L., Turner T. J., Braito V., Kraemer S. B., Crenshaw D. M., 2011, MNRAS, 414, 1965

Longair M. S., 2011, High Energy Astrophysics

Longinotti A. L., Krongold Y., Guainazzi M., Giroletti M., Panessa F., Costantini E., Santos-Lleo M., Rodriguez-Pascual P., 2015, ApJL, 813, L39

Lumb D. H., Schartel N., Jansen F. A., 2012, arXiv.org

Luo B. et al., 2014, ApJ, 794, 70

Lusso E. et al., 2010, A&A, 512, A34

Lusso E., Risaliti G., 2016, ApJ, 819, 154

Lynden-Bell D., 1969, Nature, 223, 690

Magorrian J. et al., 1998, AJ, 115, 2285

Marconi A., Hunt L. K., 2003, ApJL, 589, L21

Marinucci A. et al., 2014, MNRAS, 440, 2347

Markowitz A., Reeves J. N., Braito V., 2006, ApJ, 646, 783

Mason K. O. et al., 2001, A&A, 365, L36

Matthews J. H., Knigge C., Long K. S., Sim S. A., Higginbottom N., Mangham S. W., 2016, MNRAS

Matzeu G. A., Reeves J. N., Nardini E., Braito V., Costa M. T., Tombesi F., Gofford J., 2016, MNRAS, 458, 1311

McKernan B., Yaqoob T., Reynolds C. S., 2007, MNRAS, 379, 1359

McLure R. J., Jarvis M. J., 2002, MNRAS, 337, 109

McQuillin R. C., McLaughlin D. E., 2012, MNRAS, 423, 2162

McQuillin R. C., McLaughlin D. E., 2013, MNRAS, 434, 1332

Merloni A., Fabian A. C., 2001, MNRAS, 328, 958

Merritt D., Ferrarese L., 2001, MNRAS, 320, L30

Miller L., Turner T. J., Reeves J. N., 2008, A&A, 483, 437

Miller L., Turner T. J., Reeves J. N., 2009, MNRAS, 399, L69

Miller L., Turner T. J., Reeves J. N., Braito V., 2010, MNRAS, 408, 1928

Miller L., Turner T. J., Reeves J. N., George I. M., Kraemer S. B., Wingert B., 2007, A&A, 463, 131

Mitsuda K. et al., 2007, PASJ, 59, 1

Mortlock D. J. et al., 2011, Nature, 474, 616

Mosquera A. M., Kochanek C. S., Chen B., Dai X., Blackburne J. A., Chartas G., 2013, The Astrophysical Journal, 769, 53

Mullaney J. R. et al., 2012, ApJL, 753, L30

Nahar S. N., Pradhan A. K., Zhang H. L., 2001, ApJS, 133, 255

Nandra K., 2006, MNRAS, 368, L62

Nandra K. et al., 2013, ArXiv e-prints

Nandra K., Pounds K. A., 1994, MNRAS, 268, 405

Nardini E., Fabian A. C., Reis R. C., Walton D. J., 2011, MNRAS, 410, 1251

Nardini E., Fabian A. C., Walton D. J., 2012, MNRAS, 423, 3299

Nardini E. et al., 2015, Science, 347, 860

Nardini E., Reeves J. N., Porquet D., Braito V., Grosso N., Gofford J., 2014, MNRAS, 440, 1200

Nardini E., Risaliti G., 2011, MNRAS, 417, 2571

Nenkova M., Sirocky M. M., Ivezić Ž., Elitzur M., 2008, ApJ, 685, 147

Nomura M., Ohsuga K., 2016, ArXiv e-prints

Nowak M., 2005, Astrophysics & Space Science , 300, 159

O'Brien P. T., Reeves J. N., Simpson C., Ward M. J., 2005, MNRAS, 360, L25

Odaka H., Aharonian F., Watanabe S., Tanaka Y., Khangulyan D., Takahashi T., 2011, ApJ, 740, 103

Ohsuga K., Mineshige S., 2011, ApJ, 736, 2

Ohsuga K., Mineshige S., Mori M., Kato Y., 2009, PASJ, 61, L7

Osterbrock D. E., 1981, ApJ, 249, 462

Osterbrock D. E., 1989, Astrophysics of gaseous nebulae and active galactic nuclei

Osterbrock D. E., Pogge R. W., 1985, ApJ, 297, 166

Page K. L., O'Brien P. T., Reeves J. N., Turner M. J. L., 2004, MNRAS, 347, 316

Paltani S., Türler M., 2005, A&A, 435, 811

Parker M. L. et al., 2015, MNRAS, 447, 72

Patrick A. R., Reeves J. N., Lobban A. P., Porquet D., Markowitz A. G., 2011a, MNRAS, 416, 2725

Patrick A. R., Reeves J. N., Porquet D., Markowitz A. G., Braito V., Lobban A. P., 2012, MNRAS, 426, 2522

Patrick A. R., Reeves J. N., Porquet D., Markowitz A. G., Lobban A. P., Terashima Y., 2011b, MNRAS, 411, 2353

Pearson K., 1900, Philosophical Magazine Series 5, 50, 157

Peterson B. M., 1997, An Introduction to Active Galactic Nuclei

Petre R., Serlemitsos P. J., 1985, Applied Optics, 24, 1833

Piconcelli E., Jimenez-Bailón E., Guainazzi M., Schartel N., Rodríguez-Pascual P. M., Santos-Lleó M., 2005, A&A, 432, 15

Porquet D., Kaastra J. S., Page K. L., O'Brien P. T., Ward M. J., Dubau J., 2004a, A&A, 413, 913

Porquet D., Reeves J. N., O'Brien P., Brinkmann W., 2004b, A&A, 422, 85

Pounds K. A., Lobban A., Reeves J. N., Vaughan S., Costa M., 2016, MNRAS, 459, 4389

Pounds K. A., Reeves J. N., 2009, MNRAS, 397, 249

Pounds K. A., Reeves J. N., King A. R., Page K. L., O'Brien P. T., Turner M. J. L., 2003, MNRAS, 345, 705

Pounds K. A., Vaughan S., 2011, MNRAS, 415, 2379

Proga D., Kallman T. R., 2004, ApJ, 616, 688

Proga D., Stone J. M., Kallman T. R., 2000, ApJ, 543, 686

Rees M. J., 1984, Annu. Rev. Astron. Astrophys., 22, 471

Reeves J. N. et al., 2014, ApJ, 780, 45

Reeves J. N., Braito V., Nardini E., Behar E., O'Brien P. T., Tombesi F., Turner T. J., Costa M. T., 2016, ApJ, 824, 20

Reeves J. N., Nandra K., George I. M., Pounds K. A., Turner T. J., Yaqoob T., 2004, ApJ, 602, 648

Reeves J. N. et al., 2009, ApJ, 701, 493

Reeves J. N., O'Brien P. T., Vaughan S., Law-Green D., Ward M., Simpson C., Pounds K. A., Edelson R., 2000, Monthly Notices of the Royal Astronomical Society, astro-ph, L17

Reeves J. N., O'Brien P. T., Ward M. J., 2003, The Astrophysical Journal, 593, L65

Reeves J. N., Porquet D., Braito V., Gofford J., Nardini E., Turner T. J., Crenshaw D. M., Kraemer S. B., 2013, ApJ, 776, 99

Reeves J. N., Pounds K., Uttley P., Kraemer S., Mushotzky R., Yaqoob T., George I. M., Turner T. J., 2005, ApJL, 633, L81

Reeves J. N., Turner M. J. L., 2000a, MNRAS, 316, 234

Reeves J. N., Turner M. J. L., 2000b, MNRAS

Reeves J. N., Wynn G., O'Brien P. T., Pounds K. A., 2002, MNRAS, 336, L56

Reines A. E., Volonteri M., 2015, ApJ, 813, 82

Reis R. C., Miller J. M., 2013, The Astrophysical Journal Letters, 769, L7

Reynolds C. S., 1997, MNRAS, 286, 513

Reynolds C. S., Fabian A. C., Brenneman L. W., Miniutti G., Uttley P., Gallo L. C., 2009, MNRAS, 397, L21

Richards G. T., Vanden Berk D. E., Reichard T. A., Hall P. B., Schneider D. P., SubbaRao M., Thakar A. R., York D. G., 2002, AJ, 124, 1

Risaliti G. et al., 2009a, ApJL, 705, L1

Risaliti G., Elvis M., Fabbiano G., Baldi A., Zezas A., Salvati M., 2007, ApJL, 659, L111

Risaliti G. et al., 2009b, MNRAS, 393, L1

Rodríguez-Pascual P. M. et al., 1997, ApJS, 110, 9

Sako M. et al., 2001, A&A, 365, L168

Salpeter E. E., 1964, ApJ, 140, 796

Schmidt M., 1963, Nature, 197, 1040

Schmidt M., Green R. F., 1983, ApJ, 269, 352

Schneider P., 2015, Extragalactic Astronomy and Cosmology: An Introduction

Serlemitsos P. J. et al., 2007, PASJ, 59, 9

Seyfert C. K., 1943, ApJ, 97, 28

Shakura N. I., Sunyaev R. A., 1973, A&A, 24, 337

Shu X. W., Yaqoob T., Wang J. X., 2010, ApJS, 187, 581

Silk J., Rees M. J., 1998, A&A, 331, L1

Sim S. A., Long K. S., Miller L., Turner T. J., 2008, MNRAS, 388, 611

Sim S. A., Miller L., Long K. S., Turner T. J., Reeves J. N., 2010, MNRAS, 404, 1369

Simpson C., Ward M., O'Brien P., Reeves J., 1999, MNRAS, 303, L23

Singh K. P., Garmire G. P., Nousek J., 1985, ApJ, 297, 633

Steenbrugge K. C., Fenovčík M., Kaastra J. S., Costantini E., Verbunt F., 2009, A&A, 496, 107

Strüder L. et al., 2001, A&A, 365, L18

Sturm E. et al., 2011, ApJL, 733, L16

Tadhunter C., 2008, New Astron. Rev., 52, 227

Takahashi T. et al., 2007, PASJ, 59, 35

Takahashi T. et al., 2010, in Proc. SPIE , Vol. 7732, Space Telescopes and Instrumentation 2010: Ultraviolet to Gamma Ray, p. 77320Z

Tanaka Y. et al., 1995, Nature, 375, 659

Tarter C. B., Tucker W. H., Salpeter E. E., 1969, ApJ, 156, 943

Tatum M. M., Turner T. J., Miller L., Reeves J. N., 2013, ApJ, 762, 80

Tatum M. M., Turner T. J., Sim S. A., Miller L., Reeves J. N., Patrick A. R., Long K. S., 2012, ApJ, 752, 94

Telfer R. C., Zheng W., Kriss G. A., Davidsen A. F., 2002, ApJ, 565, 773

Thorne K. S., 1974, ApJ, 191, 507

Titarchuk L., 1994, ApJ, 434, 570

Tombesi F., Cappi M., Reeves J. N., Nemmen R. S., Braito V., Gaspari M., Reynolds C. S., 2013, MNRAS, 430, 1102

Tombesi F., Cappi M., Reeves J. N., Palumbo G. G. C., Braito V., Dadina M., 2011, ApJ, 742, 44

Tombesi F., Cappi M., Reeves J. N., Palumbo G. G. C., Yaqoob T., Braito V., Dadina M., 2010, A&A, 521, A57

Tombesi F., Meléndez M., Veilleux S., Reeves J. N., González-Alfonso E., Reynolds C. S., 2015, Nature, 519, 436

Torres C. A. O., Quast G. R., Coziol R., Jablonski F., de la Reza R., Lépine J. R. D., Gregório-Hetem J., 1997, ApJL, 488, L19

Trump J. R. et al., 2011, ApJ, 733, 60

Turner M. J. L. et al., 2001, A&A, 365, L27

Turner T. J., Miller L., Kraemer S. B., Reeves J. N., Pounds K. A., 2009, ApJ, 698, 99

Turner T. J., Miller L., Reeves J. N., Lobban A., Braito V., Kraemer S. B., Crenshaw D. M., 2010, ApJ, 712, 209

Turner T. J., Pounds K. A., 1988, MNRAS, 232, 463

Turner T. J., Reeves J. N., Kraemer S. B., Miller L., 2008, A&A, 483, 161

Urry C. M., Padovani P., 1995, PASP, 107, 803

Ursini F. et al., 2015, MNRAS, 452, 3266

Vaughan S., Edelson R., Warwick R. S., Uttley P., 2003, MNRAS, 345, 1271

Vaughan S., Reeves J., Warwick R., Edelson R., 1999, MNRAS, 309, 113

Vaughan S., Uttley P., Pounds K. A., Nandra K., Strohmayer T. E., 2011, MNRAS, 413, 2489

Veilleux S., Goodrich R. W., Hill G. J., 1997, ApJ, 477, 631

Veron-Cetty M.-P., Veron P., 1996, A Catalogue of quasars and active nuclei

Vignali C., Comastri A., Nicastro F., Matt G., Fiore F., Palumbo G. G. C., 2000, A&A, 362, 69

Walter R., Fink H. H., 1993, A&A, 274, 105

Wells D. C., Greisen E. W., Harten R. H., 1981, A&AS , 44, 363

Whewell M. et al., 2015, A&A, 581, A79

Wilkes B. J., Elvis M., 1987, ApJ, 323, 243

Wilkes B. J., Tananbaum H., Worrall D. M., Avni Y., Oey M. S., Flanagan J., 1994, The Astrophysical Journal Supplement Series, 92, 53

Wilms J., Allen A., McCray R., 2000, ApJ, 542, 914

Woo J.-H., Urry C. M., 2002, ApJ, 579, 530

Yaqoob T., George I. M., Nandra K., Turner T. J., Serlemitsos P. J., Mushotzky R. F., 2001, ApJ, 546, 759

Yaqoob T. et al., 2007, PASJ, 59, 283

Yaqoob T., Padmanabhan U., 2004, ApJ, 604, 63

Yuan W., Brinkmann W., Siebert J., Voges W., 1998, A&A, 330, 108

Yun M. S., Reddy N. A., Scoville N. Z., Frayer D. T., Robson E. I., Tilanus R. P. J., 2004, ApJ, 601, 723

Zdziarski A. A., Fabian A. C., Nandra K., Celotti A., Rees M. J., Done C., Coppi P. S., Madejski G. M., 1994, MNRAS, 269, L55

Zoghbi A., Fabian A. C., Uttley P., Miniutti G., Gallo L. C., Reynolds C. S., Miller J. M., Ponti G., 2010, MNRAS, 401, 2419

Zubovas K., King A., 2012, ApJL, 745, L34